PHASE FORMATION AND STRUCTURAL TRANSFORMATION OF STRONTIUM FERRITE SrFeO$_x$

BY

Marek Wojciech Schmidt

A thesis submitted for the degree of Doctor of Philosophy
of The Australian National University

THE AUSTRALIAN NATIONAL UNIVERSITY

April 2001

Declaration

This thesis does not incorporate any material previously submitted for a degree, or diploma at any university and to the best of my knowledge and belief, does not contain any material previously published or written by another person except where due reference is made in the text.

Marek W. Schmidt

Acknowledgements

The author would like to thank Prof. J.S. Williams of Department of Electronic Materials Engineering, The Australian National University and Prof. S.J. Campbell of the Australian Defence Force Academy for valuable comments on the manuscript of this thesis. Also I would like to express my gratitude to Dr N.J. Welham of Department of Applied Mathematics, ANU for proofreading of the manuscript, a great deal of advice and help given during the entire PhD course. I would like to thank Mr T. Sawkins of Department of Applied Mathematics, ANU and the crew of the Electronics Unit for excellent technical support. Mr D. Lewellyn, Dr S. Stowe, Mr F. Brink and other members of the Electron Microscope Unit, ANU for their great help with the collection of electron microscope micrographs. Dr G. Foran and Dr J. Hesler of the Australian National Beamline Facility in Tsukuba, Japan for their help with the collection of synchrotron x-ray diffraction patterns. Dr A.J. Studer of the Australian National Science and Technology Organization for his help with neutron diffraction experiments. Ms J. Dalco and Mr J. Irwin of the Computer Unit R.S.Phys.S.E., ANU for their help with computer related matters. The author would also thank others who helped directly or indirectly with the process of creating of this thesis.

Abstract

Non-stoichiometric strontium iron oxide is described by an abbreviated formula $SrFeO_x$ ($2.5 \leq x \leq 3.0$) exhibits a variety of interesting physical and chemical properties over a broad range of temperatures and in different gaseous environments. The oxide contains a mixture of iron in the trivalent and the rare tetravalent state. The material at elevated temperature is a mixed oxygen conductor and it, or its derivatives, can have practical applications in oxygen conducting devices such as pressure driven oxygen generators, partial oxidation reactors in electrodes for solid oxide fuel cells (SOFC).

This thesis examines the behaviour of the material at ambient and elevated temperatures using a broad spectrum of solid state experimental techniques such as: x-ray and neutron powder diffraction, thermogravimetric and calorimetric methods, scanning electron microscopy and Mössbauer spectroscopy. Changes in the oxide were induced using conventional thermal treatment in various atmospheres as well as mechanical energy (ball milling).

The first experimental chapter examines the formation of the ferrite from a mixture of reactants. It describes the chemical reactions and phase transitions that lead to the formation of the oxide. Ball milling of the reactants prior to annealing was found to eliminate transient phases from the reaction route and to increase the kinetics of the reaction at lower temperatures. Examination of the thermodynamics of iron oxide (hematite) used for the reactions led to a new route of synthesis of the ferrite from magnetite and strontium carbonate. This chapter also explores the possibility of synthesis of the material at room temperature using ball milling.

The ferrite strongly interacts with the gas phase so its behaviour was studied under different pressures of oxygen and in carbon dioxide. The changes in ferrite composition have an equilibrium character and depend on temperature and oxygen concentration in the atmosphere. Variations of the oxygen content x were described as a function of temperature and oxygen partial

pressure, the results were used to plot an equilibrium composition diagram. The heat of oxidation was also measured as a function of temperature and oxygen partial pressure.

Interaction of the ferrite with carbon dioxide below a critical temperature causes decomposition of the material to strontium carbonate and $SrFe_{12}O_{19}$. The critical temperature depends on the partial pressure of CO_2 and above the critical temperature the carbonate and $SrFe_{12}O_{19}$ are converted back into the ferrite. The resulting $SrFe_{12}O_{19}$ is very resistant towards carbonation and the thermal carbonation reaction does not lead to a complete decomposition of $SrFeO_x$ to hematite and strontium carbonate.

The thermally induced oxidation and carbonation reactions cease at room temperature due to sluggish kinetics however, they can be carried out at ambient temperature using ball milling. The reaction routes for these processes are different from the thermal routes. The mechanical oxidation induces two or more concurrent reactions which lead to samples containing two or more phases. The mechanical carbonation on the other hand produces an unknown metastable iron carbonate and leads a complete decomposition of the ferrite to strontium carbonate and hematite.

Thermally and mechanically oxidized samples were studied using Mössbauer spectroscopy. The author proposes a new interpretation of the $Sr_4Fe_4O_{11}$ ($x = 2.75$) and $Sr_8Fe_8O_{23}$ ($x = 2.875$) spectra. The interpretation is based on the chemistry of the compounds and provides a simpler explanation of the observed absorption lines. The Mössbauer results from a range of compositions revealed the room temperature phase behaviour of the ferrite also examined using x-ray diffraction.

The high-temperature crystal structure of the ferrite was examined using neutron powder diffraction. The measurements were done at temperatures up to 1273 K in argon and air atmospheres. The former atmosphere protects $Sr_2Fe_2O_5$ ($x = 2.5$) against oxidation and the measurements in air allowed variation of the composition of the oxide in the range $2.56 \leq x \leq 2.81$. $Sr_2Fe_2O_5$ is an antiferromagnet and undergoes phase transitions to the paramagnetic state at 692 K and from the orthorhombic to the cubic structure around 1140 K. The oxidized form of the ferrite also undergoes a transition to the high-temperature cubic form. The author proposes a new structural model for the cubic phase based on a unit cell with the $Fm\bar{3}c$ symmetry. The new model allows a description of the high-temperature cubic form of the ferrite as a solid solution of the composition end members. The results were used to draw a phase diagram for the SrFeO_x system.

The last chapter summarizes the findings and suggests directions for further research.

ADDENDUM

This addendum contains explanations to points raised by examiners.

1. *Question concerning x-ray diffraction lines intensity ratio I(150)/I(161) used to assess iron contamination in section 3.5.1 of the thesis.*

   An intensity ratio of 0.45 for the Fe/Sr=1.01 composition was observed from the x-ray diffraction pattern. Experiments were also conducted on several other samples with different Fe/Sr ratios. In all cases, increasing iron fraction caused an increase in the I(150)/I(161) ratio. Only samples with compositions Fe/Sr=1.01 and 1.05 were shown in the thesis for the sake of brevity to demonstrate the detection threshold. The detection method was designed to screen milled samples and discard those contaminated with iron, not to quantify the contamination level.

   SEM examination of $Sr_2Fe_2O_5$ powders has shown that $Sr_2Fe_2O_5$ microcrystals do not develop facets (see Figure 4.17). As a result, the crystals cannot align during x-ray specimen preparation and cause substantial preferred orientation. The fraction of $Sr_4Fe_6O_{13}$ phase was small and the much larger amount of $Sr_2Fe_2O_5$ should diminish potential orientation of $Sr_4Fe_6O_{13}$ crystals, which should be randomly oriented within $Sr_2Fe_2O_5$ grains.

2. *Question concerning section 3.5.2 of the thesis.*

   During the experimental work the author prepared a variety of Sr-Fe-O samples with compositions in the range 1<Fe/Sr<12 in order to confirm the phase behaviour of the Sr-Fe-O system found in the literature. These experiments were needed to investigate the transient phases occurring during synthesis of $SrFeO_x$ (see section 3.2). Special emphasis was placed on composition ranges around Fe/Sr=1.43 ($Sr_7Fe_{10}O_{22}$) and Fe/Sr=2 ($SrFe_2O_4$). The samples were examined using x-ray diffraction and simple phase identification, based on the diffraction lines, showed that, for these compositions, the Sr-Fe-O system forms only mixtures of two phases, not a single phase as claimed in the cited literature. The lack of the $SrFe_2O_4$ phase was also confirmed by the work of Vogel and Evans [A][1] found after submission of the thesis.

---

[1] The references marked with numerals refer to the bibliography section of the thesis. References marked with letters are additional and are collected at the end of the addendum.

3. *Questions concerning Chapter 6.*

Indexing of the synchrotron diffraction patterns of $Sr_4Fe_4O_{11}$ and $Sr_8Fe_8O_{23}$ yielded ambiguous results, pointing at two or three different crystal structures. The goodness-of-fit obtained during the indexing procedure was similar for all models, making it impossible to choose one structure. Rietveld refinement was not carried out since the internal structures of $Sr_4Fe_4O_{11}$ and $Sr_8Fe_8O_{23}$ are unknown and a multiple-parameter fit could lead to a wrong solution, despite a good fit (see remarks on the Rietveld method in section 2.3.1).

The use of high-resolution neutron diffraction to study $Sr_4Fe_4O_{11}$ and $Sr_8Fe_8O_{23}$ may have its advantages because of a different scattering mechanism that would enhance structural features associated with oxygen.

4. *Questions concerning the choice of symmetry group (Fm3c over Pm3m).*

The problem of the symmetry group of high-temperature cubic $SrFeO_x$ ($x<3$) was addressed because of discrepancies in the literature. Shin *et al.* [159] proposed a perovskite cell for cubic $Sr_2Fe_2O_5$ but later noticed that the cell contains only half the atoms within the oxide molecule ($Z=0.5$) [165]. The unit cell proposed in the thesis (*Fm3c*) does not overturn completely the previous findings but was constructed to incorporate the chemical makeup of the ferrite.

Atoms building the $SrFeO_x$ structure are charged when engaged in forming of a chemical compound. The unit cell is usually chosen to contain at least one chemical molecule, as illustrated in publications dealing with room temperature phases $Sr_2Fe_2O_5$, $Sr_4Fe_4O_{11}$ and $Sr_8Fe_8O_{23}$: the proposed unit cells always contain whole numbers of molecules as depicted by chemical formulae not their fractions [138,139,160,161]. In the case of high-temperature cubic phases, authors tend to use the abbreviated notation $SrFeO_{2.5}$, $SrFeO_{2.75}$ and $SrFeO_{2.875}$ to justify the perovskite model [127,128]. However, the only aspect that changes upon the transition to the cubic form is the arrangement of atoms not the chemical makeup. So, the correct chemical formulae of the high-temperature phases are still $Sr_2Fe_2O_5$, $Sr_4Fe_4O_{11}$ and $Sr_8Fe_8O_{23}$.

The analysis of cubic $SrFeO_x$ was based on the results of the neutron powder diffraction experiments. The analysis began with the $Sr_2Fe_2O_5$ phase and was then extended to the other oxygen deficient phases $Sr_4Fe_4O_{11}$ and $Sr_8Fe_8O_{23}$. Cubic neutron diffraction patterns were indexed and the simplest solution gave the small "perovskite" cell with a lattice constant of about 3.9Å. At this stage no assumption was made as to the atomic layout inside the cell. Since the volume of the cell and the chemical formula of the compound were known, the next step was to assess the number of oxide molecules in the cell. This is a standard procedure in crystal structure determination [56,B]. The number of molecules per cell, Z, the density of crystal ρ, the molecular weight M of the molecule and the volume of the unit cell, V, must fulfill the equation:

$$\rho = \frac{ZM}{N_A V}$$

where N_A is Avogadro's number. This equation was used to determine Z as:

$$Z = \frac{N_A \rho V}{M}$$

This procedure is equivalent to the density argument presented on page 137. Although the density of the high-temperature phases is difficult to measure, the room temperature values are known (see section 6.2) and the density is not expected to change dramatically with temperature (density should decrease due to lattice expansion). Hence, Z was calculated using the room temperature density of $SrFeO_x$ and the results are presented in the table:

x	Formula	M [g/mol]	ρ [g/cm^3]	$V_{PEROVSKITE}$[*] [Å^3]	Z	Comments
2.5	$Sr_2Fe_2O_5$	366.93	4.99	63.14	0.52	Volume from Table A.6, T=1223K
2.75	$Sr_4Fe_4O_{11}$	749.86	5.27	60.28	0.26	Volume from Table A.7, T=838K

The Z values obtained were substantially less than unity and the values were very close to ½ and ¼ respectively. Fractional Z values clearly indicate that the “perovskite” cell, obtained by the direct indexing, is too small. In fact the "perovskite" cell constitutes an asymmetric unit.

The bigger cell (*Fm3c*) was obtained by doubling of the perovskite lattice constant as described in the thesis. The *Fm3c* unit cell contains whole number of molecules in the case of daltonian phases, $Sr_2Fe_2O_5$, $Sr_4Fe_4O_{11}$ and $Sr_8Fe_8O_{23}$, and assures electrical neutrality of the $Sr_2Fe_2O_5$ cell (see arguments on page 138).

---

[*] Volume of the perovskite cell is equal to 1/8 of the *Fm3c* unit cell volume.

The bigger *Fm3c* cell was chosen because it gives a proper description of the crystal structure and the chemical makeup of the compounds. The proposed cell allows a description of phases with intermediate compositions in terms of a solid solution of the daltonian phases as described in the thesis.

The *Pm3m* cell could be regarded as the unit cell only if we treat atoms as colour balls and neglect the fact that they are electrically charged when engaged in forming of a chemical compound.

5. *Questions concerning Equations (4.14-4.22).*

The experimental data did not allow the oxidation of $SrFeO_x$ to be examined over the entire composition range $2.5 \leq x \leq 3.0$ nor an appropriate model to be developed. The composition range was limited to $x \leq 2.75$. Two cases were examined: a complete and a partial oxidation of $Sr_2Fe_2O_5$ to $Sr_4Fe_4O_{11}$ according to the chemical reaction (4.14).

In the case of complete oxidation the reactant and the product of the reaction are pure solids for which the activities are unity by definition. The equilibrium constant of the reaction is a function of oxygen partial pressure only (Equation (4.16)) [51]. However, this treatment of the oxidation reaction is artificial since a departure from the equilibrium conditions does not lead to a total conversion of $Sr_4Fe_4O_{11}$ back to $Sr_2Fe_2O_5$. This simplification was necessary to estimate the line of constant composition $x=2.75$ on the equilibrium composition diagram (Figure 4.6). This is also the reason why the equilibrium constant K given by Equation (4.15) does not go to $1/p_{O2}$ when $x \rightarrow 2.75$ and activities of the solids are given by Equations (4.20-4.22).

In the case of partial oxidation we deal with a mixture/solution of two phases $Sr_2Fe_2O_5$ and $Sr_4Fe_4O_{11}$, which are in equilibrium with each other and the gas phase. Changes to temperature or partial pressure of oxygen only change the concentration (activities) of the two solids. In this case it was necessary to incorporate activities of solids into Equation (4.15) in order to calculate the equilibrium constant.

6. *Question concerning the phrase "Vacant oxygen sites" (p140 lines 11-12).*

The sentence referring to this aspect should be rephrased. The author meant that, since the oxygen sites are partially occupied at any given time, there must be an unoccupied site(s) somewhere in the crystal lattice. Since $SrFeO_x$ is an oxygen conductor, diffusion (hopping) of oxygen between oxygen sites must be easier within the (400) plane than in the perpendicular direction where oxygen sites are separated by iron.

7. *Question concerning a statement (p141 lines 5-7).*

The author meant that crystal structure of any compound can be expressed in terms of a lower symmetry group e.g. Triclinic *P1* (which is true for every structure). This approach is not elegant because we neglect all symmetry relationships in the lattice but it is possible to propose. The sentence did not imply that a division of more symmetric structures by eight would yield a primitive structure.

Additional Bibliography

[A] R.H. Vogel and B.J. Evans. Solid-State and Magneto-Chemistry of the SrO-Fe_2O_3 System. III. The Non-Existence of Single-Phase $SrFe_2O_4$. *J. Magn. Magn. Mater.,* **13**:294-300, 1979.

[B] W. Clegg. *Crystal Structure Determination.* Oxford University Press, Oxford, New York, Tokyo, 1998.

Contents

List of Figures

List of Tables

Chapter 1

Introduction

The topic of this thesis is non-stoichiometric strontium-iron oxide $SrFeO_x$ ($2.5 \leq x \leq 3.0$) commonly called strontium ferrite and the purpose of this chapter is to familiarize the reader with the background associated with this material. The compound is complex and exhibits a variety of interesting properties which become apparent under certain conditions. Obviously the most interesting are those which can be directly used in our everyday life. The material becomes an ionic conductor at elevated temperatures. Because of that, first we are going to briefly describe the history of solid ionic conductors, their applications and possible use of this oxide. This chapter will also show the oxide from another angle as a member of a family of transition metal oxides which are interesting because of their magnetic properties which manifest themselves at room or lower temperatures. The last section will explain the layout of the thesis.

1.1 A Brief History of Solid Ionics

The studied oxide is an ionic conductor at elevated temperatures so it is appropriate to briefly describe the history of solid ionics. This is not by any means a comprehensive history. It is rather a set of dates and important discoveries that lead to the current state of knowledge. The short treatment of this subject is also due to the fact that this thesis does not deal with the electrochemistry of this compound. But, knowledge of applications of the material makes it easier to understand the motivation behind some experiments described in this dissertation. A comprehensive overview of the electrochemistry of solids can be found in various textbooks [1].

Liquid electrolytes are solutions of compounds that dissociate in a given solvent, however, electrolytes are not confined to the liquid state and some solids are also capable of ion conduction. Their ionic conductivity, at room temperature, is approximately 0.1mS/cm while conductivity of most of the wet electrolytes is usually greater than 100mS/cm. For this reason solid electrolytes were identified much later and this branch of electrochemistry developed separately. As it is common in science the solid electrolytes were discovered by accident and at that time were not understood. A series of unrelated experiments lead to establishing the pattern among them and a systematic study from the beginning of the 20th century. The first two solid ionics were discovered between 1833 and 1838 by Michael Faraday [2, 3]. Who found that the resistivity of silver sulphide (Ag_2S) and lead fluoride (PbF_2) significantly decreases at high temperature unknowingly discovering the first solid state silver Ag^+ and fluoride F^- conductors. In 1884 Warburg demonstrated that sodium ions could be transported through glass, an amorphous material [4]. Another important event took place in 1899, Nernst found out that yttrium doped zirconia (ZrO_2) starts conducting electricity at sufficiently high temperatures, emitting bright light due to ability to conduct oxide ions [5]. The ‘Nernst glower’ remains one of the few non-electrochemical applications of the solid ionics. In 1914 Tubandt and Lorentz studied the ionic conductivity of silver iodide (AgI) and discovered that the conductivity just below the melting point was greater than the molten material [6]! This behaviour is one of many curiosities found among solid ionics, where ions have more freedom of movement in a solid matrix than in the liquid state where they are not constrained by the crystal structure. The first solid oxide fuel cell (SOFC), based on doped zirconia, was built in 1937 by Bauer and Preis [7]. The theoretical description of ionics was developing concurrently but was limited to purely ionic conductors. This changed in the 1950s when Carl Wagner developed a theory of transport in mixed ionic conductors, materials which exhibit electronic conductivity apart from the ionic component [8]. The theory was later expanded by W. Weppner. Until the 1960s the study of ionic conductors was largely confined to doped ZrO_2 and Ag^+ conductors such as AgI. The late 1960s and beginning of 1970s saw an explosion of interest in solid state chemistry. The increased interest in this field was caused by the development of new materials used to manufacture of very efficient rechargeable sodium/sulphur batteries. They were based on the solid sodium conductor, sodium β-alumina. The oil crisis in the early 1970s sealed the fate of solid ionics. The fuel deficiency focused attention on new energy sources and storage devices and the research of ionics has been developing very rapidly ever since.

Despite humble beginnings, we now know a large number of solid electrolytes and they are not limited to the crystalline state. Glasses exhibit quite high ionic conductivity and they are capable of transporting monovalent alkali ions Li^+, Na^+, K^+, Cs^+, Rb^+ as well as Ag^+ and F^-. Crystalline electrolytes can conduct monovalent alkali and transition metals (Ag^+, Cu^+, Tl^+, Li^+, Na^+, K^+), H^+, O^{2-}, F^- and many divalent and trivalent cations. The third new and very promising group are the polymer electrolytes. They are rapidly gaining interest because of their possible application in very powerful batteries [1].

1.2 Applications of Solid Ionics

Several applications of solid ionics have already been mentioned in the previous section. The electrolytes are mainly used in rechargeable and disposable batteries. The numbers of portable electric devices is steadily growing, increasing the demand for smaller and more efficient devices. They have a lot advantages over the liquid ones. To start with there is no problem with electrolyte leakage and evaporation. Solid cells are more compact, robust and can operate in higher temperatures than the liquid ones and for these reasons are used in circuits that require high level of reliability such as pacemakers and backup power sources for computer memories.

The most important quality is their energy capacity and Table 1.1 compares a practical energy density of an ordinary lead-acid battery with solid electrolyte devices. The capacities of the solid batteries are 3 to 10 times greater than of the traditional cell although, the lead battery is still a cheaper option. Other, very important applications are fuel cells and oxygen sensors which will be described later in this chapter. Less known usage of solid ionics are stabilized zirconia heating elements. The material (stabilized zirconia)

Table 1.1: Practical energy densities of liquid and solid state batteries.

Battery	Energy density [Wh/kg]
lead-acid	40
sodium/sulphur	132
lithium polymer	425

exhibits large enough electronic conductivity to spontaneously conduct electricity at about 1373 K and this process causes self heating. Being an oxide the heating elements can operate in oxidizing atmospheres without deterioration. Furnaces equipped with the 'Nernst glower' operate above 2273 K and tests conducted at 2073 K have shown the elements can operate in oxidizing conditions for more than 10,000 h. Another potential application utilizes the conductivity and high melting point of zirconia as electrodes in experimental magnetohydrodynamic generators (MHD) working on hot exhaust gases. The use of these could increase the efficiency of conventional power plants from 42 % to 60 % [9]. Other materials, such as WO_3 or MoO_3, can be electrochemically reduced or oxidized by electric current. The process changes their colour or opacity a feature which is exploited in passive 'electrochromic' displays for portable computers. These are the well known application of solid ionics. In the next two sections we will concentrate on oxygen conductors to which the studied ferrite belongs to.

1.3 Oxygen Conducting Devices

The class of oxygen conductors has a very broad range of applications. Ionic conductors can be divided into two groups according to the conductivity. The first group comprises of pure ionic conductors having an ionic transport number t_{ion} of almost unity. The transport number is defined as the ratio of the ionic conductivity σ_i to the total conductivity σ, where $\sigma = \sigma_i + \sigma_e$ and σ_e denotes the electronic conductivity. The second group, mixed conductors, exhibit both ionic and the electronic conductivity. The presence or absence of the electronic component determines their possible use.

1.3.1 Pure Ionic Conductors

A schematic diagram of an oxygen conducting device based on the pure ionic conductor is presented in Figure 1.1. It consists of a membrane made of the solid electrolyte with porous electron conducting electrodes applied on both sides of the wall. In real devices the electrolyte has the form of a tube, a crossflow block or a stack made of corrugated electrolyte to increase the surface area exposed to gas [10].

Assuming, an oxygen partial pressure difference between the sides of the wall $p_1 > p_2$, the setup presented in Figure 1.1 constitutes a galvanic cell

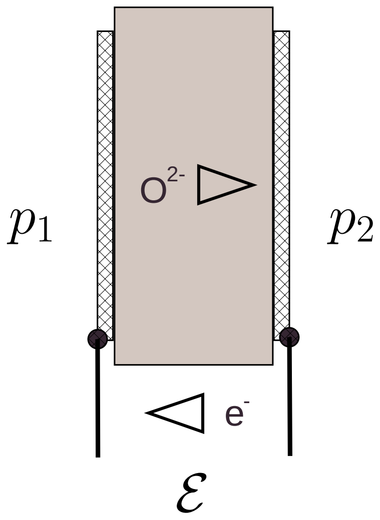

Figure 1.1: A schematic of a pure ionics electrochemical device described in the text. The conduction mechanism is not shown.

that can be schematically represented as:

$$\mu'_X/\mathrm{MX}/\mu''_X \tag{1.1}$$

where M and X denote metal and nonmetal of the MX electrolyte respectively. The potential difference $\mathcal{E}$ between the electrodes can be found using the equation:

$$\mathcal{E} = \frac{1}{Z_X F}\int_{\mu'_X}^{\mu''_X} t_{ion} d\mu = -\frac{1}{Z_M F}\int_{\mu'_M}^{\mu''_M} t_{ion} d\mu_M \tag{1.2}$$

where F denotes the Faraday constant, Z is the valence (number of electrons transferred per molecule, $Z_X = 4$ for O_2) and μ' and μ'' are the chemical potentials of the anode and the cathode respectively. In case of pure ionics $t_{ion} = 1$ Equation (1.2) simplifies to:

$$\mathcal{E} = \frac{\mu''_X - \mu'_X}{Z_X F} = -\frac{\mu''_M - \mu'_M}{Z_M F}. \tag{1.3}$$

The chemical potential of oxygen μ can be expressed as:

$$\mu = \mu^\circ + RT\ln a \tag{1.4}$$

where a is the activity and μ° is the chemical potential of oxygen at unit activity. If we assume that oxygen behaves like an ideal gas the activity is equal to its partial pressure $a = p$. Therefore, the emf of the cell, calculated by substituting Equation (1.4) into Equation (1.3), is given by:

$$\mathcal{E} = \frac{RT}{4F} \ln \frac{p_1}{p_2} \tag{1.5}$$

This formula proves that the oxygen conducting device can be used to generate electric power. By keeping the constant oxygen partial pressure difference at fixed temperature we can maintain the potential $\mathcal{E}$. This is done by introducing a gas which reacts with oxygen inside the tube, keeping its partial pressure low. At zero current there is no transport of oxygen through the wall. If we start to draw current on the oxygen rich side oxygen is reduced according to the reaction:

$$\mathrm{O_2 + 4\,e^- \rightarrow 2\,O^{2-}} \tag{1.6}$$

then it travels through the electrolyte and is oxidized at the oxygen deficient side:

$$\mathrm{2\,O^{2-} - 4\,e^- \rightarrow O_2}. \tag{1.7}$$

Electrons flow through the external leads. The enormous interest in fuel cells is due to their very high thermodynamical efficiency as a source of electric power and very favourable energy to mass ratio. They are considered to be the power generators for remote places and power sources on spacecrafts (NASA's spaceships in the Apollo missions were actually equipped with 1.5 kW alkali fuel cells).

The thermodynamic (theoretical) efficiency factor η for a chemical reaction that binds oxygen is given by:

$$\eta \equiv \frac{\Delta \mathrm{G}}{\Delta \mathrm{H}} \tag{1.8}$$

where, ΔG and ΔH are the change of Gibbs free energy and the enthalpy of the reaction respectively. The maximum efficiency of heat engines is given by the equation derived for the Carnot cycle:

$$\eta \equiv \frac{T_2 - T_1}{T_2} \tag{1.9}$$

where, T_1 is the temperature of the heat sink and T_2 is the temperature of the heat source. A comparison of the efficiencies of the Carnot cycle and

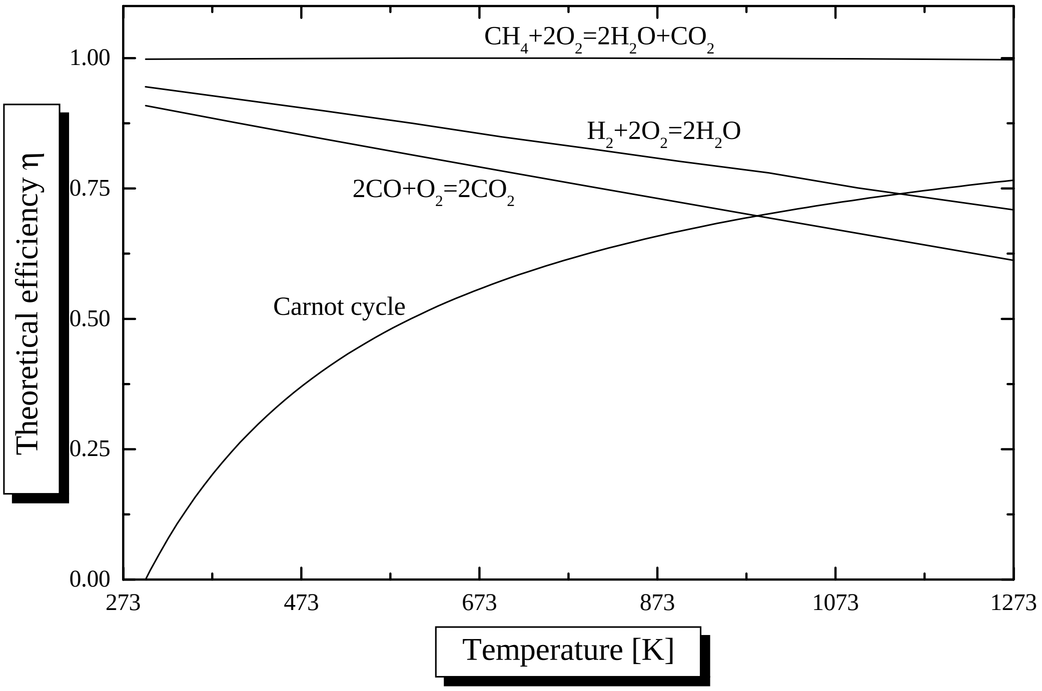

Figure 1.2: Theoretical efficiency of a perfect heat engine and fuel cells as a function of temperature. The efficiency was calculated for different oxidation reactions and the Carnot cycle as described in the text.

fuel cells completely oxidizing: hydrogen, carbon monoxide and methane is presented in Figure 1.2 as a function of temperature. The efficiency of the heat engine was calculated assuming that $T_1 = 298.15\,\mathrm{K}$ and the chemical reactions occur in the gas state according to the equations:

$$2\,\mathrm{H_2} + \mathrm{O_2} = 2\,\mathrm{H_2O} \tag{1.10}$$

$$2\,\mathrm{CO} + \mathrm{O_2} = 2\,\mathrm{CO_2} \tag{1.11}$$

$$\mathrm{CH_4} + 2\,\mathrm{O_2} = \mathrm{CO_2} + 2\,\mathrm{H_2O} \tag{1.12}$$

The theoretical efficiency of fuel cells is much greater than the heat engines other than for the high temperature range ($T > 873\,\mathrm{K}$). However, one should bear in mind that these coefficients are only theoretical and real devices are less effective. Even though the oxidation of methane gives the highest efficiency in practice, it causes problems due to coke formation. Real heat engines (turbines in electric power plants) have efficiencies around 0.42 and the practical efficiency of fuel cells is greater than 0.60 [11] and makes them very competitive. However, the solid oxide fuel cells are still in the research

Table 1.2: Operational modes of the solid oxide fuel cell. The first two columns show chemical reactions taking place at the electrodes. The FC and ER denote fuel cell and electrochemical reactor respectively. OD=oxide decomposition, PO=partial oxidation, OE=oxygen extraction from air.

Electrode 1	Electrode 2	Mode
$\frac{1}{2}O_2 + 2\,e^- \rightarrow O^{2-}$	$O^{2-} + H_2 \rightarrow H_2O + 2\,e^-$	FC
$H_2O + 2\,e^- \rightarrow H_2 + O^{2-}$	$O^{2-} \rightarrow \frac{1}{2}O_2 + 2\,e^-$	ER,OD
$\frac{1}{2}O_2 + 2\,e^- \rightarrow O^{2-}$	$O^{2-} + \frac{1}{4}CH_4 \rightarrow \frac{1}{4}CO_2 + \frac{1}{2}H_2O + 2\,e^-$	FC
$\frac{1}{2}O_2 + 2\,e^- \rightarrow O^{2-}$	$O^{2-} + 2\,CH_4 \rightarrow C_2H_6 + H_2O + 2\,e^-$	ER,PO
$\frac{1}{2}O_2(N_2) + 2\,e^- \rightarrow O^{2-}$	$O^{2-} \rightarrow \frac{1}{2}O_2 + 2\,e^-$	ER,OE
$\frac{1}{2}O_2 + 2\,e^- \rightarrow O^{2-}$	$O^{2-} + CH_4 \rightarrow CO + 2\,H_2 + 2\,e^-$	ER,PO

and development phase. The prototype SOFCs tested by Westinghouse had a power of ~3 kW. Other types of fuel cells based on liquid electrolyte (phosphoric acid PAFC and alkali solution AFC) are much more advanced and their test units reach powers of 11 MW and 25 kW respectively. However, they only operate on hydrogen, do not tolerate carbon dioxide and their electrodes contain expensive platinum catalyst [12, 13].

The solid oxide fuel cells can also operate in a ‘reverse’ mode as ceramic electrochemical reactors (CER). The cell can force the oxidation reaction to proceed in the opposite direction and be used as a high temperature electrolysers to produce hydrogen, decompose gaseous oxides or to extract oxygen from air (oxygen generators). This is accomplished by applying a potential equal or greater than the value:

$$\mathcal{E} = -\frac{\Delta G}{ZF}. \tag{1.13}$$

The ceramic reactors can also partially oxidize hydrocarbon to produce other chemicals. Usually the partial oxidation reactions require a catalyst for the reaction to proceed. Some possible modes of operation are presented in Table 1.2 [11, 14].

The devices described so far use an ion flux through the membrane to operate but are still in the research and development stage. The setup shown in Figure 1.1 is more frequently used as a potentiometric (zero current) probe to measure oxygen activity in gases or molten metals. In this instance one electrode is exposed to the environment under investigation and the other to an atmosphere with known oxygen activity. The reference atmosphere is usually air but sometimes solid oxygen partial pressure buffers are used (*e.g.*

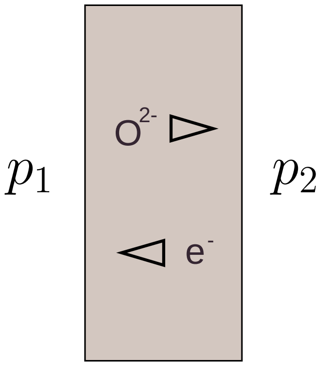

Figure 1.3: A schematic of a mixed ionics electrochemical device described in the text. The conduction mechanism is not shown.

mixture of Cr_2O_3 and Cr). The oxygen pressure is determined by measurement of the emf $\mathcal{E}$ from the Equation (1.5). This device known as a λ-probe is used in all fuel injected engines to monitor oxygen content in exhaust gases.

1.3.2 Mixed Ionic Conductors

Mixed ionic conductors have an ionic transport number smaller than unity $t_{ion} < 1$ and the ferrite $SrFeO_x$ belongs to this group. The electronic conductivity renders the oxides useless as materials for fuel cell electrolytes or potentiometric sensors since such devices would have internal electric shortcuts, although they are still quite attractive. The ionic conductivity of stabilized zirconia is around 0.1 S/cm at 1273 K and the ionic conductivity of mixed electrolytes is approximately 20 times greater. The schematic diagram of an oxygen conducting device based on the mixed conductor is presented in Figure 1.3. The device consist only of the electrolyte membrane and both oxygen ions and electrons are free to move within the electrolyte. If we assume again that there is an oxygen partial pressure difference on both sides of the wall $p_1 > p_2$, oxygen will spontaneously travel from the rich to the deficient side. Electrons now travel through the electrolyte in the opposite direction to compensate the charge.

This arrangement has a few potential applications. It can be used to build a pressure driven oxygen generator to separate oxygen from air or other gas mixtures. Since oxygen moves from high to low partial pressure, for the membrane to work we have to maintain high conductivity by keeping it at elevated temperature and oxygen partial pressure difference. The pressure inside has to be lower than 0.21 atm (the oxygen partial pressure in air) which can be easily achieved by a basic vacuum pump. Such devices are believed to be ideal for small scale oxygen generation for medical and aerospace purposes. Another use of these materials are ceramic electrochemical reactors (CER). Because of the electronic conductivity the materials can not be used as fuel cells or reduction cells (electrolyzer) but still can operate as catalytic partial oxidation reactors (see Table 1.2) [14]. Electronic conductivity and high oxygen permeability makes these materials perfect as a replacement for precious metal electrodes used in solid oxide fuel cells.

1.4 Complex Transition Metal Oxides

The ferrite can be considered not as an oxygen conductor but as a complex transition metal oxide as well. It exhibits interesting magnetic, structural and transport properties at temperatures where its ionic conductivity is negligibly low. In the 1950s this class of materials came into focus in the search for new magnetic materials. The compound belongs to the family of oxides that can be described by the general formulae: $A^{2+}B^{4+}O_3^{2-}$ or $A^{3+}B^{3+}O_3^{2-}$, where A=divalent alkali metal (Ca, Sr or Ba), or lanthanide a trivalent cation and B=Mn, Fe or Co. If the site A is occupied by lanthanide the transition metal in the site B has valence 3+. On the other hand if the lanthanide is replaced by a divalent alkali metal the transition metal ideally assumes 4+ oxidation state. However, in practice manganese, iron and cobalt in these compounds exhibit mixture of 3+ and 4+ oxidation states virtually irrespective of the oxidation state of the ion in site A. This results in a variable oxygen content, typically different from ABO_3 depending on the preparation conditions [15, 16].

In the 50s the compounds were treated as materials with the ideal composition ABO_3 since most of them have cubic perovskite structure or its less symmetric derivative [17]. The oxygen non-stoichiometry was not investigated in a systematic way, but its presence and influence on the physical properties was realized. In general all of those compounds exhibit some degree of oxygen non-stoichiometry and their composition is controlled by oxygen partial pressure and temperature. The effect is by far the most pronounced in iron and cobalt bearing systems which include $SrFeO_x$, $CaFeO_x$ [18–20], $BaFeO_x$ [21–24] or $SrCoO_x$ [25,26] and their derivatives. Early investigations were focused on the magnetism of the materials and the electrical conductivity at low temperatures [27–29]. The ionic conductivity of the oxides was detected much later [30,31]. Today the investigations of these systems are not confined to simple formulae and usually have the form: $\mathrm{A'_xA''_{1-x}B'_yB''_{1-y}O_{3-\delta}}$, where A′, A″ are alkaline metals or mixture of alkaline metal and lanthanide, B′, B″ are transition metals, or even more complex systems. The simpler oxides are no longer attractive from the electrochemical point of view but they again came into focus because of their newly discovered transport properties. Most of the ABO_3 oxides investigated in the 50s and 60s were discarded because of their impractical magnetic properties and, later, its relatively low ionic conductivity. But recently they were found to exhibit an interesting kind of magnetoresistance - colossal magnetoresistance, the greatest changes in electrical resistivity caused by the magnetic field. So far the materials known to exhibit colossal magnetoresistance are mainly manganese based oxides [32–34].

The composition of non-stoichiometric oxides is usually expressed using the notation $ABO_{3-\delta}$ or ABO_x. It implies that the oxide can exist in slightly oxygen depleted form. However, in many cases the possible composition changes are so large that the oxides form few distinctive different phases. The abbreviated notation ABO_x, very useful for presenting the experimental data, does not describe the real chemical formula of phases with $x < 3$. An improper usage of this notation can be a source of serious errors in the interpretation of experimental results.

1.5 Strontium-Iron-Oxygen System

This thesis is devoted to only one kind of ferrite ($SrFeO_x$) but it is virtually impossible to avoid other phases which show up as transient phases or byproducts in various reactions. For these reason we will briefly describe this system. The $SrFeO_x$ contains iron in an unusual 4+ oxidation state which is nowhere to be found in pure iron oxides. But, this is not the only strontium ferrite which possesses this quality. A number of oxides having a strontium to iron ratio greater than 1 also exhibit oxygen non-stoichiometry and mixed 3+ and 4+ valence. A ternary diagram of Sr-Fe-O system, based on information found in the literature, is presented in Figure 1.4. The literature references pertaining to those oxides are presented in Table 1.3. The table does not contain references to $SrFeO_x$ phase which will be presented further in this work and only two out of dozens of references on the magnetic phase $SrFe_{12}O_{19}$. The diagram is most likely complete. The $SrFe_{12}O_{19}$ phase is a

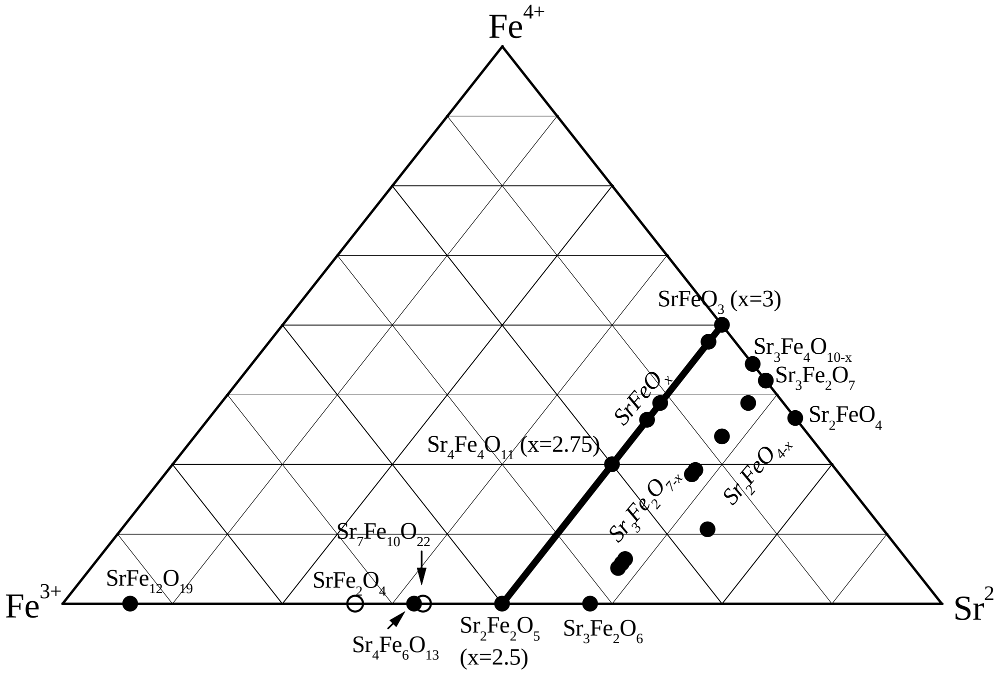

Figure 1.4: The ternary diagram for the Sr-Fe-O system. The references to the compounds are contained in Table 1.3, the symbols are described in the text. The investigated $SrFeO_x$ system is marked with the bold line.

component of permanent magnets and because of that the entire composition range was very thoroughly searched in order to find other ferromagnetic phases. Unfortunately the rest of ferrites are either antiferromagnets or paramagnets at room temperature and therefore useless for industry. However, some reported phases are questionable and are marked on the ternary plot as open circles. During the work on the non-stoichiometric ferrite system ($SrFeO_x$) some experiments indicated that $SrFe_2O_4$ and $Sr_7Fe_{10}O_{22}$ phases do not exist and are mixtures of two nearest phases on the ternary diagram.

Table 1.3: Literature references to strontium ferrites. The references to the $SrFeO_x$ system are presented in the text.

Oxide	References
$Sr_4Fe_3O_{10-x}$	[35]
$Sr_3Fe_2O_{7-x}$, $(0 \leq x \leq 1.0)$	[35–40]
Sr_2FeO_{4-x}	[37, 41, 42]
$Sr_7Fe_{10}O_{22}$	[35, 43]
$Sr_4Fe_6O_{13}$	[44, 45]
$SrFe_2O_4$	[46, 47]
$SrFe_{12}O_{19}$	[47, 48]

1.6 Thesis Layout

Previous sections have demonstrated the wide range of physical properties exhibited by the ferrite which are temperature and composition dependent. The compound has been investigated for over four decades and a continuous increase of knowledge is due to advances in instrumentation.

The knowledge gathered over this time can be divided into four general groups covering the crystal structure of the compound, transport properties at low as well as elevated temperatures, the electronic and magnetic structure and finally the interaction of the material with gaseous species. The reports published so far deal with all those properties however, they are far from a complete description and understanding of the oxide and often draw incorrect conclusions. The work presented in this thesis concentrates on the properties of the oxide at ambient and high temperatures. This thesis provides a thorough study of the non-stoichiometric system and insight into areas previously untouched using a broad range of experimental techniques. It presents a more complete description of already reported properties with new interpretation or completely new models of observed phenomena. The author based the interpretation on experimental results to avoid faults introduced by preconceptions or invalid assumptions. Of course the dissertation does not provide an answer to every possible question and does not completely cover all the properties of the material. On the contrary the present study has indicated aspects of the system which need to be clarified further.

The structure of the thesis is dictated by the experimental work and most of the presented results are interconnected. The second chapter presents a brief description of the main experimental techniques and numerical methods used in the thesis. Chapter 3 deals with the formation of the oxide from a mixture of reactants and describes the influence of the environment and the physical state of reagents on the synthesis route and its kinetics. It also reports a new route of synthesis deduced from analysis of the existing one. The oxide has variable oxygen content which is controlled by temperature and the composition of atmosphere, and the study of the oxygen non-stoichiometry is essential for understanding the properties of the oxide at elevated temperatures. Chapter 4 presents the interaction of the material with oxidizing atmospheres and carbon dioxide. It describes the behaviour of the material induced by temperature as well as mechanical treatment at ambient temperature. It also provides practical information on how to measure and adjust the composition of samples later used for structural studies. Chapter 5 presents the results of Mössbauer measurements done at room temperature on samples with composition altered by annealing and mechanical treatment. It provides a great help in studies of room temperature phases of SrFeO_x presented in Chapter 6. Finally the last experimental part (Chapter 7) contains a study of the high temperature crystal and magnetic structures of the oxide. It makes extensive use of the equilibrium composition of the oxide determined in Chapter 4. This part of the work proposes a new structural model for the high-temperature form of the oxide which allows a comprehensive description of the crystal lattice. The final chapter presents the main conclusions and recommends directions for further research.

Chapter 2

Experimental

This chapter provides a brief description of experimental methods used in the thesis. The information is provided in a short form just to refresh the reader's knowledge on the subject. Further details can be found in a wide range of textbooks on inorganic chemistry and physics [49–51] and specialized monographs cited in the text.

The oxide was studied using a wide range of experimental methods covering many properties of the material. They can be divided into groups such as the thermodynamical properties studied using thermogravimetric and calorimetric techniques. The crystal structure was investigated using x-ray and neutron powder diffraction at ambient and elevated temperatures. The results of the scattering experiments were analysed, among other methods, using Rietveld refinement. The structural study was also enhanced by results of Mössbauer measurements. The morphology of the material was investigated with scanning electron microscopy and measurements of the specific surface area of the powders. The analysis was also enriched by magnetization measurements and some thermodynamical modelling.

2.1 Thermogravimetry

Thermogravimetric analysis provides information about the mass change of the sample caused by temperature or partial pressure of gaseous species in the atmosphere. The analyser is an automatic balance. The sample is placed in a furnace with controlled atmosphere and its mass and temperature are recorded as a function of time. The mass changes are due to loss or gain of the gas phase and the device is used to study solid-gas reactions such as oxidation, reduction, decomposition or investigation of equilibrium compositions. The instrument used in this thesis was a computer controlled Shimadzu TGA-50 analyser. The balance allows maximum load of 200 mg and the manufacturer claims it has 1 % accuracy. The balance can operate using various gases at atmospheric pressure over a temperature range from room temperature up to 1773 K [52].

2.2 Calorimetry

The calorimeters used in the thesis were a differential thermal analyser (Shimadzu DTA-50) and a differential scanning calorimeter (Shimadzu DSC-50).

The difference between the DTA and the DSC is in the design of the measuring cell and as a result the temperature range they cover. The DTA measures the temperature difference using a differential thermocouple and its signal is measured in microvolts. This design allows measurements in the temperature range of 273–1773 K. The DSC measures the temperature difference and compensates the energy change between the sample and the reference using the Peltier effect. This approach makes the heat measurements much more precise. The instrument can operate in the temperature range from 93 K to 973 K [53, 54].

The sample and the reference are typically heated with constant heating rate of 5–30 K/min in a controlled atmosphere. Ideally the sample and the reference should have similar heat capacity. The differential signal indicates a physical or chemical transformation in the sample. All transformations involve evolution or absorption of heat directly or due to large changes in the heat capacity. The method is ideal for determination of phase transition temperatures and temperatures of chemical reactions. It also allows measurements of the heat of transformation.

The differential signal $\partial H/\partial \tau$ is proportional to the heat capacity of the sample C_p and the heating rate $\partial T/\partial \tau$:

$$\frac{\partial H}{\partial \tau} = \frac{\partial H}{\partial T}\frac{\partial T}{\partial \tau} = C_p\frac{\partial T}{\partial \tau} \tag{2.1}$$

where, H is the enthalpy and τ denotes time. The total energy of transformation ΔH is proportional to the area of the transition peak and the heat is obtained by integration of the signal over time after subtraction of the baseline:

$$\Delta H = \int \frac{\partial H}{\partial \tau} d\tau \tag{2.2}$$

However, the raw signal comprises of contributions from the sample, the difference in heat capacities between the sample and the reference and an instrumental contribution. The signal from the sample can in theory be separated by subtracting the results of an empty run in the same conditions. However, the mechanical make-up of the instruments did not allow such experiments and they were used only for pinpointing of phase transitions and establishing of their energies.

2.3 X-Ray and Neutron Powder Diffraction

X-ray and neutron diffraction is extensively used in this thesis not only for identification of the crystal phases but also in order to solve the crystal structure of the oxide and extract the information about the crystal size and strain. This section provides an overview of methods with much more detailed description given in the rich literature cited in this chapter.

The scattering experiments produce spectra with peaks corresponding to the characteristic inter-planar distances d in the crystal. The relationship between the d-spacing and the scattering angle θ is given by the Bragg's law:

$$n\lambda = 2d_{hkl}\sin\theta_{hkl} \tag{2.3}$$

However, the ultimate aim of crystallography is to determine the electron density or nuclear and spin density $\rho(x, y, z)$ in the unit cell. This is equivalent to providing the distribution of atoms (ions) in the cell. The density is given by the formula:

$$\rho(x, y, z) = \frac{1}{V}\sum_{h,k,l} F_{hkl}e^{-2\pi i(hx+ky+lz)} \tag{2.4}$$

where h, k, l are the Miller indexes of reflection, F_{hkl} is the structure factor and V is the volume of the unit cell. The structure factor in the general case is a complex number and can be expressed in the form of the modulus $|F_{hkl}|$ and the phase α_{hkl}:

$$F_{hkl} = |F_{hkl}|e^{2\pi i\alpha_{hkl}} \tag{2.5}$$

This allows us to rewrite Equation (2.4) in the form:

$$\rho(x, y, z) = \frac{1}{V}\sum_{h,k,l} |F_{hkl}|e^{-2\pi i(hx+ky+lz-\alpha_{hkl})} \tag{2.6}$$

The measured intensities of the diffraction lines are proportional to $|F_{hkl}|^2$ but the information about the phases is lost. This shortage of information constitutes the *phase problem*, the basic challenge of crystallography [55,56]. The difficulty in determination of the crystal structures lie in reconstructing the missing phases from the diffraction data and other physical and chemical properties of the crystal. In the ideal situation the diffraction experiment is done using a single crystal which yields a large set of observed intensities. The number of reflections is usually in order of 10,000 and they are not overlapping. They are subsequently indexed and in favourable cases the extinction conditions point at one symmetry group. The extracted structure factors are then used in the structure solution. Over years of experience a number of methods had been developed to cope with the phase problem. These are the trial and error method, Fourier synthesis, Patterson functions or direct methods. The use of a particular solution path is usually dictated by properties of the specific crystal [55–59]. Once the coordinates of atoms are found their positions and temperature factors are refined so the calculated line intensities match the observed values. However, this is the ideal situation and in many cases, for variety of reasons, it is not possible to grow a single crystal of sufficient size for the single crystal experiments. The structural data in this instance has to be extracted from powder diffraction patterns.

The solution of the crystal structure from the powder pattern is in general much more difficult. The single crystal techniques control the orientation of the crystal during the experiment scattering and the reflections are spatially resolved. The powder method on the other hand collects the data from large number of randomly oriented microcrystals which creates problems. To start with all (hkl) reflections with the same d-spacing occur at the same scattering angle 2θ determined by Equation (2.3), moreover in many cases reflections with similar d-spacing overlap making it impossible to establish the intensities of all components. The number of lines that can yield reliable structure factors is often less than 100. Highly symmetric structures can be readily solved since the reflections, apart from those with exactly the same d-spacing, usually do not overlap. Low symmetry structures require the use of diffractometers with as high as possible instrumental resolution which usually reduces the severity of the overlap. The structure factors are extracted using whole pattern fitting procedures devised by Pawley [60] and Le Bail [61]. Once the structure factors are known the atomic makeup is usually derived using the same methods as for single crystal data. The diffraction data can be additionally enriched with information from other sources such as knowledge about the bond lengths between specific atoms or the shape of the molecule obtained from other sources such as spectroscopy. This additional information can be incorporated using so called soft restraints and rigid body refinement [62]. Once the structural model exists the positions and the temperature factors of atoms are refined using the Rietveld method. It must be stressed, however, that the structure solution from powder data is not always successful since due to its nature of the experiment a great deal of information is lost which often leads to ambiguous results. The powder diffraction method apart from the structural layout provides additional information about the chemical composition of the sample, its crystal size, strain and texture [63, 64].

2.3.1 The Rietveld Method

This method was developed over 30 years ago by H.M. Rietveld to analyse neutron powder patterns [65] and it was soon adapted for analysis of x-ray powder pattern. However, the technique requires a model of atom distribution in the unit cell very close to the actual positions. It should be stressed that it is not a ‘black box’ for crystal structure solution but a very useful tool for refinement of the structural parameters. The refinements presented in this thesis were carried out using “General Structure Analysis System” (GSAS) a well established and tested program [66]. The refinement program generates a diffraction pattern using the initial model and modifies the variables to obtain the best fit by minimizing the residual S_y:

$$S_y = \sum_i w_i (y_i - y_{ci})^2 \tag{2.7}$$

where y_i is the observed intensity at the ith step, $w_i = 1/y_i$ and y_{ci} is the calculated intensity at the ith step. The sum runs over all experimental points. By its nature the method can handle patterns with very severe line overlap. The calculated intensities y_{ci} are determined by summing contributions from neighbouring Bragg reflections and the background using structure factors F_{hkl} calculated from the model. The calculated intensities also contain the factors characteristic for particular instrumental geometry and physical properties of the sample other than crystal structure (particle shape and size, chemical composition):

$$y_{ci} = s \sum_{h,k,l} L_{hkl} |F_{hkl}|^2 \psi(2\theta_i - 2\theta_{hkl}) P_{hkl} A + y_{bi} \tag{2.8}$$

where s is the scale factor, L_{hkl} contains Lorentz polarization factor and multiplicity of reflection, ψ represents the profile of the reflection, P_{hkl} is the preferred orientation function, A is the absorption factor and y_{bi} is the intensity of the background in the ith step. The least squares minimization process leads to a set of normal equations involving derivatives of all calculated intensities y_{ci} with respect to each adjustable parameter x_j. The solution is obtained by inversion of the normal matrix with elements M_{jk} given the formula:

$$M_{jk} = -2 \sum_i w_i \left[(y_i - y_{ci}) \frac{\partial^2 y_{ci}}{\partial x_j \partial x_k} - \frac{\partial y_{ci}}{\partial x_j} \frac{\partial y_{ci}}{\partial x_k} \right] \tag{2.9}$$

Since the residual function is non-linear the solution is found by an iterative procedure which calculates the parameter shifts:

$$\Delta x_k = \sum_j M_{jk}^{-1} \frac{\partial S_y}{\partial x_k} \tag{2.10}$$

The calculated shifts are applied to the initial values and they should, at least in theory, produce an improved model. The procedure is then repeated and the refinement is finished when the magnitude of shift changes fulfills the termination conditions. Because the problem is non-linear incorrect initial values of the refined parameters can lead to a divergence of the refinement or in very unfavourable situations to a false minimum. This danger is real not only for the Rietveld method but for all non-linear fitting procedures. The false minimum problem can usually be alleviated by using multiple data sets collected using different techniques or introduction of constraints on the refined parameters. However, caution should be excised during the refinement to avoid this trap. The method also requires additional information about the experimental geometry and state of the sample which have to be properly implemented. For this reason apart from the structural parameters a number of instrumental variables are simultaneously refined. The refinable phase and global parameters are presented in Table 2.1 and Table 2.2 respectively. The actual number of refined parameters depends on the specific instrument geometry and the sample. In many cases some of them can be

Table 2.1: Refinable phase parameters in the Rietveld method, separate set required for each phase.

x_i, y_i, z_i	Coordinates of ith atom in the unit cell. The coordinates may be fixed by the symmetry group
N_i	Site occupancy parameter
U_{iso} or u_{mn}	Isotropic or anisotropic temperature factors. Refinement from neutron data usually gives more reliable results.
s	Scale factor. Can be used for quantitative analysis of mixtures.
$U, V, W...$	Profile breadth parameters. Contain information about crystal size and strain.
$a, b, c, \alpha, \beta, \gamma$	Lattice parameters. Number depends on crystal symmetry.
P_{hkl}	Preferred orientation
	Extinction

Table 2.2: Refinable global parameters in the Rietveld method.

2θ-Zero
Profile asymmetry
Background
Wavelength
Specimen displacement
Specimen transparency
Absorption

neglected without any harm to the result of the procedure.

This is only an overview and now we will briefly describe the most important components of the refinement. The structure factors are calculated by the program using the formula below. They make extensive use of the symmetry group to generate all atom positions in the unit cell.

$$F_{hkl} = \sum_j N_j f_j e^{2\pi i(hx_j+ky_j+lz_j)} e^{-M_j} \tag{2.11}$$

where, x_j, y_j, z_j are the coordinates of of the jth atom in the unit cell, f_j is the scattering factor (scattering length) of jth atom and M_j is the temperature factor (Debye-Waller factor). There are many ways of expressing this variable, but in this thesis in the isotropic case M_j has the form:

$$M_j = 8\pi^2 U_{iso} \sin^2\theta/\lambda^2 \tag{2.12}$$

When the anisotropic model is used the factor has the form:

$$M_j = 2\pi^2(u_{11}h^2a^{*2}+u_{22}k^2b^{*2}+u_{33}l^2c^{*2}+2u_{12}hka^*b^*+2u_{13}hla^*c^*+2u_{23}klb^*c^*) \tag{2.13}$$

where U_{iso} is the anisotropic mean square displacement and u_{ij} are the elements of the matrix for the anisotropic motion, a^*, b^*, c^* are the reciprocal lattice constants. The position of the diffraction peaks are generated using the lattice parameters $a, b, c, \alpha, \beta, \gamma$ and the symmetry group of the model.

The shape of the diffraction peaks depends very much on the experimental geometry and modern refinement programs offer a very broad selection of profiles. Reflections produced by neutron diffractometers are usually well described using an asymmetric Gauss function. The peak profile h of other constant wavelength devices are usually convolutions of two or more components arising from the spectrometer itself and the sample:

$$h(x) = \int g(\xi)f(x-\xi)d\xi \tag{2.14}$$

where $x = 2\theta_i - 2\theta_{hkl}$, $g(x)$ is the instrumental profile and $f(x)$ is the specimen contribution. They are often simulated using the Voigt function, which is a convolution of the Gauss and the Lorentz profiles. However, to make the calculations faster the profile is very often approximated using so called pseudo-Voigt function which is a sum of the Gauss and the Lorentz profiles.

The profile width varies with scattering angle θ and the width of Gaussian component σ_G is usually well modeled using the Caglioti formula [67]:

$$\sigma_G^2 = U\tan^2\theta + V\tan\theta + W \tag{2.15}$$

The Lorentzian width σ_L is given by the formula:

$$\sigma_L = (X + X_e\cos\phi)/\cos\theta + (Y + Y_e\cos\phi)\tan\theta \tag{2.16}$$

where $U, V, W, X, X_e, Y, Y_e, \phi$ are refinable parameters; they carry information about the geometry as well as the crystalline size and strain of the sample. The angle ϕ allows an introduction of the size and the strain anisotropy [65, 68–75].

The background is usually modelled using polynomials, Fourier series or other functions and is not treated as a source of information about the sample. On rare occasions some information about an amorphous component can be derived from the background but the usual approach is just to obtain the best fit since the background does not carry useful information about the crystal structure.

Every fitting method requires a quantity which indicates the goodness of fit. The theory of fit criteria is complicated and beyond the scope of this chapter. The criteria indicate the minimum however, they should not be blindly trusted as they make no distinction between the local and the global minimum. Moreover they cannot make the distinction between right and incorrect structural models if the wrong model is sufficiently similar to the correct one. Apart from the numerical criteria the calculated difference between the observed intensities and the refined model plotted together with the experimental data usually help avoiding the false minima but still does not guarantee the correctness of the model. The most frequently used criteria are 'R-pattern':

$$R_p = \frac{\sum |y_i - y_{ci}|}{\sum w_i y_i^2} \tag{2.17}$$

and 'R-weighted pattern':

$$R_{wp} = \left(\frac{\sum w_i (y_i - y_{ci})^2}{\sum w_i y_i^2} \right)^{1/2} \tag{2.18}$$

The most meaningful from the mathematical point of view is the latter since the numerator is equal to the residual which is being minimized (see Equation (2.7)). Discussion of the fit criteria can be found in [76].

Despite its shortcomings the Rietveld method is now a recognized technique for dealing with powder patterns. It is not perfect but it is the only one that can cope with overlapping reflections.

2.3.2 Crystal Size and Strain

Powder diffraction techniques also provide information about the size and the strain of the microcrystals. The size and strain are causes of the diffraction lines broadening which is superimposed on the instrumental profile. The size and strain can be extracted from carefully measured peak widths. The line breadth due to crystal size is inversely proportional to the size ε and cosine of the scattering angle.

$$\beta \propto \frac{1}{\varepsilon \cos\theta} \tag{2.19}$$

However, the accuracy of size determination is hampered by the mathematical nature of this relationship and relatively precise measurements are possible only if the size is small, say below 500 nm. Above this value even very small inaccuracy in the breadth determination causes large changes to the result. The limit for the method is believed to be about 2 μm provided that the measurements were made very accurately. The second contribution to the line breadth is the strain η defined by the equation:

$$\eta \equiv \frac{\Delta l}{l} \tag{2.20}$$

as the change of length of a stressed body to its initial length. Investigation of strain is very important especially in metallurgy and metal constructions. Its contribution to the line breadth is proportional to the strain and $\tan\theta$

$$\beta \propto \eta \tan\theta \tag{2.21}$$

However, the measured peak width contains contributions from the size, the strain and the instrumental profile. The line breadth measurements are done using very elaborate fitting programs utilizing peak profiles which are sometimes convolutions of several Gauss and Lorentz profiles to accommodate not only simple stress and size but to allow for a crystal size distribution [77–79]. The strain and stress can be separated using a variety of sophisticated methods such as Fourier analysis [80–82] or deconvolution of the measured profile [79]. However, the elaborate techniques work well if the material is single phase and relatively symmetric with little or no peak overlap. In most cases when only one or two non-overlapping lines are available, the size is evaluated using the Scherrer formula:

$$\varepsilon = \frac{K\lambda}{\beta_{size}\cos\theta} \tag{2.22}$$

where K is a constant depending on the shape of the crystals. The strain is usually found using the equation:

$$\eta = \frac{\beta_{strain}}{4\tan\theta} \tag{2.23}$$

Of course the measured width is first corrected to remove the instrumental contribution. In the case of the size it is done by a simple subtraction

$$\beta_{size} = \beta_{measured} - \beta_{instrumental} \tag{2.24}$$

The true strain breadth is given by the formula:

$$\beta_{strain} = (\beta^2_{measured} - \beta^2_{instrumental})^{1/2} \tag{2.25}$$

If there are more resolved peaks, the stress and strain can be separated using Hall's method [83]:

$$\frac{\beta \cos\theta}{\lambda} = \eta \frac{\sin\theta}{\lambda} + \frac{1}{\varepsilon} \tag{2.26}$$

The experimental data plotted using Equation (2.26) forms a straight line, the strain and the reciprocal of the size are given by the slope and the intercept of the line.

The instrumental contribution to the peak breadth can be calculated by analysing the x-ray or neutron optics of the diffractometer or found experimentally. The instrumental breadth $b(2\theta)$ of the x-ray diffractometer used in this thesis was found experimentally by collecting diffraction patterns of well crystallized elements and compounds. Only results having the smallest breadth were accepted and are presented in Figure 2.1. The experimental points were fitted with a parabola:

$$b(2\theta) = 1.960 \times 10^{-5} \, (2\theta)^2 - 0.002 \, (2\theta) + 0.182 \tag{2.27}$$

and the polynomial then used to evaluate the instrumental contribution.

Because of the nature of the investigated ferrites only Scherrer and Hall methods were used to determine the size and strain of the compounds. An extensive review of the size and strain measurement techniques can be found in [63, 64].

2.3.3 Phase Identification

Crystalline substances form unique crystal structures and yield sets of powder diffraction lines of certain positions and intensities. Comparison of line position and intensities against a set of patterns of known substances allows their identifications. Theoretically three well measured lines are enough to identify the material, however because of the large number of known compounds the

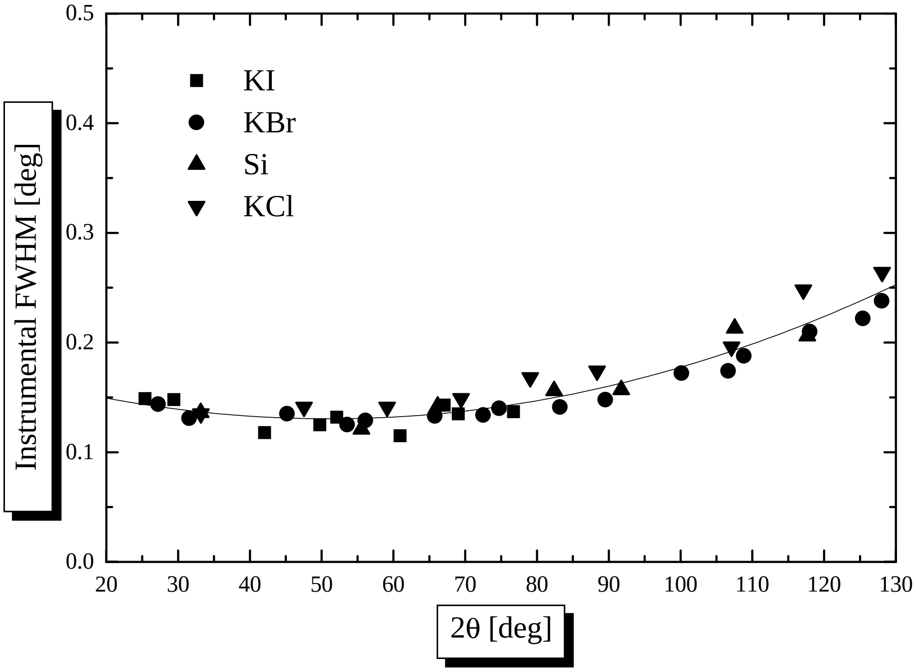

Figure 2.1: The instrumental breadth (full width at half maximum) of Philips PW1050 diffractometer, used in this thesis, as a function of scattering angle. The solid line denotes the parabolic fit described in the text.

analysis has to be supported by the positions of other lines, elemental composition of the sample, colour, sample history and other properties. If the compound forms isomorphs it is necessary to establish the lattice parameters of the material to unambiguously identify it. In this thesis the diffraction patterns were identified by comparing the lines positions and intensities against JCPDS-ICDD PDF-2 database (sets 1–42), patterns found in literature and patterns of substances collected in-house.

2.3.4 Experimental Geometries

Powder diffraction patterns presented in this thesis were collected using x-rays as well as neutrons in three experimental configurations. Both neutron and x-ray methods and differences in instrument optics influence the outcome of the experiment (relative intensities and resolution of the lines). The most important difference between x-ray and neutron methods is the scattering mechanism. X-rays are scattered by electron shells of atoms and the scattering intensity is roughly proportional to the atomic number of the element and decays with scattering angle. Neutrons on the other hand are scattered by nuclei, the scattering length can be positive or negative and the scattering length varies randomly even between isotopes of the same element. Also since neutrons have a finite magnetic moment they are sensitive to the magnetic order in the material. Since the investigated material contains strontium, iron and oxygen, the x-ray method is most sensitive to strontium ($Z = 38$) and the least scattering component is oxygen ($Z = 8$). Of course the effective scattering amplitudes are slightly different since we are dealing with ions. The neutron scattering amplitudes of strontium and oxygen are almost equal $0.57{\cdot}10^{-12}$ cm and $0.577{\cdot}10^{-12}$ cm respectively, but the scattering length of iron ($0.96{\cdot}10^{-12}$ cm) is 1.7 times greater. The lengths do not depend on the scattering angle. So the neutron method is almost equally sensitive to all three elements and allows the thermal parameters of the atoms to be determined. The last very important feature is the absorption of x-ray and neutron radiation by the sample. If the absorption is substantial it strongly affects the outcome of experiments in the Debye-Scherrer geometry. The investigated oxide strongly absorbs x-rays the linear absorption coefficient calculated for $Sr_2Fe_2O_5$ ($x = 2.5$) is 489 cm^{-1}[*] while in case of neutrons is only 0.05 cm^{-1}[†]. More information about neutron scattering and its comparison with x-ray diffraction can be found in [84–87]. The scattering and absorption factors used in the calculations were taken from the International Tables for Crystallography [88]

Bragg-Brentano Diffractometer

Most of the x-ray diffraction experiments were performed using a Philips PW1050 diffractometer utilizing CoK_α radiation and operating in the Bragg-Brentano geometry [89–91]. It is a pseudo-focusing setup in which a flat sample rotates about the diffractometer axis with half the angular speed of the detector and the absorption is practically independent of the scattering angle. The instrument has a radius of 173 mm and consists of: primary Soller slits[‡], fixed 1° divergence slit, 0.2° receiving slit, 1° scattering slit, a graphite diffracted beam monochromator and a proportional counter. The axial irradiated length of the sample was about 12 mm. Typically the sample was prepared by spreading fine powder on a frosted end of microscope glass slide with a droplet of alcohol. After drying it leaves a thin uniform layer of material and is good enough for fixing most of samples. In the case of

---

[*] calculated for CoK_α radiation

[†] calculated for 1.66 Å neutron wavelength

[‡] unknown acceptance angle

materials sensitive to water or alcohol the powder was pressed against the glass with another glass slide. The frosted glass minimizes the influence of the preferred orientation to which the Bragg-Brentano geometry is very susceptible to. However, the $SrFeO_x$ system does not exhibit pronounced preferred orientation. The scans were made in the angular range 5–130° with step size of 0.05–0.1° for phase identification and 0.01–0.02° for structural studies, the counting time varied between 2 and 10 seconds per step.

Synchrotron Radiation

Selected samples were studied using synchrotron radiation using the Debye-Scherrer camera at the Australian National Beamline Facility at the Photon Factory, Tsukuba Japan. The experiments were made using wavelength of 1.95 Å and the patterns were recorded on imaging plates [89, 92, 93]. The intensity of synchrotron radiation exceeds the brilliance of a sealed x-ray tube by 9 orders of magnitude [57] and therefore allows formation of a very well defined beam with a very narrow emission width $\Delta\lambda$ without substantial loss of the intensity. This, combined with large camera (radius=573 mm) produces a low instrumental profile width and therefore much greater resolution. However, this geometry is hampered by angle dependent absorption. The samples were prepared by packing fine powder into 0.3 mm glass capillary.

Neutron Diffractometer

The neutron scattering experiments were made using the Medium Resolution Powder Diffractometer (MRPD) at the Australian National Science and Technology Organization in Lucas Heights. The instrument operates in Debye-Scherrer geometry typically using a neutron wavelength of 1.66 Å [94, 95]. However, like many constant wavelength neutron devices it suffers from low instrumental resolution. The instrument was used at ambient temperature and elevated temperatures in controlled atmospheres. The samples for room temperature studies were packed in thin-walled vanadium cans, 10 mm in diameter and approximately 7 cm^3 volume. Samples for high-temperature studies were in the form of sintered pellets, 15 mm in diameter.

2.4 Electron Microscopy

The ferrite was investigated using a scanning electron microscope (Hitachi S4500 Field Emission SEM). The studies were limited to investigations of the morphology of mechanically and thermally treated powders. The samples were prepared by applying a droplet of alcohol containing dispersed powder on a graphite tape glued to a sample stab. The samples were then dried and sputter coated with a thin layer of platinum to prevent charging in the beam.

A transmission technique (TEM) allows study of the crystal structure using electron diffraction patterns. However, the ferrite especially in the highly oxidized form is very unstable in the microscope. The sample is bombarded with 200–300 keV electrons and the conditions in the beam resemble high-temperature annealing in an ultra-high vacuum. The ferrite under these conditions tends to lose oxygen thus changing its composition and the crystal structure. This feature of the material makes it very difficult to study and this line of work was not pursued.

2.5 Mössbauer Spectroscopy

The Mössbauer effect involves the recoil-free resonant absorption of gamma photons by atoms of the same isotope. The photons are absorbed by nuclei and their energy levels can be probed by changing the energy of the incident radiation and analysing the spectrum of gamma rays after interaction with the sample. The method ideally suits the ferrite since it contains significant amount of iron however, only ^{57}Fe exhibits the effect and its natural abundance is about 2 %. But the molar fraction of iron in the sample is large enough to carry out experiments without enriching the samples with the isotope. The suitable gamma radiation was produced by radioactive decay of ^{57}Co. The nuclear reaction produces ^{57}Fe in its excited state $I = 5/2$ as a result of the electron capture.

$$^{57}\mathrm{Co} \rightarrow {}^{57}\mathrm{Fe}(5/2) \tag{2.28}$$

where, I is the nuclear spin of iron. The ground state is characterized by spin number $I = 1/2$ and the excited nucleus can directly return to the ground state emitting photon of energy equal to 136 keV according to the reaction:

$$^{57}\mathrm{Fe}(5/2) \rightarrow {}^{57}\mathrm{Fe}(1/2) + \gamma(136\,\mathrm{keV}) \tag{2.29}$$

or via intermediate state $I = 3/2$ according to the reaction:

$$^{57}\mathrm{Fe}(5/2) \rightarrow {}^{57}\mathrm{Fe}(3/2) + \gamma(121.6\,\mathrm{keV}) \rightarrow {}^{57}\mathrm{Fe}(1/2) + \gamma(14.4\,\mathrm{keV}) \quad (2.30)$$

Both reactions are not equally favourable and the direct route Equation (2.29) makes up only 9 % events and the second route is more frequent occurring in 91 % of cases (Equation (2.30))[§]. The 14.4 keV radiation was utilized for the experiments. The nuclear energy levels and their degeneration are sensitive to the electron density and magnetic fields in the crystal structure. The electric and magnetic fields cause the levels to shift or split and therefore enable us to probe the ^{57}Fe environment. To investigate the energy levels the energy of the incident spectrum was varied in a controlled manner using the Doppler shift. The source is mounted on an oscillating holder and the energy is changing according to the equation:

$$E(v) = E_0 \frac{v}{c} \quad (2.31)$$

and the velocity v is in order of millimeters per second. The spectrometer changes and measures the velocity v of the source and collects the gamma spectrum after interaction with the sample as a function of the velocity using a proportional counter. The changes in energy due to the Doppler shift are very small and to reduce the background, which would obscure the results, the unused part of the cobalt emission spectrum was removed using an energy discriminator. The discriminator (known also as a single channel analyser) passes only the electrical impulses from the detector which correspond to the energy in the vicinity of the 14.4 keV peak and suppresses everything else. The description of the instrument used for the experiments can be found in [96]. The changes of the energy levels of iron are caused by temperature, the surrounding of iron atom and the magnetic field.

2.5.1 Isomer Shift (IS)

The isomer shift δ is a result of the differences in the electron densities at the nucleus between the emitting and absorbing atoms. The difference changes the Mössbauer transition energy and the spectrum is shifted. If we neglect the relativistic effects the shift δ (in mm/s) can be expressed using the following

---

[§] The energy partition among the two energy bands is idealized and in practice there are several emission lines originating from the interaction of gamma radiation with the matter.

formula:

$$\delta = C\frac{\Delta R}{R}\left(|\Psi(0)|_a^2 - |\Psi(0)|_s^2\right) \tag{2.32}$$

where C is a constant, R is the effective nuclear radius $|\Psi(0)|_a^2 - |\Psi(0)|_s^2$ is the difference in electron density at the nucleus in absorber and the source respectively [97, 98]. The ΔR denotes the difference in the nuclear radius between the excited and the ground state. Equation (2.32) shows that the shift is sensitive to the electronic surrounding of the nucleus in particular the changes affecting s shells which have a finite electron density at the nucleus. The isomer shift only alters the energy levels and its value is obtained directly from the position of the absorption line.

2.5.2 Quadrupole Splitting (QS)

The quadrupole splitting Δ is a result of the interaction of the nuclear quadrupole moment with the crystal field gradient. The quadrupole moment Q is characteristic for each state/isotope and is non-zero if the charge distribution of the nucleus is not spherical. The splitting of the energy levels can be expressed using the following formula:

$$\Delta = eQV_{zz} \tag{2.33}$$

where, V_{zz} is the largest component of the electric gradient. The energy level split creates a doublet in the Mössbauer spectrum.

2.5.3 Magnetic Splitting

A nucleus with quantum spin number I has $2I+1$ degenerated energy levels. They become separated upon the introduction of an external or internal magnetic field $\mathbf{B}$ due to the Zeeman effect. The $2I+1$ states are described by quantum numbers m_I:

$$m_I = -I, -I+1, \ldots, I-1, I \tag{2.34}$$

and their energy are shifted from the zero field value by a value given by the formula:

$$\Delta E = -g\mu_N B m_I \tag{2.35}$$

where, $\mu_N \equiv \frac{e\hbar}{2m_p}$ is the nuclear magneton, m_p is the proton mass and g is the Landé factor. The magnetic field splits $I = 1/2$ state into two energy levels and the $I = 3/2$ state into four separate levels. However, the selection rule allows only six possible transitions between these levels and the splitting appears as a sextet instead of an octet in the Mössbauer spectrum.

2.5.4 Experimental Procedure

All patterns were collected at room temperature, the radioactive gamma source ^{57}Co was embedded in a rhodium matrix and the spectrometer was calibrated using α-Fe foil. The SrFeO$_x$ samples were not enriched with ^{57}Fe and to obtain satisfactory statistics, the counting was carried out for a period of 1–2 weeks per specimen. The samples were prepared by spreading a fine powder on the glue side of a sticky tape and after removal of an excess material the sample was preserved by sandwiching it with another layer of tape. The layer of powder obtained that way was slightly translucent.

A numerical analysis of all spectra was carried out by fitting the absorption lines with Lorentz profiles.

2.6 Ball Milling

Ball milling is a common name for mechanochemistry or mechanical alloying. This branch of science had been developing quite rapidly for last few decades. It is not new, the first experiments were carried out at the beginning of the twentieth century but only recently it gained momentum. Mechanochemistry deals with chemical reactions or alloying processes induced by mechanical energy usually at room temperature. The reactions are carried out in a relatively simple grinding devices ‘mills’ where the kinetic energy is passed on the material during impact or shearing. Using the technique it is possible to carry out a range of solid-solid or solid-gas reactions which for variety of reasons are difficult to conduct at high temperature. This includes formation of refractory metal alloys, intermetallics and complex chemical compounds. However, the exact mechanism of the energy transfer is not known and the experimental reports are usually limited to the description of the reaction in a particular grinding device. Because the mechanism is unknown it is difficult to judge what design of mill gives the best result [99–104].

The ball mill used in this thesis consists of a vertical stainless steel drum (6” in diameter) filled with four 1” ball bearing as grinding media. The movement of the balls is controlled by an external magnet and the rotation speed [105]. The usual load of material is about a table spoon of powder and the reaction can be carried out in vacuum or gas atmosphere. This particular design has few flaws limiting its use for investigation of properties of solids. It cannot be used for milling of materials harder than steel (this includes some iron oxides *e.g.* hematite), materials that form alloys with iron (*e.g.* gallium) or substances containing elements soluble in steel such as carbon or boron without substantial iron contamination. The iron contamination often forms compounds impossible to remove from the product [106] or directly reacts with the milled material changing its oxidation state [107, 108]. On rare occasions the iron contamination has a positive effect being a catalyst of a nitridation reaction [109]. The mill is slow and even though the device was never directly compared with other mills, a theoretical estimations show that the milling process takes 300–700 times longer than in vibratory mills [110]. The mill can not be scaled up so it is not possible to make a larger version with proportionally higher yield.

The use of mill in this thesis was limited chiefly to mixing of the reactants and investigation of the oxidation and carbonation reactions caused by mechanical energy. Fortunately the materials or their mixtures used in this thesis did not abrade the mill making the study possible without visible iron contamination. The milled materials were carefully checked for excess iron using the procedure described in section 3.5.

The constructors of the mill claim that the energy transferred to the material can be regulated by speed and position of the magnet. But for all experiments described in this dissertation the axis of the bar magnet was inclined at angle of 45° to the vertical direction and the speed was set to produce maximum noise. This ensured the maximum frequency of impact and corresponded to about 180–200 rpm.

2.7 Miscellaneous Methods

2.7.1 Specific Surface Area

The surface area of powder exposed to gas atmosphere was measured by controlled adsorption of nitrogen onto the powder [51,111]. The method provides information not only about the specific surface area but also can indicate the existence of pores and determine their size. Surface plays an important role in solid-gas reactions since it determines the kinetics of and allows to estimate the amount of gas adsorbed on the surface. The measurements were performed using an automatic Gemini II 2370 Surface Area Analyzer [112].

2.7.2 Vibrating Sample Magnetometer (VSM)

The device measures the magnetic moment of sample as a function of an external magnetic field. The interpretation of the measurements provide information about magnetic order in the sample and the strength of the interactions. The operation of the magnetometer is based on Faraday's law of induction. The sample is vibrated and induces an electric signal in the pickup coils. Its magnitude is proportional to the moment and usually the moment is studied as a function of the external magnetic field [113,114]. The measurements were made at room temperature using a EG&G Princeton Applied Research Vibrating Sample Magnetometer, Model 155.

2.7.3 Thermodynamical Calculations

The thermodynamical calculations provide valuable information about the behaviour of the system at various temperatures and concentration of species. If the Gibbs free energy of formation of all components of the system are known they can be used for predicting the equilibrium composition and indicate whether the particular reaction can proceed or not. However, thermodynamical information about Sr-Fe-O system is very scarce and such calculations are not possible. But, the thermodynamic properties of strontium and iron compounds are known and the calculations for these simple substances are presented in the thesis as auxiliary arguments. Most of the presented calculations were made using a computer program HSC Chemistry v2.03 and the data were taken from thermodynamical tables [115–118].

Chapter 3

Formation of $SrFeO_x$

This chapter presents a study of the chemical transformations that lead to the formation of ferrite from a mixture of reactants. There are virtually no reports concerning the formation of phases in the $SrFeO_x$ system. The barium bearing ferrites $BaFeO_x$, $BaFe_2O_4$ [119] and magnetic materials such as $SrFe_{12}O_{19}$ [46, 47] and $BaFe_{12}O_{19}$ [120, 121] are much better researched. The formation processes are important since the synthesis method affects the morphology of crystals and therefore their physical properties.

The $SrFeO_x$ system is formed during a solid state reaction at elevated temperature. The process is strongly influenced by many factors such as the physical state of reactants and the composition of the atmosphere. However, the most important physical property appears to be the homogeneity of mixture on the micrometer length scale. The influence of the mechanical treatment of the reactant mixture on the route and the kinetics of reaction are shown and the existence of an alternative way of preparing the material is presented. We explore the possibility of ferrite formation by milling. Since all milling experiments presented in this thesis were made using a stainless steel mill, one of the sections describes the influence of iron contamination and the methods of detecting it. The final section describes the procedure used to prepare large quantities of the oxide for other experiments.

3.1 Choice of Reactants

The oxide can be synthesized from a variety of iron and strontium bearing compounds. However, to obtain the required stoichiometry, the chemicals have to be non-hygroscopic, stable in air and available in pure form. These requirements are fulfilled by iron (III) oxide (hematite) and strontium carbonate. Additionally these compounds have cations in oxidation states present in the ferrite which simplifies the synthesis.

Most of the samples were made using hematite (Fe_2O_3) 99–99.9 % pure and the strontium carbonate ($SrCO_3$) 99–99.9+ % pure mixed in the molar ratio 1:2.

3.2 The Reaction

The formation of $SrFeO_x$ was investigated using its oxygen deficient phase $Sr_2Fe_2O_5$ in an argon atmosphere. The formation of the oxidized phases ($x > 2.5$) is similar but is accompanied by a temperature dependent oxidation processes described in the next chapter. The overall formation reaction can be written as follows:

$$Fe_2O_3 + 2\,SrCO_3 = Sr_2Fe_2O_5 + 2\,CO_2. \tag{3.1}$$

However, reports of the formation of another strontium ferrite $SrFe_{12}O_{19}$ indicate the presence of transient phases during its formation [46, 47] and these phases are an inherent part of the process.

In order to investigate the formation a mixture of hematite and strontium carbonate (∼5 g) was hand ground for 30 min using a mortar and pestle. The mixture was subsequently annealed at 1473 K for different periods of time. The materials after annealing were examined using x-ray diffraction and the results are presented in Figure 3.1. One hour of the heat treatment produced $Sr_2Fe_2O_5$ and transient phases in form of $Sr_4Fe_6O_{13}$ and SrO. These phases gradually vanish and convert into the ferrite as shown in the subsequent patterns. To remove all traces of unwanted phases the thermal treatment had to be carried out for more than 35 h. The same mixture of hematite and strontium carbonate was also ball milled for 24 h prior to annealing and produced only pure $Sr_2Fe_2O_5$ after 1 h of heat treatment. The absence of the transient phases ($Sr_4Fe_6O_{13}$ and SrO) in the milled mixture indicates that the formation of the ferrite occurs according to Reaction (3.1) and the transient phases are the result of the inhomogeneity of the reactant mixture. This was confirmed by firing of the milled mixtures at lower temperatures down to 773 K for 1 h. X-ray examination of the products revealed only $Sr_2Fe_2O_5$ and some unspent reactants.

Milling of the reactants prior to annealing also improved the reaction

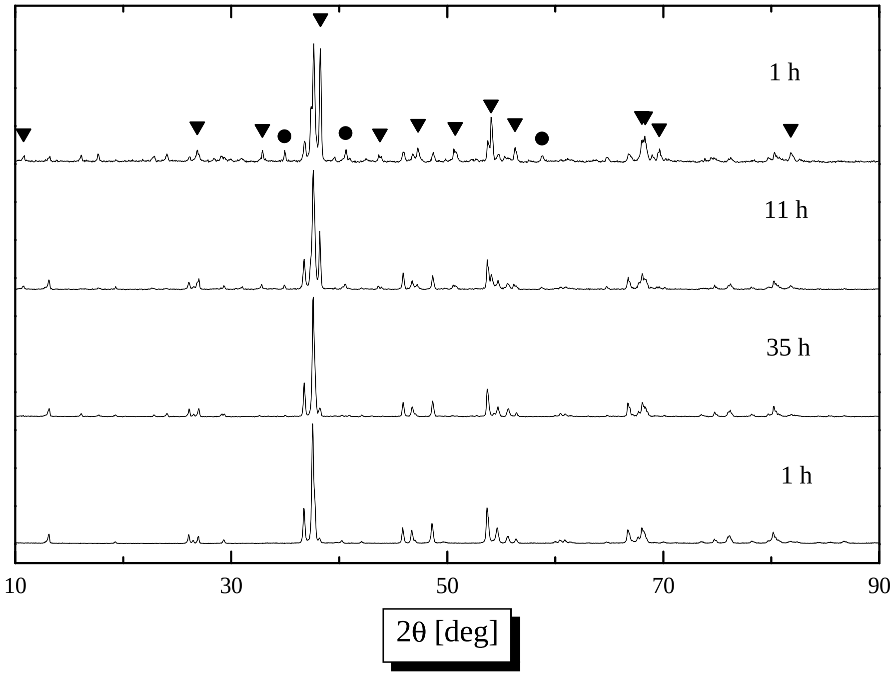

Figure 3.1: X-ray diffraction patterns of the hand ground hematite-strontium carbonate mixture annealed for different periods and a pattern of a milled mixture fired for 1 h (bottom). The mixtures were annealed at 1473 K in argon. The figures denote annealing time, triangle denote the main diffraction lines of $Sr_4Fe_6O_{13}$, circles mark lines of SrO. The bottom pattern contains the trace of pure $Sr_2Fe_2O_5$. The patterns were normalized and are presented in the linear scale.

kinetics. Figure 3.2 shows thermogravimetric traces corresponding to the reactions in the unmilled and the milled mixtures. The trace of the milled material shows higher reactivity at lower temperatures and milling effectively reduces the temperature needed to carry out the reaction. However, milling did not shift the onset of mass loss into lower temperatures. The thermodynamical temperature above which the reaction starts is the same, since it is characteristic for the particular mixture of reactants and the milling did not change their chemical makeup (there was no trace of any phase transformations in milled mixtures of reactants analysed by x-ray diffraction).

Thermogravimetric experiments done on reactant mixtures milled for longer than 24 h showed that prolonged milling does not improve the kinetics significantly but it increases the possibility of iron contamination.

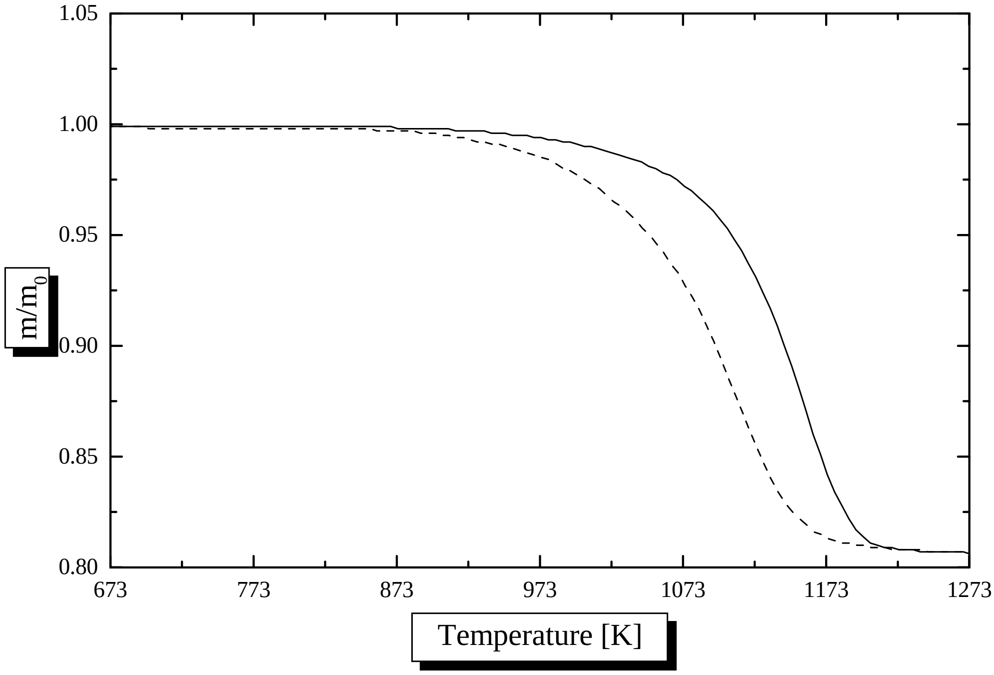

Figure 3.2: Thermogravimetric traces of reactions in the hand-ground (solid line) and the milled (24 h, dashed line) hematite-strontium carbonate mixtures. The samples were heated at a rate of 20 K/min in argon.

3.2.1 Morphology

The morphology of the hand ground and the milled samples were examined using scanning electron microscopy. The images of reactants and mixtures are presented in Figure 3.3.

Analysis of x-ray diffraction line breadth showed that 24 h of milling reduced the average size of hematite crystals from 550 nm to 180 nm and the crystal size of $SrCO_3$ from 50 nm to 28 nm.

The images show that raw hematite and carbonate form sintered clusters several micrometers in size. The size of the clusters is a few orders of magnitude larger than the crystal sizes derived from diffraction analysis. In the case of the carbonate, the rod like particles observed with the SEM consist of few microcrystals since the size obtained from the x-ray diffraction are smaller than the average length of the rods ($\sim$ 300 nm).

The mixing by hand does not disperse the clusters well and only brings them into contact. Milling on the other hand caused the particles to intermix and coalesce into larger grains. The milled microcrystals lost their initial shape which indicates that single grains were broken into parts and the coalescence brought different phases together.

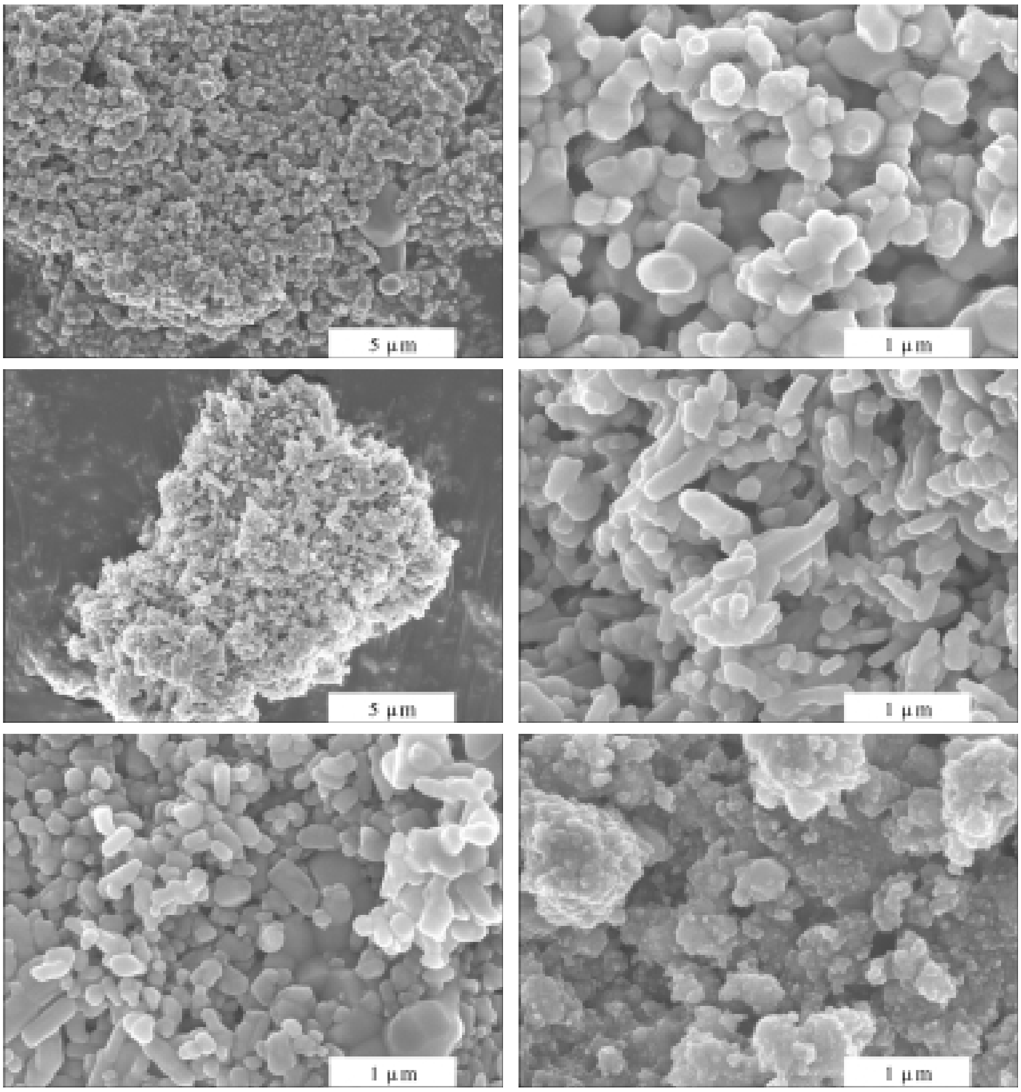

Figure 3.3: Scanning electron microscope images of starting materials: hematite (top row), strontium carbonate (middle row) and the hand-ground and the milled mixtures of the two (bottom left and right respectively).

Figure 3.2 suggests a correlation between the crystal size of the reactants and the kinetics of the reaction. However, the correlation is only coincidental, solid-solid reactions occur at the interface between the phases and the contact area plays a decisive role. This area is very difficult or impossible to measure. The contact area in the hand ground mixtures is defined by the size of clusters not the microcrystals. In the case of the milled mixture, the compounds are brought into contact but the crystal size gives only an estimate of the total surface area of compound and does not provide any information about the contact area between the species.

3.2.2 Thermodynamics of Hematite and an Alternative Route of Synthesis of $Sr_2Fe_2O_5$

Hematite decomposes to magnetite according to the reaction:

$$6\,Fe_2O_3 = 4\,Fe_3O_4 + O_2 \tag{3.2}$$

if the partial pressure of oxygen falls below the equilibrium value at constant temperature or if the temperature exceeds a critical value at constant pressure of oxygen. The calculated critical temperature for hematite decomposition is presented in Figure 3.4 as a function of the partial pressure of oxygen.

Argon used in the synthesis of $Sr_2Fe_2O_5$ had an oxygen concentration around 10^{-6} atm and Figure 3.4 shows that hematite in this atmosphere decomposes above 1184 K. However, the decomposition reaction at this temperature is relatively slow and it takes about an hour to reduce hematite to magnetite at 1473 K.

Figure 3.2 indicates that most of the ferrite formation takes place during heating before the reactant mixture reaches the temperature of 1183 K. Above this temperature the formation reaction, indicated by the mass loss, is still visible (especially in hand ground mixtures). However, magnetite not hematite is the thermodynamically stable phase of iron oxide under these conditions ($T > 1183\,\mathrm{K}$, $p_{O_2} = 10^{-6}\,\mathrm{atm}$). It is an indication that $Sr_2Fe_2O_5$ can be synthesized from Fe^{2+} bearing oxide such as magnetite.

Since $Sr_2Fe_2O_5$ contains only the trivalent iron, Fe^{2+} has to be oxidized to Fe^{3+}. The argon does not contain enough oxygen to carry out the complete oxidation of magnetite in the time so the only source of oxygen is strontium carbonate. The synthesis has to be carried out at the expense of evolved

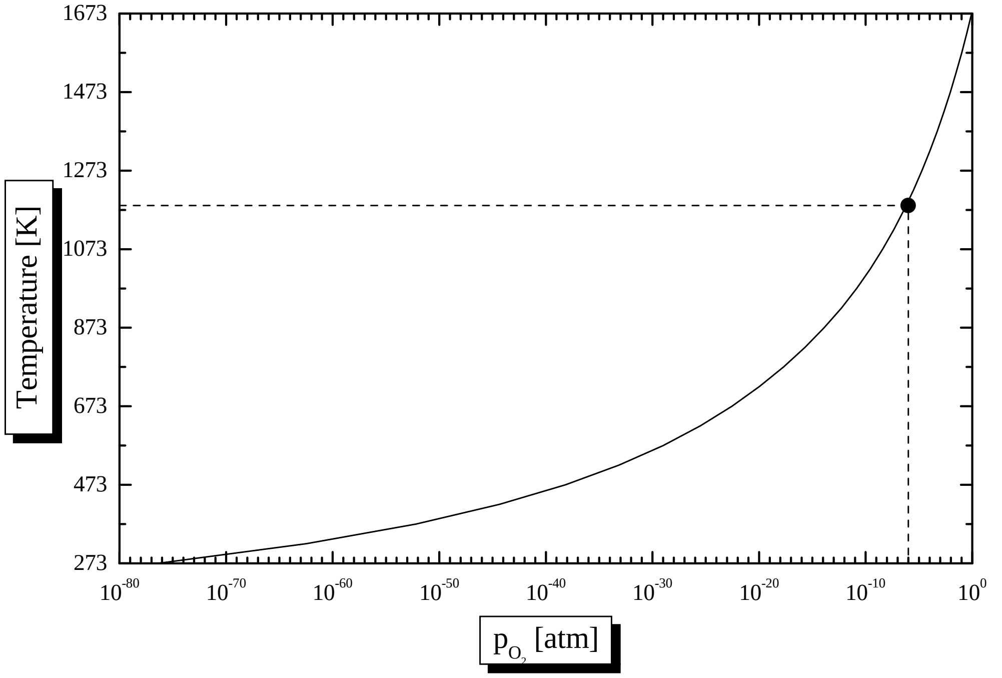

Figure 3.4: The calculated decomposition temperature of hematite as a function of the oxygen partial pressure as discussed in the text. The point marks the decomposition temperature for the argon used in the experiments ($p_{O_2} \approx 10^{-6}$ atm).

carbon dioxide according to the reaction:

$$6\,\mathrm{SrCO_3} + 2\,\mathrm{Fe_3O_4} = 3\,\mathrm{Sr_2Fe_2O_5} + 5\,\mathrm{CO_2} + \mathrm{CO} \tag{3.3}$$

However, direct oxidation of magnetite to hematite by carbon dioxide according to the reaction:

$$2\,\mathrm{Fe_3O_4} + \mathrm{CO_2} = 3\,\mathrm{Fe_2O_3} + \mathrm{CO}, \tag{3.4}$$

is impossible. This fact is well known from steel manufacturing processes and was confirmed by thermodynamical calculations which yielded a positive change of Gibbs free energy for this reaction. But it only proves that hematite is not formed as a step in the synthesis reaction. For the synthesis of $Sr_2Fe_2O_5$ described by Reaction (3.3) to proceed the change of Gibbs free energy must be lower than the change of Gibbs free energy for the formation of carbon dioxide:

$$2\,\mathrm{CO} + \mathrm{O_2} = 2\,\mathrm{CO_2}. \tag{3.5}$$

In other words the line corresponding to the formation of $Sr_2Fe_2O_5$ should lie

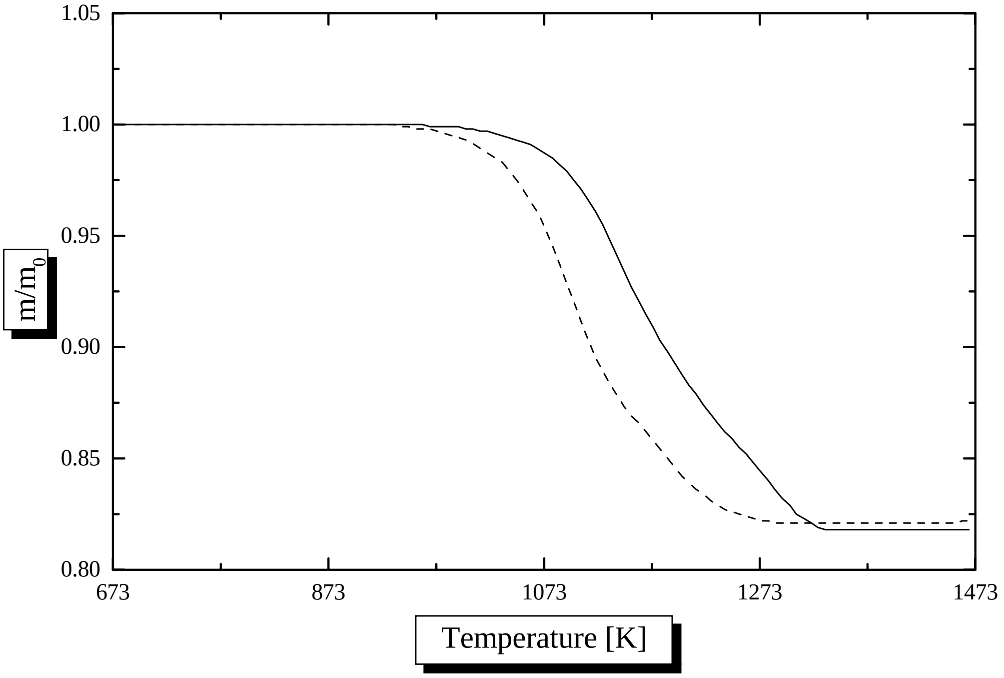

Figure 3.5: Thermogravimetric traces of reactions in the hand-ground (solid line) and the milled (24 h, dashed line) magnetite-strontium carbonate mixtures. The samples were heated at a rate of 20 K/min in argon.

below the line corresponding to Reaction (3.5) on the Ellingham plot [51,122].

The only known estimate of the free energy for $Sr_2Fe_2O_5$ has a value of -381 kJ/mol at 1273 K [14,123]. The energy for the Reaction (3.5) is equal to -344 kJ/mol at the same temperature so Reaction (3.3) is thermodynamically viable.

The possibility of such a reaction was tested using mixtures of strontium carbonate and magnetite (Fe_3O_4, 98 % purity) combined in the molar ratio 3:1. The magnetite contained approximately 1.5 % of hematite and the mixtures were hand ground and milled in argon for 24 h. Both specimens were analysed using the thermobalance and the results are presented in Figure 3.5. Onset of the reaction observed on the TG curves is approximately 50 K higher than for the formation from hematite-carbonate mixture (compare Figure 3.4). X-ray diffraction analysis of the products revealed only $Sr_2Fe_2O_5$ in the milled and the hand ground mixtures. The product was also tested for the divalent iron using the procedure described on page 96. The test did not detect Fe^{2+} in the product. The absence of any intermediate phases might be an indication that $Sr_2Fe_2O_5$ has the lowest free energy of formation among all strontium ferrites and other ferrites can not decompose

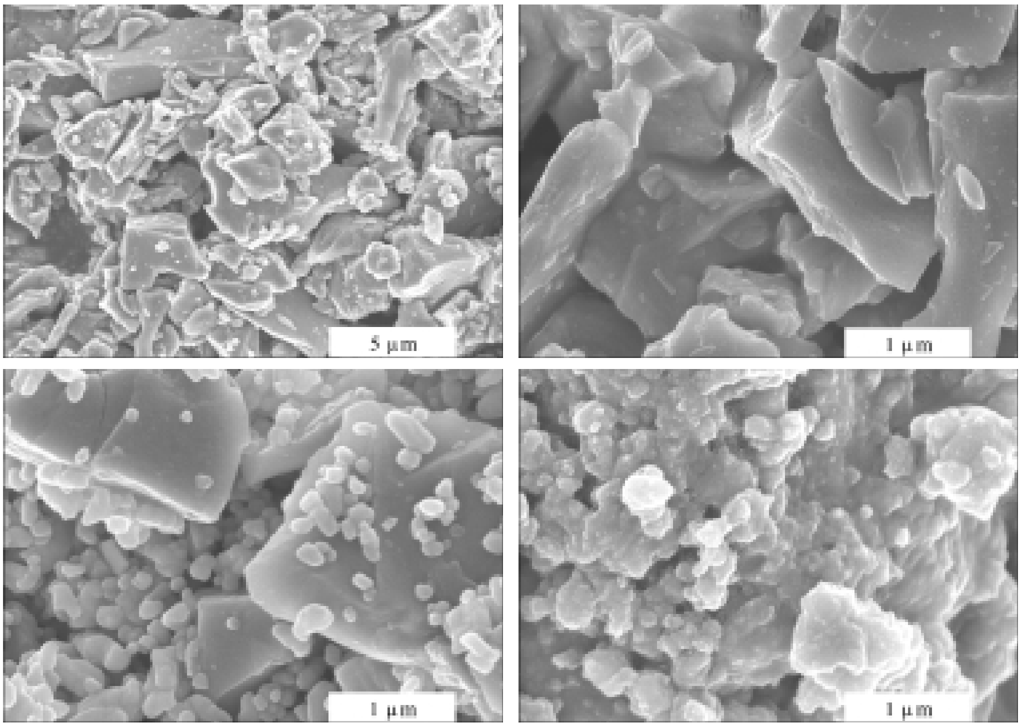

Figure 3.6: Scanning electron microscope images of magnetite (top row) and the hand-ground and the milled magnetite-carbonate mixtures (bottom left and right respectively).

CO_2 upon their formation. But testing of this hypothesis is beyond the scope of this work. The presence of $Sr_2Fe_2O_5$ as the product of reaction proves that the stoichiometry $x = 2.5$ is the lower limit of the composition range and the system $SrFeO_x$ does not extend into compounds containing divalent iron.

Mechanical processing of the reactant mixture also increased the kinetics of reaction as in the case of hematite based mixtures. Scanning electron microscope images of raw and milled materials are presented in Figure 3.6. Magnetite does not form sintered clusters but milling has similar effect on the morphology of powders to that found in the hematite-carbonate mixture.

3.3 Heat of Formation

The heat of formation was measured using DTA by heating the milled mixtures at constant rate. The endothermic peaks corresponding to the reactions span the temperature ranges found using the TGA for all of the samples (the temperature range corresponding to the mass loss). However, measured values are difficult to interpret because the formation process is always accompanied by other phenomena.

The experiments in argon, producing $Sr_2Fe_2O_5$, yielded 0.52 kJ/g and 0.12 kJ/g for the hematite and the magnetite mixtures respectively. However, the endothermic reaction peaks were not very well defined and the product ($Sr_2Fe_2O_5$) undergoes a phase transition around 1140 K which coincides with the reaction peak. The energy corresponding to this transition is approximately 40.9 J/g as described in detail in Chapter 4 and Chapter 7.

The reaction carried out in air, using the hematite mixture[*], gave 540 J/g which is, within experimental error, equal to the value for the hematite mixture in argon. However, as in previous cases the endothermic peak spans over a wide temperature range and in air the product changes its oxygen content at the same time. So the peak is in fact a superposition of the formation heat and an oxidation reaction.

The contributions from the phase transitions and other chemical reactions can not be removed by a simple subtraction since the amount of product ($SrFeO_x$) increases with temperature.

3.4 Mechanochemical Synthesis

The synthesis of $Sr_2Fe_2O_5$ involves annealing at high temperature but some chemical reactions can be carried out at ambient temperature using mechanical energy. Room temperature mechanical reactions of alkali metal carbonates and transition metal oxides are not thermodynamically favourable [124] (the change of the Gibbs free energy is positive) and the present author did not observe any signs of reaction in the milled mixtures of strontium carbonate and iron oxides. However, alkaline earth oxides are reactive towards transition metal oxides and reactions can be triggered by milling [124] so the possibility of a room temperature synthesis using milling was explored.

Since we can not make any theoretical predictions due to lack of thermodynamical data, the reaction:

$$\mathrm{Fe_2O_3} + 2\,\mathrm{SrO} = \mathrm{Sr_2Fe_2O_5}, \tag{3.6}$$

was tested experimentally.

---

[*] Magnetite in air, oxidizes rapidly above 473 K and converts to hematite before the formation of ferrite.

Strontium oxide is very reactive towards water and carbon dioxide so fresh SrO was prepared by a thermal decomposition of $SrCO_3$ at 1473 K in a flow of dry nitrogen. The oxide was immediately combined with an appropriate amount of hematite and milled in an argon atmosphere. Unfortunately mechanical processing up to 200 h did not caused any visible reaction. X-ray diffraction study of the milled mixtures revealed only hematite, SrO, some $SrCO_3$ and $Sr(OH)_2$ formed by a reaction with moisture and CO_2 from air[†].

A thermally induced Reaction (3.6) was studied using the DTA by heating a mixture of oxides, milled for 12 h, at a constant heating rate of 20 K/min in argon. The result was a small exothermic reaction peak at 1123 K with an area corresponding to energy of 5 J/g. However, this value of energy is underestimated since the product of reaction undergoes the endothermic phase transition at 1140 K as explained in the previous section.

The high temperature of the thermally induced reaction indicates that mechanical treatment cannot provide enough energy to trigger the synthesis.

3.5 Iron Contamination

The ball mill used in this thesis can cause problems by contaminating some milled materials with iron as explained in section 2.6. The iron contamination affects experiments in two ways: by upsetting the composition of the sample or by changing the oxidation state of cations in the material. The latter phenomena does not occur every time but has to be borne in mind since the ferrite contains Fe^{4+}, Fe^{3+} and elemental iron can act as a reducing agent:

$$3\,Fe^{4+} + Fe^{0} \rightarrow 4\,Fe^{3+}, \tag{3.7}$$

$$2\,Fe^{3+} + Fe^{0} \rightarrow 3\,Fe^{2+}. \tag{3.8}$$

For example pure hematite can be reduced to magnetite by milling with iron powder in an inert gas. Using the present mill it takes less than 48 h to complete the reaction:

$$4\,Fe_2O_3 + Fe = 3\,Fe_3O_4. \tag{3.9}$$

However, if iron is not added deliberately the same process in the stainless

---

[†] The carbonate and the hydroxide were formed during the preparation of the x-ray specimen and collection of the spectra.

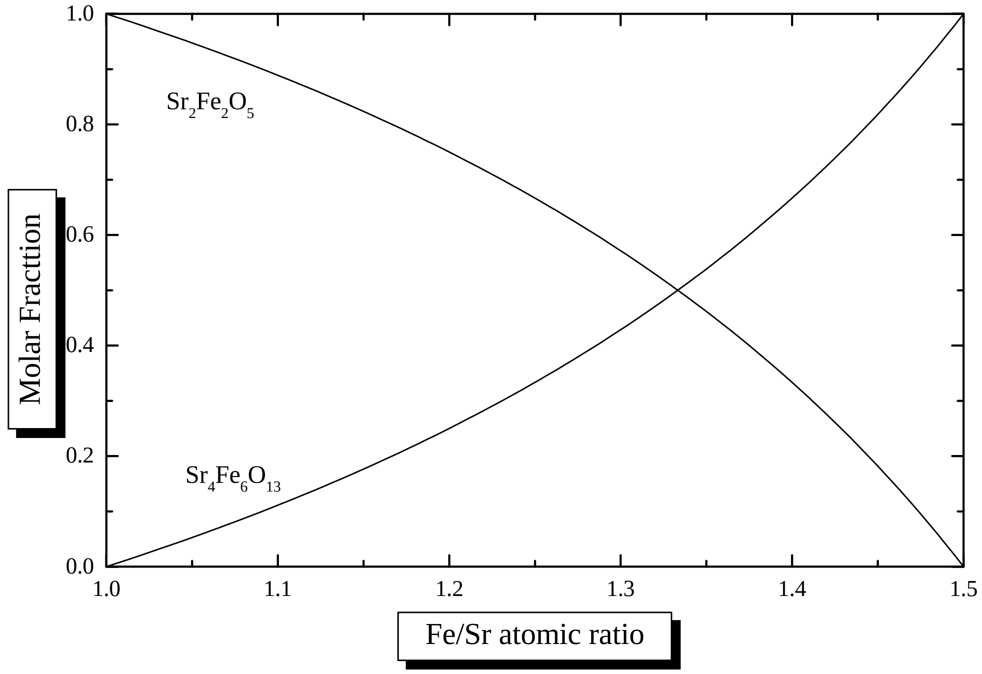

Figure 3.7: Calculated molar fractions of $Sr_4Fe_6O_{13}$ and $Sr_2Fe_2O_5$ as a function of the iron to strontium ratio in the sample.

steel mill takes approximately a week depending the amount of hematite and milling conditions. Iron is introduced into the system by a mechanical abrasion of the mill [107].

Because of the possibility of the iron contamination all milling experiments presented in this thesis were followed by an assessment of excess iron as described below. Materials with even minute iron excess were discarded.

3.5.1 Detection Procedure

Direct detection of the iron excess in milled materials can be difficult if its fraction is small or it had already reacted with the material. However, the present author found that annealing of the sample at a temperature of 1473 K in argon reduces the ferrite to $Sr_2Fe_2O_5$ and the excess iron forms $Sr_4Fe_6O_{13}$[‡]. This two phase mixture is formed when the molar ratio of iron to strontium has values from the range $1 < Fe/Sr < 1.5$. Calculated molar fractions of both phases are presented in Figure 3.7 as a function of the average cation ratio Fe/Sr.

The presence of $Sr_4Fe_6O_{13}$ was detected using x-ray powder diffraction.

[‡] The annealing can be carried out in an oxidizing atmosphere but the interpretation of results is difficult due to severe overlap of $Sr_4Fe_6O_{13}$ and $SrFeO_x$ diffraction lines.

However, in samples with small contamination levels only the strongest diffraction line of $Sr_4Fe_6O_{13}$ is visible and it overlaps with the (150) line of $Sr_2Fe_2O_5$. The presence of iron contamination was determined by comparison of the integrated intensities of the (150) ($d = 2.727\,Å$) and the (161) ($d = 2.170\,Å$) $Sr_2Fe_2O_5$ lines. Pure $Sr_2Fe_2O_5$ yields the intensity ratio $I(150)/I(161) = 0.25$[§]. Departure from the ideal composition causes the (150) line of $Sr_2Fe_2O_5$ to intensify. The (161) line of $Sr_2Fe_2O_5$ was chosen as the reference since it does not coincide with diffraction lines of other phases.

The sensitivity of the method was tested using mock hematite-strontium carbonate mixtures with excess iron in the form of hematite. The test samples were prepared with contamination levels from 1 at.% ($Fe/Sr = 1.01$) upwards by thorough mixing of approximately 0.5 g of reactants using a mortar and pestle[¶]. The mixtures were subsequently fired at 1423 K[‖] in the argon atmosphere for several hours. Fragments of diffraction patterns of pure and contaminated $Sr_2Fe_2O_5$ are presented in Figure 3.8. The picture clearly shows the increase of the (150) line ($2\theta = 38.3°$) with an iron impurity. Above $Fe/Sr = 1.05$ other diffraction lines of $Sr_4Fe_6O_{13}$ become apparent. In the case of the sample with composition $Fe/Sr = 1.01$ the intensity ratio was $I(150)/I(161) = 0.45$. Thus the analysis of the line intensities allows detection of contamination levels smaller than 1 at.%.

3.5.2 Other Strontium Ferrites

Investigation of iron contamination in the $SrFeO_x$ system, which required preparation and x-ray analysis of samples with various compositions, also showed that certain phases reported as original compounds are not single phase species (refer to section 1.5). One of these phases is $Sr_7Fe_{10}O_{22}$ ($Fe/Sr = 1.43$) reported by Brisi and Rolando [35] and Lucchini *et al.* [43], which is in fact a mixture of $SrFeO_x$ and $Sr_4Fe_6O_{13}$.

Another example is $SrFe_2O_4$ ($Fe/Sr = 2$) reported by Beretka and Brown [46]. X-ray diffraction analysis of this compound revealed only a mixture of $Sr_4Fe_6O_{13}$ and $SrFe_{12}O_{19}$.

[§] The line intensities were determined using the Bragg-Brentano diffractometer described on page 27.

[¶] Small amount of reactants can be well mixed using mortar and pestle so they do not form transient phases.

[‖] The annealing was carried out below 1473 K since $Sr_4Fe_6O_{13}$ melts just above this temperature.

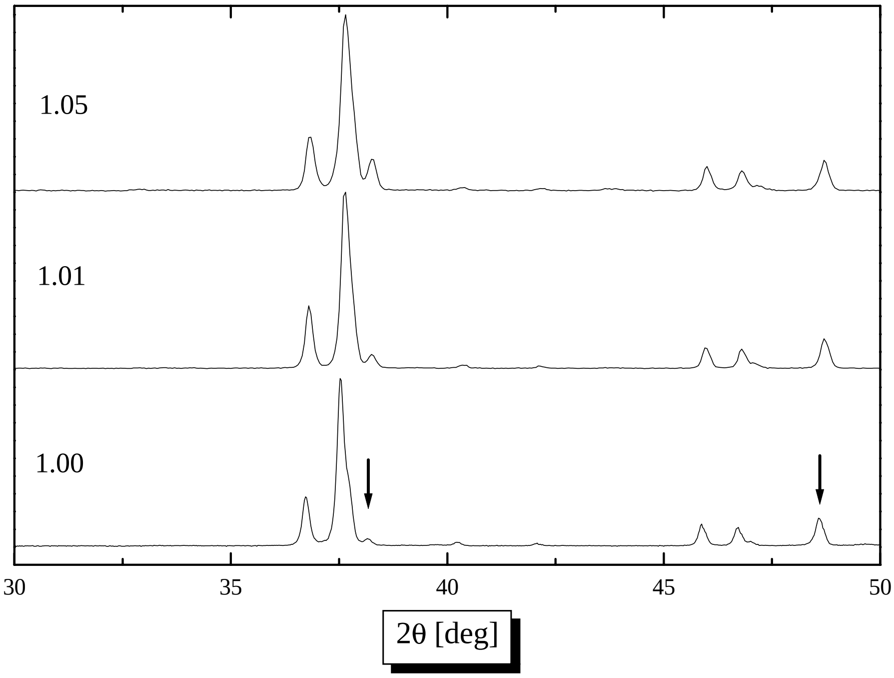

Figure 3.8: X-ray diffraction patterns of pure $Sr_2Fe_2O_5$ and ferrites with excess iron after annealing. The figures denote Fe/Sr molar ratio, the arrows mark the positions of the (150) and the (161) $Sr_2Fe_2O_5$ lines. The spectra were normalized and are presented in the linear scale.

3.6 Preparation Routine

The following procedure was used to prepare large quantities (> 10 g) of well crystallized ferrite. Because of experimental convenience and reasons given in the next chapter, the ferrite was synthesized in its oxygen deficient form ($Sr_2Fe_2O_5$).

The reactants (hematite and strontium carbonate) were dried in air at 647 K, overnight as a precaution and weighed. The mixture (20–50 g) was dry milled for 12 h in air and then annealed at 1373 K on an alumina combustion boat in air for few hours. The annealing in air was carried out to reduce the volume of the powder and remove any traces of transient phases. The ferrite was then reduced to $Sr_2Fe_2O_5$ ($x = 2.5$) by annealing at 1473 K for at least 1 h in a stream of high purity or ultra high purity argon and the final product was examined using x-ray diffraction.

Even though milling of pure hematite (6.5 on the Moh hardness scale) abrades the mill, prolonged milling of the hematite-strontium carbonate mixture does not introduce detectable iron excess. The absence of the contamination seems to be a result of dilution of hematite with a large volume of substantially softer $SrCO_3$ (3.5–4 on the Moh scale).

3.7 Summary

Strontium ferrite ($SrFeO_x$) is formed directly during solid-solid reaction. Any transient phases in the formation reaction are due to inhomogeneity of the reactant mixture. Ball milling of the reactant mixture apart from elimination of transient phases increases the reactivity at lower temperatures. However, the thermodynamical onset of reaction remains the same.

The ferrite can be synthesized from a magnetite-strontium carbonate mixture and the ferrite reduces part of the evolved carbon dioxide. The onset of this reaction occurs at approximately 50 K higher temperature than in the case of hematite-carbonate mixture. The magnetite route does not exhibit any transient phases even with poorly intermixed reactants. However, the product does not contain divalent iron which proves for the first time that the $SrFeO_x$ system does not extend into lower than 3+ oxidation states of iron.

The measured enthalpy of formation is difficult to interpret since the formation reactions occur at temperatures where the product undergoes a phase transition or other concurrent chemical reaction (changes of the oxygen content). The measured heat is different for the hematite and the magnetite based synthesis reactions indicating different reactions mechanisms.

Ball milling does not provide enough energy to initiate formation of the ferrite from a mixture of strontium oxide and hematite at room temperature.

Chapter 4

Interaction with Gaseous Species

The oxide ($SrFeO_x$) contains iron in two oxidation states and their ratio is affected not only by temperature but also composition of the atmosphere. The oxygen content affects the crystal structure and many other properties of the material so studies of the interaction of the ferrite with the gas phase are crucial for understanding of the nature of the material.

Since the amount of oxygen in the oxide can vary, the interaction with oxygen under different partial pressures is the most obvious subject of study and it has been since the discovery of the material [17, 125–128]. However, oxygen bearing atmospheres do not exhaust all possibilities and other complex gaseous oxides also interact with the material. Shin *et al.* [129] reported a catalytic decomposition of NO by the oxygen deficient phase of ferrite ($Sr_2Fe_2O_5$).

This chapter consists of two parts. The first one depicts the interaction of the oxide with oxygen under different partial pressures and temperatures. It presents information about the equilibrium composition of the material, the heat of oxidation and the methods that can be used to measure and adjust the composition of the ferrite. The oxidation reactions were induced by temperature and mechanical energy. The second part presents the interaction of the material with carbon dioxide induced by temperature as well as mechanical energy. Oxidation of the ferrite by milling and the carbonation process are completely new and have not been reported in the literature so far.

4.1 Composition Determination

Investigation of a non-stoichiometric compound requires a reliable method of assessing its oxygen content (stoichiometry). During the course of the experimental work we usually deal with two kinds of situations: (i) determination of the oxygen content in a given sample, (ii) and determination of the stoichiometry *in situ* at elevated temperatures.

Compounds with oxygen non-stoichiometry are analogous with solid solutions which are well known in mineralogy *e.g.* olivine [130]. Usually some physical property of the solution such as lattice constant varies with composition in a systematic way and this property can be used to calculate the composition based on a calibration curve. But, this method can only be applied to the high-temperature, cubic form of the ferrite (see Chapter 7).

However, oxygen is not strongly bound in the crystal structure and the amount can be determined by means of controlled oxidation or reduction reactions. The reaction can be carried out at high temperature and the stoichiometry calculated from the mass change or using wet chemistry methods at ambient temperature. An overview of these methods is presented in the next sections. Particular emphasis was placed on the high temperature reactions since they were exclusively used for composition assessment, although wet techniques are also briefly described for the sake of completeness.

4.1.1 Reference Phase

The high temperature method relies on a mass change relative to a chosen phase of the ferrite, called hereafter the reference phase.

$SrFeO_x$ can change its oxygen content in a broad range of $2.5 \leq x \leq 3.0$ and any phase can be used as a reference material. However it should fulfill certain requirements. The phase must be easy to identify and prepare in large quantities. The obvious choice is one of the composition end members. The fully oxidized $SrFeO_3$ form was dismissed since it is made by high pressure annealing [126, 127, 131] and therefore difficult to obtain in large quantities. For this reason the other end member $Sr_2Fe_2O_5$ ($x = 2.5$) was used. It is easy to prepare and contains only the trivalent iron. However, like every other reference material it should be as pure as possible and in the case of $Sr_2Fe_2O_5$ it means oxygen content $x = 2.5$. Phases with $x > 2.5$ contain the tetravalent iron.

The purity of $Sr_2Fe_2O_5$ was validated using x-ray diffraction. The oxidation of $Sr_2Fe_2O_5$ also causes change of colour from brown to black (in powdered form) which is useful indicator. Other chemical methods cannot be used since there is no known spot test for Fe^{4+} unlike ferrous and the ferric which can be detected even in very low concentrations [132]. Physical methods such as Mössbauer spectroscopy cannot yield conclusive evidence to the sample's purity (see Chapter 5). $Sr_2Fe_2O_5$ is an antiferromagnet and any absorption line from Fe^{4+} would be buried under a dozen lines originating from the magnetic order in the sample. Even though, $Sr_2Fe_2O_5$ has a characteristic diffraction pattern the excess of oxygen is not straight forward to determine. The material with composition $2.5 < x < 2.75$ forms a mixture of $Sr_2Fe_2O_5$ and $Sr_4Fe_4O_{11}$ at room temperature.

Any excess oxygen is indicated by the presence of $Sr_4Fe_4O_{11}$ and since its strongest diffraction line overlaps with $Sr_2Fe_2O_5$ reflection the purity test relies on changes to the intensity ratio of the diffraction lines. The detection procedure is the same as for the detection of excess iron in the material described on page 45. The strongest lines of $Sr_4Fe_4O_{11}$ and $Sr_4Fe_6O_{13}$ occur at similar diffraction angle and overlap with the (150) reflection of $Sr_2Fe_2O_5$. But, it is easy to distinguish between the oxygen excess and the iron excess in the system. The intensity ratio of the peaks decreases upon annealing in argon in the case of oxygen excess but remains unaffected in the case of iron excess. The diffraction patterns of $Sr_2Fe_2O_5$ with a slight oxygen excess (*e.g.* $x = 2.53$) are similar to the spectra with small iron contamination presented in Figure 3.8.

For the purpose of work presented in this thesis the oxygen deficient material was prepared by a prolonged annealing of the ferrite at 1473 K in a flow of high purity or ultra high purity argon. The following sections of this chapter will show that annealing at high temperature resets the oxygen stoichiometry to 2.5 which can be preserved by fast cooling to room temperature in atmosphere with low oxygen activity. Despite the shortcomings of the chosen reference phase ($Sr_2Fe_2O_5$) other phases of the $SrFeO_x$ system are even more difficult to prepare.

4.1.2 Oxygen Assay

The oxygen content of $SrFeO_x$ was calculated from mass loss upon reduction to $Sr_2Fe_2O_5$ ($x = 2.5$) at elevated temperature. The material does not require strongly reducing atmospheres such as hydrogen or carbon monoxide. It is enough to lower the partial pressure of oxygen below approximately 1 ppm.

This task was readily achieved using commercially available inert gases such as high-purity argon or nitrogen. These gases have oxygen partial pressures $p_{O_2} \leq 1\,\mathrm{ppm}$ and annealings were carried out in a stream of gas to maintain constant oxygen activity.

The sample was placed in a thermogravimetric analyser and annealed at 1473 K to constant mass. The procedure can be carried out in a furnace but TGA is better since the mass is continuously monitored. The sample after the reduction was inspected using x-ray diffraction for traces of $Sr_4Fe_4O_{11}$. The reduction takes place according to the reaction:

$$2\,\mathrm{SrFeO}_x = \mathrm{Sr_2Fe_2O_5} + (x - 2.5)\,\mathrm{O_2} \tag{4.1}$$

and the oxygen stoichiometry was calculated from the mass loss using the equation:

$$x = 2.5 + \frac{M_{Sr} + M_{Fe}}{M_O}\,\frac{m_i - m_f}{m_f} \tag{4.2}$$

where M_A is the molecular weight of the element A, m_i and m_f are the initial and the final mass of the sample respectively.

Sometimes $Sr_2Fe_2O_5$ is the starting material for an experiment and its composition after oxidation can be easily determined from its mass gain using Equation (4.5) described in the next section.

The annealing temperature of 1473 K was chosen arbitrarily, it should be as high as possible but still lower than the melting point of the ferrite and low enough not to decompose the oxide. Experience showed that the temperature should not be lower than 1373 K but temperatures higher than 1473 K did not really cause any further visible changes in the mass.

The alternative to the mass change technique is a chemical analysis which determines the amount of oxygen by establishing the fractions of tetravalent and trivalent iron. The method can be applied not only to the ferrite but also to manganese based oxides [17, 125, 127]. During the procedure the oxide is dissolved in hydrochloric acid and the solution is combined with an excess of standardised ferrous salt solution (ferrous ammonium sulphate, the Mohr's salt). The tetravalent iron oxidizes ferrous iron to ferric according to the equation:

$$\mathrm{Fe^{4+}} + \mathrm{Fe^{2+}} = 2\,\mathrm{Fe^{3+}}. \tag{4.3}$$

The residual ferrous iron is then titrated with a solution of potassium dichromate or ceric ammonium nitrate in the presence of a redox indicator, usually diphenylamine. The amount of the tetravalent iron is then calculated from the remaining ferrous iron. The total iron content is obtained by a reduction of all iron in solution to 2+ state and titration with potassium dichromate. [133, 134]. The knowledge of the tetravalent and the total iron content is enough to establish the oxygen stoichiometry since the trivalent iron constitutes the difference between the two measured quantities.

The chemical and mass loss methods deliver the same accuracy [127] and face the same limitations when applied to the phases with a low oxygen concentration. However, the method using the weight change is simpler and faster and its result is only influenced by the weighing error provided that the reduction product is carefully checked for traces of $Sr_4Fe_4O_{11}$. On the other hand the accuracy of the chemical methods is influenced by other factors such as cumulative errors made during preparation of solutions and the influence of oxygen dissolved in water or coming from the atmosphere [125, 127] which can seriously interfere with the ferrous iron titration. For these reasons the high temperature reduction was exclusively used in this thesis for composition determination.

4.1.3 *In Situ* Determination

Composition of the oxide is highly sensitive to temperature and oxygen partial pressure in the atmosphere. The material fairly quickly equilibrates with the atmosphere making it impossible to study by annealing of the sample and cooling since the final product will change its oxygen content. One solution is to equilibriate the sample at a given temperature in a given atmosphere and to quench it into liquid nitrogen or water hoping that the composition and possibly the crystal structure will be preserved. The stoichiometry of the sample is later determined using the methods described in the previous section. However, the method has a few shortcomings, it is virtually impossible to determine whether or not the sample gained any oxygen during its fall into the cooling bath, and also it is difficult to establish if the annealing time was sufficient to reach the equilibrium.

The task is easier with use of a thermogravimetric analyser as the mass of sample is constantly monitored and it is easy to judge if equilibrium has been reached. Moreover the recorded mass gives the exact composition at fixed temperature and oxygen activity.

If the atmosphere is relatively rich in oxygen the equilibrium composition can be determined by mass gain due to oxidation of the reference phase

($Sr_2Fe_2O_5$). The oxidation reaction can be written:

$$\mathrm{Sr_2Fe_2O_5} + (x - 2.5)\,\mathrm{O_2} = 2\,\mathrm{SrFeO}_x \tag{4.4}$$

and the oxygen stoichiometry x calculated from the equation:

$$x = 2.5 + \frac{M_{Sr} + M_{Fe}}{M_O}\,\frac{m_f - m_i}{m_i} \tag{4.5}$$

where m_i denotes the mass of $Sr_2Fe_2O_5$ and m_f is the equilibrium mass. The method works well in oxygen rich atmospheres, however its use in low partial pressures becomes troublesome. In principle, the method is still valid but in very low oxygen concentrations the equilibration times are impractically long since the probability of collision of oxygen molecule with the oxide is very small. The maximum oxygen intake per unit time and surface area is given by the Hertz-Langmuir [122, 135] equation:

$$j = \frac{p_{O_2}}{\sqrt{2\pi MRT}} \tag{4.6}$$

where M is the molecular weight of oxygen. The equation gives the maximum theoretical value which is much lower in practice due to oxygen depletion of the atmosphere surrounding the sample and the finite supply of the oxidizing gas.

In many cases completion of the oxidation process would require large volumes of gas to provide the required amount of oxygen. According to this formula the rate of oxygen intake at a partial pressure of 1 ppm at 1000 K is about 0.001 mol/(h cm^2). In this case it is better to use an oxidized sample of known composition $SrFeO_y$ and equilibriate it with the atmosphere. The composition of the sample should exceed the equilibrium oxygen stoichiometry. The sample is reduced according to the reaction:

$$2\,\mathrm{SrFeO}_y = 2\,\mathrm{SrFeO}_x + (y - x)\,\mathrm{O_2} \tag{4.7}$$

and the equilibrium composition can be found from the mass loss using the equation:

$$x = y - \frac{M_{Sr} + M_{Fe}}{M_O}\,\frac{m_i - m_f}{m_f} \tag{4.8}$$

This method is slightly less precise since it is based on the earlier determined composition of $SrFeO_y$ but is much faster and indication of the equilibrium is clearer.

The last very important factor during the equilibration is maintaining a constant oxygen activity over the sample. It is easy to achieve by keeping a high gas flow through the furnace.

4.2 Thermal Oxidation

The experiments were carried out under a total pressure of 1 atm and the partial pressure of oxygen was regulated by mixing oxygen with inert gas. The presented results are essential for understanding of the high temperature crystal structure of the compound described in Chapter 7.

4.2.1 Equilibrium Composition

The equilibrium compositions at elevated temperature were determined *in situ* using the thermogravimetric analyser. For experimental convenience the measurements were made by varying temperature at constant oxygen partial pressure. The different oxygen activities were achieved using mixtures of gases.

Simple gases such as oxygen, nitrogen or argon under atmospheric pressure at temperatures above 293 K are far enough from the boiling point on their phase diagrams to be treated as ideal gases. For a mixture of ideal gases the total pressure p can be expressed as a sum of contributions from all components, given in the form of Dalton's law:

$$p = \sum_i p_i \tag{4.9}$$

Applying the ideal gas law to Equation (4.9) we find that the partial pressure of every component p_i in the mixture is proportional to its molar fraction x_i:

$$p_i = x_i p \tag{4.10}$$

and the molar fraction x_i is equal to the volume fraction f_i of the ith component in the mixture:

$$x_i = f_i \equiv \frac{V_i}{V} \tag{4.11}$$

so the partial pressure of ith component can be expressed by its volume fraction:

$$p_i = \frac{V_i}{V} p \tag{4.12}$$

The total volume is the sum of all the components given in form of Leduc's law:

$$V = \sum_i V_i \tag{4.13}$$

The Equation (4.12) and Equation (4.13) were used to calculate the oxygen partial pressure in the gas mixtures used for experiments.

The different mixtures were prepared from oxygen or air combined with nitrogen using two flowmeters. The measurements were made in the oxygen partial pressure range from 0.999 atm (oxygen 99.9 % purity) to 0.003 atm. Lower pressures would require use of mixtures of carbon monoxide and carbon dioxide or hydrogen and steam. Even smaller partial pressures of oxygen can be obtained using solid buffers, mixtures containing a metal and its oxide such as Fe-FeO, Co-CoO, Ni-NiO, or zirconia cells [136]. However, oxygen pressure in the indirect mixtures or buffers is temperature dependent and because of the sensitivity of the thermogravimetric analyser, measurements were not carried out below 0.003 atm.

The oxygen stoichiometry x was determined as a function of temperature by oxidation of $Sr_2Fe_2O_5$. The equilibrium composition was calculated using Equation (4.5). During the experiment the temperature was increased stepwise and kept constant for periods of time to equilibrate the sample. An example of a raw TGA result is presented in Figure 4.1, showing several equilibration steps in air atmosphere. Between the steps the temperature was increased at a rate of 10 K/min. It is clear that the material reaches equilibrium quickly and the mass change during the heating cycle follows the linear temperature raise. This fast equilibration is the reason why the oxide's composition has to be studied using the TGA or quenching, otherwise samples oxidize during cooling.

The thermogravimetric results were corrected to remove a small temperature dependent drift mainly due to buoyancy and the calculated equilibrium compositions were plotted in Figure 4.2 as functions of temperature and partial pressure of oxygen. It is obvious that the oxygen content decreases with temperature and decreasing partial pressure of oxygen in the atmosphere. The oxygen concentration decreases almost linearly in temperature region from approximately 673 K to roughly 1273 K in atmospheres rich in oxygen. The stoichiometry seems to approach $x = 2.5$ irrespective of oxygen partial

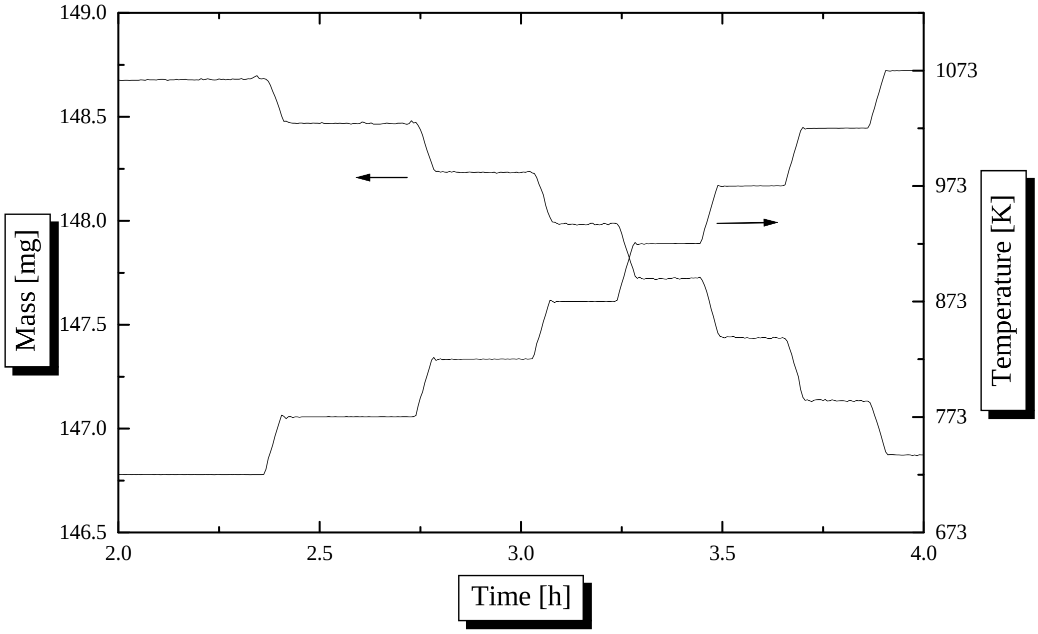

Figure 4.1: An example raw thermogravimetric data used for determination of the equilibrium composition of $SrFeO_x$. The experiment was carried out in the air atmosphere as discussed in the text.

pressure at sufficiently high temperature. Below, approximately 673 K the rate of composition change decreases with decreasing temperature.

The equilibration times at lower temperatures are strongly affected by the decreasing oxidation rate. The kinetics of reaction slows down considerably with decreasing temperature and oxygen partial pressure. This is why the equilibrium compositions were established only at relatively high temperature for lower oxygen activities. The low oxidation rate is partially caused by decreasing ionic conductivity which is responsible for the transport of oxygen within the crystal [30, 137, 138].

Figure 4.2 contains only equilibrium points, but it is possible to obtain even higher stoichiometry by prolonged annealing of the oxide at lower temperatures. However, the process takes days and because of very small mass changes it is difficult to establish if they are the equilibrium compositions. Nonetheless prolonged annealing or annealing combined with a slow decrease in temperature is a good method for preparation of highly oxidized samples.

The equilibrium compositions presented in Figure 4.2 were found only for selected temperatures, but the behaviour of oxide during the heating period suggests that the material can continuously change its composition within the composition range $2.5 \leq x \leq 3.0$. Additional thermogravimetric runs

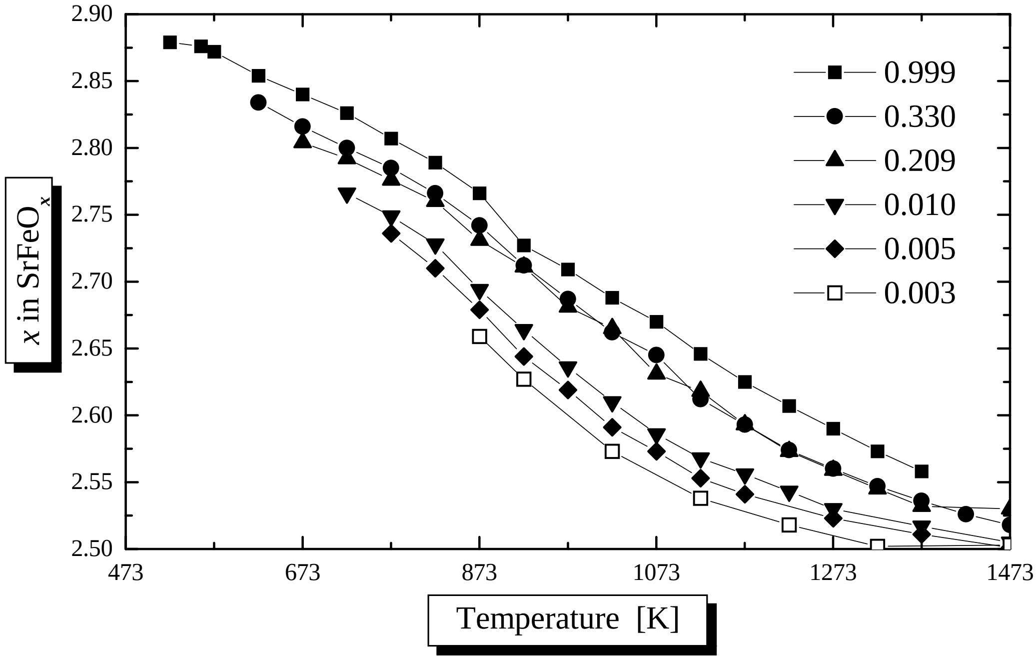

Figure 4.2: The equilibrium composition of SrFeO$_x$ as a function of temperature under different partial pressures of oxygen. The figures denote the oxygen partial pressure in atmospheres.

made at constant heating rate did not show any steps in the mass curves which would indicate the presence of phases with discrete composition.

The gravimetric observations are consistent with other authors findings. Previous results were obtained using quenching [125, 127] as well as thermogravimetry [126, 128]. However, except for Tofield *et al.* [126] the results were presented incorrectly. The lines of equilibrium composition were plotted in form of the equilibrium temperature as a function of composition. It is improper since temperature defines the composition not the other way around [125, 127, 128].

Mizusaki *et al.* [128] used a thermogravimetric analyser to study the ferrite in a broad oxygen pressure range. Their experiments were carried out at fixed temperatures and variable oxygen partial pressure. However, the oxygen pressure was varied from as low as 10^{-12} atm up to 1 atm and the group observed sudden mass gains at certain pressures. The pressures at which the phenomena occurred were found to increase with temperature and the amplitude of the jump decreasing with increasing temperature. The jumps were interpreted as a phase transitions on a phase diagram, but they are nothing else than a result of increased reaction kinetics. The constant mass at very low partial pressures of oxygen was the result of low oxygen concentration and created an illusion of an equilibrium state as discussed on page 55.

Thermal treatment under atmospheric pressure cannot produce samples from the entire composition range. The highest oxygen content attained in this thesis by slow cooling of the material in oxygen is $x = 2.915$. There are some discrepancies over the maximum oxygen content that can be achieved by annealing under 1 atm of oxygen and the other reports [126, 127] claim slightly lower values. But, the very slow oxidation reactions are influenced by many conditions such as powder particle size and the area of the powder exposed to the gas. These two factors and the annealing time may be the cause of lower yield.

Materials with close to $x = 3$ can be produced by high pressure annealing. However, because of the technical difficulties caused by high-pressure thermogravimetric experiments there are no genuine equilibrium data but only a list of temperatures and pressures at which the experiments were made and their outcome. Different authors report different conditions that lead to the same product [125–127, 131, 139]. Almost all of these experiments were done by quenching a pressurized vessel into water. Because of its considerable thermal mass the cooling process would have been slowed and the material could gain some oxygen during cooling giving overestimated values for the given annealing temperature. Another problem is pressure in the vessel which from the descriptions given in the publications was not kept constant during the experiment. So the reported annealing conditions should be treated as a guideline.

Wattiaux *et al.* [140] reported an interesting electrochemical method of oxidation. They claim successful oxidation of the ferrite to the composition $SrFeO_3$. It an indication that the fully oxidized material is not a high pressure form but that an extreme pressure of oxygen is required to overcome slow oxidation kinetics at low temperatures.

4.2.2 Equilibrium Composition Diagram

The results shown in Figure 4.2 were used to plot the equilibrium composition of the oxide as a function of temperature and oxygen partial pressure on a (T, p_{O_2}) plane.

This was done using a simple phenomenological model based on experimentally observed phase relations. The model is applicable to the composition range $2.5 < x < 2.75$. Experimental observations made by the present author and reported elsewhere [126–128] indicate that in this range the oxide forms a mixture of $Sr_2Fe_2O_5$ and $Sr_4Fe_4O_{11}$ or a cubic solid solution (see section 7.4.1). So in this composition range $Sr_2Fe_2O_5$ and $Sr_4Fe_4O_{11}$ coexist in equilibrium. If the oxygen content does not exceed $x = 2.75$, the oxidation reaction can be written:

$$4\,\mathrm{Sr_2Fe_2O_5} + \mathrm{O_2} = 2\,\mathrm{Sr_4Fe_4O_{11}}. \tag{4.14}$$

The equilibrium constant K for this reaction is given by the following formula:

$$K = \frac{a^2_{\mathrm{Sr_4Fe_4O_{11}}}}{a^4_{\mathrm{Sr_2Fe_2O_5}}\, p_{O_2}} \tag{4.15}$$

where, a_γ is the activity of the γ phase.

When the oxidation is complete (all $Sr_2Fe_2O_5$ is converted to $Sr_4Fe_4O_{11}$) the equilibrium constant given by Equation (4.15) simplifies to:

$$K = p_{O_2}^{-1}. \tag{4.16}$$

Analysis of Figure 4.2 shows that for every partial pressure of oxygen there is a temperature at which the oxide has composition equal to $x = 2.75$*. For these pairs of temperatures and pressures the material exists as single phase $Sr_4Fe_4O_{11}$ and it is possible to calculate the change of Gibbs free energy ΔG_f for the Reaction (4.14) using the formula [51,122]:

$$\Delta G_f = -RT\ln K = RT\ln p_{O_2} \tag{4.17}$$

The energy ΔG_f plotted as a function of temperature forms the Ellingham plot for $Sr_4Fe_4O_{11}$ phase. The Ellingham plot allows comparison of the chemical stability of $Sr_4Fe_4O_{11}$ with the other oxides and calculation of the equilibrium partial pressure of oxygen as a function of temperature using Equation (4.17).

The equilibrium temperature for a given partial pressure of oxygen was extracted from Figure 4.2 by fitting a third order polynomial to the experimental points and solving it for $y = 2.75$. The plot was constructed using the pairs of temperatures and pressures and is presented in Figure 4.3. The experimental points lie on a straight line and value of the energy increases with temperature which is characteristic for most of known oxides [122,136].

---

*The lines for pressures $p_{O_2} \leq 0.005$ atm do not reach $x = 2.75$ due to sluggish kinetics at low temperatures.

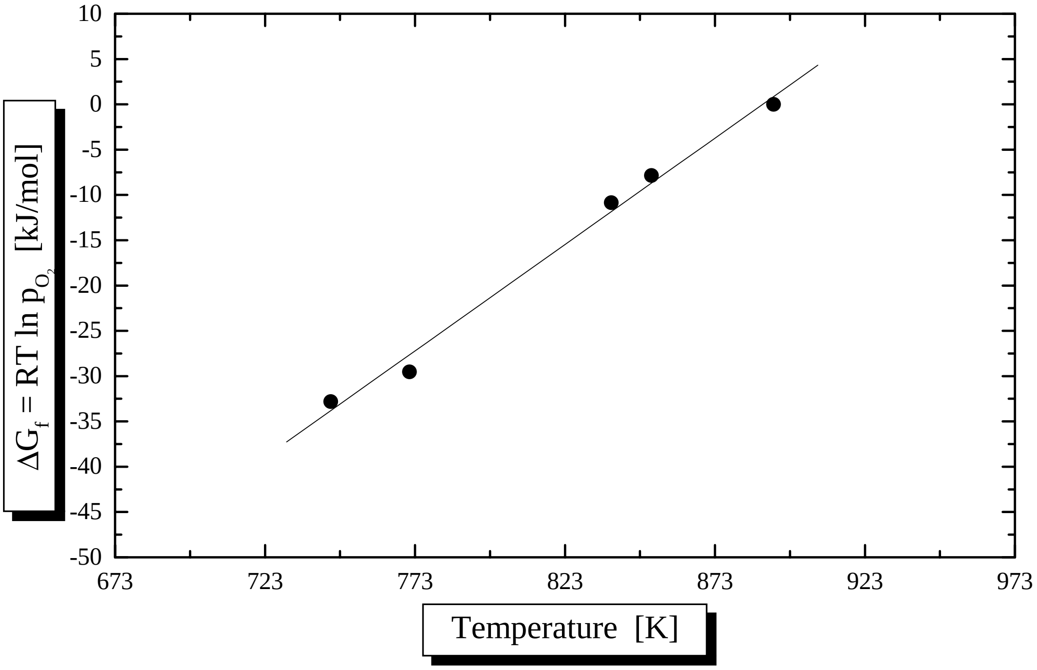

Figure 4.3: The Ellingham plot of $Sr_4Fe_4O_{11}$. The solid line is the best linear fit as described in text

Fitting of the points with a straight line gave the energy (in kJ/mol) as a function of temperature:

$$\Delta G_f(T) = 0.23487\,T - 208.77 \tag{4.18}$$

$Sr_4Fe_4O_{11}$ exists as a single phase when oxygen partial pressure and temperature fulfill the relation given by Equation (4.18). Any departure from these conditions causes further oxidation or reduction which is clearly illustrated by the results of the thermogravimetric experiments. The Gibbs energy of formation of $Sr_4Fe_4O_{11}$ reaches zero at 889 K and above it the compound does not exist as a single phase under atmospheric pressure. Comparison with free energies of other oxides [122] shows that $Sr_4Fe_4O_{11}$ is very unstable. Its chemical stability is comparable with noble metal oxides such as PtO or Ag_2O and is significantly less stable than any transition or alkali metal oxide. The Ellingham plots of the oxides are presented in Figure 4.4.

When the oxidation is only partial, the two phases of the ferrite ($Sr_2Fe_2O_5$, $Sr_4Fe_4O_{11}$) coexist in equilibrium. The equilibrium constant is now given by Equation (4.15) and the activities of both phases are needed to evaluate it. The fractions of both components can be calculated by partitioning oxygen

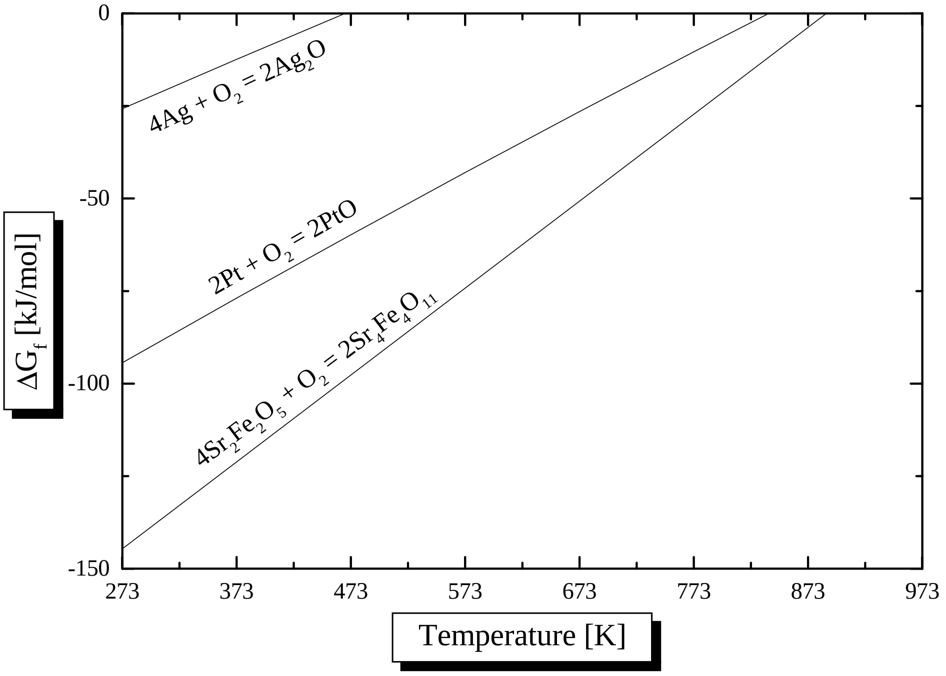

Figure 4.4: The Ellingham plots of PtO, Ag_2O and $Sr_4Fe_4O_{11}$ oxides as discussed in the text.

between the two phases according to the equation:

$$\mathrm{SrFeO}_x = A\,\mathrm{Sr_2Fe_2O_5} + B\,\mathrm{Sr_4Fe_4O_{11}} \tag{4.19}$$

where A, B are constants. The activities of both phases in the mixture are equal to their molar fractions. The solution gives us the molar fractions of both phases and therefore their activities as functions of composition x:

$$a_{\mathrm{Sr_2Fe_2O_5}} = \frac{A}{A+B} = \frac{5.5-2x}{3-x} \tag{4.20}$$

$$a_{\mathrm{Sr_4Fe_4O_{11}}} = \frac{B}{A+B} = \frac{x-2.5}{3-x} \tag{4.21}$$

$$a_{\mathrm{Sr_2Fe_2O_5}} + a_{\mathrm{Sr_4Fe_4O_{11}}} = 1 \tag{4.22}$$

The activities of both phases were calculated for every equilibrium composition $x < 2.75$ found using the TGA. The logarithm of the equilibrium constant was plotted in Figure 4.5 as a function of reciprocal temperature. The experimental points lie on a straight line which indicates that the system obeys the Gibbs-Helmholtz equation [51]. There is certain amount of noise in the data mainly due to weighing error of the thermobalance. The influ-

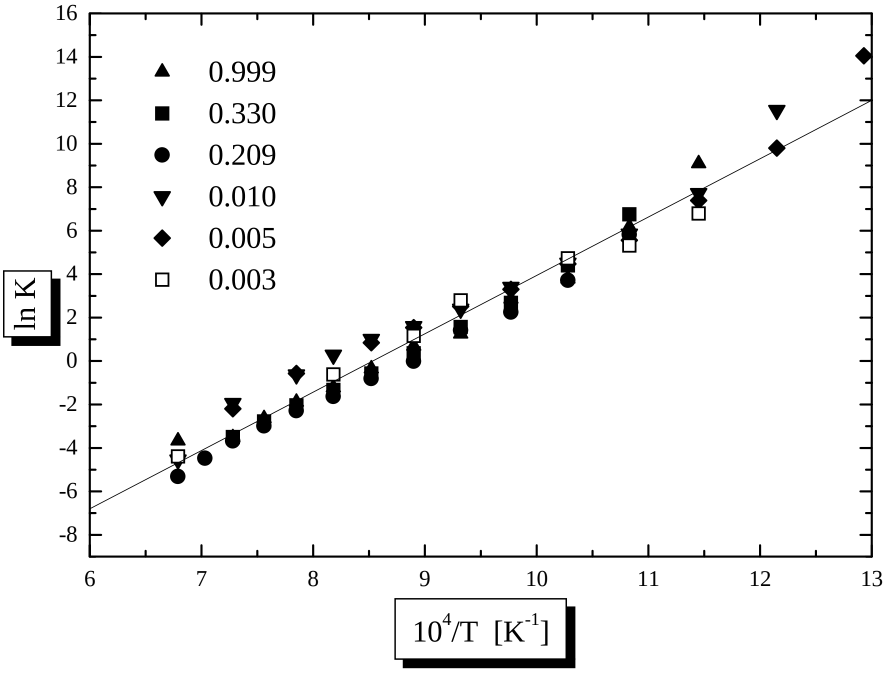

Figure 4.5: Logarithm of the equilibrium constant as a function of reciprocal temperature. The figures denote partial pressure of oxygen in atmospheres, the line is the best linear fit described in the text.

ence of the weighing error is larger at lower temperatures since the activity of $Sr_2Fe_2O_5$ is low and even small errors project as huge changes in K due to the structure of Equation (4.15). The straight line is described by the formula:

$$\ln K = 2.68593 \frac{10^4}{T} - 22.92 \tag{4.23}$$

The equilibrium constant, by definition, is only a function of temperature. The parameters of the straight line can be used to calculate activities and therefore the oxygen stoichiometry for an arbitrary temperature and partial pressure of oxygen using Equations (4.15), (4.20) and (4.22).

The model describes only half ($2.5 < x \leq 2.75$) of the total composition range ($2.5 \leq x \leq 3.0$) and the (T, p_{O_2}) plane has to be divided into two parts, where the oxide has the oxygen content higher and lower than $x = 2.75$. The dividing line was calculated from the Ellingham plot of $Sr_4Fe_4O_{11}$ and the composition of the oxide below this line was derived from the equilibrium constant $K(T)$. The calculated lines of constant composition are presented in Figure 4.6.

The diagram (see Figure 4.6) is missing the part corresponding to the compositions higher than $x = 2.75$. However, there are not enough exper-

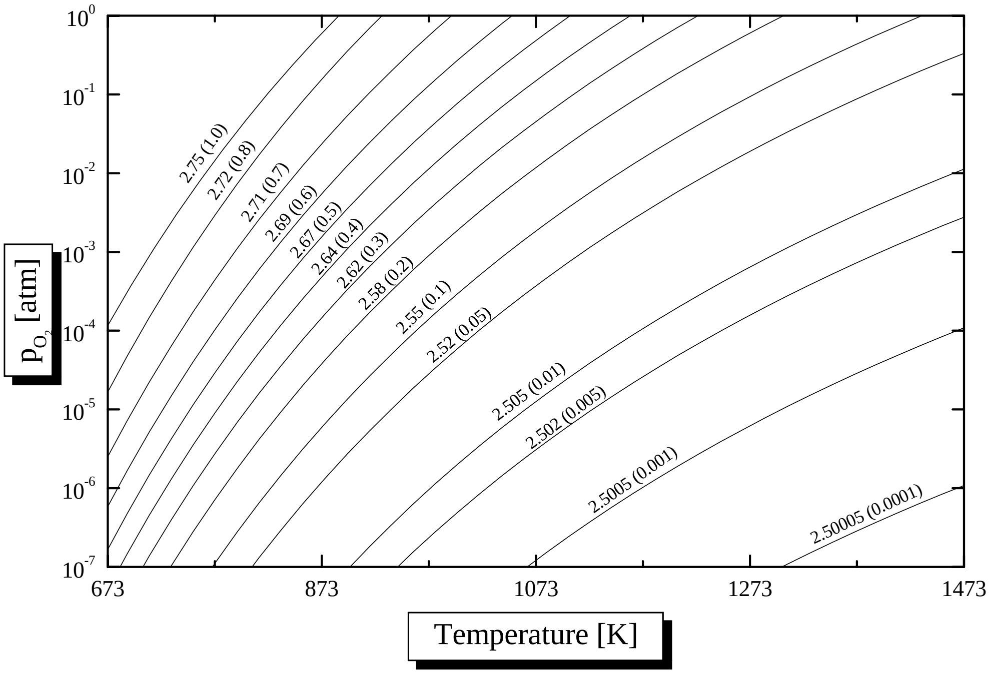

Figure 4.6: The equilibrium composition diagram of the $SrFeO_x$ system. The curves join points of equal composition. The figures denote the oxygen stoichiometry, the numbers in parentheses mark the activity of $Sr_4Fe_4O_{11}$ as discussed in the text.

imental points to carry out the analysis for compositions $x > 2.75$. This is due to long equilibration times at low temperatures and oxygen partial pressures. The experimental points below 673 K in Figure 4.2 may not be completely equilibrated with the atmosphere. But the diagram for $x > 2.75$ is expected to have a similar form.

The line of constant composition $x = 2.75$ was plotted only down to 673 K because $Sr_4Fe_4O_{11}$ undergoes a phase transition at this temperature (see Figure 7.1) which may change the slope of the Ellingham plot (further experimental data are required to verify this). The minimum value of oxygen partial pressure was chosen arbitrarily. From the thermogravimetric experiments we know that the oxygen content of the oxide decreases with decreasing partial pressure of oxygen at fixed temperature. If we lower the pressure far enough the oxide will reach the line of constant composition $x = 2.5$ and this line is the true lower limit of pressure, below which the ferrite decomposes to SrO and elemental iron or FeO. Unfortunately, there is no thermodynamical data for $Sr_2Fe_2O_5$ and we cannot plot this line. The theoretical estimations, mentioned in the previous chapter, place the Gibbs free energy value for $Sr_2Fe_2O_5$ at -381 kJ/mol at 1273 K [14,123]. The energy corresponds to the equilibrium partial pressure of 2.3×10^{-16} atm. This estimate gives a wide safety margin and means that the diagram can be safely used in the given pressure range.

The thermogravimetric results presented in Figure 4.2 are sections through the equilibrium composition diagram at constant oxygen partial pressure. Analysis of the diagram confirms the conclusions drawn from Figure 4.2. The oxygen content of $SrFeO_x$ visibly decreases with decreasing partial pressure and increasing temperature. Since the lines of constant composition do not intercept the material at any oxygen pressure, should reach the composition of $x = 2.5$ if the temperature is raised high enough. Parts of the diagram corresponding to low temperatures or low partial pressures (below $\sim 10^{-5}$ atm) are not experimentally accessible because of the very long equilibration times due to scarce oxygen and low ionic conductivity of the material. This diagram explains why it possible to set the oxygen stoichiometry close to 2.5 by annealing it in high purity argon with oxygen pressure around 10^{-6} atm.

The equilibrium composition diagram also gives us the idea about the accuracy of the oxygen stoichiometry determination by reduction to $Sr_2Fe_2O_5$. Annealing at 1473 K in argon ($p_{O_2} = 10^{-6}$ atm) resets the composition to about 2.50005 (see Figure 4.6) but in the ideal situation the composition should be set to exactly 2.5. However, calculated mass loss difference due to imperfect reduction is only 0.0006 % which corresponds to 6 μg in 1 g of material. This accuracy is well within the systematic error of most laboratory balances and is certainly below the resolution of the thermogravimetric analyser used for the experiments.

4.2.3 Heat of Oxidation

Chemical reactions are always accompanied by heat effects. The equilibrium composition information presented in Figure 4.2 and Figure 4.6 indicate that the product of $Sr_2Fe_2O_5$ oxidation varies with temperature and oxygen partial pressure so the heat of oxidation should change too.

The heat (enthalpy) can be determined using differential thermal analysis. These experiments usually heat a sample at a constant heating rate in an oxidizing atmosphere and at a certain temperature the sample ignites. However, in our case this approach is not appropriate since the product is temperature dependent. The heat of oxidation was determined as a function of temperature using the following procedure. A sample of $Sr_2Fe_2O_5$ was heated to the desired temperature in an argon atmosphere. When the tem-

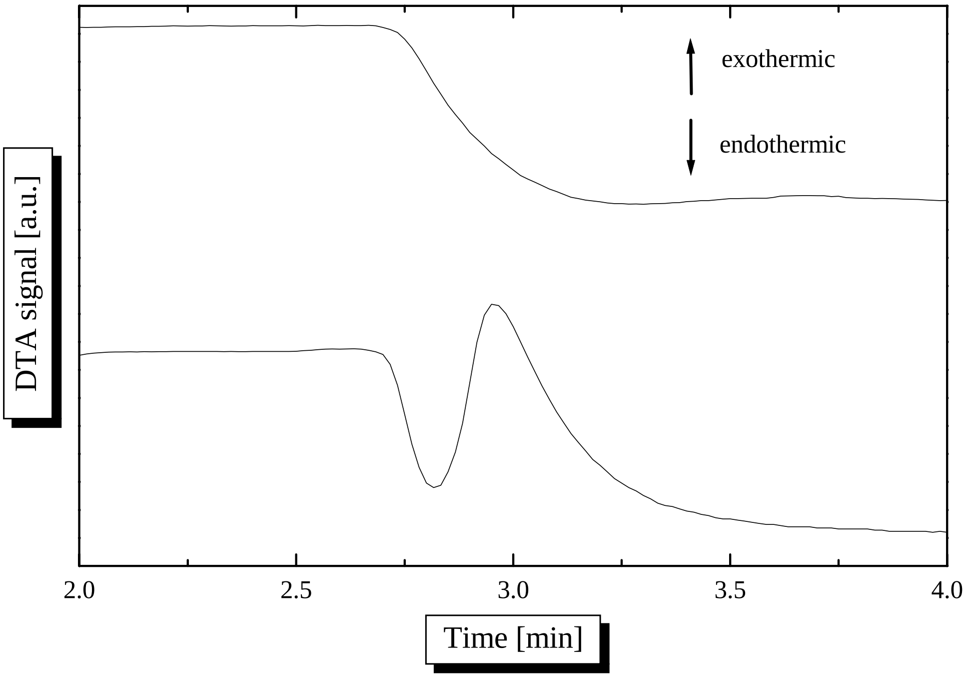

Figure 4.7: An example oxidation peak of $Sr_2Fe_2O_5$ measured with the DTA at constant temperature of 1073 K in air. The top line shows the result of a blank run, the drop in the signal is caused by the introduction of air. The bottom line shows the exothermic oxidation peak superimposed on the baseline

perature had stabilized, the argon was replaced by an oxidizing gas and the heat was measured by integrating the exothermic DTA peak. To make sure that the results were genuine blank runs were made and they caused a step like change in the baseline. An example of an oxidation peak and a blank run made at the same temperature are presented in Figure 4.7. However, use of the DTA has its limitations. This type of calorimeter is only suitable for detection of fast reactions producing large power (heat per unit time). If the reaction takes a couple of minutes or hours it is impossible to measure the heat since its difficult to distinguish between the baseline and the peak. For this reason the heat measurements were made for narrower temperature and pressure ranges than the thermogravimetric measurements. Because of the technical difficulties with suppling gas mixture to the analyser, the determinations were made only in air and oxygen.

The heat of oxidation as a function of temperature and atmosphere is presented in Figure 4.8. At temperatures below approximately 773 K the heat is almost constant, with the exception of air. But the sudden decrease of the heat for air atmosphere at 673 K is caused by rapidly decreasing reaction

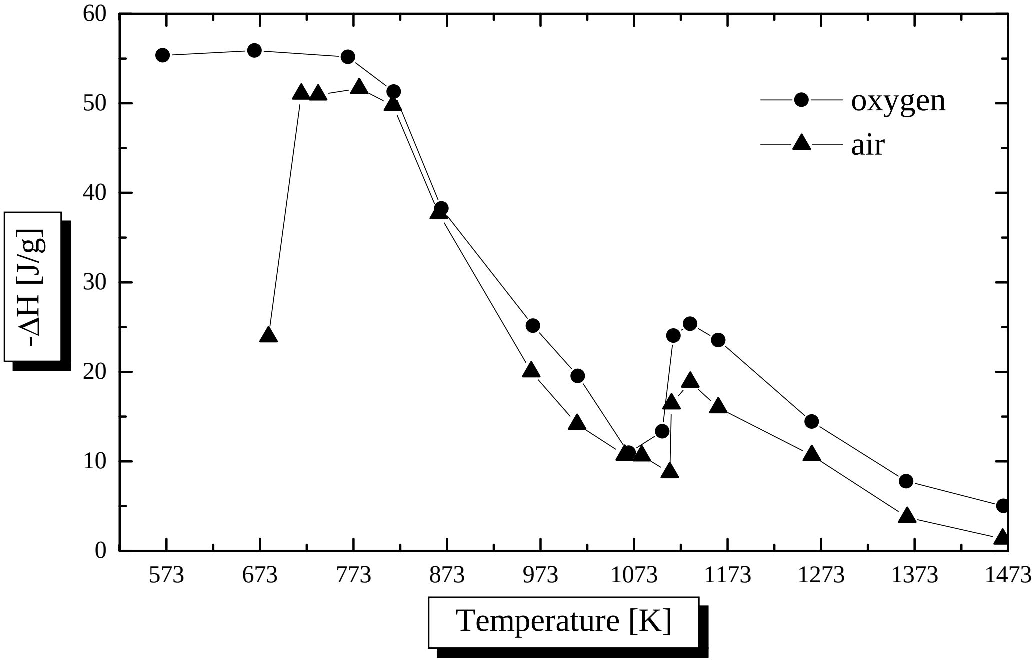

Figure 4.8: The enthalpy of $Sr_2Fe_2O_5$ oxidation as a function of temperature in air and oxygen atmospheres. The lines are guides to the eye.

kinetics and the value is underestimated since the exothermic peak becomes very broad. Above 773 K the oxidation heat decreases with temperature. This is understandable since the amount of gained oxygen decreases with temperature at the same time. Both curves experience a sudden increase around 1123 K and then continue to decay with temperature. The oxidation heat approaches zero with increasing temperature irrespective of the oxygen partial pressure. Close to zero heat at high temperatures is a direct consequence of the thermogravimetric findings. The oxygen stoichiometry tends to $x = 2.5$ if the temperature is high enough, so there is no compositional change and no oxidation heat.

Since the heat jump occurred in both atmospheres despite yielding different products at the same temperature the phenomenon must be associated with temperature induced changes in the reactant ($Sr_2Fe_2O_5$).

Indeed, $Sr_2Fe_2O_5$ undergoes a transformation from the orthorhombic to the cubic form around this temperature. As it will be explained in Chapter 7 this is a transition from an ordered to a disordered structure.

The enthalpy of oxidation changes because the reactant ($Sr_2Fe_2O_5$) has different configurational entropy below and above the transition temperature. The oxidized form (the product) does not undergo a phase transition

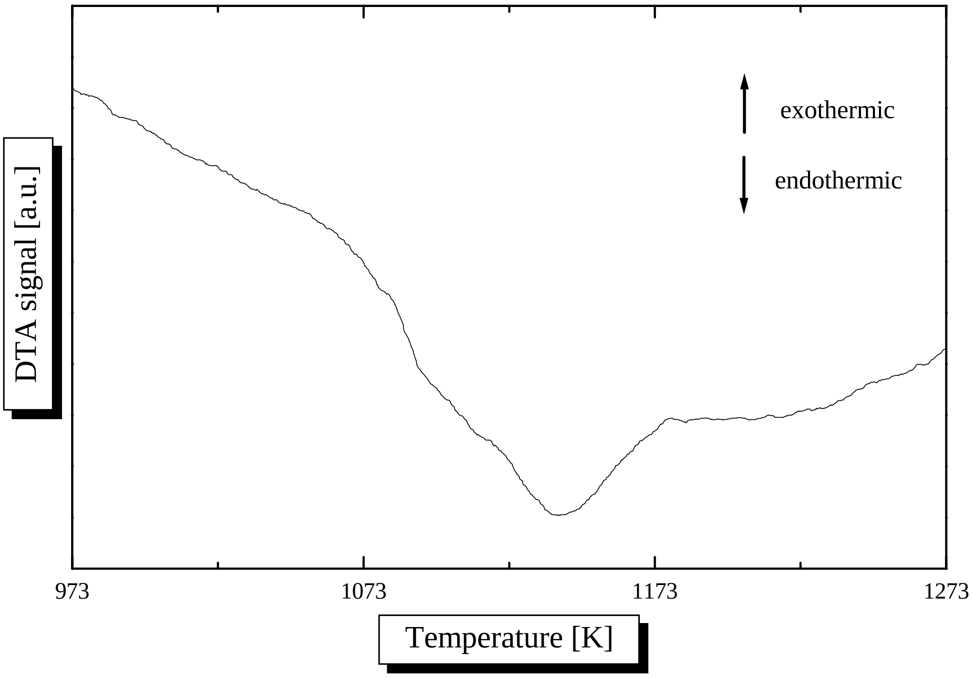

Figure 4.9: The DTA trace of the phase transition in $Sr_2Fe_2O_5$ at 1140 K. The curve was obtained by heating at a constant rate of 20 K/min in argon.

around 1123 K and has a cubic structure (see section 7.4.2). Below the phase transition in $Sr_2Fe_2O_5$ ($T < 1123$ K) the oxidation causes a crystal symmetry change from orthorhombic to cubic. On the other hand above the transition point there is no symmetry modification. From the energetic point of view above the transition temperature, energy that would have been spent on the symmetry change is released as excess heat.

The phase transformation in $Sr_2Fe_2O_5$ was observed using DTA by heating the oxide at constant rate in argon. A fragment of the DTA curve is presented in Figure 4.9. This transformation was regarded as the first order transition [127, 138] mainly due to the peak area which corresponds to an energy of approximately 40.9 J/g. However, the peak shape does not exhibit the characteristic features of a first order transformation. The onset of transformation is not well defined and the slope of the baseline starts slowly changing around 1073 K. First order transitions have very sharp onsets of the peaks followed by steep fall of the DTA signal due to absorption of the transition heat. For these reasons the first order nature of the transformation should be dismissed and the peak of heat capacity at 1140 K was taken as the transition temperature. The shape of the heat jump (see Figure 4.8) is not very steep. A first order transition would cause a discontinuity in the heat curve and we observe a relatively slow increase with temperature. This indicates a continuous transformation and coexistence of two phases of $Sr_2Fe_2O_5$ during the transition. This conclusion will be supported by the results of neutron diffraction experiments presented in Chapter 7.

4.2.4 Adjustment of Composition

Study of the composition changes with temperature and partial pressure of oxygen are essential for preparation of phases with different oxygen content for room and sub-ambient temperature research. The main difficulty with sample preparation lies in the volatile nature of oxygen as shown in the previous sections. The difficulties can be overcome, the recipes for different compositions usually yield materials with stoichiometry close to the desired. But, it should be born in mind that the oxidation process is affected by a number of factors that cannot be fully controlled.

The following sections describe techniques which can be used to adjust the oxygen content and their advantages and disadvantage.

An Ideal Method

The equilibrium composition diagram presented in section 4.2.1 gives an idea of an equilibration method which should yield samples with the desired oxygen content x. The method was not used in the thesis but the idea can be applied not only to $SrFeO_x$ but to other non-stoichiometric materials as well.

The thermogravimetric results presented in Figure 4.2 show that the oxygen content increases if the sample is cooled in atmosphere with constant oxygen activity. However, a simultaneous reduction of oxygen partial pressure should prevent further oxidation. The composition will be preserved when during the cooling, the oxygen activity is reduced in such a way that annealing conditions follow a line of constant composition on the equilibrium composition diagram. The line of constant composition should be followed until the oxidation rate becomes unsignificantly low, which in practical terms is below 473 K[†]. To ensure thorough equilibration the sample should be annealed at the relatively high temperatures and oxygen pressures found using the thermogravimetric experiments.

[†] This temperature depends on oxygen partial pressure and should be established using the TGA.

The line of constant composition x can be derived from the equilibrium composition diagram. Its use is advantageous since it gives an analytical description of the line. But, if the diagram is not known sufficient information can be extracted from thermogravimetric experiments in different atmospheres. This approach requires collection of several equilibrium composition curves which cross the desired composition x. It is important to make the measurements using small intervals of pressure and study the equilibration at low pressure since it will help to establish the cutoff temperature. Intercepts of the curves with composition x give pairs of temperatures and pressures lying on the line of constant composition. So cooling with discrete changes of temperature and pressure combined with equilibration at every point should yield the same result as continuous change. The sample should be kept at every point to correct possible small deviations from stoichiometry caused by the stepwise cooling. Of course the more points the better since the deviation from the composition caused by traveling between them are smaller.

The apparatus for this procedure is not complicated and can be built relatively easily with current technology. It requires two automatic gas flowmeters which dispense gases that form an oxidizing atmosphere of the desired composition, a zirconia cell to measure oxygen partial pressure and a furnace. These elements combined together and controlled using a computer can measure and alter temperature and oxygen partial pressure to follow the constant composition curve.

Other Methods

Without the apparatus described in the previous section it is still possible to produce different compositions. However, there is less control over the outcome of the oxidation and the methods require more experimental effort to get close to desired results.

Since cooling of the material leads to its inevitable oxidation an obvious choice is to use quenching. Although, the method preserves the composition, thermal shock may be a source of crystal strain or even structural modifications.

The oxidation during slow cooling can be used to our advantage. As the temperature decreases, the reaction kinetics also rapidly slow down. From the discussion of thermogravimetric results (Figure 4.2) we know that for different oxygen partial pressures the reactions become slow at different temperatures and yield different stoichiometries. So, by altering the oxygen partial pressure in the atmosphere it is possible to prepare different compositions by the slow reduction of temperature. The oxygen content of the product increases with oxygen pressure. However, the disadvantage of this method is that the final composition depends on the cooling rate and amount of equilibrated material. The rule of thumb is the smaller the mass and lower the cooling rate the higher the final oxygen content. This approach allows relatively large volumes of samples to be produced if the annealing is long enough. Fortunately the composition variations at constant partial pressure of oxygen are not large. The time necessary for equilibration can be estimated by analysis of TGA results using the same partial pressure and temperature.

Oxidation during cooling can also be limited by annealing the powder in a closed vessel with a fixed amount of oxygen. It will yield a variety of compositions but this method requires a great deal of experimental effort and the desired composition has to be obtained on a trial and error basis.

Another possible approach is to partially reduce oxidized samples. Oxidation by slow cooling is very time consuming at the low oxygen partial pressures required for preparation of samples with stoichiometry x only slightly greater than 2.5. To completely reduce the sample it has to be annealed at 1473 K in argon but it can be partially reduced using lower temperatures, say, 873 K. In this case only small volumes can be prepared and the final stoichiometry depends on annealing time which is in the order of a few minutes. After annealing the sample has to be pulled out of the furnace and cooled in the inert atmosphere.

The last method was used for preparation of $Sr_4Fe_4O_{11}$ in the large quantity ($\sim$ 40 g) required for neutron diffraction studies. The technique is a variation of the quenching method but does not involve cryogenic liquids. It is based on relatively slow reduction kinetics. To achieve the desired composition the ferrite was annealed overnight at 838 K in flowing air. Reference to Figure 4.2 shows that this temperature corresponds to composition $x = 2.75$ in an atmosphere of air. However, cooling in air would cause immediate oxidation; on the other hand the reduction rate in an argon atmosphere at the same temperature is relatively slow as shown in Figure 4.10. So, to preserve the composition the furnace was quickly flushed with argon to remove air at a rate of approximately two furnace volumes in approximately 2 minutes. The sample was then allowed to cool outside the furnace but still in the argon atmosphere. For the operation to succeed the flushing should be done

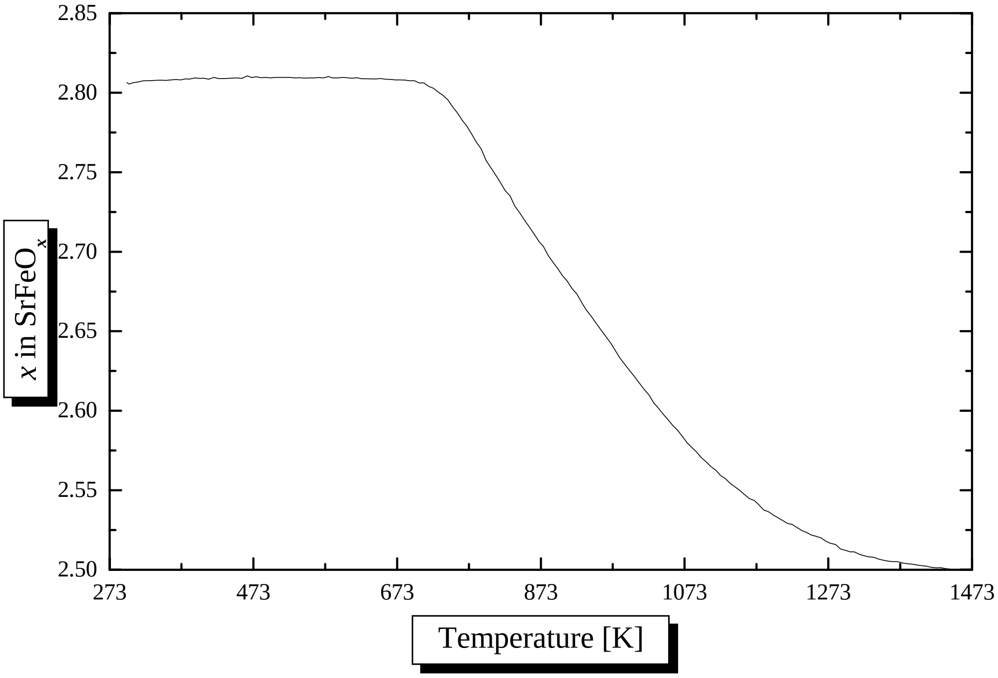

Figure 4.10: A thermogravimetric trace of the reduction of SrFeO$_x$ ($x = 2.81$). The sample was heated at a constant rate of 20 K/min in argon.

as quickly as possible to minimize the reduction and even higher flushing rates are recommended. Also to speed up the cooling, the annealing was carried out in a tube furnace equipped with a thin walled silica tube. As can be seen from Figure 4.10 the composition does not change significantly once temperature is below 673 K. This technique relies on sluggish kinetics and can be adapted to produce other compositions. It should be noted that the method becomes more reliable as the annealing temperature decreases.

Systematic preparation of materials with different compositions should be based on the results of thermogravimetric experiments. If samples are to be prepared in large quantities the annealing has to be done in a furnace. However, to make sure that the conditions are the same, the furnace temperature controller has to be calibrated and the materials annealed in flowing gases to ensure a constant partial pressure of oxygen. Samples heated at low temperatures should be well pulverized and spread on a combustion boat to ensure that a large surface area is exposed to gas. Also for low temperature annealings it is better to start the process at higher temperature and reduce the temperature to the desired value since it makes the process faster (the kinetics of oxidation increases with temperature).

The samples in this thesis were prepared mainly by the slow cooling

Table 4.1: Composition of $SrFeO_x$ samples and annealing conditions used for their preparation as discussed in the text.

Composition x	p_{O_2} [atm]	Annealing conditions
2.915	0.999	573 K/2 h, 523 K/20 h, 473 K/78 h
2.890	0.999	573 K/96 h, 523 K/48 h, 473 K/87 h (~40 g)
2.884	0.999	598 K/21 h
2.823	0.800	TGA
2.846	0.209	598 K/23 h
2.810	0.209	673 K/224 h (~40 g)
2.799	0.330	TGA
2.745	0.023	TGA
2.661	0.010	TGA
2.569	0.003	TGA

TGA- denotes free cooling in the thermogravimetric analyser from 1473 K.

method; the examples of compositions and short descriptions of the annealing atmosphere and conditions are presented in Table 4.1

4.3 Mechanical Oxidation

As discussed above, the thermal oxidation rate becomes negligibly low below 473 K. Attempts to oxidize $Sr_2Fe_2O_5$ at this temperature in air caused only a change of colour from brown to black on the surface of powder after 3 weeks of annealing. If the reaction rate changes with temperature according to the Arrhenius law, at room temperature the oxidation should be few orders of magnitude slower. In practical terms it means that the material will retain its composition for years. However, the process can be induced at room temperature, by mechanical energy. Milling causes the reaction in a matter of hours but the product differs significantly from the thermally oxidized materials. The differences are mainly caused by small crystalline size and the accumulated stress.

4.3.1 Milling

Milling of $Sr_2Fe_2O_5$ was carried out in the ball mill described on page 32. The vial was charged with 8 g of the ferrite and milled in oxygen under an

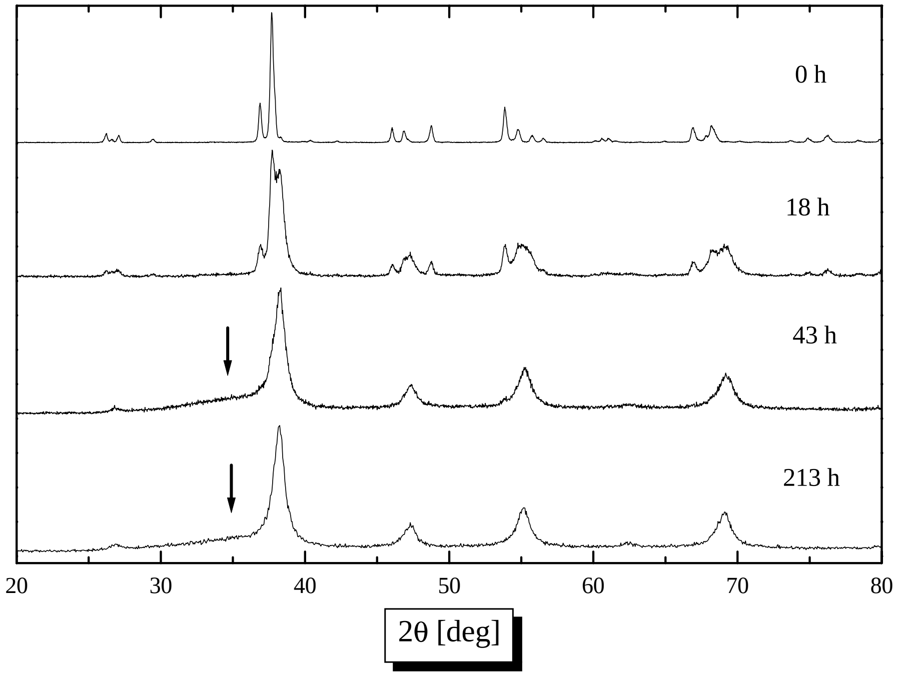

Figure 4.11: X-ray diffraction patterns of $Sr_2Fe_2O_5$ milled in oxygen for different periods of time. Figures denote total milling time with 0h marking the starting material. The arrows mark the position of an amorphous peak as discussed in the text. Patterns are normalized and presented on a linear scale.

initial pressure of 300 kPa. Because of technical difficulties milling was not carried out at constant pressure although the vial was pressurized to supply enough oxygen.

The oxide was also milled in argon to investigate a possibility of phase transitions caused by mechanical energy alone. During the processing small samples of material were taken for analysis and the vials were refilled with gases to the initial pressure. Although, pressure drop can be used as a reaction indicator it was not recorded because of unavoidable leaks. Nonetheless, the pressure never dropped below atmospheric. Milling was carried out at a constant speed of 200 rpm for up to 213 h.

4.3.2 The Reaction

Mechanical treatment in oxygen introduced changes to both the morphology and crystal structure of the material. X-ray diffraction analysis revealed that the material underwent a transition. The diffraction spectra of samples milled for different periods of time are presented in Figure 4.11. The orthorhombic

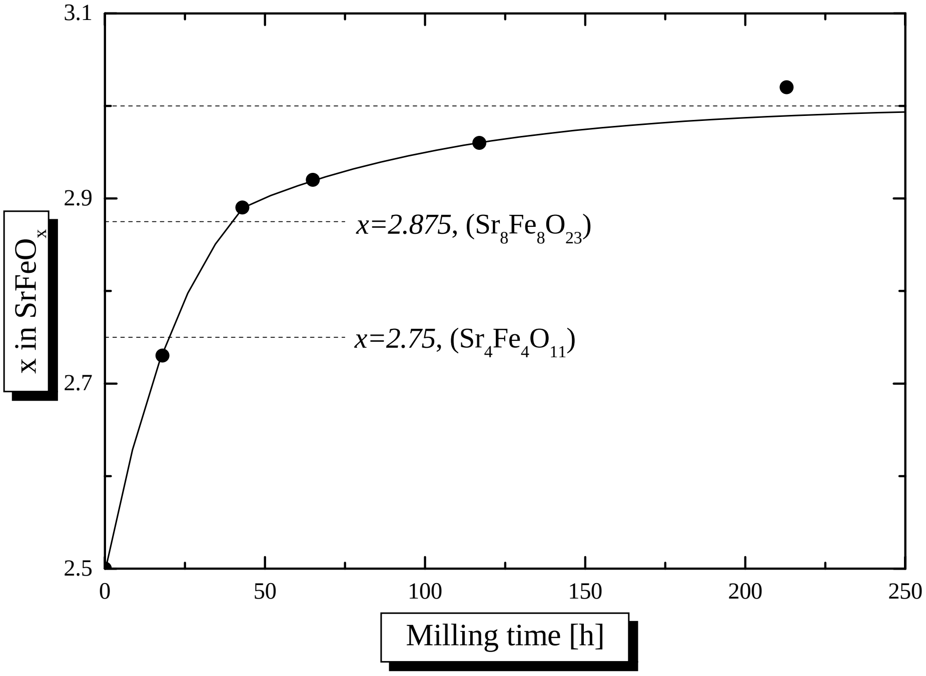

Figure 4.12: The oxygen content of the ferrite as a function of milling time. The line is a result of the fit described in the text.

starting material, denoted by milling time 0 h, was replaced by another phase during early stages of the treatment. But, traces of the starting material are still visible in the 43 h sample. The new phase was indexed as a primitive cubic structure and it remained in this form until the end of the experiment. Milling also changed the colour of the oxide from brown to black.

The control sample, milled in argon, did not undergo any transitions apart from the expected reduction of crystal size and partial amorphisation. The absence of structural changes in the inert gas proves that observed phenomenon was caused by a genuine oxygen intake.

The results of the X-ray analysis were confirmed by thermogravimetry. Milled samples were reduced to $Sr_2Fe_2O_5$ by heating up to 1473 K in argon to constant mass and their oxygen stoichiometry calculated from the weight loss using Equation (4.2). The results are presented in Figure 4.12. X-ray examination of the reduction product revealed only $Sr_2Fe_2O_5$, the absence of $Sr_4Fe_6O_{13}$ suggests that milling in the stainless steel mill did not upset the strontium to iron ratio in the compound.

Inspection of Figure 4.12 shows that the reaction has at least two stages with different oxidation rates. The first stage is completed once the stoichiometry reaches approximately 2.9 and then the reaction progresses much more slowly. The material after 18 h of milling has an oxygen stoichiometry $x = 2.73$ which is very close to the ideal phase $\mathrm{Sr_4Fe_4O_{11}}$ ($x = 2.75$). As mentioned earlier room temperature phases with stoichiometry $2.5 < x < 2.75$ form a mixture of $\mathrm{Sr_2Fe_2O_5}$ and $\mathrm{Sr_4Fe_4O_{11}}$. The diffraction pattern of the 18 h shown in Figure 4.11 indicates a large fraction of $\mathrm{Sr_2Fe_2O_5}$ however, in a sample with the oxygen stoichiometry $x = 2.73$ the fraction of $\mathrm{Sr_2Fe_2O_5}$ should be barely detectable by x-ray diffraction. Significant amount of $\mathrm{Sr_2Fe_2O_5}$ in the 18 h sample indicates that the material contains $\mathrm{Sr_2Fe_2O_5}$, $\mathrm{Sr_4Fe_4O_{11}}$ and at least one more phase with oxygen content $x > 2.75$. The same behaviour was observed in the 43 h sample, which contains traces of $\mathrm{Sr_2Fe_2O_5}$ while its overall stoichiometry is $x = 2.89$. Materials milled for longer times exhibit only a single phase in their diffraction spectra.

The coexistence of more than two phases indicates that the mechanical reaction differs from the thermally induced one. Thermal oxidation proceeds quickly and in the ideal case the whole volume of the material is continuously exposed to the same conditions. The thermal reaction produces single or two phase samples in equilibrium with each other and the atmosphere. Thermal oxidation carried out by small changes in the equilibrium conditions (slow changes to temperature or oxygen partial pressure) should convert the material along the following route:

$$\mathrm{Sr_2Fe_2O_5} \rightarrow \mathrm{Sr_4Fe_4O_{11}} \rightarrow \mathrm{Sr_8Fe_8O_{23}} \rightarrow \mathrm{SrFeO_3} \tag{4.24}$$

On the other hand during mechanical processing the reaction occurs only during collision of powder with milling media. Since the process is random not every grain of material undergoes the same treatment and as the result there are few oxidation reactions occurring concurrently and the borders between consecutive stages of reaction are smeared across a wide composition range. This is the reason why the change of the reaction rate occurs around $x = 2.89$ while it should take place at the ideal composition $\mathrm{Sr_8Fe_8O_{23}}$ ($x = 2.875$). Since the milling conditions were the same for the entire process the slower oxygen intake above $x = 2.89$ is an intrinsic property of the material.

Reaction Rate

The kinetics of the two stage mechanical oxidation can be described analytically. The oxygen content was expressed in terms of a reaction extent parameter α. The parameter $\alpha = 0$ when the average oxygen stoichiometry

$x = 2.5$ and $\alpha = 1$ in the case of $x = 3.0$ (the material is fully oxidized). Since the reaction was carried out at constant temperature, the rate $d\alpha/dt$ was expressed in the following manner:

$$\frac{d\alpha}{dt} = f(\alpha)k \tag{4.25}$$

where, $f(\alpha)$ is a function and depends on a reaction kinetics, k is a reaction rate constant. The form of function $f(\alpha)$ is usually determined from experimental data by fitting several possible models.

For a first order reaction the function has the form $(1 - \alpha)$ and Equation (4.25) simplifies to:

$$\ln(1 - \alpha) = -kt \tag{4.26}$$

This is equivalent to the formula:

$$f_R = 1 - \alpha = e^{-kt} \tag{4.27}$$

where f_R is the molar fraction of the ferrite with oxygen content less than 3.0. The formula (Equation (4.27)) is the well known radioactive decay law and seems to be very appropriate in this case as the reaction is driven by random mechanical impacts of balls.

The thermogravimetric results from the Figure 4.12 were replotted using Equation (4.26) and are presented in Figure 4.13. Despite the small number of experimental points the two different stages of reaction are obvious and the first order reaction model appears to fit the experimental points quite well. The slopes of the fitted lines give the rate constant $-k$ as presented in Table 4.2. These rate constants were used to calculate the continuous line in Figure 4.12.

Table 4.2: The reaction rate constants for two stages of the mechanical oxidation of $Sr_2Fe_2O_5$ discussed in the text.

Reaction step	Rate constant k [h^{-1}]
I	0.0353(5)
II	0.01367(25)

The derived rate constants are not true rate constants from the chemical point of view since the process consists of overlapping reactions but, the results can be interpreted as an effective oxygen intake. The reaction rate constant is the ‘effective impact frequency’ and indicates how often the col-

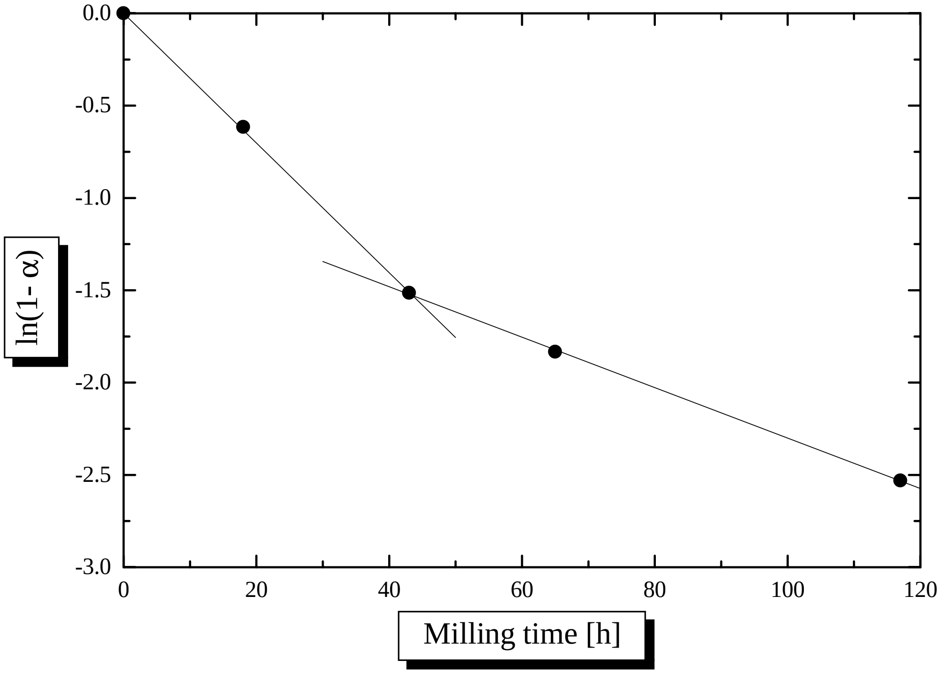

Figure 4.13: The logarithm of the reactant fraction in the mechanically oxidized $SrFeO_x$ as a function of milling time. The lines denote the linear fits described in the text.

lision parameters meet the condition required by the chemical reaction to proceed. The change of the rate constant by a factor of 2.58 proves that the second stage of oxidation is more demanding as far as energy supplied by the mill is concerned. The constant k is determined not only by the material but is also device dependent. The device contribution is a function of several factors such as speed, volume of milled material, the geometry of the mill *etc*, so the process will take different times to complete in different grinding devices and the constants are characteristic for a particular mill. However two oxidation steps should still be observed.

4.3.3 Structure and Morphology

Crystal Structure

The diffraction patterns of the product were successfully indexed as a primitive cubic structure. However, the small crystal size and lattice strain are responsible for substantial line broadening and the peaks may as well be a result of overlapping reflections of low symmetry phase or phases indicated in the previous sections. The peak width (FWHM) of the oxidized phase

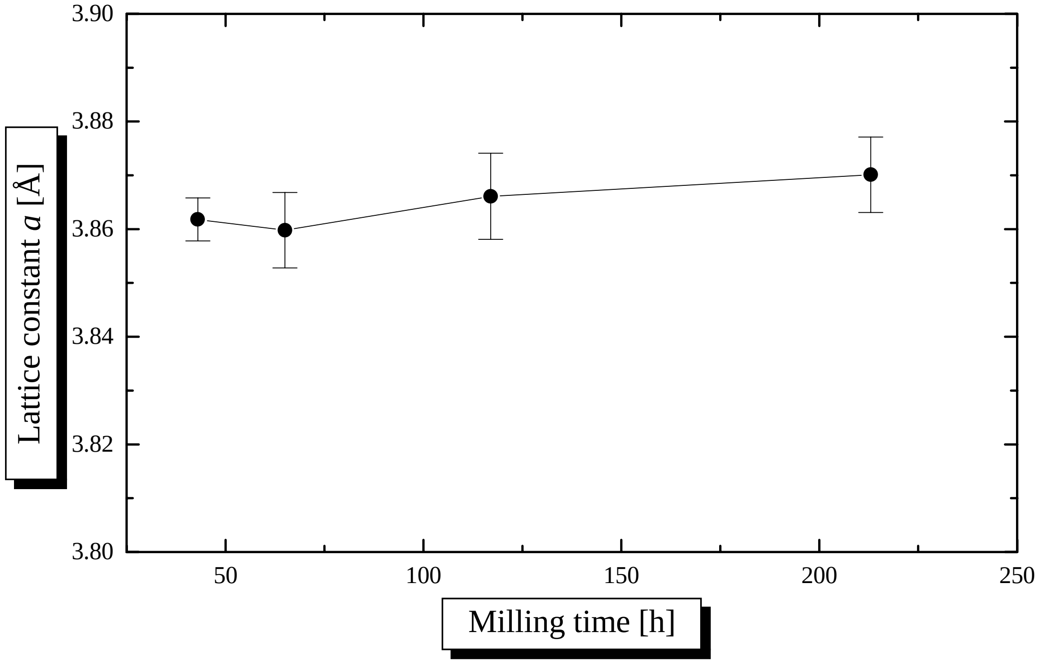

Figure 4.14: The cubic lattice constant of the product of $Sr_2Fe_2O_5$ oxidation as a function of milling time. The line is a guide for eye.

exceeds 1°, the instrumental breadth for the diffractometer used in the experiments is much smaller (see Figure 2.1) and even the use of high resolution diffraction method would not be able to resolve the reflections since the sample contribution is overwhelming. Also the absolute amplitude of the diffraction peaks is much smaller than in the thermally oxidized materials. Since the integrated intensity remains constant, weak, broad reflections become indistinguishable from the background. For these reasons it is impossible to positively identify the phases using powder diffraction. Nonetheless, the patterns are characteristic for the perovskite structure so the constituting phases have to be related to this phase.

As shown in Figure 4.14 the lattice constant of the cubic phase increases with milling time. This is the opposite what is normally expected in oxidized materials since intake of oxygen in ionic crystals causes the lattice to shrink. This unusual behaviour is likely to be due to the destructive action of the mechanical treatment which introduces a lot of crystal defects into the structure.

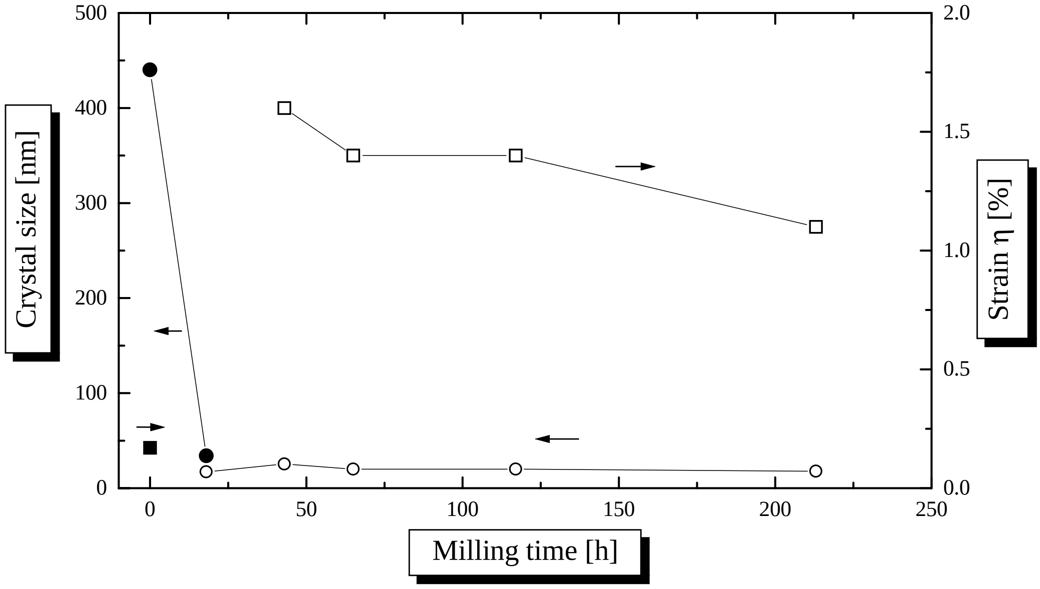

Figure 4.15: The average crystal size and lattice strain of $Sr_2Fe_2O_5$ and the product of its oxidation as a function of milling time. Filled and empty circles denote crystal sizes of the reactant and the product respectively. Filled and empty squares mark lattice strains of the reactant and the product respectively. The lines are guide for eye.

Crystal Size and Strain

The crystal size and stress were derived from the width of the x-ray diffraction lines corrected to remove the instrumental contribution. The size and strain were separated using Hall's formula described on page 25 and the results are presented in Figure 4.15.

The starting material had a crystal size of 440 nm and relatively low lattice strain (0.17 %). The mechanical treatment reduced its crystal size to about 34 nm after 18 h of milling. At the same time the oxidized phase had a crystal size around 17 nm. Heavily overlapping lines in the 18 h sample, due to the presence of $Sr_2Fe_2O_5$, did not allow separation of the size and the strain. So the crystal size was estimated using the Scherrer formula (see Equation (2.22)), assuming that there is no strain ($\eta = 0$). This approach leads to an underestimated value. Further milling reduced the crystal size of the product to 17.8 nm.

The strain decreased with milling time reaching 1.1 % after 213 h. Yet still it was 6.5 times greater than the strain of starting powder. The buildup of strain in the milled material is due to the nature of method. The interaction of milling media with the oxide causes the chemical reaction and deforms the

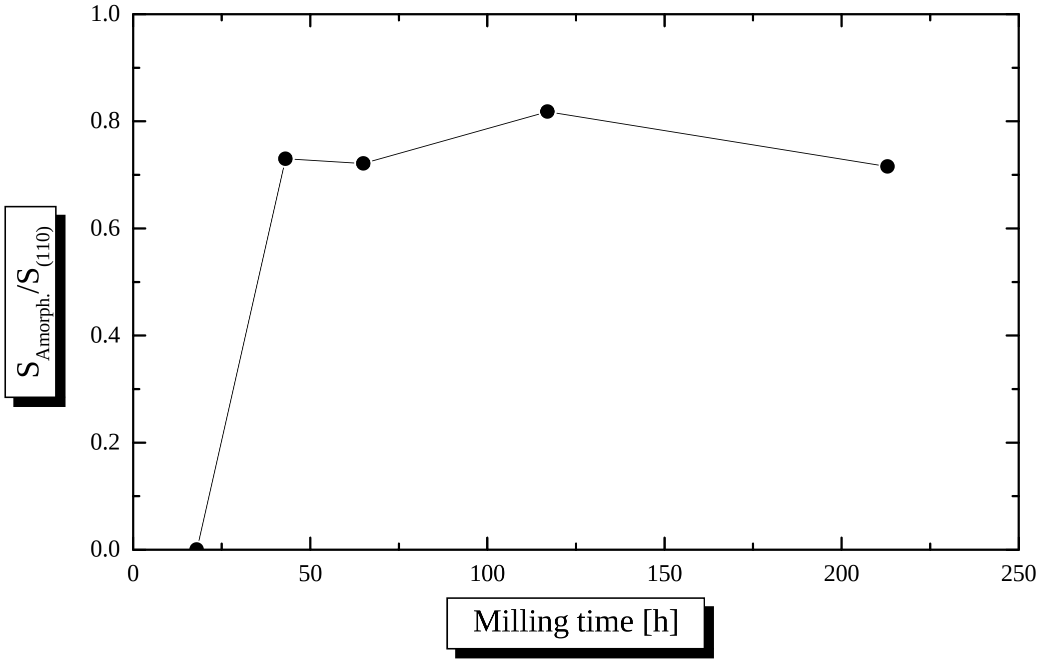

Figure 4.16: The integrated intensity ratio of the amorphous phase peak to the (110) cubic line as a function of milling time in mechanically oxidized $Sr_2Fe_2O_5$. The ratio was calculated using the x-ray diffraction patterns as discussed in the text, the line is a guide for eye.

lattice at the same time. Since the process lasts for a fraction of a second any possible local increase of temperature is short lived, the lattice does not relax and retains the deformation.

Amorphous Phase

An amorphous peak, centered around $2\theta = 35.5°$, appeared after 43 h of milling. The peak appears as a shoulder next to the strongest x-ray lines in Figure 4.11. The integrated intensity ratio of the amorphous peak $S_{\mathrm{amorph.}}$ to the cubic (110) strongest line $S_{(110)}$ is presented in Figure 4.16 as a function of milling time. The almost constant intensity ratio indicates that the fraction of the amorphous phase was not changing throughout the milling and was most likely located on the surface of the grains.

The observed peak position corresponds to characteristic interatomic distance of 2.9 Å. However, it is difficult to judge what exactly the amorphous phase is made of. Due to the simplicity and similarity of amorphous x-ray patterns it is not possible to carry out identification like in the crystalline case [63]. The chemical composition is most likely similar to the composition of the crystalline phase. We can exclude the possibility that the amorphous phase is the product of oxide's decomposition since $Sr_2Fe_2O_5$ is stable in lower oxygen partial pressures. Also we can exclude the formation of carbonate from residual carbon dioxide in the gas since the carbonate forms a crystalline phase. This property will be described in the next part of this chapter.

Morphology

Figure 4.17 shows scanning electron microscope images of the starting $Sr_2Fe_2O_5$ and the milled oxide.

The crystal size of the starting $Sr_2Fe_2O_5$ obtained from x-ray diffraction indicate a crystal size of 440 nm. The powder used as the starting material consisted of large, macroscopic agglomerates. Crushed with a mortar and pestle and dispersed using an ultrasonic probe the material forms agglomerates of several tens of micrometers in size. A representative particle is presented in Figure 4.17. The sintered fragments appear solid and free of cracks. $Sr_2Fe_2O_5$ does not develop crystal facets which would help establishing of the crystal size distribution. Examination of the micrographs indicates that there are microcrystals smaller than 440 nm but their population is small since they does not cause a visible x-ray diffraction line broadening. Also it is feasible to expect crystals larger than 2 μm but they are not detectable using diffraction since their contribution to the line breadth is indistinguishable from the instrumental breadth.

The milled material has the same appearance irrespective of the treatment duration (see Figure 4.17). The crystal size found by x-ray diffraction is around 17 nm. However, the milled material forms aggregates several micrometers across consisting of grains approximately 1 μm across. The milling causes crystal fragmentation and simultaneous coalescence.

Surface Adsorption

The small crystal size of the milled material implies a large surface area which is covered by water and gases. Since the oxygen content was determined from mass loss upon annealing, desorbed gases would artificially increase the calculated composition. The maximum mass loss due to loss of oxygen from the structure is only 4.18 % and significant gas adsorption would interfere with the results.

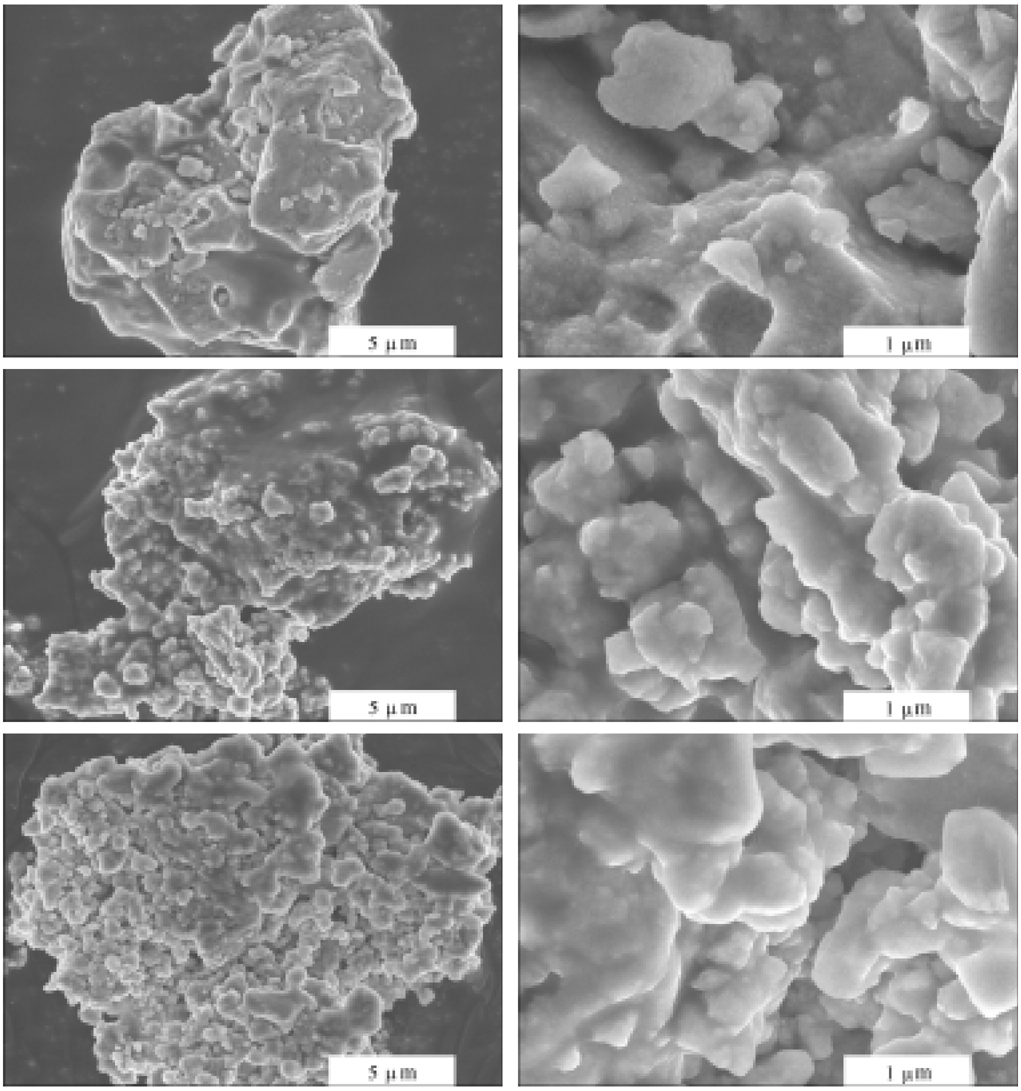

Figure 4.17: Scanning electron microscope images of $Sr_2Fe_2O_5$ milled in oxygen for 0 h (the starting material, top row), 43 h (middle row) and 213 h (bottom row). The pictures are discussed in the text.

The microscope images, presented in the previous section, suggest a porous structure so the surface area of the final product (the 213 h sample) was measured using nitrogen adsorption and found to be 2.2 $\mathrm{m^2/g}$.

The theoretical specific area of the final product, assuming that all grains are divided, was estimated using the crystal size determined by diffraction. The calculations were simplified assuming a monodisperse crystal size and that all crystals are spherical. These two simplifications artificially maximize the result. The specific area s was determined as the ratio of the surface of spherical microcrystal to its mass derived using the density calculated from the lattice constant:

$$s = \frac{6N_A V}{\varepsilon M_{SrFeO_3}} \tag{4.28}$$

where, V is the unit cell volume, N_A Avogadro number, M_{SrFeO_3} molecular mass of the fully oxidized material and ε the crystal size. The calculated area is equal to 61 $\mathrm{m^2/g}$ and the measured value is 27 times smaller than expected. Therefore gas adsorption does not play an important role in the stoichiometry determination and the fragments of milled oxide are not porous.

4.4 Thermal Carbonation

Interaction of the ferrite with CO_2 is interesting from the scientific point of view but is also very important from the application perspective since ionic conductors as part of fuel cells are exposed to this gas.

Decomposition of strontium carbonate is controlled by temperature and CO_2 partial pressure in the atmosphere.

$$\mathrm{SrCO_3 = SrO + CO_2} \tag{4.29}$$

The reaction is similar to the decomposition of calcium carbonate, a well known example from chemistry textbooks. When, at constant temperature, the pressure of carbon dioxide drops below a critical value the carbonate converts into oxide. If on the other hand the pressure is higher the oxide converts into carbonate. Similar behaviour is observed for constant pressure of carbon dioxide and variable temperature.

The ferrite is expected to behave in a similar fashion and its temperature of formation should depend on carbon dioxide concentration. The influence of carbon dioxide on the formation is not obvious in air or argon atmospheres since its concentration is low, but it becomes apparent in carbon dioxide

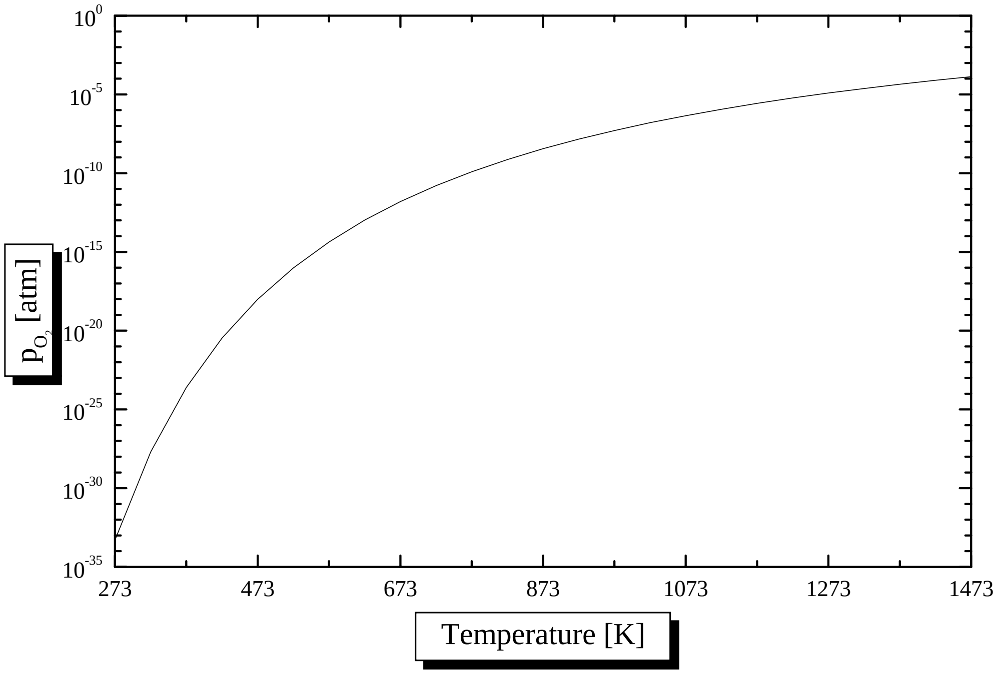

Figure 4.18: The calculated oxygen partial pressure due to dissociation of CO_2 as a function of temperature.

atmosphere. It should be possible to reverse the formation of the ferrite described by Reaction (3.1).

4.4.1 Atmosphere Characteristics

The carbon dioxide used in these experiments was a food grade gas of 98 % purity. The behaviour of gaseous oxides is more complicated than simple oxygen-inert gas mixtures. The dioxide, apart from forming carbonates, dissociates into carbon monoxide and oxygen and has to be considered an oxidizing gas as well [141].

The partial pressure of oxygen in CO_2 is temperature dependent and was calculated from the Gibbs free energy of formation assuming that the dissociation reaction has the following form:

$$2\,CO_2 = 2\,CO + O_2. \tag{4.30}$$

The calculated oxygen activity as a function of temperature is presented in Figure 4.18. The oxygen partial pressure exceeds 10^{-5} atm only when temperature approaches 1273 K so below this value the oxidation caused by the dissociation is insignificant.

However, the gas used for the experiments was only 98 % pure. The remaining fraction was most likely air so this impurity gives rise to an oxygen partial pressure of approximately 0.004 atm which is much more than the dissociation contribution and is constant across entire temperature range. The oxygen contamination causes visible oxidation of the ferrite and should be borne in mind during the analysis (see the equilibrium compositions for 0.003 atm of oxygen presented in Figure 4.2).

4.4.2 The Reaction

The reaction was tested using the thermogravimetric analyser by heating $Sr_2Fe_2O_5$ in CO_2 at constant rate. The result was a weak peak around 1142 K whose ascending slope corresponds to reaction with CO_2 and the descending one to the decomposition. However, the mass change was very small ($\sim$ 0.5 %) and the peak was barely distinguishable from the baseline. So the experiment was repeated, with the same heating rate of 10 K/min, but this time the material was kept at 1073 K, below the critical temperature, for 1 h. The result is presented in Figure 4.19, the material gained nearly 7 % of mass below and at 1073 K substantially more than due to oxidation alone so the gain corresponds to the CO_2 intake.

The shape of the TG curve during the isothermal step of heating suggests that the reaction was not completed (lack of saturation) and increasing the temperature resulted in decomposition at 1142 K. On the cooling cycle the material gained some mass due to oxidation and carbonation, however the carbonation reaction is relatively slow therefore the gain was low. X-ray diffraction examination afterwards revealed signs of oxidation ($Sr_4Fe_4O_{11}$ present) and traces of strontium carbonate.

The critical temperature found from the experiments was determined from the positions of peaks in the thermogravimetric traces. The peaks are the result of overlap of the carbonation and the decomposition reactions and it is difficult to assess where the decomposition starts. The value of critical temperature was clarified by the following experiment.

The reaction of the ferrite with carbon dioxide below the critical temperature should lead to a complete decomposition to strontium carbonate and hematite. From the thermodynamical point of view the critical temperature is the same for the decomposition as well for the formation of the ferrite from Fe_2O_3 and $SrCO_3$. To establish the precise value of the critical temperature a milled mixture of hematite and strontium carbonate in a molar ratio 1:2

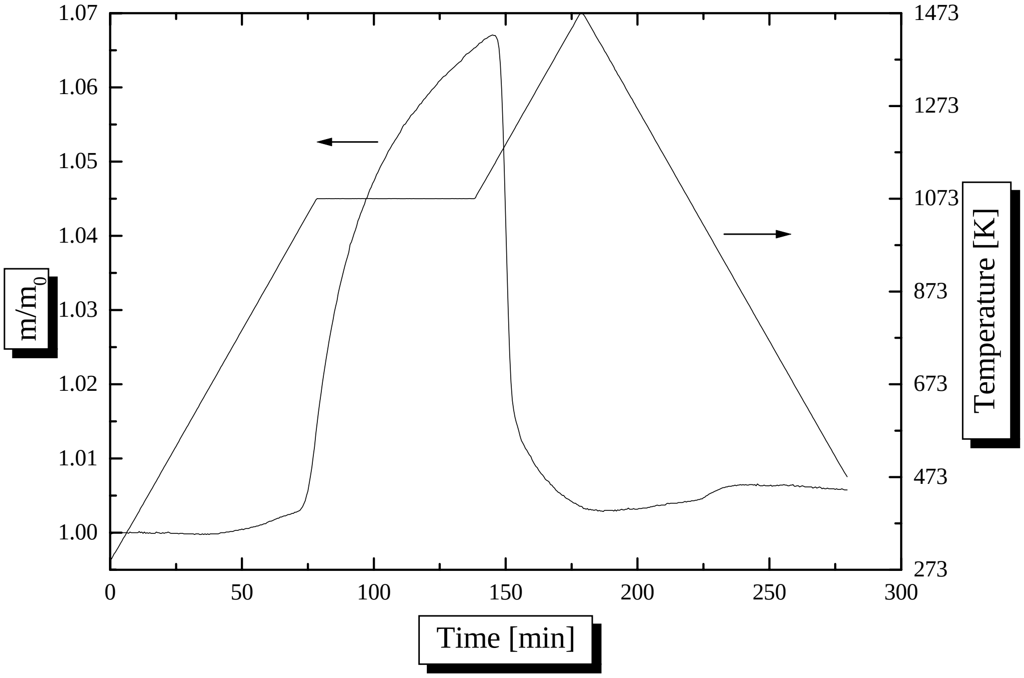

Figure 4.19: A thermogravimetric trace of the reaction of $Sr_2Fe_2O_5$ with CO_2 as discussed in the text.

was examined by heating in CO_2 in the thermogravimetric analyser and the result is presented in Figure 4.20. The critical temperature for the formation (decomposition) of the ferrite in CO_2 was derived from the onset of the mass loss and found to be $1128 \pm 5\,K$.

The observed formation temperature is significantly higher than for the reaction in argon (approximately 873 K, compare with Figure 3.2) and the onset of reaction is much clearer.

Reaction Route and Kinetics

Investigation of the phases formed during carbonation was carried out using samples annealed in a furnace at 1073 K under a flow of carbon dioxide. The oxide was placed in small crucibles, the extent of the reaction was established from the mass gain and the composition determined using x-ray diffraction. The treatment was carried out for up to 480 h.

X-ray examination revealed diminishing amounts of $Sr_2Fe_2O_5$ and the presence of $Sr_4Fe_4O_{11}$ due to oxygen contamination. Product of the reaction at all stages were strontium carbonate ($SrCO_3$) and strontium hexaferrite ($SrFe_{12}O_{19}$). The fraction of the oxidized ferrite was also decreasing which suggests that the presence of Fe^{4+} does not inhibit the carbonation. The

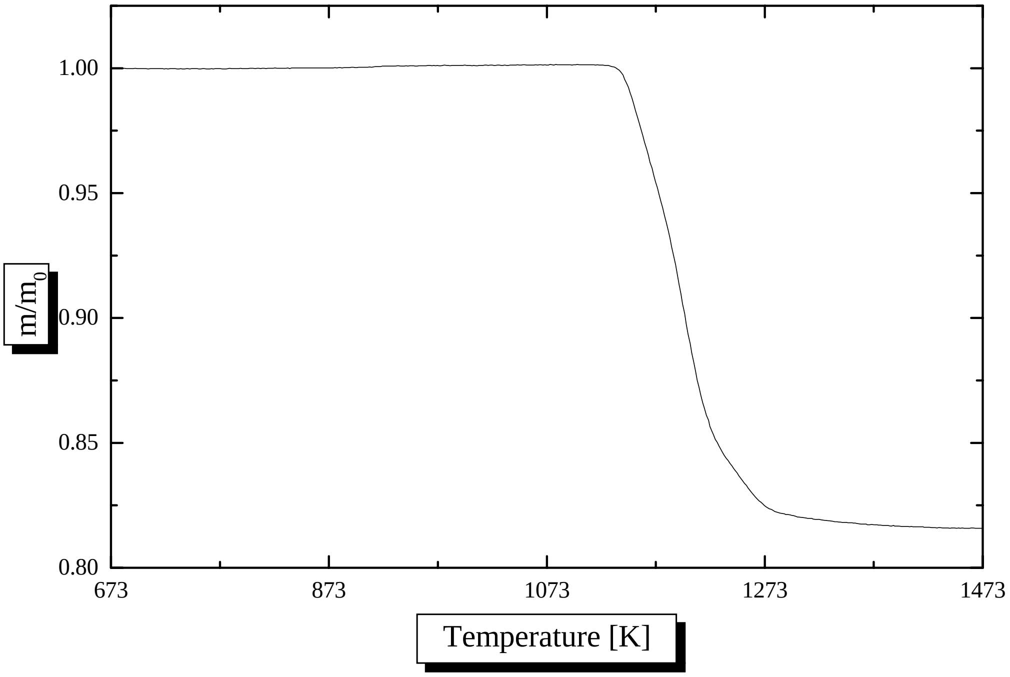

Figure 4.20: A thermogravimetric trace of the hematite and strontium carbonate mixture heated in CO_2 at the rate of 10 K/min as discussed in the text.

material after 480 h of annealing contained strontium carbonate, strontium hexaferrite and traces of the original ferrite.

Strontium hexaferrite is formed as a strontium deficient phase however, reference to the ternary diagram for the Sr-Fe-O system (Figure 1.4) shows that the carbonation process directly forms $SrFe_{12}O_{19}$ and does not form $Sr_4Fe_6O_{13}$ as an intermediate phase.

Figure 4.21 shows the extent[‡] of Reaction (4.31) as a function of annealing time.

$$6\,Sr_2Fe_2O_5 + 11\,CO_2 = SrFe_{12}O_{19} + 11\,SrCO_3 \tag{4.31}$$

The data shown in Figure 4.21 clearly indicate that formation of the hexaferrite has two stages with distinctive different kinetics mechanisms. The first step takes few hours and produces approximately 40 % of the product then the reaction visibly slows down.

Since the carbonation was not complete the results were analysed to find an approximate time required for the completion. Several kinetics models were fitted to the second stage of the reaction however, the results were not conclusive, indicating a complicated mechanism. However, considering the

---

[‡] The extent of reaction α was introduced on page 77.

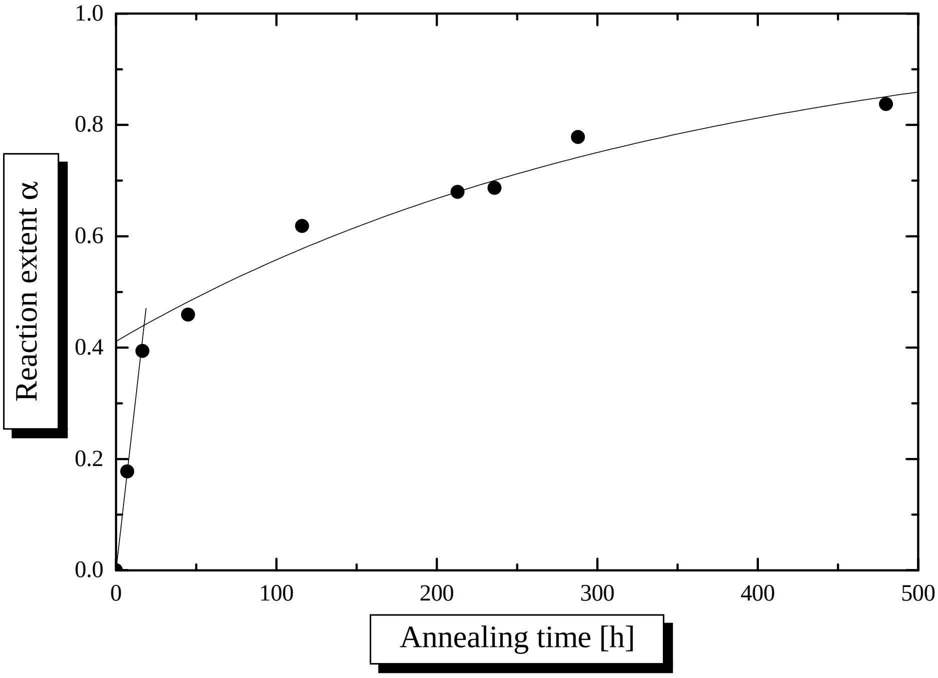

Figure 4.21: The extent of Reaction (4.31) as a function of annealing time. $Sr_2Fe_2O_5$ was annealed at 1073 K in CO_2. The solid lines represent two different kinetics mechanisms of the carbonation reaction as discussed in the text.

process as a first order reaction resulted in the fit shown as a solid line in Figure 4.21. Even though the kinetic model was not unambiguously assigned, the first order gives an estimate of the time needed for the complete conversion to $SrFe_{12}O_{19}$. The calculation for 99 % of completion ($\alpha = 0.99$) show that the material would require total of 1500 h of annealing.

The reaction rate cannot be increased by temperature since the annealing temperature was close to the critical value. The only possibility would be to increase the pressure of CO_2 which would allow an increase in temperature.

Since $SrFeO_x$ should in theory decompose to hematite and strontium carbonate upon exposure to carbon dioxide, the hexaferrite should finally decompose according to the equation:

$$SrFe_{12}O_{19} + CO_2 = 6\,Fe_2O_3 + SrCO_3, \tag{4.32}$$

so the carbonation reaction of $SrFeO_x$ follows the scheme:

$$Sr_2Fe_2O_5 \rightarrow SrFe_{12}O_{19} \rightarrow \alpha\text{–}Fe_2O_3, \tag{4.33}$$

with Sr in the form of $SrCO_3$.

$SrFe_{12}O_{19}$ and Carbon Dioxide

Since $SrFe_{12}O_{19}$ is a prominent phase in the carbonation reaction and does not show evidence of decomposition up to 480 h, its interaction with the gas was examined.

The absence of hematite in the carbonation reaction of $SrFeO_x$ has two possible causes. Firstly, $SrFe_{12}O_{19}$ does not decompose until the strontium rich phase ($SrFeO_x$) vanishes or the second, that $SrFe_{12}O_{19}$ is very resilient and its carbonation rate is extremely slow. These possibilities were tested by annealing pure strontium hexaferrite in CO_2 at 1073 K for several hours followed by x-ray examination. It did not show any traces of the carbonate. However, lack of reaction signs is not a sufficient proof that the compound is not influenced by the gas. The interaction of $SrFe_{12}O_{19}$ with carbon dioxide was additionally tested using milled mixtures of hematite and strontium carbonate in a molar ratio 6:1 by annealing in argon and CO_2. The annealing was carried out in the thermogravimetric analyser at constant heating rate. The experiments yielded onsets of reactions at approximately 883 K and 1088 ± 5 K in argon and carbon dioxide respectively, x-ray examination of the product revealed only $SrFe_{12}O_{19}$ as the product. The temperature for the argon environment could be even lower since the reaction rate in this temperature range is low and it is difficult to establish a precise onset of reaction.

However, the radically different temperatures for $SrFe_{12}O_{19}$ formation in argon and CO_2 show that the compound is affected by the pressure of CO_2 and the lack of carbonation is caused by sluggish kinetics, this is the reason why hematite is not observed in the thermally carbonated samples.

The thermogravimetric experiment experiment in CO_2 also demonstrates that the annealing temperature of 1073 K was correctly chosen below the critical value for the carbonation of $SrFe_{12}O_{19}$.

Morphology

The carbonated samples were examined using the scanning electron microscope. The images collected are presented in Figure 4.22 and all thermally carbonated samples look alike irrespective of the treatment time.

The morphology of the starting material ($Sr_2Fe_2O_5$) was previously de-

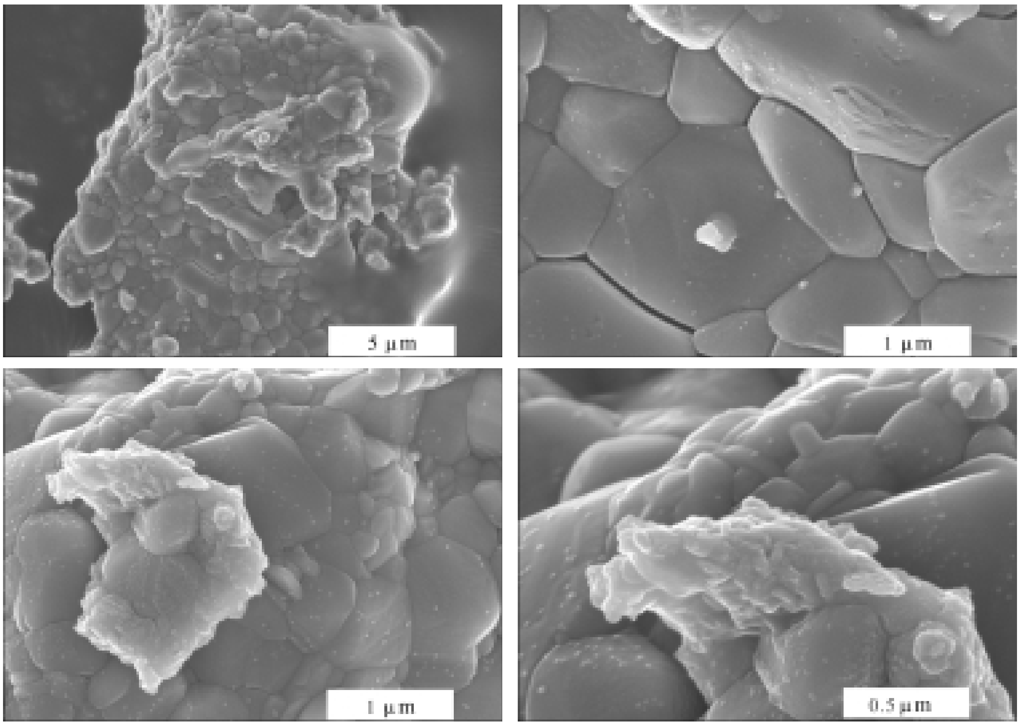

Figure 4.22: Scanning electron microscope images of $Sr_2Fe_2O_5$ annealed in CO_2 at 1073 K for 45 h.

scribed on page 83 (see Figure 4.17) and the ferrite appeared as solid sintered grains.

Annealing in CO_2 did not change the size of particles and the carbonated material consists of sintered grains up to several tens of micrometers across. However, the grains are now divided by obvious cracks, images taken at higher magnifications show clearly separated domains of material approximately 1–2 μm in size not observed in pure $Sr_2Fe_2O_5$.

Apart from the ferrite there are elongated crystals visible on the surface of grains. Even though, the electron microscope was not equipped with an energy dispersive detector which would facilitate an elemental analysis the strong scattering of electrons by the rod like crystals (they appear as lighter on the micrographs) indicate that they contain large fraction of strontium.

Since $SrCO_3$ and $SrFe_{12}O_{19}$ constitute most of the material the crystals must be made of the carbonate. Their shape is similar to the pure carbonate crystals shown in Figure 3.3.

The cracked surface of the grains leads to a likely explanation of the two different kinetics mechanisms of conversion to $SrFe_{12}O_{19}$. Figure 4.21 shows that first stage of reaction was very rapid and produced approximately 40 %

of the product. The initial stages of solid-gas reaction are rapid since the surface material is consumed. It appears that carbon dioxide can diffuse along the grain boundaries, effectively increasing the surface area which explains the initial rate of reaction. The cracks in the material appeared as a result of molar volume changes between the starting material and $SrFe_{12}O_{19}$. Once the material from the surface converts to the hexaferrite it shrinks exposing the gaps. At the end of the first stage of reaction the ferrite consist of $SrFe_{12}O_{19}$ grains with a $SrFeO_x$ core. Since the hexaferrite is resistant to carbonation further reaction is limited by diffusion of Sr through the layer of $SrFe_{12}O_{19}$ slowing down the process and changing the rate determining step from gaseous diffusion to solid state diffusion which is typically much slower.

4.5 Mechanical Carbonation

The carbonation reaction was also carried out using mechanical methods. Since the critical temperature for carbonation reaction of the ferrite is 1128 K under 0.98 atm of CO_2, the formation of carbonate is even more favourable at room temperature (the change of Gibbs free energy for the reaction is lower than at elevated temperature).

8 g of $Sr_2Fe_2O_5$ was milled at 200 rpm under an initial carbon dioxide pressure pressure of 300 kPa for up to 656 h. Small samples of the material were taken at different periods for analysis and the vial refilled to the initial pressure.

Milling was carried out without any liquid although it is possible to use water which leads to very rapid formation of the carbonate due to the action of carbonic acid [142,143]. However, this line of experiments was not pursued for two reasons. First of all, the acid forms a corrosive environment which attacks the mill [144] and the products of corrosion would spoil the analysis. The contamination would increase with time due to continuous mechanical removal of the tarnished layer during milling. Secondly, water is not inert towards iron oxides and it would most certainly form hydrated forms of the oxides [143]. The route for the hydration reaction depends on the amount of added water which would greatly complicate the analysis since there would be several chemical reactions occurring simultaneously.

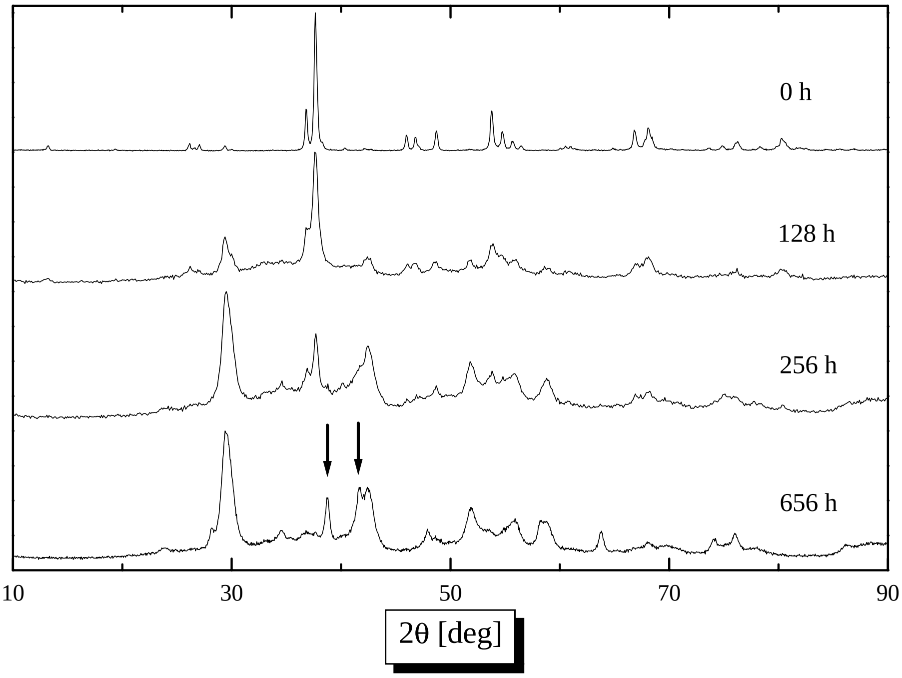

Figure 4.23: X-ray diffraction patterns of $Sr_2Fe_2O_5$ milled in CO_2 for various periods of time. The arrows denote two strongest lines of hematite, the figures mark the milling time. The pure $Sr_2Fe_2O_5$ is denoted by 0 h milling time. The reflections in the bottom pattern belong to $SrCO_3$ and hematite. The patterns are normalized and presented on a linear scale.

4.5.1 The Reaction

The milled samples were examined using x-ray diffraction and selected patterns are presented in Figure 4.23. As expected the main product of the reaction is strontium carbonate; it appeared after just 4 h of milling and its presence is marked by the strongest line at $2\theta = 29.3°$ (the observed line is actually a doublet). The fraction of carbonate and thus the intensity of line increased with time as the intensity of $Sr_2Fe_2O_5$ lines decreased. At the same time, the lines broadened due to decreasing crystal size and accumulated strain. The crystal size and strain analysis in this case is very complicated as a result of severe line overlap. An amorphous phase appeared after 32 h of milling and persisted to the end of the process.

Formation of strontium carbonate should lead to a simultaneous appearance of a strontium deficient ferrite like $SrFe_{12}O_{19}$ in the thermally carbonated samples or hematite. However, up to 256 h of milling there were no signs of any crystalline form of iron compound (apart from $Sr_2Fe_2O_5$ of course). On further milling hematite lines become visible but after 656 h the line intensity ratio of hematite to carbonate was smaller than expected for a mixture of $2SrCO_3+Fe_2O_3$. There was no evidence for $SrFe_{12}O_{19}$ in the diffraction patterns, although the samples were slightly magnetic implying its presence. However, their magnetic nature was not nearly as strong as in the thermally carbonated ferrite. The lack of an iron compound and the small intensity of hematite lines indicates that Fe was bound in some metastable compound, possibly a form of iron carbonate.

The unknown phase decomposed slowly during milling with hematite as a product. The decomposition to hematite starts before the starting phase ($Sr_2Fe_2O_5$) vanishes (the 256 h pattern in Figure 4.23 contains traces of hematite). However, this overlap may be caused by the randomness of the milling method discussed in section 4.3. The carbonation reaction appears to follows the scheme:

$$Sr_2Fe_2O_5 \rightarrow \text{Unknown Phase(s)} \rightarrow Fe_2O_3 \tag{4.34}$$

and produces $SrCO_3$ during both stages.

The mechanically carbonated samples were analysed using the thermogravimetric analyser by heating them at constant rate up to 1473 K in argon atmosphere. The results are presented in Figure 4.24 and the traces confirm the presence of an unknown carbonate in the system. The figure also shows the reaction trace of a hematite-strontium carbonate mixture (dashed line). The mixture shows only one stage of reaction which corresponds to decomposition of $SrCO_3$ and formation of $Sr_2Fe_2O_5$. On the other hand the milled samples exhibit an additional low temperature reaction, marked with an arrow in Figure 4.24, which commences around 473 K and overlaps with the decomposition of $SrCO_3$. An attempt to separate the stages by decreasing the heating rate was unsuccessful. Extended annealing in argon and CO_2 below 873 K did not cause crystallization of the unknown phase.

The mass loss due to the low temperature stage increased significantly up to 256 h of milling with only a slight increase to 656 h of milling (compare the curves for 256 h and 656 h in Figure 4.24). It corresponds to the increasing fraction of the metastable phase. Samples milled for longer than 256 h exhibit greater total mass loss than expected from Reaction (3.1).

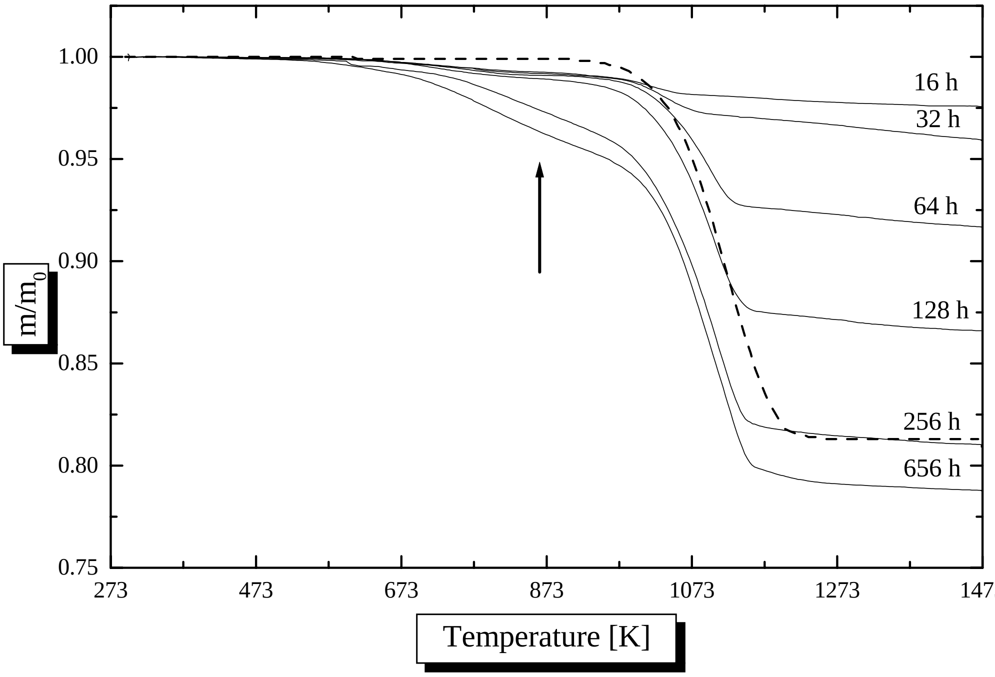

Figure 4.24: Thermogravimetric traces of $Sr_2Fe_2O_5$ milled in CO_2 for various periods of time (solid lines) and a trace of hematite-strontium carbonate mixture (dashed line). The samples were analysed in argon at the constant rate of 20 K/min; the figures denote the milling time.

4.5.2 Nature of the Unknown Carbonate

The unknown carbonate is metastable and decomposes upon annealing and milling. Since hematite appeared after 256 h of mechanical treatment the compound must contain a significant amount iron and the presence of some strontium in the compound cannot be excluded.

X-ray diffraction did not show any unexplained lines that might correspond to the unknown carbonate phase proving, that the carbonate is either amorphous or its reflections overlap with broad lines of the other phases. However, intensities of lines characteristic to the particular compounds are not visibly changed so the former supposition is likely to be true.

There are two known iron carbonates, ferrous carbonate $FeCO_3$ which occurs in nature as a mineral (siderite) and ferric carbonate $Fe_2O_2CO_3$ found and described by Erdös and Altorfer [145]. The starting material contained only ferric iron so to form siderite, the iron would have to be reduced. The discussion of iron contamination from the mill presented in section 3.5, shows that such a reduction is feasible.

The milled materials were tested for divalent iron using a 0.1 % water solution of o-Phenanthroline (1,10-Phenanthroline Hydrate, $C_{12}H_8N_2{\cdot}H_2O$). A small amount of material was dissolved in hydrochloric acid and a drop of the solution was quickly transferred onto a spot plate and mixed with a drop of the reagent. The test did not show the presence of Fe^{2+} despite a concentration limit for the test of 1 in 1,500,000 [132]. A negative result was also returned with potassium ferricyanide as an indicator.

The tests exclude siderite as a potential iron carbonate. Additionally the materials were examined for excess iron using the procedure described in section 3.5. This procedure was carried out because the absence of ferrous iron does not exclude iron contamination. The surplus iron was sought by x-ray examination of the samples reduced during the thermogravimetric analysis. The examination did not reveal any excess iron so it can be safely concluded that the unidentified carbonate does not contain ferrous iron and the milling did not change the overall iron to strontium ratio in the compound.

Even though the gas used for experiments contained small amount of oxygen there was no visible signs of oxidation which would be indicated by the presence of $Sr_4Fe_4O_{11}$. Therefore, the fraction of tetravalent iron has to be negligibly small and the unknown carbonate has to contain the trivalent iron. Lack of any structural information does not allow positive identification of the carbonate as $Fe_2O_2CO_3$ since its strongest diffraction line at $2\theta = 20.24°$ was not observed in Figure 4.23.

4.5.3 Morphology and Surface Adsorption

The ferrites carbonated by milling were examined using the scanning electron microscope. However, due to the destructive nature of milling the carbonation products are featureless compared with the thermally carbonated samples and looked very similar irrespective of the milling time. These images are presented in Figure 4.25. The material looks similar to the mechanically oxidized ferrites (compare with Figure 4.17) with the powder consisting of grains up to several micrometers across formed by a coalescence of smaller (submicron) crystals.

Although a comprehensive crystal size analysis is difficult due to the strong line overlap, the crystal size of $SrCO_3$ is approximately 13 nm and hematite has a crystal size around 40 nm, so even the smallest particles visible under the microscope are polycrystalline.

The microscopic observations were confirmed by surface area measurements with the specific surface area of the 656 h sample being only $2.66\,m^2/g$

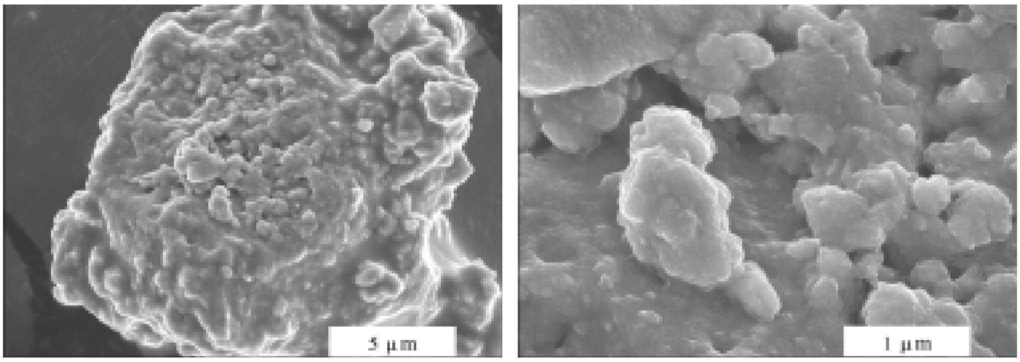

Figure 4.25: Scanning electron microscope images of $Sr_2Fe_2O_5$ milled in CO_2 for 256 h.

which precludes any porosity or a large fraction of loose microcrystals. It also shows that surface adsorption is not responsible for the mass loss observed during the thermogravimetric analysis.

4.6 Summary

Both temperature and oxygen concentration in the atmosphere have a profound effect on the composition and chemical reactions of the ferrite. Temperatures above 473 K and variation in oxygen partial pressure, under a total pressure of 1 atm, lead to changes in the composition within the range $2.5 \leq x \leq 2.915$.

The composition changes with temperature and oxygen pressure have an equilibrium character (see section 4.2.1) and, as one can imagine, lead also to changes in the crystal structure and other physical properties.

The composition can be expressed as a function of temperature and oxygen activity to form an equilibrium composition diagram as shown in section 4.2.2. This information is indispensable for any *in situ* studies of the material, construction of an equilibrium phase diagram and preparation of samples for ambient temperature research.

The compositional changes in the ferrite can also be induced by mechanical energy at room temperature, where thermally induced composition changes are negligibly slow. Milling in oxygen causes full oxidation however, the small crystal sizes and the crystal lattice strain of the product hamper analysis making it difficult to identify phases and fully characterize the material. The oxidation process itself is different from the thermal one. It is a non-equilibrium process and consist of both parallel and consecutive chemical reactions.

Oxygen bearing atmospheres are not the only environments that affect the material. Carbon dioxide at high temperature reacts with the ferrite causing it to decompose. However, decomposition occurs only below a certain critical temperature which depends on the CO_2 partial pressure and above which the ferrite forms again.

The thermal carbonation reaction does not have $Sr_4Fe_6O_{13}$ as an intermediate phase and directly forms $SrFe_{12}O_{19}$ which is very resistant to carbonation. The carbonation reaction is considerably slower than oxidation at the same temperature and it is expected that complete conversion of $SrFeO_x$ to strontium carbonate and hematite would take several thousands hours at 1073 K.

The carbonation reaction can also be induced by mechanical energy. The reaction is is faster than the thermal process but the mechanism is considerably different. $SrFe_{12}O_{19}$ was not formed as an intermediate phase but an unknown metastable ferric carbonate which decomposes forming hematite was evident.

Chapter 5

Mössbauer Spectroscopy

The thermally and mechanically oxidized samples of $SrFeO_x$ were investigated by Mössbauer spectroscopy at room temperature using the experimental and analytical procedures described in Chapter 2.

The literature devoted to the Mössbauer effect in the $SrFeO_x$ system is much more plentiful than work concerning any other property of the material. Published reports describe room temperature as well as sub-ambient spectra of the material because of its interesting magnetic properties [127, 131, 140, 146–148]. Since the material undergoes compositional changes induced by temperature and partial pressure of oxygen it was also investigated at high temperatures [147–151] and pressures [152]. However, in many cases the interpretation of results is questionable and the overall picture is still far from being clear. The present author provides an alternative interpretation of some room temperature results and discusses high temperature data published by other authors which are relevant to the results presented in Chapter 7.

5.1 Thermally Oxidized Ferrites

The $SrFeO_x$ system has a very broad range of non-stoichiometry ranging from $x = 2.5$ to $x = 3$, however the investigation was limited to samples with the oxygen content $x \geq 2.75$ and $Sr_2Fe_2O_5$. X-ray diffraction examination of ferrites with composition $2.5 < x < 2.75$ show that the ferrite forms mixtures of $Sr_2Fe_2O_5$ ($x = 2.5$) and $Sr_4Fe_4O_{11}$ ($x = 2.75$) in this composition range.

Selected spectra of oxidized ferrites are presented in Figure 5.1 as a function of oxygen content and the patterns agree with results published by other authors [127, 131, 146, 147, 149]. The spectra change with increasing oxygen content and inspection of Figure 5.1 indicates that in the composition range $2.75 < x < 2.89$ the spectra are the sum of $x = 2.750$ and $x = 2.890$ patterns in different ratios. For $x \geq 2.890$ the patterns consist of two or three overlapping lines. The weaker line with positive isomer shift disappears in favour of a singlet characterised close to zero isomer shift.

5.1.1 $Sr_4Fe_4O_{11}$ Phase ($x = 2.75$)

The $Sr_4Fe_4O_{11}$ pattern, presented at the bottom of Figure 5.1, consists of three overlapping absorption peaks. Fitting with Lorentz profiles showed that widths of the lines are equal and their relative intensity ratio is approximately 2:1:1. The same width for all lines indicates that there is no other absorption lines overlapping with the observed ones unless the lines lie very close to each other.

$Sr_4Fe_4O_{11}$ contains equal fractions of iron in tetravalent and trivalent states. This means that iron occupies at least two different crystallographical positions in the lattice and the intensity of the tetravalent iron lines are expected to be equal the intensities of the trivalent lines.

However, without knowledge of the atom distribution in the unit cell the interpretation of the spectrum is ambiguous. Takeda *et al.* [127] and Takano *et al.* [147][*] proposed a very elaborate four iron site model to describe the spectrum. Two of the sites were small in intensity ($\leq 9\,\%$) and seem to have been introduced to get the correct calculated oxygen stoichiometry using the formula:

$$x = 0.5 f_{Fe^{4+}} + 2.5, \tag{5.1}$$

where $f_{Fe^{4+}}$ is the fraction of tetravalent iron in the compound. The model assumes strongly overlapping lines producing the three observed peaks without any experimental evidence for such overlap. The spectrum can be explained in much simpler way.

An obvious interpretation of the pattern as three singlets is not acceptable. The strong singlet would have to belong to one iron species and the remaining two weaker lines to the other one to get the correct calculated composition. In this case the third line would have substantial isomer shift ($\sim 1\,\mathrm{mm/s}$). The shift is within the range observed in iron compounds [98, 153] but it is characteristic of divalent iron.

---

[*] The two papers report the same room temperature results and were written by almost the same groups of authors.

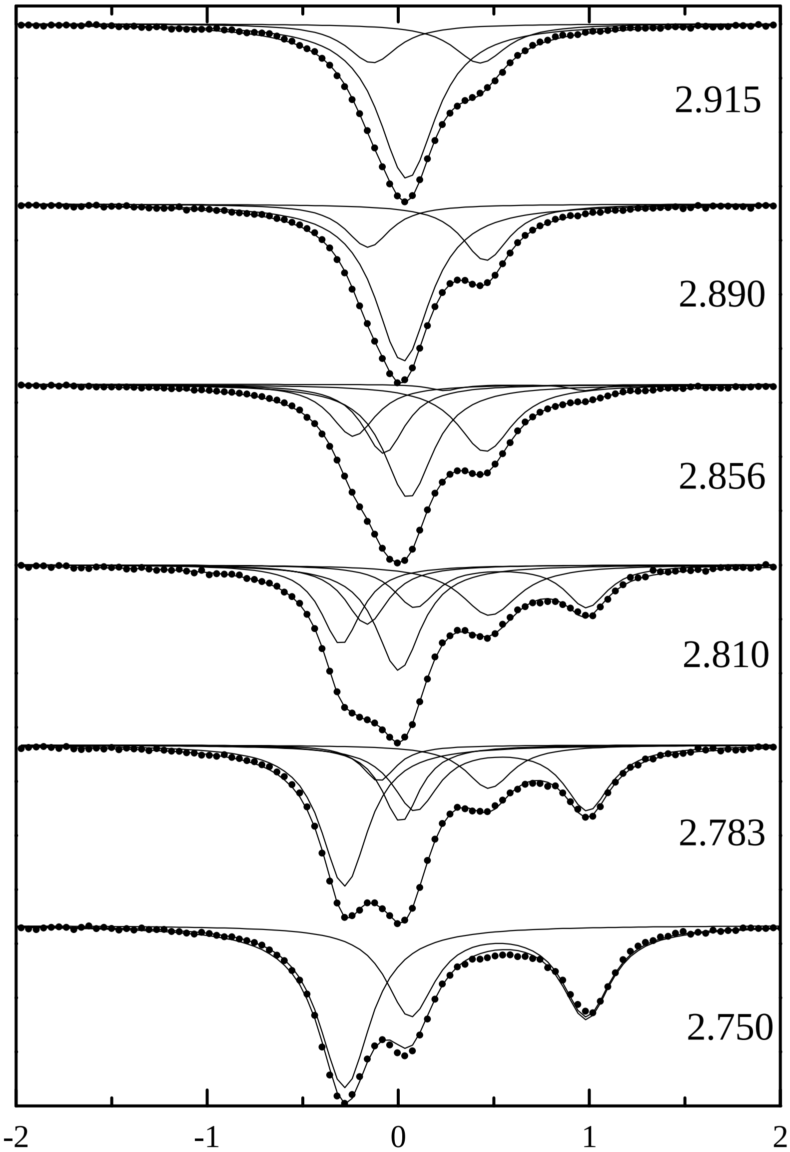

Figure 5.1: Room temperature Mössbauer spectra of thermally oxidized $SrFeO_x$ as a function of composition. The figures denote the oxygen content x. The points show the observed intensities, the solid lines denote result of fitting and the components of spectrum described in the text. The spectra were normalized.

Table 5.1: The components of the room temperature Mössbauer spectra of the thermally oxidized SrFeO$_x$. The models used for fitting are discussed in the text.

	Phase 1 ($Sr_4Fe_4O_{11}$)			Phase 2 ($Sr_8Fe_8O_{23}$)	
x	IS δ [mm/s]	QS Δ [mm/s]	Fraction	IS δ [mm/s]	Fraction
2.750	-0.280(1)	—	0.49	—	—
	0.525(2)	0.921(3)	0.51	—	—
2.776	-0.283(3)	—	0.34	-0.10(2)	0.08
	0.498(12)	0.932(24)	0.37	0.09(1)	0.13
	—	—	—	0.507(6)	0.08
2.783	-0.281(4)	—	0.36	-0.10(5)	0.07
	0.540(11)	0.901(23)	0.32	0.01(3)	0.15
	—	—	—	0.475(5)	0.11
2.790	-0.307(22)	—	0.19	-0.18(3)	0.15
	0.544(8)	0.863(23)	0.20	0.001(15)	0.25
	—	—	—	0.501(6)	0.21
2.810	-0.300(24)	—	0.19	-0.17(3)	0.15
	0.537(19)	0.90(4)	0.21	0.003(23)	0.28
	—	—	—	0.479(7)	0.17
2.856	-0.234(15)	—	0.16	-0.075(13)	0.20
	0.611(13)	0.736(28)	0.02	0.054(15)	0.37
	—	—	—	0.455(4)	0.25
2.884†	—	—	—	-0.162(14)	0.14
	—	—	—	0.028(6)	0.64
	—	—	—	0.445(5)	0.22
2.890†	—	—	—	-0.158(9)	0.14
	—	—	—	0.024(4)	0.66
	—	—	—	0.457(2)	0.20
2.915†	—	—	—	-0.136(18)	0.15
	—	—	—	0.047(6)	0.69
	—	—	—	0.428(6)	0.16

†- two phase sample, the contribution from $SrFeO_3$ is unresolved.

The model adopted in this thesis assumes that the strongest singlet (see Figure 5.1, $x = 2.750$) belongs to one iron species and the two remaining lines form a doublet resulting from quadrupole splitting belonging to the other valency. The fit resulting from this model is presented as a solid line in Figure 5.1. The isomer shift of the doublet (Table 5.1) is characteristic for Fe^{3+} with spin $S = 5/2$ and the measured value does not overlap with shifts of other Fe^{3+} states [98]. The negative shift of the singlet is close to the range $-0.125 \leq \delta \leq 0.125\,\text{mm/s}$ observed for Fe^{4+} with spin $S = 2$ in complex salts such as o-phenylene-bis-(dimethylarsine) [98, 153]. However, the tetravalent state is rare and departure ($\sim$0.155 mm/s) from the reported values indicates that the isomer shift for this state could have a broader span.

5.1.2 $Sr_8Fe_8O_{23}$ Phase ($x = 2.875$)

Peaks for the $Sr_4Fe_4O_{11}$ phase vanished when the oxygen content reached approximately $x = 2.89$. The traces of this phase are still visible in sample with composition $x = 2.856$ in form of slight shoulders at velocities of -0.3 and $\sim 1\,\text{mm/s}$ (see Figure 5.1). The room temperature single phases of the $SrFeO_x$ system presented so far are $Sr_2Fe_2O_5$, $Sr_4Fe_4O_{11}$ and $SrFeO_3$ they correspond to the tetravalent iron fractions equal 0, 1/2 and 1 respectively. The $x = 2.89$ composition is close to the ideal composition of $x = 2.875$ which corresponds to a tetravalent iron fraction of 3/4 and the formula $Sr_8Fe_8O_{23}$.

The present author did not managed to obtain exactly the ideal composition but samples with oxygen content $x = 2.884$ and $x = 2.890$ are close enough for the analysis. The spectrum of the sample with $x = 2.890$ appears as two lines (see Figure 5.1), however numerical analysis indicates that the stronger line is actually a pair of lines.

The $Sr_8Fe_8O_{23}$ phase was previously reported by Takeda *et al.* [127] and Takano *et al.* [147] and the authors assigned the strong singlet to the tetravalent state and two remaining lines were interpreted as a doublet resulting from a quadrupole splitting. However, if the doublet is to be regarded as the trivalent iron contribution the model yields an incorrect calculated oxygen content. Takeda *et al.* and Takano *et al.* proposed that the iron corresponding to the doublet is in a 3.5+ oxidation state and results from a fast electron transfer between Fe^{4+} and Fe^{3+}. Such an arrangement gives the correct calculated composition although no other experimental evidence to support this proposal has been presented.

The spectrum of $Sr_8Fe_8O_{23}$ can explained in a more straightforward manner. The new model assigns the tetravalent state to the strongest line and to the weak singlet with negative isomer shift (see Figure 5.1, $x = 2.890$). The weak tetravalent singlet overlaps with the strongest line. The trivalent state was assigned to the weak peak with positive isomer shift. In the present model, shown as solid lines in Figure 5.1, there are two distinct crystallographical sites occupied by Fe^{4+} and one site occupied by Fe^{3+}. The model yields the correct calculated composition when applied to the present results and data published by Takeda *et al.* and Takano *et al.* [127,147] as well. The present author and Takeda *et al.* and Takano *et al.* observed that the two weaker lines belonging to the tetravalent and the trivalent states have almost equal intensities. The $Sr_8Fe_8O_{23}$ phase contains 1/4 of iron in the trivalent which gives one weak trivalent peak and as a result the other weak line must also correspond to 1/4 of the total iron. Since there are only three observed lines, in pure $Sr_8Fe_8O_{23}$ iron is partitioned among the sites like $\frac{1}{4} : \frac{2}{4} : \frac{1}{4}$ and yield relative intensities of the Mössbauer lines in the ratio 1:2:1.

The observed intensity ratios (1:4.7:1.4 for $x = 2.890$ and 1:4.6:1.1 for $x = 2.915$) depart from the ideal since the oxygen content in the examined samples was higher than the ideal $x = 2.875$. The discrepancies in intensities are caused by the strong overlap of the tetravalent iron lines and the fact that above $x = 2.875$ the samples contain $SrFeO_3$ which yields a singlet with isomer shift close to zero [127,131,140,147]. The $SrFeO_3$ contribution enhances the strongest peak and is impossible to distinguish from the $Sr_8Fe_8O_{23}$ tetravalent peak. Takeda *et al.* and Takano *et al.* [127,147] examined a sample with composition $x = 2.86$ and their line intensity ratio was 1:1.6:1[†] since the stoichiometry was less than $x = 2.875$.

The observed isomer shifts (samples $x = 2.884, 2.890, 2.915$) are characteristic for Fe^{3+} in $S = 5/2$ spin state and Fe^{4+} with spin $S = 2$. The departure of the observed shift of the weak tetravalent line from the reported values [98,153] is smaller than in the $Sr_4Fe_4O_{11}$ case (see the previous section).

5.1.3 Two Phase Regions

Most of the examined samples had oxygen contents far from the ideal compositions of $Sr_4Fe_4O_{11}$, $Sr_8Fe_8O_{23}$ and $SrFeO_3$. As pointed out during the initial visual analysis of Figure 5.1 the spectra of the intermediate composi-

---

[†] The intensities of the weaker lines were assumed to be equal to 1/2 of the doublet intensity.

tions contain lines of $Sr_4Fe_4O_{11}$ and $Sr_8Fe_8O_{23}$. The two phase spectra with composition $2.75 < x < 2.875$ were fitted with models comprising of the ideal phases ($Sr_4Fe_4O_{11}$ and $Sr_8Fe_8O_{23}$) and the parameters obtained are presented in Table 5.1. The refined spectral parameters are also plotted in Figure 5.2 as a function of composition x. However due to severe overlap of the absorption lines the extracted intensities depart from the values exhibited by the Daltonian compounds. It is caused by the fact that fitting was unconstrained and in the least favourable situation the fitting varied up to 16 parameters (positions, widths and intensities of lines). The discrepancies are visible in the samples containing a small amount of one of the phases. However, the isomer shifts and quadrupole splittings of lines remained essentially constant.

The samples with composition $2.875 < x < 3.0$ are also two phase however the contribution from $SrFeO_3$ is impossible to resolve so the patterns were fitted as single phase materials as explained in the previous section.

5.2 $Sr_2Fe_2O_5$ Phase ($x = 2.5$)

The oxygen deficient form of ferrite is the only phase in the $SrFeO_x$ system which exhibits magnetic order at room temperature. The oxidized materials have ordering temperatures well below ambient [29,125,131,154].

The Mössbauer spectrum is presented in Figure 5.3 and consists of 11 absorption lines. The occurrence of eleven lines indicates that there are at least two iron sites in $Sr_2Fe_2O_5$ and that two lines overlap. The spectrum was fitted with two sextets however, the two features did not yield a satisfactory fit. The material is antiferromagnet and magnetization measurements using a vibrating sample magnetometer did not show any uncompensated magnetic moment at zero external field so the fraction of iron in both sites must be equal. An exact fit was obtained by an introduction of a singlet which accounts for 6 % of absorption. The single line is broad and has a negative isomer shift (see Table 5.2 for the results) and the resulting occupancy of sites corresponding to the sextets are not equal.

Calculated isomer shifts and hyperfine fields in $Sr_2Fe_2O_5$ are similar to the values published by Fournes *et al.* [148]. However, they observed similar irregularities in the intensities of sextets.

The broad singlet was added just to account for all iron sites and a single line might not be a proper description of the phenomenon which causes the uneven areas of the sextets. The line could be interpreted as a sign of

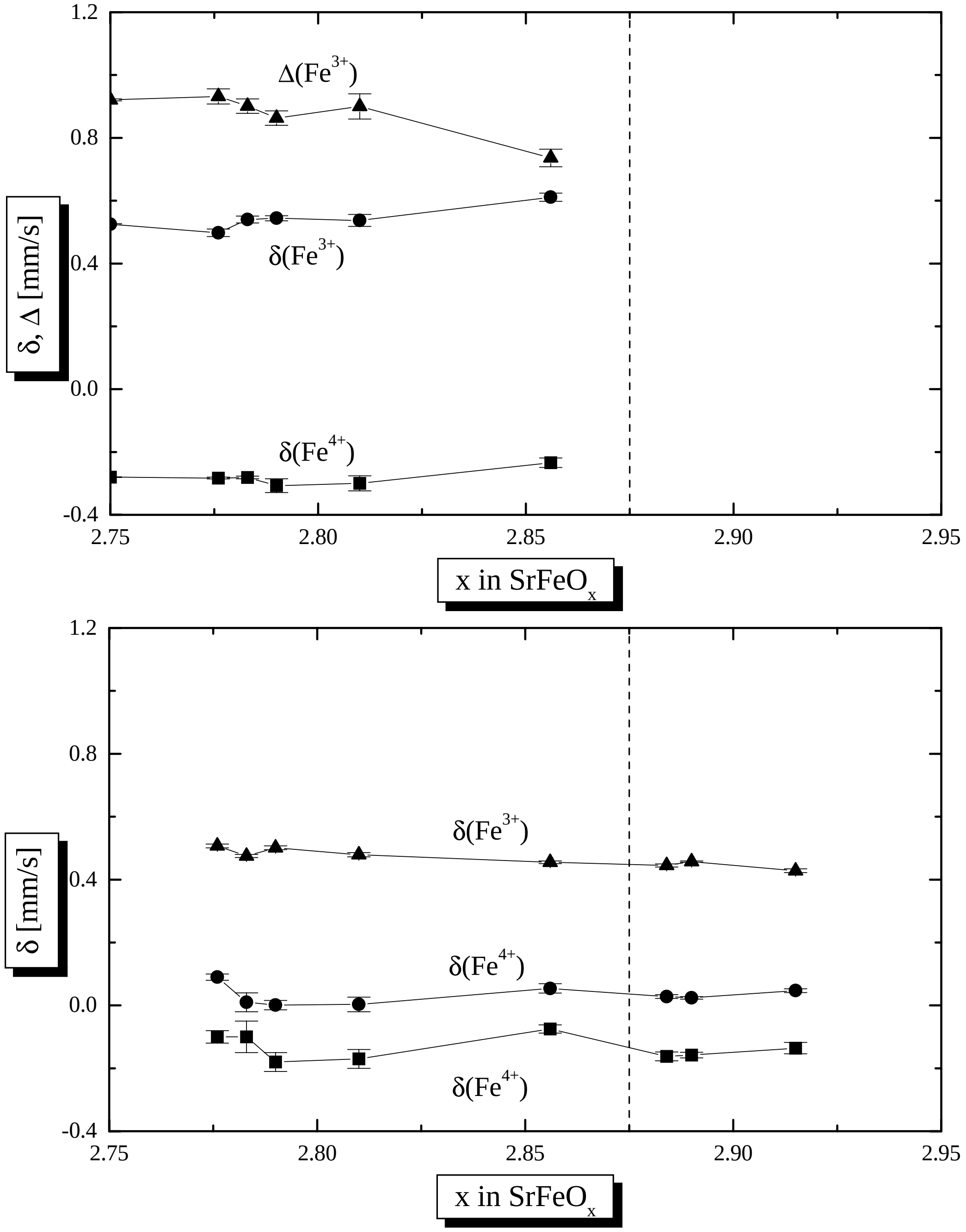

Figure 5.2: Refined parameters of the Mössbauer spectra of the two phase $SrFeO_x$ samples as a function of composition in the range of $2.750 \leq x \leq 2.915$. The top and the bottom plots present the parameters of $Sr_4Fe_4O_{11}$ and $Sr_8Fe_8O_{23}$ lines respectively as discussed in the text. The dashed line marks the composition of $x = 2.875$ ($Sr_8Fe_8O_{23}$), the results are also contained in Table 5.1. The error bars represent standard deviations resulting from fitting which are smaller than actual error.

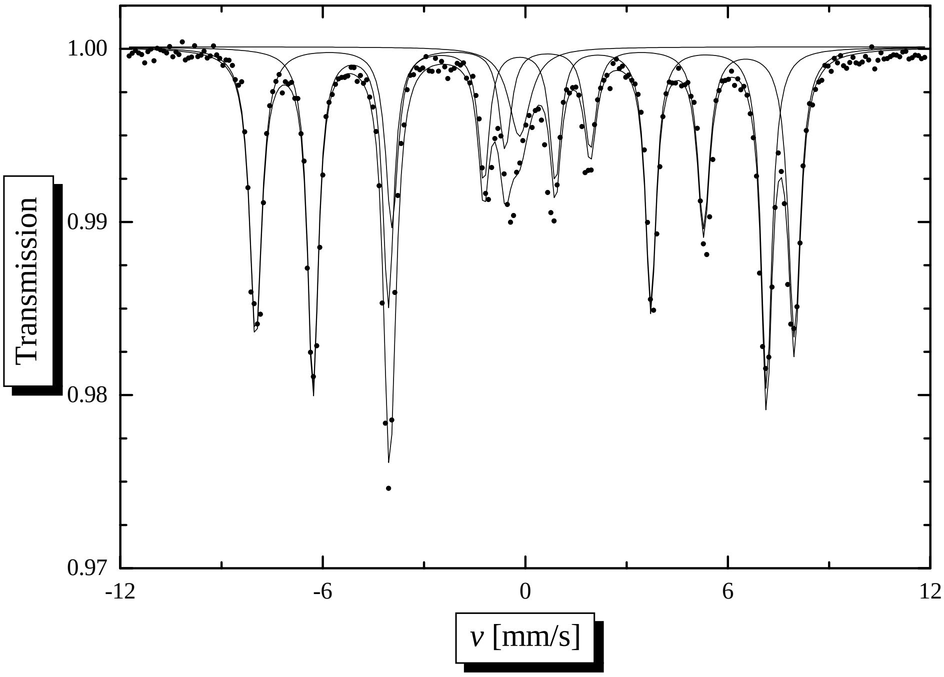

Figure 5.3: Room temperature Mössbauer spectrum of $Sr_2Fe_2O_5$. The points show the observed intensities, the solid lines denote result of fitting and the components of spectrum described in the text.

Table 5.2: Hyperfine parameters of $Sr_2Fe_2O_5$ at room temperature.

Site	IS δ [mm/s]	QS Δ [mm/s]	B [T]	Fraction	Comments
Sextet 1	0.326(4)	-0.336(4)	49.48	0.44	$HWHM = 0.20$
Sextet 2	0.128(3)	0.299(3)	41.66	0.50	$HWHM = 0.20$
Singlet 1	-0.17(3)	—	—	0.06	$HWHM = 0.39$

oxidation, since the strongest absorption line of $Sr_4Fe_4O_{11}$ has negative isomer shift. However, 6 % of tetravalent iron would yield oxygen stoichiometry $x = 2.53$ which can be readily detected by x-ray diffraction. The isomer shift of the singlet is characteristic for Fe_xO [155] however tests made on $Sr_2Fe_2O_5$, using the procedure described on page 96, exclude the presence of ferrous iron in the system. The other more feasible possibility is the existence of structural disorder in $Sr_2Fe_2O_5$ and the singlet is actually an unresolved doublet.

5.3 Mechanically Oxidized Ferrites

Mössbauer spectra of the mechanically oxidized $SrFeO_x$ samples, described in section 4.3, are presented in Figure 5.4. The observed spectra contain two broad, overlapping lines and additionally the sample milled for 18 h contains traces of $Sr_2Fe_2O_5$. The lines are broadened due to the small crystal size and strain resulting in a distribution of spectral parameters and completely obscure features which were only partially resolved in the spectra of the thermally oxidized materials.

Numerical analysis showed that the strongest line contains an additional absorption peak so the patterns were fitted using a singlet and a doublet and the results are presented in Table 5.3 and in Figure 5.4 as solid lines. The doublet was chosen to obtain a better fit however, it can not be directly assigned to any structural feature. This ambiguity is due to the samples being mixtures of two or more phases as discussed in section 4.3. The negative isomer shift of the strongest line in the 18 h sample indicates the presence of $Sr_4Fe_4O_{11}$, in higher oxidized samples ($x \geq 2.89$) the line has a shift close to zero which is characteristic for $Sr_8Fe_8O_{23}$ and $SrFeO_3$. The isomer shift and quadrupole splitting of the doublet remains approximately constant in samples milled for longer than 18 h but the area of the doublet increases with milling time from 0.48 after 18 h to 0.58 after 213 h.

The increase in the doublet is consistent with the observed increase in the lattice constant of the milled material (see Figure 4.14). It indicates that crystal structure of the mechanically oxidized material is very complex and the observed cubic pattern (see Figure 4.11) is in fact much more complicated. The increase in the lattice constant and the fraction of doublet is exactly the opposite behaviour to the one found in the thermally oxidized ferrites, where the spectrum collapses into one line upon oxidation (Figure 5.1) and the unit cell usually shrinks. Highly oxidized samples, after 117 h and 213 h of milling, exhibit a two line character. It proves that the final product of milling is not a pure cubic perovskite $SrFeO_3$ which is characterised by a single absorption line at room temperature [127, 131, 140, 147].

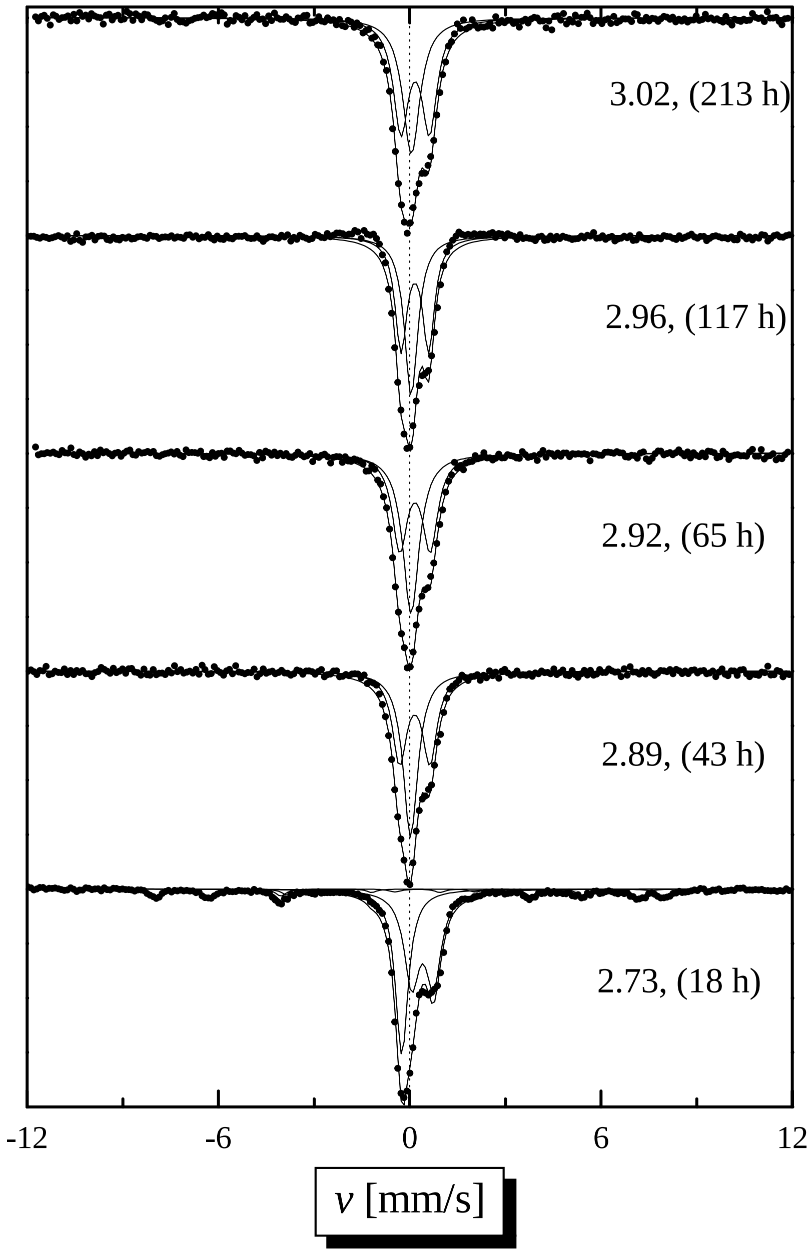

Figure 5.4: Room temperature Mössbauer spectra of mechanically oxidized $SrFeO_x$ as a function of milling time. The materials were characterised in section 4.3 and the spectral fits are discussed in the text. The figures denote the measured oxygen content x and milling time. The spectra were normalized.

Table 5.3: Components of the Mössbauer spectra of the mechanically oxidized ferrites at different stages of milling. The spectral models are discussed in the text.

Milling time [h]	Measured Composition x	IS δ [mm/s]	QS Δ [mm/s]	Fraction
18†	2.73	-0.248(3)	—	0.37
		0.406(5)	0.685(7)	0.48
43	2.89	0.026(6)	—	0.49
		0.157(9)	0.95(2)	0.51
65	2.92	0.042(6)	—	0.48
		0.165(9)	0.95(2)	0.52
117	2.96	0.047(5)	—	0.45
		0.160(5)	0.864(12)	0.55
213	3.02	0.05(1)	—	0.42
		0.17(1)	0.90(2)	0.58

†- sample contains $Sr_2Fe_2O_5$ responsible for approximately 0.15 of absorption

5.4 Thermally and Mechanically Carbonated Ferrites

The carbonated samples, described in section 4.4, were not examined by Mössbauer spectroscopy as it was anticipated that the spectra would be too complicated to reach any firm conclusions. The thermally carbonated materials form mixtures of $Sr_2Fe_2O_5$, $Sr_4Fe_4O_{11}$ and $SrFe_{12}O_{19}$. $Sr_2Fe_2O_5$ and $SrFe_{12}O_{19}$ are magnetically ordered and have iron in two and five crystallographical positions [156, 157] respectively and would produce seven overlapping sextets.

The situation with the milled materials described in section 4.5 is similar since almost all of them would contain spectra from $Sr_2Fe_2O_5$, antiferromagnetic hematite and the amorphous iron compound. The analysis would be complicated by the line broadening as in the case of the mechanically oxidized ferrites.

5.5 Published High-Temperature Spectra

High temperature experiments were not performed by the author however, a discussion of published results is relevant to structural studies presented in

Chapter 7.

Mössbauer spectra provide valuable information about the number of different iron sites which is very helpful in structure determination. The relevant experiments were conducted by Gibb [149] and Fournés *et al.* [148, 150], Takano *et al.* [147], Wißmann and Becker [151] using oxidized samples as well as $Sr_2Fe_2O_5$. The experiments on oxidized materials were made under equilibrium conditions in an air/oxygen atmosphere [150,151] as well as under vacuum and in inert gases [147, 149, 150]. $Sr_2Fe_2O_5$ was studied in vacuum [147, 148]. The data cover a broad range of compositions. Gibb [149] heated oxidized material in vacuum causing an inevitable oxygen loss and failed to reconcile this fact during the analysis, however the raw data is the same as reported by others.

All authors observed a transition in the $SrFeO_x$ system from structures similar to those at room temperature to a singlet[‡]. The single line indicates only one iron site in the crystal structure. The oxidized ferrites contain mixture of Fe^{4+} and Fe^{3+} oxidation states and the single line proves that both states have the same surroundings (the same average number of oxygens irrespective of the oxidation state). This leads to the conclusion that the oxygen sites must be disordered. Otherwise two different oxidation states of iron are expected to form different surroundings (*e.g.* tetrahedrons and octahedrons) and yield more complicated Mössbauer spectra.

5.6 Summary

Room temperature investigation of thermally oxidized ferrites showed the existence of two composition ranges: $2.75 < x < 2.875$ and $2.875 < x < 3.0$, where the ferrite forms two phase mixtures of $Sr_4Fe_4O_{11}$ and $Sr_8Fe_8O_{23}$ and $Sr_8Fe_8O_{23}$, and $SrFeO_3$ respectively. Room temperature spectra of $Sr_4Fe_4O_{11}$ and $Sr_8Fe_8O_{23}$ were interpreted in a much more straightforward way and the proposed models were justified on the basis of chemical composition of the materials. However the interpretation problem is still open and can be fully resolved only when the crystal structures of these compounds are solved.

Examination of mechanically oxidized ferrites, showed that the fully oxidized sample does not form the cubic perovskite. However, full analysis

---

[‡] $Sr_2Fe_2O_5$ is an exception since it becomes paramagnetic on heating and crosses the Néel point before transition into the singlet. The paramagnetic phase yields two overlapping doublets instead of two sextets observed at room temperature.

of the results is impossible because of line broadening which obscures fine details in the spectra as it did in case of x-ray diffraction.

Discussion of published high temperature results shows that the high temperature cubic form of the oxide has one iron site in the unit cell which indicates disorder in the oxygen sites.

Chapter 6

Room Temperature Phases of SrFeO_x

This chapter presents information about the room temperature phases of the SrFeO_x system. This knowledge is not important as far as application of the ferrite is concerned since the ionic conductivity of the oxide is very low but is presented for the sake of completeness. The literature on the room temperature crystal structure of the ferrite is extensive [125–127, 131, 138, 139, 147, 158–161] but of crystal structure of some SrFeO_x phases has not been fully explained yet. Apart from x-ray diffraction, this chapter is based on the results of Mössbauer experiments presented in the previous chapter and measurements of the density of the ferrite.

6.1 Phase Behaviour

The SrFeO_x system, at room temperature, forms phases with an oxygen content over the entire composition range $2.5 \leq x \leq 3.0$. However, as explained in Chapter 4 the changes in oxygen content at room temperature are negligibly small and the oxide's composition at ambient temperatures is constant regardless of the oxygen partial pressure. The different room temperature phases are the result of different thermal history of particular materials (annealing temperatures and composition of atmospheres).

There is a finite number of crystallographically different phases in the SrFeO_x system despite the fact that the composition of the ferrite varies continuously. The fraction of tetravalent iron in the phases is given by $f_{Fe^{4+}} = n/4$, where $n = 0, 2, 3, 4$. These fractions correspond to the phases:

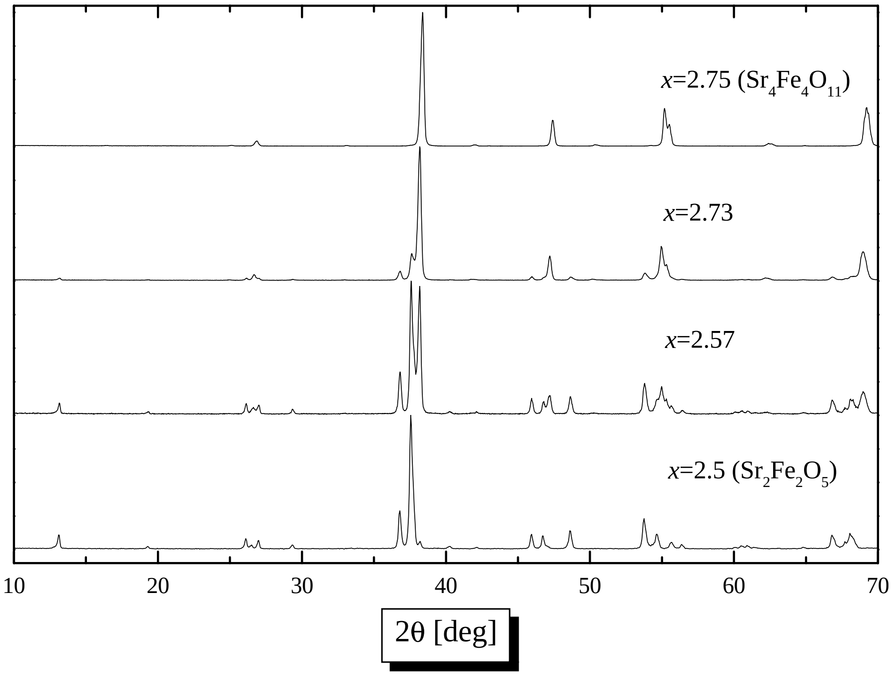

Figure 6.1: X-ray diffraction spectra of $Sr_2Fe_2O_5$ (top pattern), $Sr_4Fe_4O_{11}$ (bottom pattern) and ferrite samples with intermediate compositions.

$Sr_2Fe_2O_5$ ($x = 2.5$), $Sr_4Fe_4O_{11}$ ($x = 2.75$), $Sr_8Fe_8O_{23}$ ($x = 2.875$) and $SrFeO_3$ ($x = 3$) respectively. The phase with the tetravalent iron fraction $f_{Fe^{4+}} = 1/4$ and corresponding composition of $Sr_8Fe_8O_{21}$ ($x = 2.625$) does not exist at room temperature.

X-ray diffraction of samples with compositions from the range: $2.5 < x < 2.75$ revealed that the ferrite forms mixtures of $Sr_2Fe_2O_5$ and $Sr_4Fe_4O_{11}$. The examples of x-ray patterns are presented in Figure 6.1 which shows that $Sr_4Fe_4O_{11}$ fraction increases with oxygen content x. Since the ferrite forms a two phase system, and the only variable is the oxygen content, the fractions of $Sr_2Fe_2O_5$ and $Sr_4Fe_4O_{11}$ were calculated as a function of the average composition and presented in Figure 6.2.

Phases with the oxygen content $x > 2.75$ are more difficult to analyse with x-ray diffraction since the diffraction patterns of the constituent phases have reflections with similar d-spacings and thus are difficult to resolve using the laboratory diffractometer used in this thesis. However, the Mössbauer measurements presented in the previous chapter have demonstrated that the ferrite forms two phase mixtures in the composition ranges $2.75 < x < 2.875$ and $2.875 < x < 3.0$ (see section 5.1.3). In the former range the ferrite consists of $Sr_4Fe_4O_{11}$ and $Sr_8Fe_8O_{23}$, in the latter range the oxide is a mixture

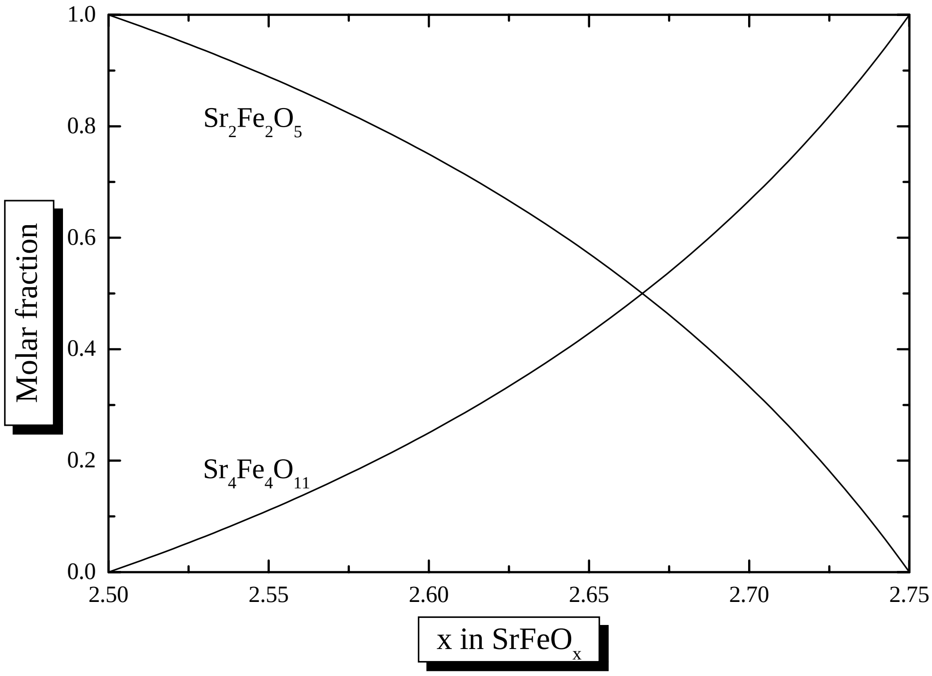

Figure 6.2: Molar fractions of $Sr_2Fe_2O_5$ and $Sr_4Fe_4O_{11}$ as a function of the oxygen content x, calculated for room temperature phases of $SrFeO_x$ with the average oxygen content from the range $2.5 \leq x \leq 2.75$.

of $Sr_8Fe_8O_{23}$ and $SrFeO_3$. The calculated molar fractions of the components are presented in Figure 6.3 and Figure 6.4.

The changes of the molar fractions with the average composition presented in Figure 6.3 have similar character (shape) to the changes for the $Sr_2Fe_2O_5$–$Sr_4Fe_4O_{11}$ mixture presented in Figure 6.2. This similarity is a result of the fact that the phase with the greater oxygen content in the mixture contains twice as much iron per molecule ($Sr_2Fe_2O_5$–$Sr_4Fe_4O_{11}$ and $Sr_4Fe_4O_{11}$–$Sr_8Fe_8O_{23}$) and the oxidation of two molecules of the oxygen deficient phase in the mixture creates one molecule. The third composition range ($2.875 < x < 3.0$) is different since the oxidation of $Sr_8Fe_8O_{23}$ creates eight molecules of $SrFeO_3$. This is the reason why the fraction of $Sr_8Fe_8O_{23}$ quickly decreases with the oxygen content. For instance the sample with composition $x = 2.915$ which is not far from the ideal composition of $x = 2.875$ contains only 21 molar % of $Sr_8Fe_8O_{23}$ and for this reason the Mössbauer spectrum of this sample was predominantly $SrFeO_3$ (see section 5.1.2).

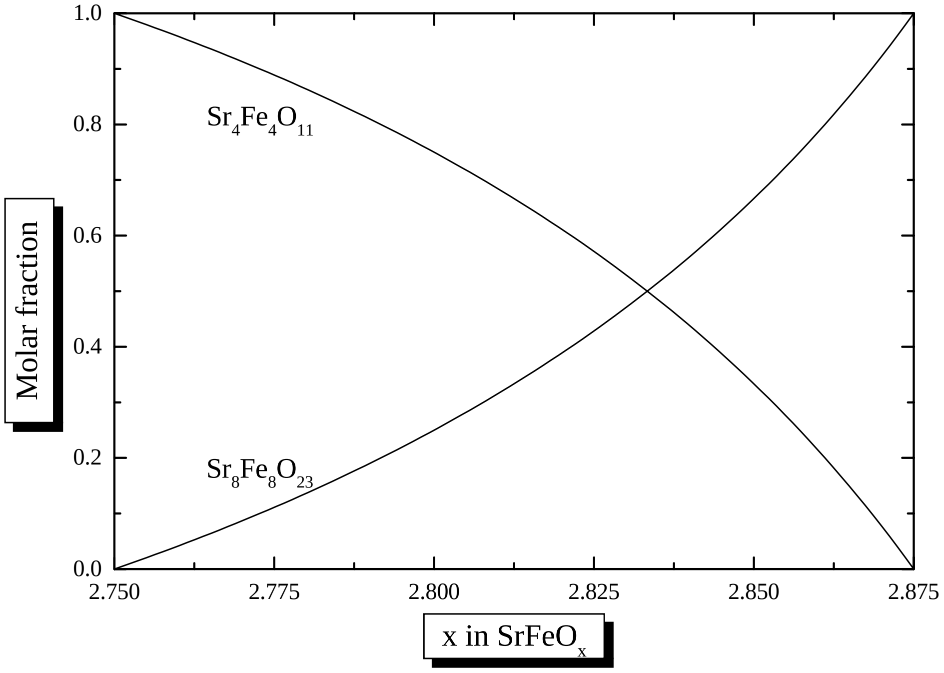

Figure 6.3: Calculated molar fractions of $Sr_4Fe_4O_{11}$ and $Sr_8Fe_8O_{23}$ as a function of the average oxygen content x. These two phases coexist in the composition range of $2.75 < x < 2.875$ at room temperature.

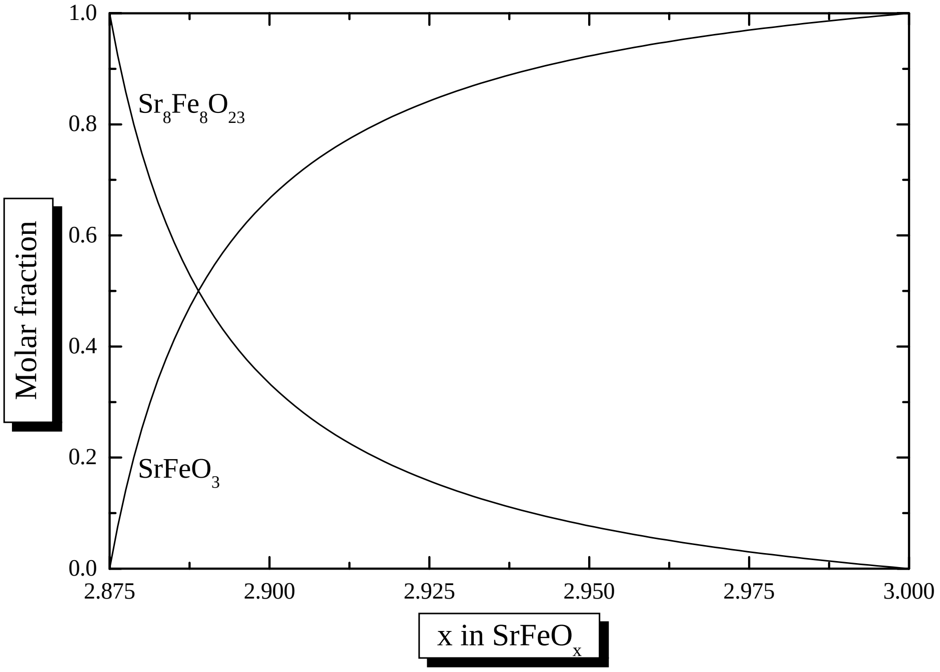

Figure 6.4: Calculated molar fractions of $Sr_8Fe_8O_{23}$ and $SrFeO_3$ as a function of the average oxygen content x. These two phases coexist in the composition range of $2.875 < x < 3.0$ at room temperature.

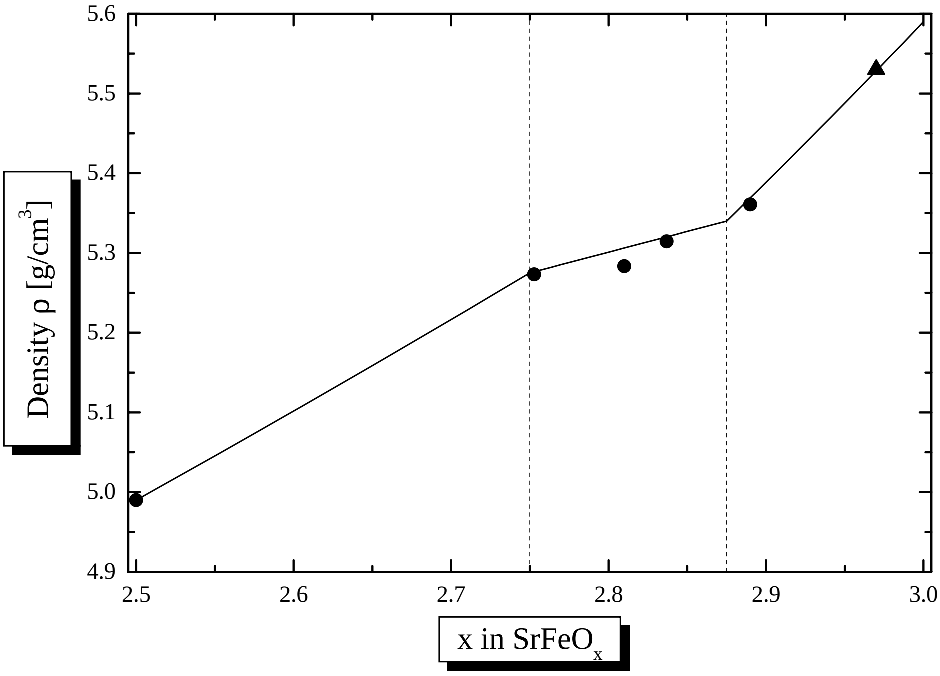

Figure 6.5: Density of $SrFeO_x$ as a function of composition at room temperature. The density was obtained using a pycnometer as described in the text, the value at $x = 2.5$ was derived from neutron scattering experiments described in Chapter 7, the point marked with the triangle represents the density calculated from data published by Takeda *et al.* for $x = 2.97$ [127]. The solid line is calculated density as described in the text. The dashed lines mark the borders of the composition ranges.

6.2 Density

The densities of oxidized phases were measured using a 10 cm^3 pycnometer and water as the liquid. The measurements were performed only on samples available in large quantities. The density measurements of powders using a pycnometer frequently yield underestimated values due to gas trapped in voids within powder grains. The accuracy of the present measurements is believed to be no worse than 1 %. A test run on sintered hematite, treated in the same way as the studied ferrite, yielded 0.4 % error compared with the density obtained from x-ray diffraction*.

The results are presented in Figure 6.5, the density increases with the oxygen content and ranges from 4.99 g/cm^3 at $x = 2.5$ to 5.54 g/cm^3 at $x = 2.97$. The results cannot be fitted with a single straight line since the

---

*Most of the trapped gas was replaced with the liquid by degassing of the powder in the bottle partially filled with water using a vacuum pump.

values from the ranges $2.75 < x < 2.875$ and $2.875 < x < 3.0$ depart from the line. The departure is a simple consequence of the phase behaviour described in the previous section (three two-phase mixtures across the entire composition range).

Density of $SrFeO_x$ as a function of composition was also calculated and is presented as the solid line in Figure 6.5. The calculations were performed using the molar fractions of the constituting phases presented in Figures 6.2, 6.3 and 6.4 and their densities. Density of $Sr_8Fe_8O_{23}$ was assumed to be around $5.34\,g/cm^3$ and density of $SrFeO_3$ was taken from Table 7.8 (it is a value derived from neutron diffraction experiments). Calculated density increases linearly with composition and the straight lines have different slopes in each of the composition ranges.

6.3 Crystal Structure

The crystal structure of the composition end-members is known. The fully oxidized $SrFeO_3$ has a cubic perovskite structure, confirmed by several different groups [127, 139, 140, 147, 158]. The other end-member of the composition range $Sr_2Fe_2O_5$ ($x = 2.5$) has an orthorhombic crystal structure [127, 131, 138, 159–161] which will be described in detail in the next chapter. This structure can be seen as a derivative of the perovskite structure.

The high-resolution x-ray diffraction pattern of $Sr_4Fe_4O_{11}$ ($x = 2.75$), collected using synchrotron radiation is presented in Figure 6.6. The experimental setup was described in section 2.3.4. This pattern provides much more detail than patterns collected using an ordinary x-ray laboratory diffractometer (compare with Figure 6.1)[†]. The structure is related to the perovskite and main reflections can be indexed as a cubic phase. The symmetry of the compound is lower and manifests itself as additional peaks and line splitting. However, the present author was unable to unambiguously index the synchrotron diffraction pattern. The indexing solutions point at monoclinic and orthorhombic structures and the goodness-of-fit to both models is similar. This precludes any further analysis since the crystal system is unknown. This ambiguity could possibly be resolved by single crystal diffraction experiments. The measured density of $Sr_4Fe_4O_{11}$ ($5.28\,g/cm^3$) indicates that the

---

[†] Different relative intensities of peaks are result of strong polarization of synchrotron radiation and different experimental geometries. The patterns were collected using similar wavelengths.

unit cell has a volume which is a multiplicity of 236 Å^3 (it is the volume occupied by one chemical formula of the oxide) and the Mössbauer measurements show the existence of two iron sites of equal occupancy (see section 5.1.1).

The structure of $Sr_4Fe_4O_{11}$ was analysed by Takeda *et al.* [127] and more recently by Hodges *et al.* [139]. Takeda *et al.* indexed a pattern collected using a laboratory diffractometer but did not compare the measured peak intensities to any structural models. Hodges *et al.* [139] collected spectra of $Sr_4Fe_4O_{11}$ using a time-of-flight neutron spectrometer and carried out Rietveld refinement of the structure. However, Hodges *et al.* [139] also obtained two indexing solutions pointing at orthorhombic and monoclinic structures and resolved the ambiguity on the basis of a small difference in the goodness-of-fit of the models to the observed intensities. However, such an approach does not guarantee the correct solution since the crystal system should be unambiguously chosen from the indexing alone.

The crystal structure of $Sr_8Fe_8O_{23}$ is even more troublesome. The synchrotron diffraction pattern of a sample containing a significant amount of $Sr_8Fe_8O_{23}$ is presented in Figure 6.7. The oxygen content of this sample is $x = 2.884$ which corresponds to 62 molar % of $Sr_8Fe_8O_{23}$ and the remaining impurity is cubic $SrFeO_3$. The presence of $SrFeO_3$ was deduced from the Mössbauer measurements presented in the previous chapter. As in the case of $Sr_4Fe_4O_{11}$ the structure of $Sr_8Fe_8O_{23}$ is a perovskite derivative but the line splitting is even less pronounced. The observed reflections did not allow successful indexing of the pattern mainly due to the presence of a significant amount of the second phase. Because of rapid changes of the $Sr_8Fe_8O_{23}$ concentration with the oxygen content (see Figure 6.3 and Figure 6.4) the samples for the investigation should have stoichiometry as close to $x = 2.875$ as possible. Samples with $x < 2.875$ are even more complex since they contain the low symmetry $Sr_4Fe_4O_{11}$ as the impurity.

Figure 6.5 indicates that the density of pure $Sr_8Fe_8O_{23}$ should be around 5.34 g/cm^3 and therefore the unit cell must be a multiplicity of 470 Å^3. The Mössbauer experiments indicate three different iron sites in the structure. Two sites belonging to the tetravalent iron and one site corresponding to the trivalent state. The number of iron atoms in the sites forms the ratio Fe^{4+}:Fe^{4+}:Fe^{3+} = 1:2:1.

The pattern of $Sr_8Fe_8O_{23}$ was indexed by Takeda *et al.* [127] as a tetragonal structure. Hodges *et al.* [139] obtained three different indexing solutions (tetragonal, orthorhombic and monoclinic) and selected the tetragonal struc-

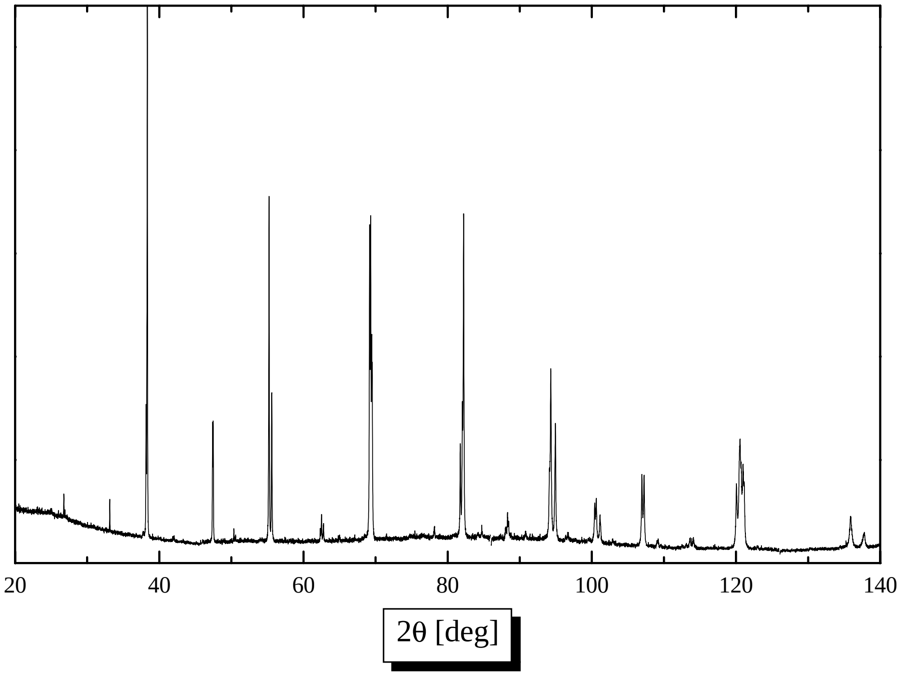

Figure 6.6: High-resolution synchrotron x-ray diffraction pattern of $Sr_4Fe_4O_{11}$.

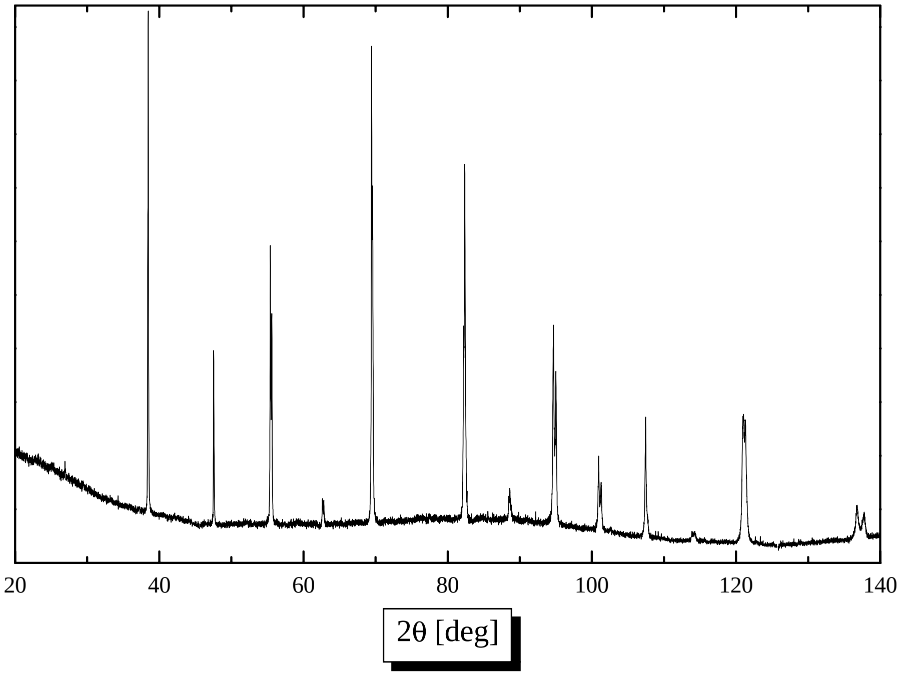

Figure 6.7: High-resolution synchrotron x-ray diffraction pattern of $Sr_8Fe_8O_{23}$. The actual composition of the sample is $x = 2.884$ and it contains approximately 38 molar % of the cubic $SrFeO_3$.

ture on the basis of small differences in the goodness-of-fit as in the case of $Sr_4Fe_4O_{11}$.

6.4 Summary

There are four distinct phases in the $SrFeO_x$ system at room temperature with oxygen contents $x = 2.5, 2.75, 2.875, 3$. The phases with intermediate oxygen stoichiometry are mixtures of two closest single phases with higher and lower oxygen concentration.

The density of the ferrite at room temperature increases with the average oxygen content, however the increase rate is different in all three two-phase regions.

The fully oxidized form of the ferrite $SrFeO_3$ has the cubic perovskite structure and all other phases are derivative of this structure. The other end-member of the composition range $Sr_2Fe_2O_5$ is orthorhombic. The crystal structure of the remaining phases is still unclear. Mössbauer experiments and density measurements show that $Sr_4Fe_4O_{11}$ has two different iron sites and the volume of the unit cell is a multiplicity of 236 Å^3. The $Sr_8Fe_8O_{23}$ on the other hand has three different iron sites and its unit cell volume is a multiplicity of 470 Å^3. However, single crystal diffraction experiments are needed to unambiguously establish the crystal structure of $Sr_4Fe_4O_{11}$ and $Sr_8Fe_8O_{23}$.

Chapter 7

High Temperature Crystal Structure of $SrFeO_x$

The crystal structure of the oxide at elevated temperature constitutes a very important piece of information from scientific point of view but also if the oxide is considered to be a material for oxygen conducting membranes. The oxygen content in the material is strongly influenced by temperature and composition of the atmosphere and this behaviour was shown in Chapter 4. So as one can imagine these changes should affect the crystal structure as well.

Indeed, the composition has a profound effect on the crystal structure. It has already been investigated by a few groups using x-ray diffraction however, the results were misinterpreted [127, 128, 138, 159]. The high temperature structure studies presented in this chapter were made using neutron powder diffraction and this is the first high temperature neutron investigation of the $SrFeO_x$ system. Due to limited beam-time and existing hardware the investigation was limited to two cases. The first case is the investigation of $Sr_2Fe_2O_5$ in an argon atmosphere (this atmosphere prevents oxidation) and the second case is the study of the ferrite in equilibrium with an air atmosphere. The results were analysed using the Rietveld method. The results presented in this chapter combined with information known so far (i) allows sketching of an equilibrium phase diagram, (ii) a new structural model for the cubic phase and (iii) a new interpretation of the cubic phase in terms of solid solution are proposed. The chapter embodies a significant amount of numerical information which is presented in the form of tables in Appendix A.

7.1 Preliminary Calorimetric Study

Approximate temperatures of phase transitions in the SrFeO_x system were established using calorimetric methods to avoid loss of time on blind probing of the (T, p_{O_2}) plane.

In order to locate the transitions, samples with different oxygen stoichiometry were heated up in the differential thermal analyser up to 773 K at heating rate of 20 K/min in argon and the results were examined for endothermic peaks associated with the transformations. However, the oxide is non-stoichiometric and annealing in argon changes the composition of the oxidized phases ($x > 2.5$) since the material is trying to equilibrate. The mass loss is pronounced above 773 K (see Figure 4.10) and for this reason the DTA scans were limited to this temperature. The only exception is $\mathrm{Sr_2Fe_2O_5}$ ($x = 2.5$), since annealing in argon does not affect its composition the sample was examined in the temperature up to 1473 K.

The temperatures of phase transitions are presented in Figure 7.1 as a function of composition however, the values are only approximate and the true values have to be derived from scattering experiments made under equilibrium conditions. Study with the DTA and the more sensitive differential scanning calorimeter revealed the existence of two phase transitions in $\mathrm{Sr_2Fe_2O_5}$. Apart from compositions x close to 2.5 the temperature of transition increases up to $x = 2.75$ and then falls. This behaviour is accompanied by similar changes in the energy of the transformation which follows the temperature trend. However, the endothermic peaks are mostly poorly defined without sharp onsets. The exception is the transition for $x = 2.75$ ($\mathrm{Sr_4Fe_4O_{11}}$) indicating a possible first order process. The research conducted by other authors has already identified the endothermic peaks as signs of structural transitions [127, 128].

7.2 Structure of $\mathrm{Sr_2Fe_2O_5}$

The scattering experiments presented in this section deal with the crystal and magnetic structures of the oxygen deficient form of the oxide $\mathrm{Sr_2Fe_2O_5}$ ($x = 2.5$). The measurements were performed in an argon atmosphere which preserves the composition of the sample at temperatures from room up to 1123 K. The oxide undergoes two phase transitions in this temperature range and diffraction patterns were collected to explore these changes.

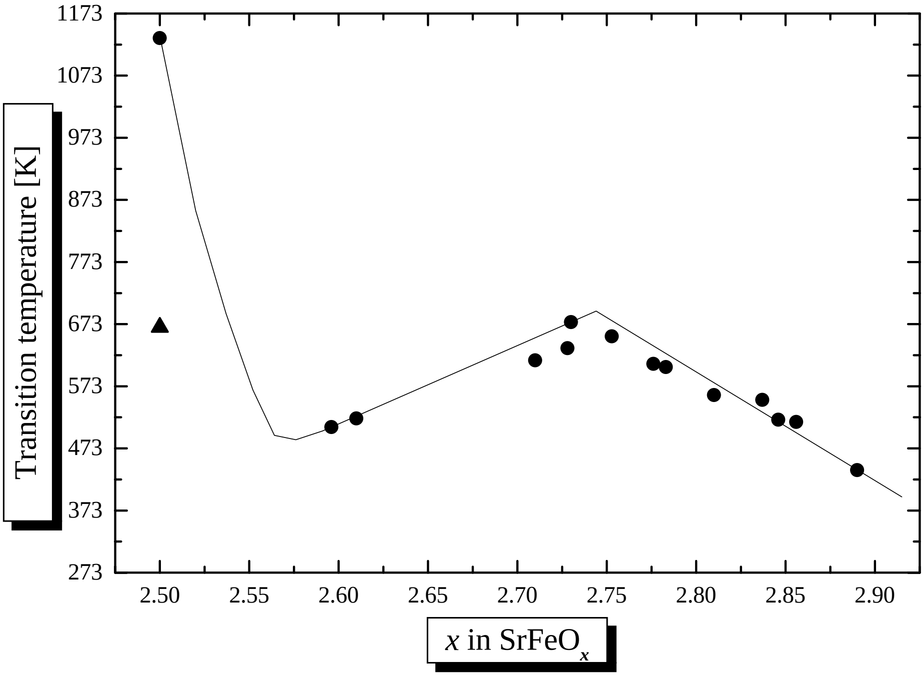

Figure 7.1: Temperatures of phase transitions in $SrFeO_x$ as a function of the initial composition x, found using DSC and DTA by heating at constant rate in argon atmosphere. The line is a guide for eye.

7.2.1 Phase Transitions

The phase transition temperatures found using the calorimeters in $Sr_2Fe_2O_5$ are indicated in Figure 7.1. The fragment of the calorimetric trace containing the first transition peak is presented in Figure 7.2. The transition causes very small changes to the heat capacity of the sample and the resulting thermal effect is barely distinguishable from the background. $Sr_2Fe_2O_5$ is an antiferromagnet and magnetic measurements on the compound indicate a Néel point in the vicinity of this temperature [29, 138]. So the observed peak was assigned to the magnetic transition in the system. Grenier *et al.* [138] interpreted the peak as the effect associated with appearance of a tetragonal phase in the system, however this phase has not been observed by anybody else. As the antiferromagnet to the paramagnet transition is second order, the temperature of 662 K corresponding to the peak of heat capacity (Figure 7.2) was taken as the ordering temperature. The second observed transition was detected around 1140 K and the profile of this transition peak was shown in Figure 4.9 in Chapter 4. This particular transition was believed to be of a first order due to the energy associated with the transformation [127, 138]. The area under the peak corresponds to 40.9 J/g. However, as discussed earlier

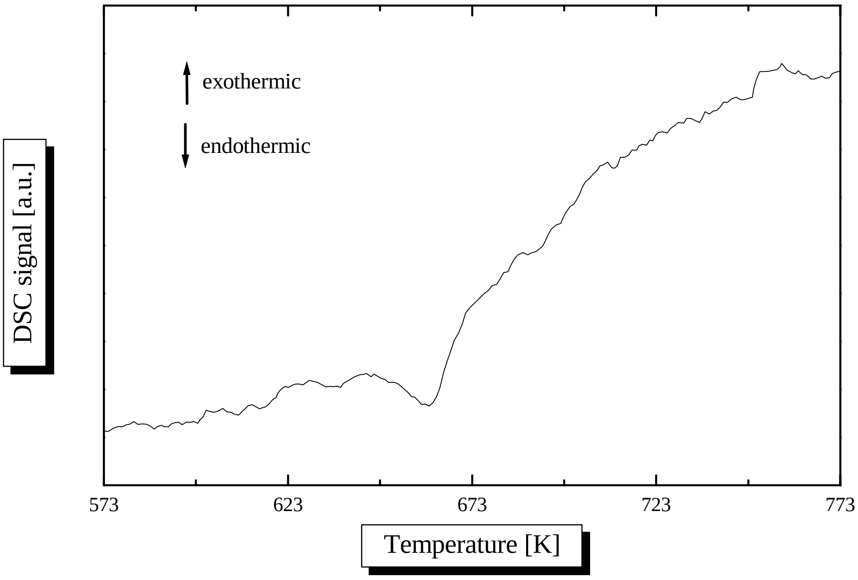

Figure 7.2: The DSC trace of $Sr_2Fe_2O_5$ obtained by heating at constant rate of 30 K/min in argon. The endothermic peak at 662 K indicates a phase transition discussed in the text.

(see page 66) the peak profile is very broad and lacks the distinctive features of a first order transition. For this reason the peak at 1140 K was again taken as the transition temperature. The temperature of this transformation observed using the calorimetric methods agrees with the findings of most of other authors ($1103 \leq T \leq 1123$ K) [126, 127, 138] the only exception is the value reported by Shin *et al.* [159] ($\sim$ 973 K). However, Grenier *et al.* [138] pointed out that the discrepancies are due to purity of inert gases used in the experiments as protective atmospheres.

7.2.2 Sample and Data Treatment

The composition of the sample is controlled by temperature and oxygen partial pressure, the equilibrium composition diagram (see Figure 4.6) indicates that at temperatures below 1473 K the equilibrium composition significantly exceeds $x = 2.5$. However, the equilibration time in low partial pressures of oxygen is extremely long due to scarce oxygen and under these conditions the material retains its initial composition. Prolonged annealing of $Sr_2Fe_2O_5$ at low temperatures (773 K) in ultra-high purity argon ($p_{O_2} < 1$ ppm) caused no visible oxidation after 70 h. This atmosphere will be referred to hereafter as ‘argon’.

Neutron diffraction experiments require a considerable volume of the sample (a few cubic centimeters) in shape of a cylinder. The oxide for this experiment was prepared using the usual way described in section 3.6 and pressed into pellets under a pressure of 98 MPa. The pellets were subsequently sintered at 1473 K in an argon atmosphere resulting in cylinders 15 mm in diameter, total height of 5.4 cm and mass approximately 33 g. To protect the material against oxidation during the scattering experiments the pellets were placed in a large diameter silica tube under a flow of argon. Unfortunately the tube introduced a quite complicated amorphous background and the diffractometer furnace produced a small diffraction peak centered around 27.4°. The data were analysed using the Rietveld method. Unfortunately the furnace peak overlaps with the (121) reflection of orthorhombic $Sr_2Fe_2O_5$ and for this reason a range from 26.5° to 28.5° was excluded from the refinements. The diffractometer peak profiles were modeled using an asymmetric Gauss profile and the troublesome amorphous background using a linear interpolation function (23 coefficients) [66].

7.2.3 Results of Scattering Experiments

Visual inspection of the diffraction patterns and comparison with the room temperature x-ray spectrum indicate the presence of reflections arising from long range magnetic order in the sample. The intensity of the magnetic lines decreased with temperature and vanished in the vicinity of the ordering temperature determined using the calorimeter. However, the magnetic transition did not cause changes to the crystal structure. There are no new peaks or missing reflections that would indicate a change of symmetry group. In the temperature range $723 \leq T < 1148\,\mathrm{K}$ the diffraction patterns indicate a single phase material. However, the measurement at 1148 K, in the vicinity of the second phase transition, yielded a two phase pattern containing the orthorhombic and a cubic structure. The scans made at higher temperatures show only a single phase cubic structure.

All structural parameters were extracted using the Rietveld method and the next part of this section contains a detailed analysis of properties of the material.

Table 7.1: Results of the fitting of the orthorhombic lattice parameters of $Sr_2Fe_2O_5$ with the polynomials as described in the text.

Lattice parameter	Polynomial coefficients		
	α_0	α_1	α_2
a	(5.6638 ± 0.0009)	$(89 \pm 27) \times 10^{-7}$	$(2.7 \pm 0.2) \times 10^{-8}$
b	(15.456 ± 0.005)	$(4.54 \pm 0.13) \times 10^{-4}$	$(-9.9 \pm 0.9) \times 10^{-8}$
c	(5.516 ± 0.002)	$(2.6 \pm 0.5) \times 10^{-5}$	$(3.17 \pm 0.33) \times 10^{-8}$
V	(481.8 ± 0.2)	(0.02044 ± 0.00026)	—

Lattice Parameters

The orthorhombic lattice constants as functions of temperature are presented in Figure 7.3. The values were reduced by dividing the constants by the room temperature value, allowing comparison of all parameters. The expansion of the lattice is anisotropic and the variation of the constants between room temperature and 1073 K were satisfactorily described using a parabolic equation: $y(T) = \alpha_2 T^2 + \alpha_1 T + \alpha_0$. The results of the fitting with the polynomials are presented in Table 7.1 and plotted in Figure 7.3 as solid lines. The expansion reaches 1.6 % which is comparable with metals such as nickel or copper in the same temperature range. The expansion along the b axis slows down with temperature. Above 1073 K all three axes expand more rapidly. The unit cell volume of $Sr_2Fe_2O_5$ as a function of temperature is presented in Figure 7.4. Surprisingly, the different rates of expansion of the unit cell edges yield a linear increase of the orthorhombic unit cell volume between room temperature and 1073 K. For this range it is possible to calculate the volume thermal expansion coefficient:

$$\alpha \equiv \frac{1}{V}\left(\frac{\partial V}{\partial T}\right)_p \tag{7.1}$$

using a linear approximation. The result is shown in Figure 7.5, its value decreases with temperature but above 1073 K it is expected to increase however, there are not enough points to calculate the derivative. The volume thermal expansion coefficient can be useful for thermodynamical calculations such as evaluation of the entropy changes $(\frac{\partial S}{\partial p})_T = V\alpha$ and comparing the thermal expansion among different phases of the ferrite.

The values of the orthorhombic lattice parameters depart from the fitted parabolas above 1073 K (see Figure 7.3) and this departure coincides with the temperature range of the transition peak found at 1140 K. The departure

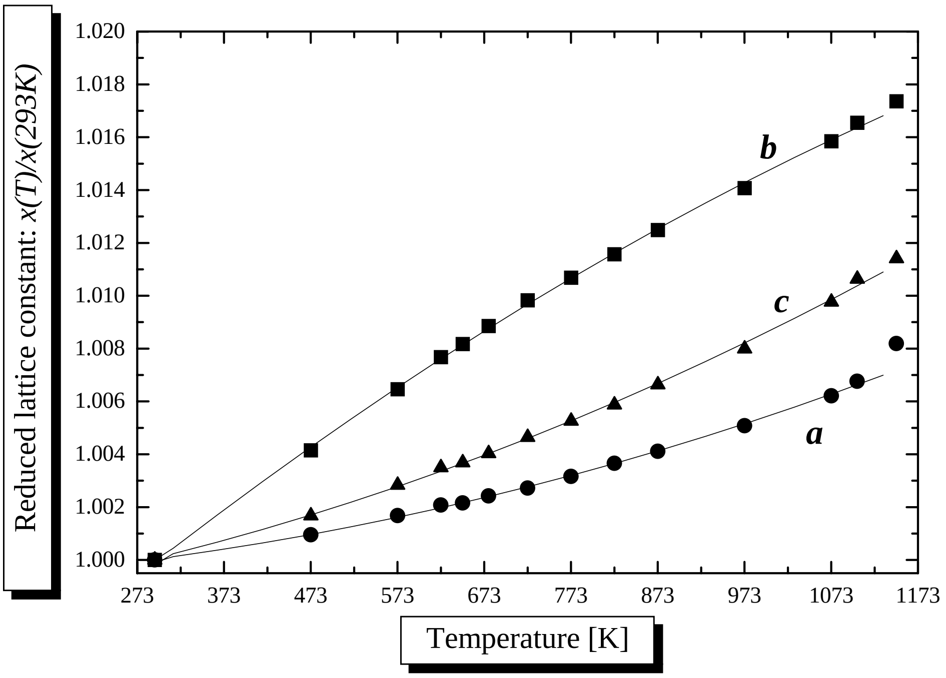

Figure 7.3: Reduced orthorhombic lattice constants of $Sr_2Fe_2O_5$ as a function of temperature. The solid lines represent a polynomial fit as described in the text

indicates that the second transition in $Sr_2Fe_2O_5$ spans over wide range of temperature (approximately 100 K). This behaviour excludes the possibility of the transition being of the first order and is even more obvious from plot of the unit cell volume as a function of temperature (Figure 7.4). It should be noted that the volume before the transformation (at 1073 K) is almost equal to the volume of the cubic cell just after the transition (at 1173 K).

The increase of the lattice constants and volume with temperature is consistent with observations by Takeda *et al.* [127] and Grenier *et al.* [138]. However, they do not provide an analytical description of the changes so it is difficult to make a detailed comparison.

Atomic Layout of the Orthorhombic Phase

The refinement of the orthorhombic $Sr_2Fe_2O_5$ structure was conducted simultaneously with the magnetic component using *Ib′m′2* Shubnikov group and *Ibm2* group above the Néel point. The choice of the magnetic group will be described in the next section. It is the first Rietveld analysis of $Sr_2Fe_2O_5$ at elevated temperatures. Previously the refinement was only carried out at 4.2 K by Greaves *et al.* [160] using *Icmm, Ibm2* and *Pcmn* symmetry

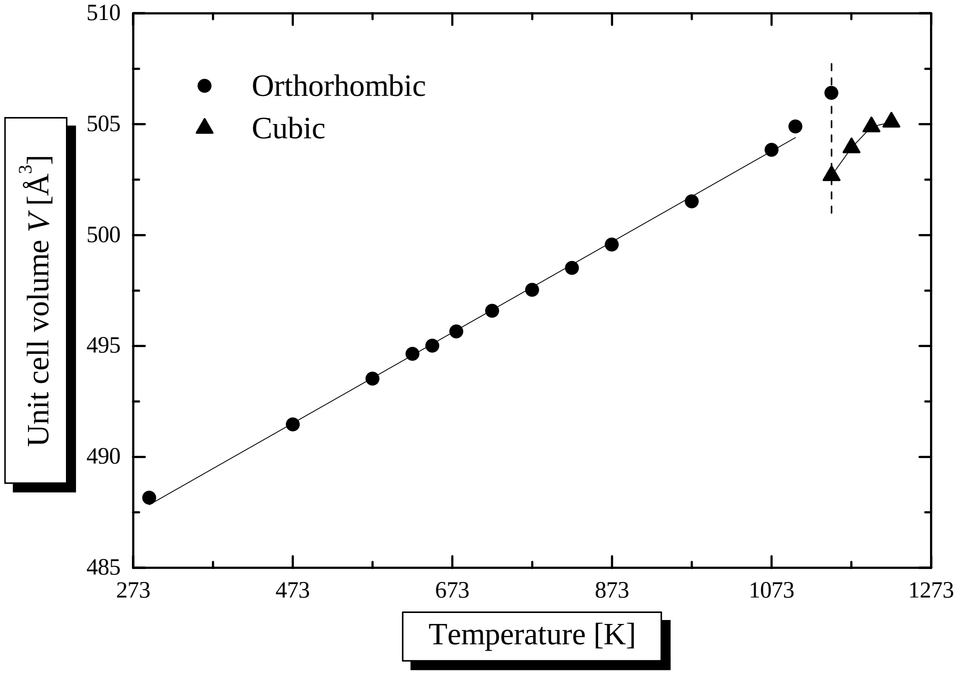

Figure 7.4: Unit cell volume of $Sr_2Fe_2O_5$ as a function of temperature. The solid line represents the linear fit described in the text, the dashed line indicates a two phase sample. The unit cell volume of cubic $Sr_2Fe_2O_5$ was calculated using the new structural model described in section 7.2.3.

groups. However, the *Ibm2* group was assigned to the material as a result of x-ray single crystal diffraction experiments reported by Harder and Müller-Buschbaum [161]. The initial positions of atoms were taken from this work and the refinement was carried out assuming isotropic thermal vibrations of atoms. This is of course a simplification, but it seems that reliable values of the anisotropic thermal coefficients can only be found by analysing larger data sets originating from time-of-flight neutron spectrometers. The structure in this symmetry group is ordered and all sites are fully occupied, the refinable atom coordinates are presented in Table 7.2.

The results of refinements are presented in Table A.1 and Table A.2 for the antiferromagnetic and the paramagnetic state respectively. Examples of refined patterns below and above the Néel point are presented in Figure 7.6. The most conspicuous feature in the figure is disappearance of the magnetic reflections. The refined reduced coordinates of atoms are similar to the initial single crystal values and do not change significantly with temperature. The only difference is that the z coordinate of O(2) is virtually zero. The values of the thermal parameters increase with temperature and the thermal

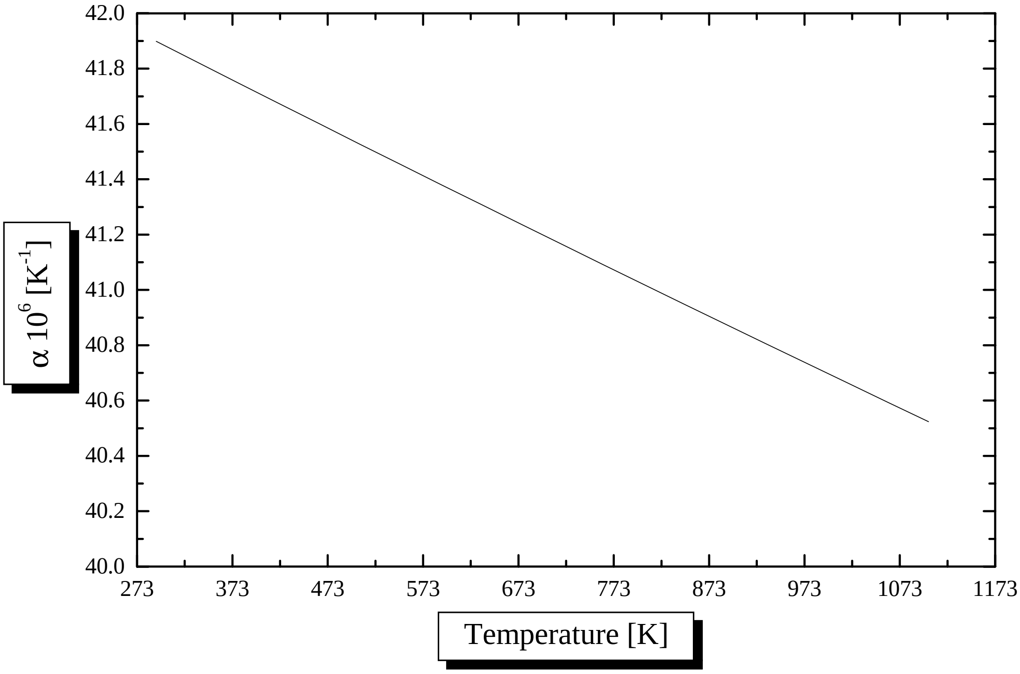

Figure 7.5: Volume thermal expansion coefficient of orthorhombic $Sr_2Fe_2O_5$ as a function of temperature.

vibrations of iron Fe(2) and oxygen O(3) are found to be abnormally high compared with the vibration of other atoms, as previously reported [160]. The increased thermal displacement of Fe(2) and O(3) becomes less significant as temperature increases. This is an indication of the short range disorder in the structure which was also observed in the Mössbauer spectrum (see section 5.2).

The distribution of atoms in the crystal structure is shown in Figure 7.15 and will be discussed fully in section 7.2.4. This figure also allows to envisage bonds and angles between the bonds described below.

Table 7.2: Coordinates of atoms in the orthorhombic unit cell of $Sr_2Fe_2O_5$ varied during the refinement. (S.G. *Ibm2*, r = refined)

Atom	Wyckoff notation	x	y	z
Sr	8c	r	r	r
Fe(1)	4a	0	0	0
Fe(2)	4b	r	0.25	r
O(1)	8c	r	r	r
O(2)	8c	r	r	r
O(3)	4b	r	0.25	r

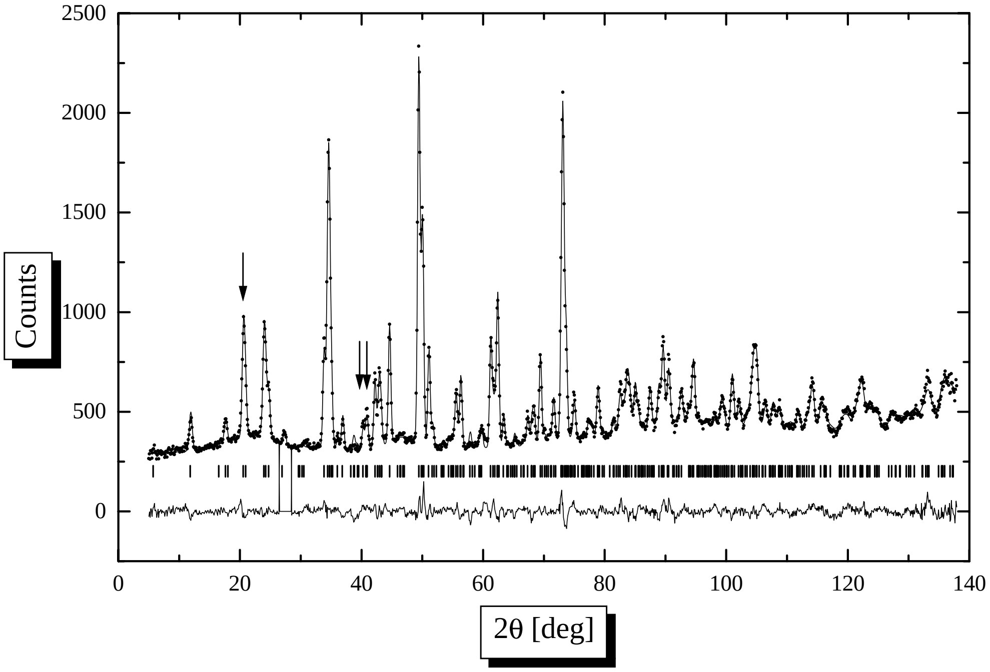

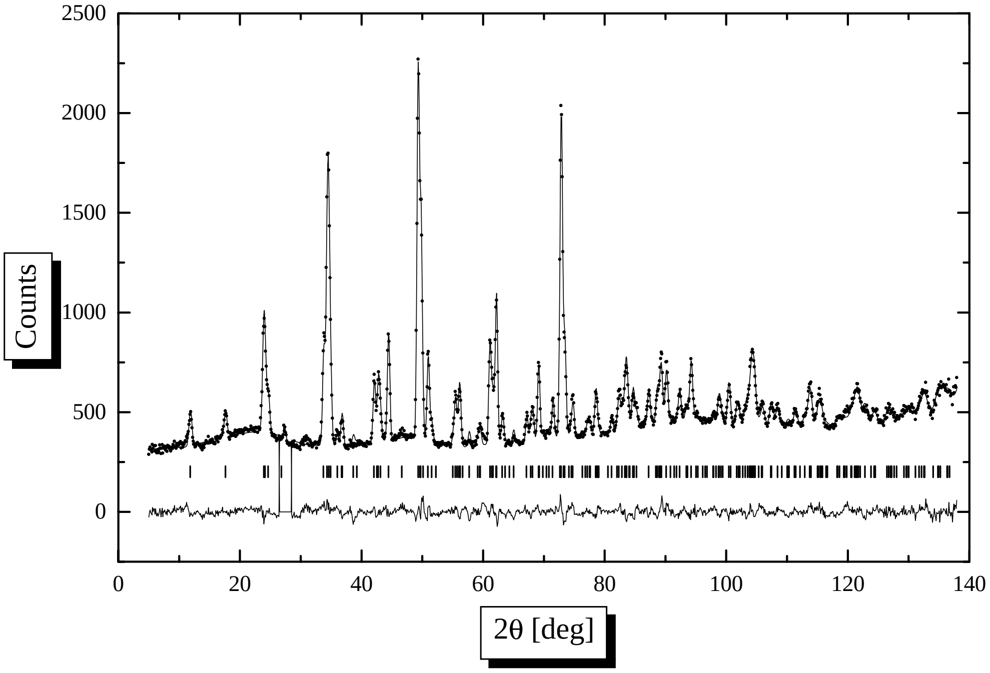

Figure 7.6: Examples of refined neutron diffraction patterns of $Sr_2Fe_2O_5$ collected below (the top spectrum) and above (the bottom spectrum) the Néel point at temperatures of 573 K and 773 K respectively. The arrows show the positions of three strongest magnetic reflections. The short vertical strokes represent positions of Bragg reflections and the long vertical lines mark the excluded region. The line at the bottom of the graphs represents the difference between the observed and the calculated intensities.

The iron atoms have two different surroundings with iron Fe(1) octahedrally and Fe(2) tetrahedrally coordinated. The values of the Fe(1) bond lengths and angles are presented in Table A.3. Since, oxygen O(1) does not lie in the same plane with iron Fe(1) the resulting octahedra are distorted. Also the non-zero x coordinate of oxygen O(2) causes the octahedron (Fe(1)-O(2) bond) to tilt in the ab plane. The calculated tilt angle decreases with temperature from 7.4° at room temperature to 7° at 1073 K. The neighbouring rows of octahedrons along the c axis are tilted in the opposite direction. The structure of $Sr_2Fe_2O_5$ constructed from the tetrahedra and octahedra is presented in Figure 7.7 and presents the view along c axis and clearly shows the tilt. The lengths of Fe(1)-O(1) bonds do not change and only the Fe(1)-O(2) distance visibly increases with temperature. Also small changes in the octahedral angles are noticeable.

The tetrahedral surrounding of iron Fe(2) is created by oxygens O(2) and O(3). The obtuse angles and bonds are presented in Table A.4. Oxygen atoms do not form an ideal tetrahedron. The lengths of both Fe(2)-O(2) bonds are equal and constant and only one of Fe(2)-O(3) bonds and the O(2)-Fe(2)-O(2) angle increase with temperature.

Just for the sake of completeness the bond lengths of the strontium polyhedra are presented in Table A.5, it is formed by oxygen atoms closest to the Sr^{2+} cation.

The Magnetic Structure

Neutron diffraction is sensitive to the magnetic order in the sample and this information had to be taken into consideration. Investigation of the magnetic structure is hampered by the fast decay of the magnetic form factor with scattering angle and the fact that we can only observe three reasonably strong magnetic reflections. A thorough study of this structure should employ longer neutron wavelengths which allow separation of the overlapping magnetic reflections.

The magnetic reflections were generated simultaneously with the nuclear peaks using a Shubnikov group derived from *Ibm2* symmetry group. The Shubnikov groups are extension of 230 space groups by addition of the time inversion operator. The new symmetry element results in 1651 dichromatic groups which can be used in description of magnetic structures [162, 163]. The magnetic *Ib′m′2* group was selected on the basis of the best fit to the observed intensities. This group constrains the magnetic moment of the

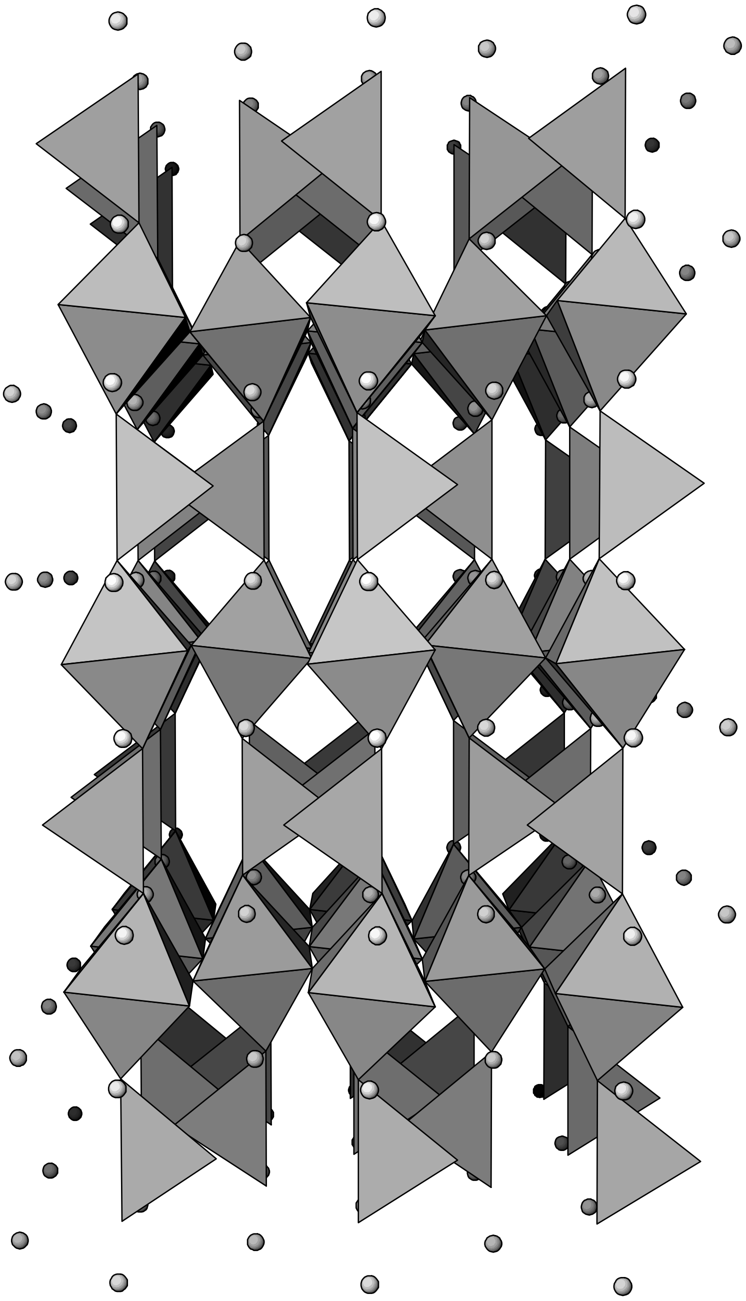

Figure 7.7: A view of the $Sr_2Fe_2O_5$ structure along the orthorhombic c axis ($[00\bar{1}]$ direction) drawn using polyhedra. The a axis is horizontal and lies in plane, the spheres represent strontium atoms.

octahedral iron Fe(1) along the c axis and allows the magnetic moment of the tetrahedral iron Fe(2) to assume any direction in the ac plane. But, the tetrahedral moment was constrained along the c axis too because any attempts to refine the component along the a axis led to rapid divergence of the refinement. The resulting magnetic model is the same as used in the previous investigations of the structure at low temperatures [160, 164]. So in the model the spins of two iron species are antiparallel and are aligned along the c axis. The neighbouring layers of iron atoms along the b axis have opposite magnetization.

However, analysis of the magnetic structure at elevated temperatures is cramped by the decreasing value of the antiferromagnetic coupling which manifests itself as a decaying magnetic moment. The resulting weak magnetic reflections can yield corrupted results. So, the refinement was stabilized by an additional constraint: $m_z(\mathrm{Fe}(2)) = -m_z(\mathrm{Fe}(1))$. It assures zero net magnetic moment of the structure and can be introduced since the magnetic susceptibility measurements [29,138] and magnetization measurements using a vibrating sample magnetometer (VSM), did not show any net magnetic moment in the absence of an external field. The values of the refined magnetic moment as a function of temperature are presented in Figure 7.8. The moment decreases as the temperature approaches the Néel point. However, the ordering temperature found using the calorimeter ($T_c = 622\,\mathrm{K}$) is underestimated and the long range magnetic order vanishes at slightly higher temperature. The neutron measurements give the true value of the transition point since the method is sensitive to the magnetic structure and the calorimeter can also pick up heat changes caused by other phenomena preceding the transition. The diffraction data does not allow establishment of the temperature by a simple extrapolation. Molecular-field theory shows, that in the vicinity of the critical temperature T_N the moment should tend to zero with temperature like $(T_N - T)^\beta$ as $T \rightarrow T_N$, where $\beta = 1/2$, more sophisticated theories and other experimental results indicate that $\beta \simeq 1/3$ [87]. So the magnetic moment as a function of temperature close to the Néel point should vary according to the equation:

$$m_z = A(T_N - T)^\beta \tag{7.2}$$

where, A is a constant. The value of the critical temperature T_N and the

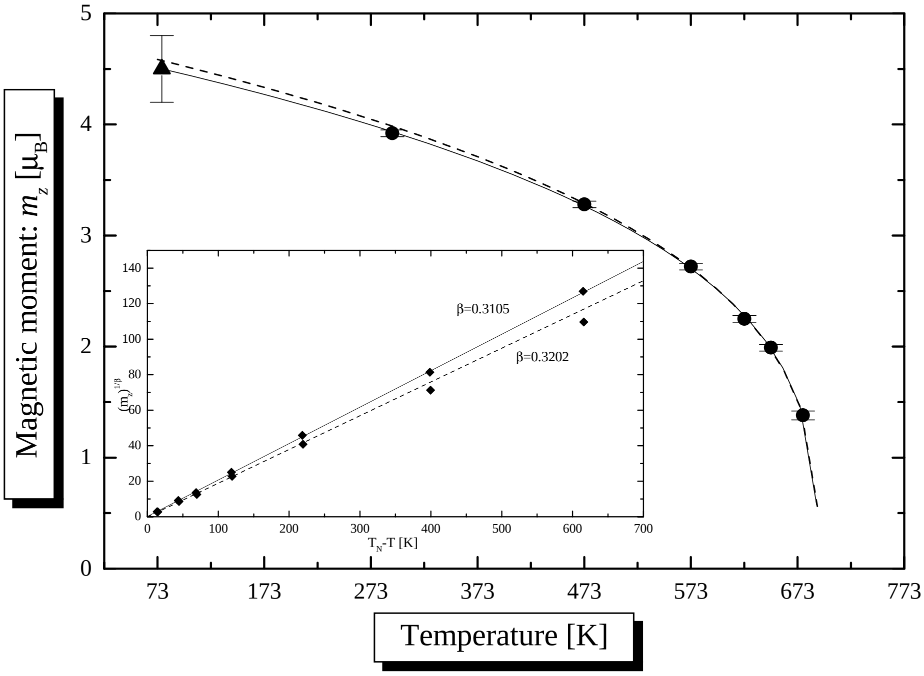

Figure 7.8: The refined magnetic moment of iron in the antiferromagnetic $Sr_2Fe_2O_5$ as a function of temperature. The circles denote the present experimental results and the error bars show the standard deviation. The triangle marks the value found by Takeda *et al.* [164], its error bar denotes the absolute error. The lines show results of fitting described in the text. The inset shows the same results in the linear form.

critical index β were found by a non-linear fitting of the equation:

$$\ln m_z = \beta \ln(T_N - T) + \ln A \tag{7.3}$$

The results vary depending how many points were used for the calculations. We should bear in mind that this approximation works only close to the critical temperature. Fitting of all six points yields the result shown as the solid line in Figure 7.8, it also contains the value of magnetic moment at 77 K found by Takeda *et al.* [164]. However, this point was not used for the calculations and is there for the reference only. The same curve was drawn as a straight line in the inset by recalculating the data using the equation:

$$(m_z)^{1/\beta} = B(T_N - T) \tag{7.4}$$

where B is a constant. It gives an almost perfect fit and $\beta = 0.3105$, $T_N = 691.8$ K. This result is not physically possible because the derivative $\partial m_z/\partial T$ should tend to zero as temperature approaches 0 K. Simple calculation of the temperature derivative of Equation (7.2) shows that it is negative at 0 K. In other words the moment should saturate and the points at lower temperatures ought to lie below the calculated curve. The values of the critical temperature and the critical index, obtained from the six point fit, should be treated as the low limit of the real values. From the physical point of view the best solution is obtained by fitting the curve to four points closest to the transition temperature. It yields, $\beta = 0.3202$, $T_N = 692.8\,\mathrm{K}$ and the fit is presented in Figure 7.8 as the dashed line. The the new value of the Néel point is very close to the number obtained by the six point fit and the low temperature points lie under the curve. More precise determination of the temperature and the critical index require collection of more experimental points in the direct proximity of the transition point and the values just presented should be seen as the best result that can be obtained from a fairly small data set. The long range magnetic order vanishes at 692.8 K however, some residual short range ordering remains and manifests itself as a small diffused peak around 30.9° which persists until the structure changes into the cubic.

The Cubic Phase

$Sr_2Fe_2O_5$ transforms into a cubic form above 1148 K. This phase was reported for the first time by Tofield *et al.* [126] and investigated by other groups [127, 138, 159]. By analogy to the fully oxidized, cubic perovskite $SrFeO_3$ the cubic form of $Sr_2Fe_2O_5$ was regarded as an oxygen deficient perovskite. Shin *et al.* [159,165] reported a lattice constant of 3.982 Å at 1173 K and the symmetry group *Pm3m* with disordered oxygen sites. Indeed, the diffraction patterns can be indexed as the primitive cells and the Mössbauer measurements indicate the disorder in the oxygen sites (see section 5.5). However, this choice of a unit cell creates a lot of problems.

One of the problems created by the perovskite model is a density of material calculated using a unit cell volume obtained from diffraction. If we assume that the unit cell contains only one chemical formula (molecule) of the oxide ($Sr_2Fe_2O_5$), this choice of the unit cell gives unreasonable high density $\varrho = 9.65\,\mathrm{g/cm^3}$. The calculated value is almost twice the density of the material at room temperature. Moreover, it is impossible to accommodate a nine-atom molecule in the cell and get the perovskite structure. A reasonable value of density was obtained by Shin *et al.* [165] but on the assumption that the unit cell contains only half of the chemical formula $Z = 0.5$ ($SrFeO_{2.5}$). This assumption clearly indicates that the perovskite choice is inadequate

Table 7.3: Coordinates of atoms in the cubic unit cell of $Sr_2Fe_2O_5$ used for the Rietveld refinement. Symmetry group: *Fm3c* (226), *Z*=4.

Atom	Wyckoff notation	x	y	z	Site occupancy
Sr	8a	0.25	0.25	0.25	1.0
Fe	8b	0	0	0	1.0
O	24c	0.25	0	0	20/24

and the unit cell is too small. However, some researchers are very fond of the oxygen deficient perovskite model and its disadvantages will be discussed in more detail.

If we assume that the cubic $Sr_2Fe_2O_5$ is described by the oxygen deficient perovskite model the content of the unit cell has the composition $SrFeO_{2.5}$. Since we can not have fractions of atoms the entire crystal lattice consists of two kinds of building blocks with compositions $SrFeO_3$ and $SrFeO_2$. There are equal fractions of these two cells and they yield the average composition of $SrFeO_{2.5}$. The existence of two different building blocks already contradicts the perovskite being the proper unit cell. Moreover, since $Sr_2Fe_2O_5$ contains only the trivalent iron the blocks are oppositely charged. An electrically neutral cell is a combination of $SrFeO_3$ and $SrFeO_2$ blocks however, it produces a tetragonal cell which is not observed in the scattering experiments. But combination of four blocks of each kind yields a cube.

The new cell was produced by doubling of the perovskite lattice constant. This cell has eight times greater volume and if we assume that it contains four chemical formulas ($Z = 4$) the calculated density yields the sensible value of $4.83\,g/cm^3$. As the result the primitive Miller indexes (hkl) are multiplied by two and give a new set of conditions for the observed reflections: *hkl:* $h+k, k+l, l+h = 2n$; *hhl:* $h, l = 2n$; *0kl:* $k, l = 2n$, they are fulfilled by the *Fm3c* (226) symmetry group. The Mössbauer results presented in section 5.5 indicated only one iron site in cubic $Sr_2Fe_2O_5$ which implies disordered oxygen sites. The atoms were placed in the special positions of the group as outlined in Table 7.3. The proposed unit cell consists of eight adjacent perovskite-like blocks. The iron ions are situated in the octahedral sites, however, statistically four of them have one oxygen missing. The positions of the atoms in the cell are fixed by the spacegroup and were not refined. The oxygen atoms in this arrangement are randomly distributed among the 24 available sites.

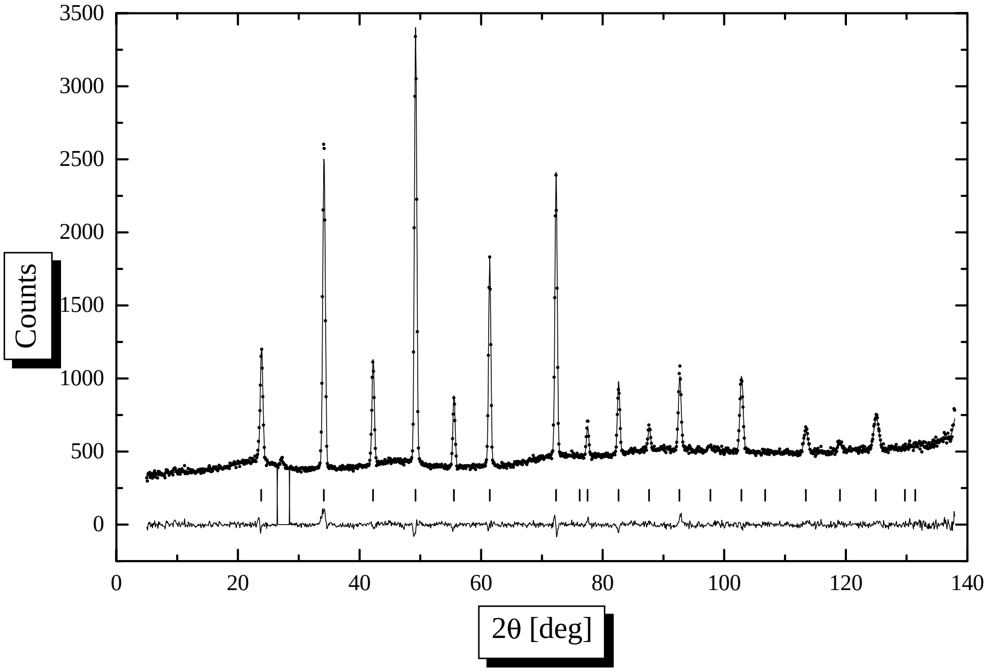

Figure 7.9: The refined neutron diffraction pattern of cubic $Sr_2Fe_2O_5$ at 1223 K.

The refinement was carried out with fixed site occupancy and the only variable parameters were the lattice constant and the anisotropic temperature factors u_{ij}. At the end of the refinement the occupancy factor for the oxygen was refined, it lead to convergence, however it did not significantly improved the fit. The refined occupancy value corresponded to approximately 19.66 oxygen atoms per unit cell. This implies that the oxide may contain significant amount (8.5 %) of iron in the 2+ oxidation state. The ferrite was tested for the presence of the ferrous ion using o-Phenanthroline as described on page 96. The test did not show the presence of the Fe^{2+}, so the oxygen occupancy was set back to the initial value of 20/24 and kept fixed. The results of the refinement at different temperatures are presented in Table A.6 and the example of the refined pattern in Figure 7.9. The off-diagonal elements $u_{ij}, i \neq j$ are zero because of the symmetry conditions and for the same reason the diagonal temperature elements $u_{11} = u_{22} = u_{33} = u_{ii}$ of strontium and iron ions respectively are equal. In effect strontium and iron vibrate isotropically and only the thermal movement of the oxygen ions is anisotropic. The $u_{\parallel} = u_{11}$ coefficient corresponds to the movement of oxygen along the [100] direction between two iron ions. The $u_{\perp} = u_{22} = u_{33}$ coefficient depicts the oxygen motion in the perpendicular (400) plane. The thermal motion

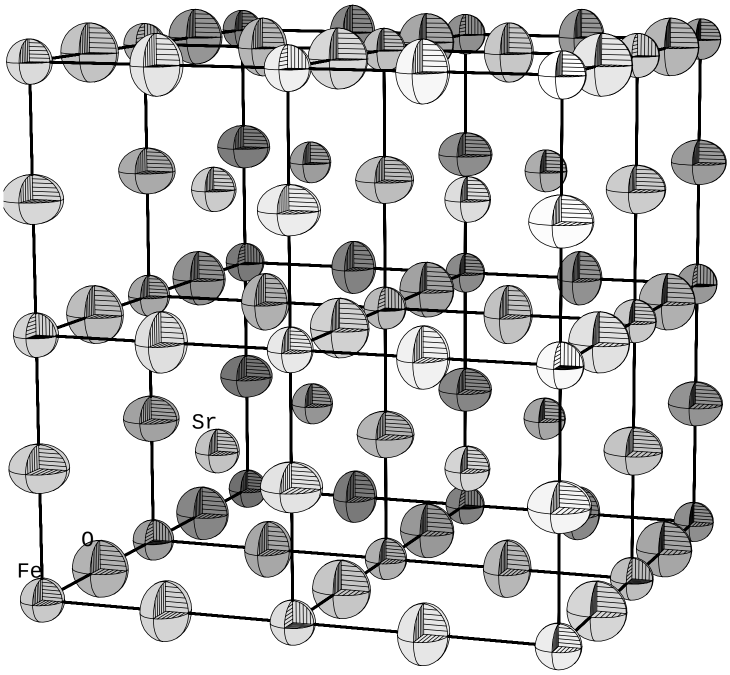

Figure 7.10: Thermal motion of atoms in the cubic unit cell of $Sr_2Fe_2O_5$ at 1223 K as discussed in the text. The ellipsoids represent 50 % probability surfaces.

of atoms in the unit cell is presented in Figure 7.10 using ellipsoids. In the picture all the oxygen sites are occupied and the oxygen and iron atoms are connected using straight lines. They visualize the 'Fe-O bonds', however, the oxide forms an ionic crystal, at least an ionic mechanism seems to dominate, and the bonds should be treated as a guide for eye. The strontium ions are presented as unconnected spheres. All the anisotropic temperature factors increase with temperature and the vibrations of the strontium and iron ions are comparable in magnitude and much smaller than the thermal motion of the oxygen. However oxygens' thermal displacement between neighbouring irons is significantly smaller than the vibrations in the perpendicular direction. The large thermal displacement of oxygen within the (400) plane is possible since it contains the vacant oxygen sites. The temperature dependence of the cubic lattice constant is presented in Figure 7.11, it increases with temperature and the increase rate seems to decrease with temperature, however, more experimental points are needed to confirm this trend.

Since the positions of atoms are fixed by symmetry the angles between the bonds are constant and the bonds (interatomic distances) are linked to the lattice constant a by the simple geometrical relations outlined in Table 7.4.

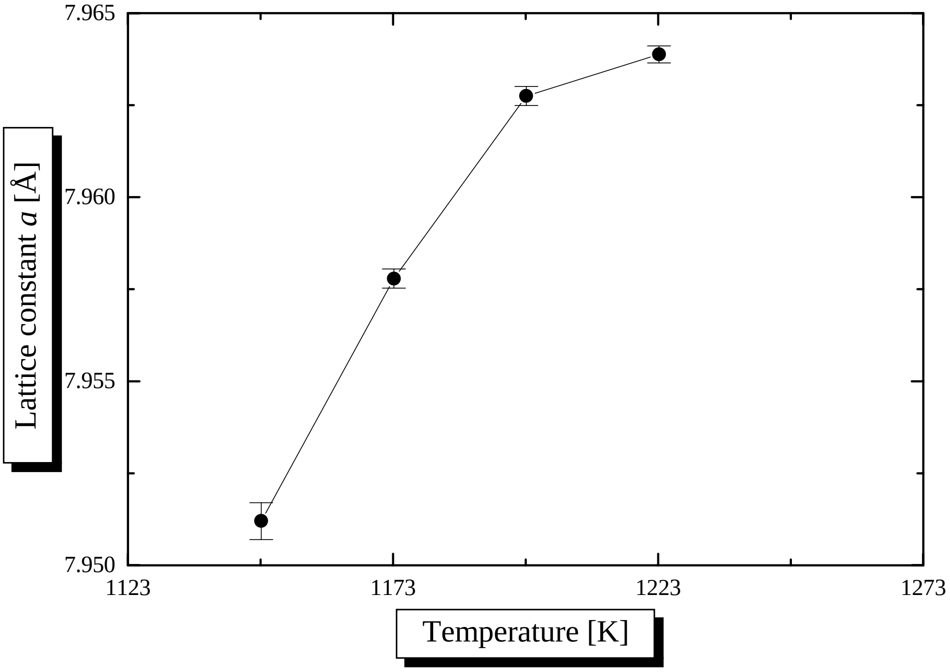

Figure 7.11: The cubic lattice constant of $Sr_2Fe_2O_5$ as a function of temperature.

Table 7.4: Bond lengths (interatomic distances) in the cubic form of $Sr_2Fe_2O_5$ as a function of the lattice constant a.

Bond	Length
Fe-O	$a/4$
O-O	$a\sqrt{2}/4$
Fe-Sr	$a\sqrt{3}/4$
O-Sr	$a\sqrt{2}/4$

The structure was refined in *Fm3c* symmetry however, it is possible to refine the structure in the improper *Pm3m* symmetry group with primitive lattice constant using the parameters outlined in Table 7.5. The refinement converges and yields the same results since the face-centered cell consists of perovskite blocks and is mimicked by the less symmetrical *Pm3m* group. It should be recalled that every high symmetry structure can be expressed in terms of a primitive less symmetrical cell.

The perovskite model is not the only one developed to describe cubic $Sr_2Fe_2O_5$. The disordered perovskite approach was also questioned by Grenier *et al.* [138], but for completely different reasons than crystallographical density, who examined the behaviour of brownmillerite compounds ($A_2Fe_2O_5$, A= Ca, Sr) doped with either a transition metal or a trivalent

Table 7.5: Coordinates of atoms in the unit cell used for the refinement of cubic $Sr_2Fe_2O_5$ in the *Pm3m* symmetry group.

Atom	Wyckoff notation	x	y	z	Site occupancy
Sr	1b	0.5	0.5	0.5	1.0
Fe	1a	0	0	0	1.0
O	3d	0.5	0	0	5/6

lanthanide such as: $Sr_{0.8}Nd_{0.2}FeO_{2.6}$ [166], $La_{1-x}Ca_xFeO_{3-y}$ $(2/3 \leq x \leq 1; 0.25 \leq y \leq 0.40)$ [167], $CaFe_xMn_{1-x}O_{3-y}$ [168], $Ca_2LaFe_3O_{8+z}$ [169] and $SrFe_{1-x}V_xO_{2.5+x}$ [170]. These compounds undergo a similar phase transition to a cubic form and their high-resolution transmission electron microscope (HRTEM) study of quenched samples revealed the existence of microdomain structures containing orthorhombic brownmillerite and giving cubic x-ray diffraction patterns as the result. The model proposes the same mechanism for pure brownmillerite $Sr_2Fe_2O_5$ however, Grenier *et al.* [138] did not provide any experimental evidence to support the claim and close analysis of the reports reveals several important differences between $Sr_2Fe_2O_5$ and the doped compounds. Firstly the domains are present only if the material is doped with tetravalent or pentavalent metal such as Mn^{4+} or V^{5+}. If the lanthanide constitutes the impurity the domain structure is observed only if part of iron is tetravalent or the lanthanide is present in large concentration. Their x-ray diffraction patterns have cubic symmetry but exhibit signs of a superstructure such as broadened or diffused reflections. Papers dealing with high temperature cubic $Sr_2Fe_2O_5$ do not report such anomalies in x-ray diffraction spectra [127, 138, 147, 159] and both Grenier *et al.* [138] and Takano *et al.* [147] examined the spectra thoroughly in order to confirm the microdomain model. The present author did not observed any signs of superstructure in the neutron patterns either despite oxygen having scattering power comparable with strontium and structural features involving oxygen would be much more pronounced than in the case of x-ray experiments. Also, high temperature Mössbauer measurements failed to provide a conclusive evidence for the microdomain structure [147]. The last difference is that when doped samples were slowly cooled below the transition temperature they decomposed into two or three phase mixtures while $Sr_2Fe_2O_5$ remains a single phase, Nakayama *et al.* [170] concluded that the microdomain structure observed with the HRTEM is in fact a quenched early stage of phase separation.

In conclusion, the experimental evidence known so far cannot support the microdomain model for the cubic $Sr_2Fe_2O_5$.

7.2.4 Transition to the Cubic Form

The energy of phase transition in $Sr_2Fe_2O_5$ at 1140 K lead Takada *et al.* [127] and Grenier *et al.* [138] to claim it was first order. However, this transformation is not first order as already discussed in section 4.2.3. Additionally with the new unit cell model the difference in the volume of the cell before and after the transformation is only $V(1173K) - V(1073K) = 0.098\text{Å}^3$ and can be accounted for by the thermal expansion of the material. So the transformation is not the main cause of the volume change, a characteristic of a first order transitions [122].

The diffraction pattern collected at 1148 K, just above the peak of on the DTA trace of $Sr_2Fe_2O_5$ (see Figure 4.9), is presented in Figure 7.12 and contains both cubic and orthorhombic phases. The presence of the cubic phase is not obvious at first but this conclusion can be drawn after careful examination of the relative peak intensities and comparison with the single phase patterns (Figure 7.6 and Figure 7.9). The material had been kept at this temperature for 15 min before the measurement so what we are looking at is most likely an equilibrium state. All cubic reflections overlap heavily with the orthorhombic peaks however, the Rietveld method allows us to deal with this situation and the pattern was refined as a two phase spectrum. It yielded the fractions of the cubic $f_c = 0.37$ and the orthorhombic $f_o = 0.63$ phases respectively, due to the heavy overlap the refined parameters are less reliable than for the single phase samples. The volumes of the orthorhombic and cubic cells are different (see Figure 7.4) but they do not cause large changes in the volume of the sample. The weighed average cell volume (average volume occupied by four molecules) is only $f_oV_o + f_cV_c = 505.02\,\text{Å}^3$ which is not far from the volumes of the single phase samples before and after the transformation.

The mechanism of the transformation to the cubic form is actually quite simple with the orthorhombic structure itself containing the distorted cubic cells. The pseudo-cubic cells can be clearly seen if we divide the crystal into identical blocks larger than the unit cell. The division is schematically presented in Figure 7.13, the block has the same height as the b orthorhombic lattice constant and its base is made out by the diagonals of bases of four adjacent orthorhombic cells. The pseudo-cell has twice the volume of the

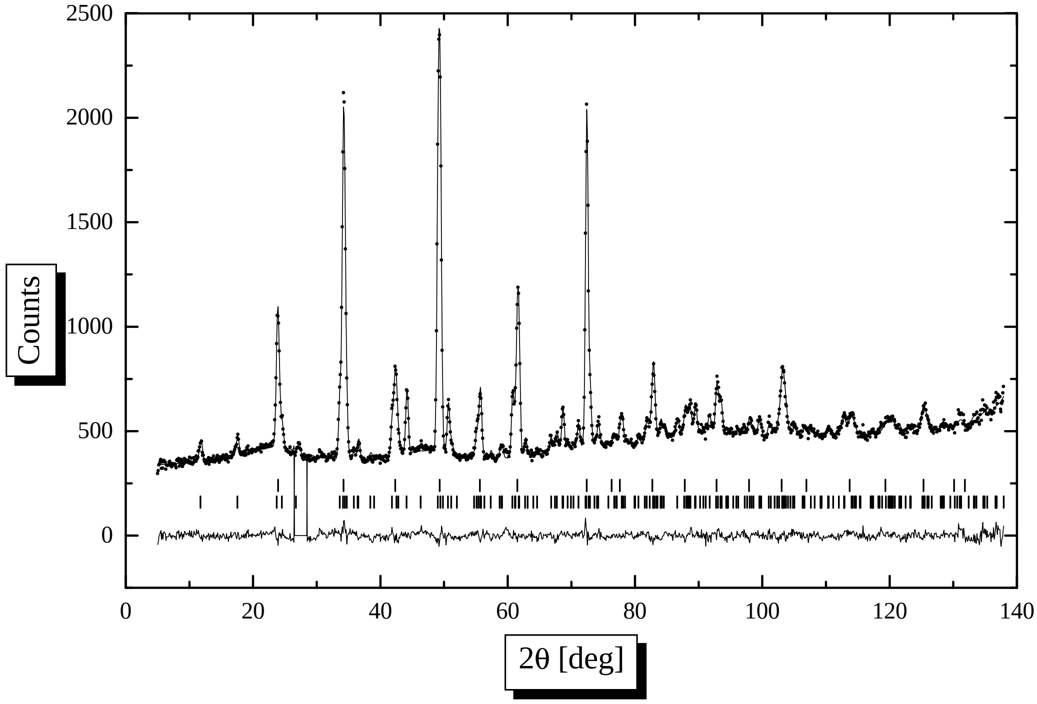

Figure 7.12: The refined two phase neutron diffraction pattern of $Sr_2Fe_2O_5$ at 1148 K. The top and the bottom row of peak markers denote the cubic and the orthorhombic reflections respectively.

orthorhombic unit cell and splits at $y = 1/2$ into two cubic cells upon the transition. Even though the block is larger than the unit cell it has transition symmetry and can fill the entire space. The dimensions and angles between the edges of the block are close to the parameters of the cube. The ratio of the base edge length $\sqrt{a^2 + c^2}$ to the half of the height $b/2$ is close to one and the acute angle of the rhombus base exceeds 88°, it is the acute angle between the diagonals in the base of the orthorhombic cell. The changes of these parameters with temperature are presented in Figure 7.14. The edge ratio slowly decreases with temperatures reaching the value of 1.008 at 1103 K, at the same time the angle approaches the value of 88.76°. The content of the pseudo-cell derived form the refinement results at 1073 K is presented in Figure 7.15. As previously, the iron and oxygen ions are connected and the strontium is shown as unconnected spheres. The block consists of layers of iron in octahedral Fe(1) and tetrahedral Fe(2) sites divided by layers of oxygen O(2). Oxygen O(1) lying slightly off the plane containing the octahedral iron. Oxygen O(3) occupies the planes at $y = 1/4$ and $y = 3/4$. The block can be subdivided into 16 distorted perovskite cells all of which contains strontium in the middle.

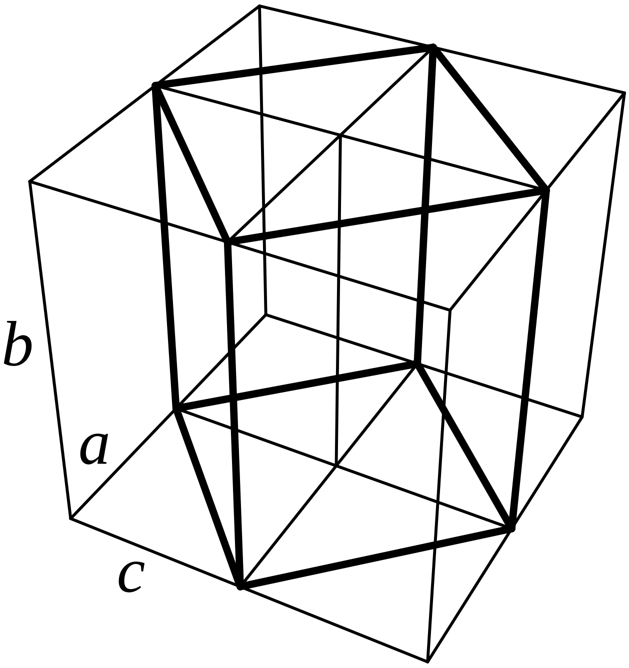

Figure 7.13: A schematic division of the orthorhombic structure of $Sr_2Fe_2O_5$ into blocks containing two distorted cubic cells.

While doing the comparison of Figure 7.10 and Figure 7.15 one should remember that there are 24 fully occupied oxygen sites in the former figure but the latter picture contains only 20 oxygens per cell. This is why there appears to be less oxygen atoms in Figure 7.15. The transition from the orthorhombic to the cubic phase is just a matter of small changes to the positions of atoms.

7.3 Structure of SrFeO$_x$ in Air

The second series of experiments explores the crystal structure of the ferrite in air. Since the composition of the material changes with temperature the data were collected on equilibrated samples and their composition was determined using the thermogravimetric methods presented in Chapter 4.

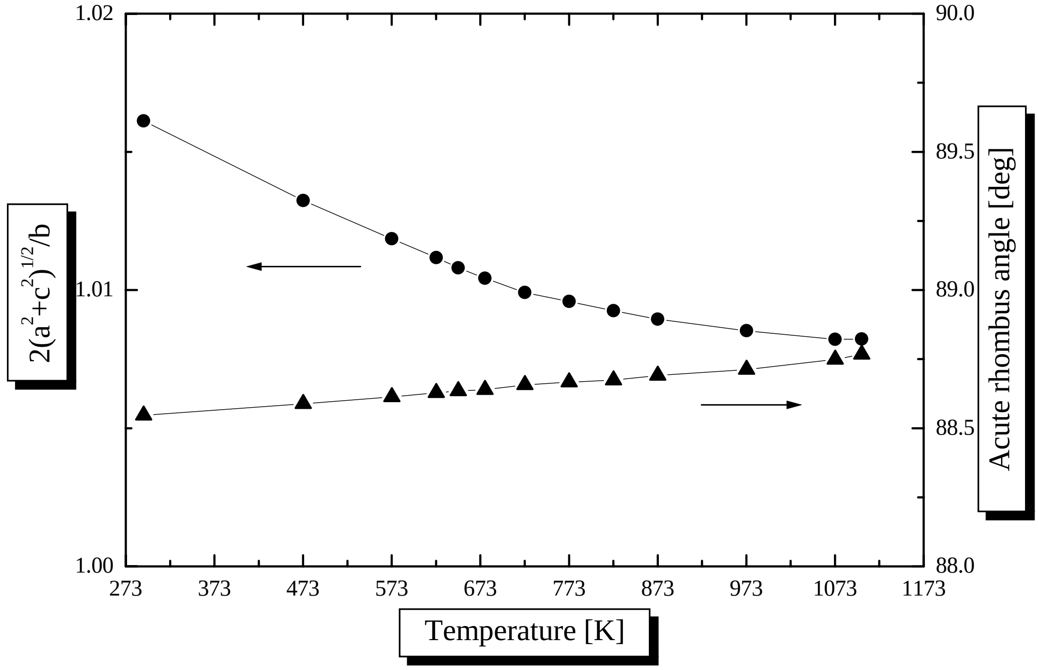

Figure 7.14: The cell edge ratios and angles of the distorted cubic cells of $Sr_2Fe_2O_5$ in the orthorhombic lattice as a function of temperature. The edge ratios and the angles are defined in the text.

7.3.1 Sample Treatment and Analysis Methods

As in previous experiments the sample had the form of sintered pellets. Before measurements the sample was annealed at 673 K in air for 48 h to adjust its oxygen content to $x = 2.81$. Annealing at lower temperatures can increase the oxygen content above this value but the reaction rate is low and equilibration requires several days. The pellets were placed in the furnace without the protective silica tube and to maintain constant oxygen partial pressure an air flow was maintained. The measurements were made between room temperature and 1273 K. The sample was equilibrated with the atmosphere only at 673 K and higher temperatures. The equilibration time was estimated from the TGA measurements and varied from 4 h at 673 K to 0.5 h at 1273 K. Patterns at lower temperatures were collected 15 min after the temperature reached the desired value. The analysis was carried out using the Rietveld method using pseudo-Voigt profiles to model the peaks. However, it was discovered that the Lorentz component in the diffractometer profile is negligibly small and effectively the peaks were modeled with Gauss profiles. The background was simulated using a cosine Fourier series (6 coefficients).

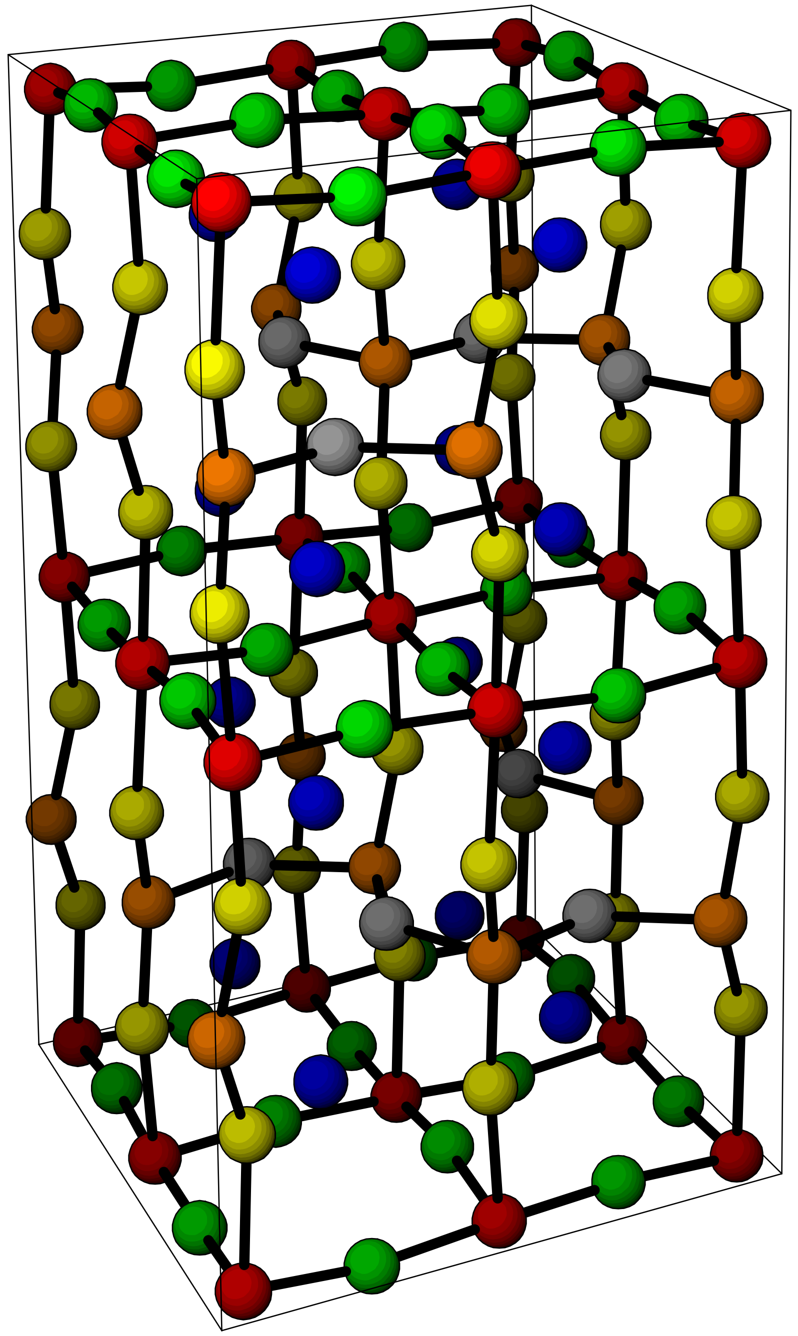

Figure 7.15: Contents of the block obtained by the division of the orthorhombic $Sr_2Fe_2O_5$ lattice using the schematic shown in Figure 7.13. Positions of atoms were derived from the refinement of the neutron diffraction pattern at 1073 K. Atoms in each crystallographic position are marked with different colour: Fe(1) red, Fe(2) orange, O(1) green, O(2) yellow, O(3) gray, Sr blue.

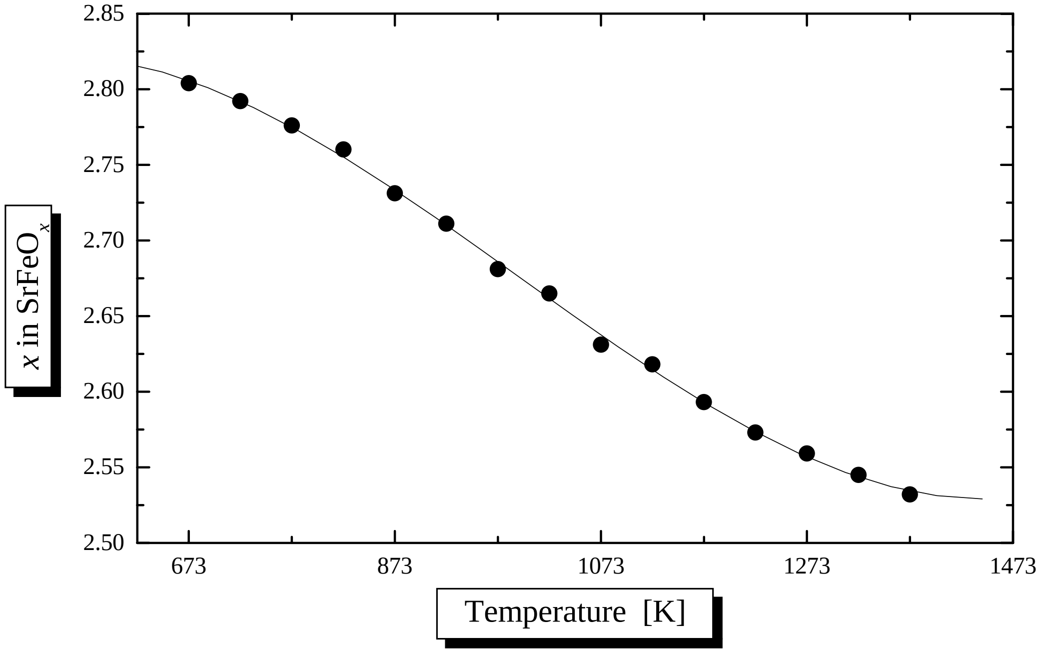

Figure 7.16: The oxygen content of SrFeO$_x$ as a function of temperature in air. The solid line represents the polynomial fit described in the text.

7.3.2 Results of Experiments

The composition of material is temperature dependent and the exact value is crucial for the analysis so the thermogravimetric results for an air atmosphere, presented in Figure 4.2, were fitted with a third order polynomial to obtain the composition as a function of temperature. The experimental points and the polynomial fit is shown in Figure 7.16.

$$x(T) = 8.05 \times 10^{-10}\,T^3 - 2.40 \times 10^{-6}\,T^2 + 0.002\,T + 2.37 \tag{7.5}$$

The oxygen content was calculated by evaluating the polynomial at the temperature of interest.

The results of calorimetric experiments presented in Figure 7.1 indicated that the starting material with composition $x = 2.81$ undergoes a phase transition at 558 K and this was confirmed by the neutron patterns collected at 523 K and 573 K which show a transformation from the low symmetry to the cubic state. All spectra collected above the phase transition have cubic symmetry and apart from small changes in peak positions and intensities do not vary dramatically across the entire temperature range. Also there were no other peaks or diffuse reflections that would indicate the presence of any superstructure (the small peak at $2\theta = 27.4^\circ$ was introduced by the furnace).

Table 7.6: Coordinates of atoms in the unit cell of cubic SrFeO$_x$ used for the Rietveld refinement. Symmetry group: *Fm3c* (226).

Atom	Wyckoff notation	x	y	z	Site occupancy
Sr	8a	0.25	0.25	0.25	1.0
Fe	8b	0	0	0	1.0
O	24c	0.25	0	0	δ

The cubic form of the oxide in oxidizing atmospheres was regarded as the oxygen deficient perovskite [127, 128] as it was in the case of Sr$_2$Fe$_2$O$_5$. However, with the perovskite model we run into similar problems as in the case of Sr$_2$Fe$_2$O$_5$. The diffraction patterns of the cubic SrFeO$_x$ have similar peak intensity ratio as the cubic Sr$_2$Fe$_2$O$_5$ and the Mössbauer results discussed in section 5.5 indicate disordered oxygen sites. The cubic spectra measured in air were refined with structural parameters given in Table 7.6 using the *Fm3c* symmetry group. However, in this case the oxygen site occupancy δ is greater than 20/24 and was calculated from the thermogravimetric measurements using the formula:

$$\delta = x/3 \tag{7.6}$$

The results of the refinement are presented in Table A.7 and an example of the refined pattern in Figure 7.17. The thermal motion of atoms in the unit cell has the same character as in the cubic Sr$_2$Fe$_2$O$_5$, the vibration of strontium and iron is isotropic and the thermal motion of oxygen is again larger within the (400) plane than in the perpendicular direction. The magnitudes of the displacements increase with temperature.

Lattice Constant and Density

The crystal lattice expands with temperature however, the increase is not linear. The temperature dependence of lattice constant is presented in Figure 7.18 and was successfully fitted with a third order polynomial $y(T) = \sum \alpha_n T^n$, obtained coefficients are presented in Table 7.7. The lattice expansion rate has a maximum at 1018 K. The thermal expansion is more complicated since with increasing temperature the system changes its composition. Similar non-linear behaviour was observed by Mizusaki *et al.* [128] but at lower oxygen partial pressure and the lattice constant was reported using

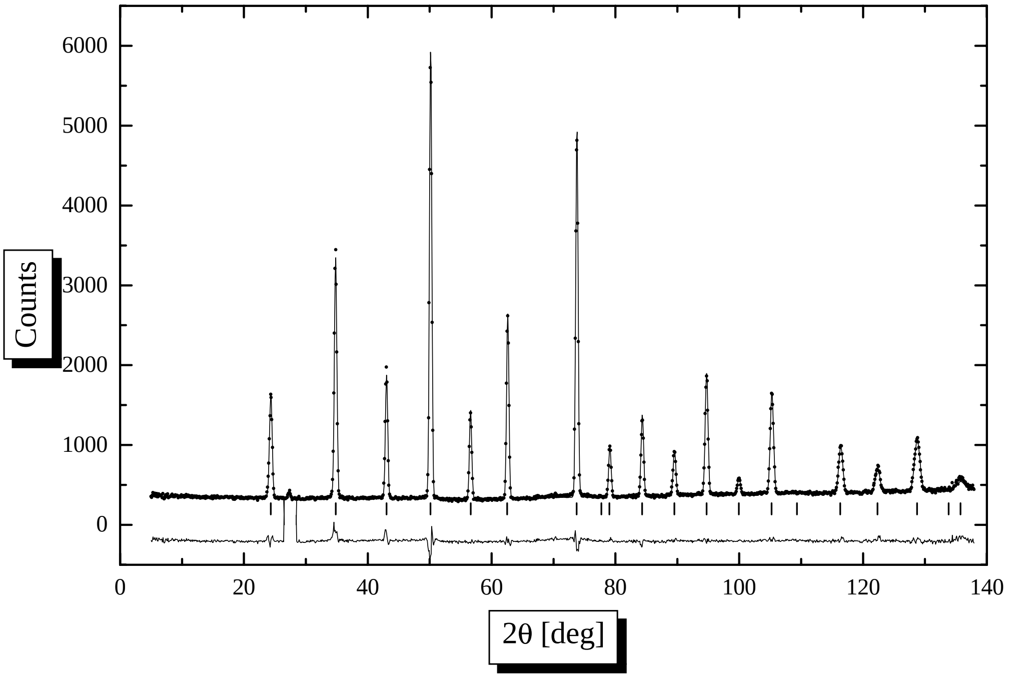

Figure 7.17: The refined neutron diffraction pattern of cubic SrFeO$_x$ at 873 K in air.

the perovskite model which gives the true lattice constant divided by two. The volume thermal expansion coefficient was calculated from Equation (7.1) using the polynomial approximation and is presented in Figure 7.19. The coefficient has a much higher value than for $Sr_2Fe_2O_5$ (Figure 7.5).

The SrFeO$_x$ system in equilibrium with air seems to obey Vegard's law. The plot of the lattice constant as a function of the tetravalent iron fraction yields an almost perfect straight line. The plot is presented in Figure 7.20, the linear correlation coefficient for the fit is equal to -0.99982. The fraction of tetravalent iron was calculated from Equation (5.1).

The thermal expansion and oxygen depletion of the ferrite cause the density to decrease with temperature as presented in Figure 7.23. However, the density of the material in equilibrium with the atmosphere plotted as a function of composition gives the straight line presented in Figure 7.21. The non-equilibrium points at 573 K, 623 K and 648 K depart from the line and are not displayed. The linear fit here is much better than for the lattice constant (Figure 7.20) and the linear correlation coefficient is equal to 0.99995 for the same set of points. The density can be calculated without any knowledge about the actual positions of atoms in the unit cell, so its value is not biased by the structural model other than the number of molecules (chemical

Table 7.7: Polynomial coefficients describing the temperature dependence of the cubic lattice constant and the cell volume of $SrFeO_x$ in air. The polynomials are plotted in Figure 7.18 as solid lines.

Polynomial coefficient	Lattice parameters	
	lattice constant	volume
α_0	(7.93 ± 0.02)	(499.6 ± 3.8)
α_1	$(-7.3 \pm 0.7) \times 10^{-4}$	(-0.136 ± 0.013)
α_2	$(1.02 \pm 0.07) \times 10^{-6}$	$(1.89 \pm 0.14) \times 10^{-4}$
α_3	$(-3.4 \pm 0.3) \times 10^{-10}$	$(-6.1 \pm 0.5) \times 10^{-8}$

formulae) of oxide in the unit cell. The decreasing density with decreasing oxygen content points at an oxygen vacancy formation mechanism [50] and the linear dependence show that the same mechanism applies to the entire investigated composition range ($2.56 \leq x \leq 2.81$). In this sense it is an indirect confirmation of the crystal structure model assuming the presence of disordered oxygen sites. The linear relationship can be used to extrapolate the density and the cubic lattice constant outside of the measured composition range. The better linear fit for the density, as indicated by the linear correlation coefficient, proves that the system slightly departs from Vegard's law and for this reason the density plot was used for calculations.

The linear plots do not provide any information about the equilibrium temperature. But allow the density or lattice constant to be calculated if the equilibrium composition is known at given temperature. It should be remembered that the linear approximation was obtained for air and the slope of the line will most likely change under a different partial pressure of oxygen. However, it is feasible to assume that lines for different p_{O_2} lines will intercept in the same point at $x = 3.0$ or very close to one point since this stoichiometry exists only at relatively low temperature where thermal expansion is small.

The extrapolated values of densities and lattice constants are presented in Table 7.8. Takeda *et al.* [127, 171] reported the perovskite lattice constant of 3.855(3) Å for $SrFeO_{2.97}$ which is very close to the ideal perovskite $SrFeO_3$. The calculated perovskite lattice constant $a_{perovskite} = a/2 = 3.854\,\text{Å}$ obtained by extrapolation of the line in Figure 7.21 to $x = 2.97$ is within experimental error that reported Takeda *et al.*

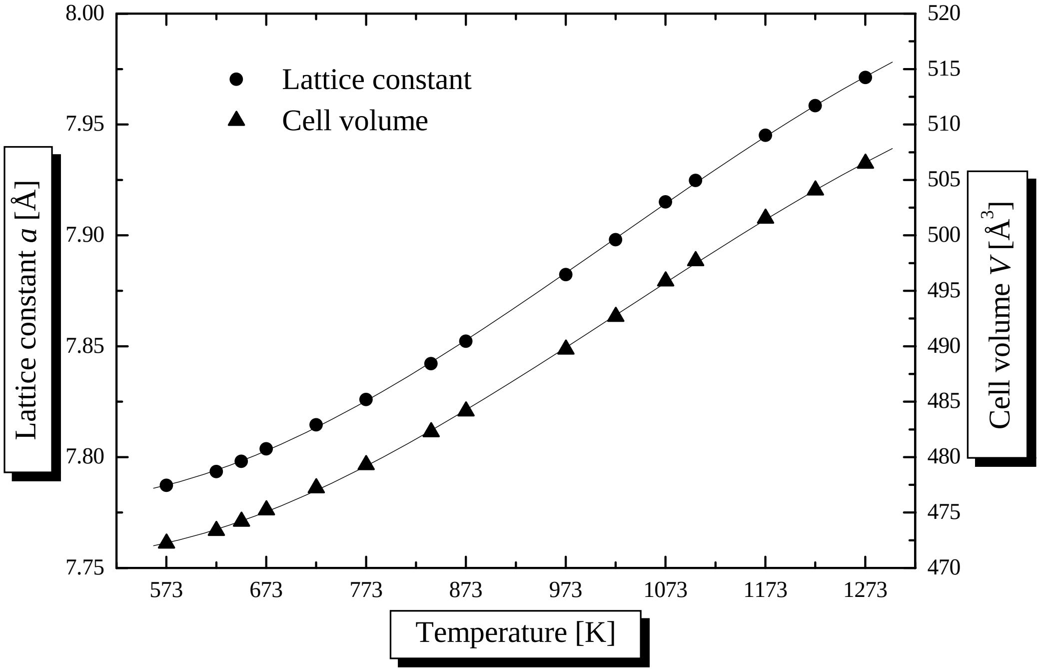

Figure 7.18: The lattice constant and the cell volume of cubic $SrFeO_x$ as a function of temperature in air. The solid lines show the polynomial fits described in the text.

Table 7.8: The extrapolated density and lattice constant of cubic $SrFeO_x$ in the equilibrium with air. The parameters were calculated using the linear fit shown in Figure 7.21.

Composition x	Density ρ [g/cm^3]	Lattice constant a[Å]
2.5	4.74	8.011
3.0	5.59	7.690
2.97	5.54	7.708

7.4 Summary and Conclusions

Even though, only two series of experiments were performed and the coverage of the (T, p_{O_2}) plane is far from complete, there are several general conclusions that can be drawn from this work. They concern the phase behaviour and the mechanical properties of the material.

7.4.1 Nature of the Cubic Phase

The cubic form of $SrFeO_x$ exists over the entire composition range $2.5 \leq x \leq 3.0$ but only fully oxidized material $SrFeO_3$ is stable at room temperature.

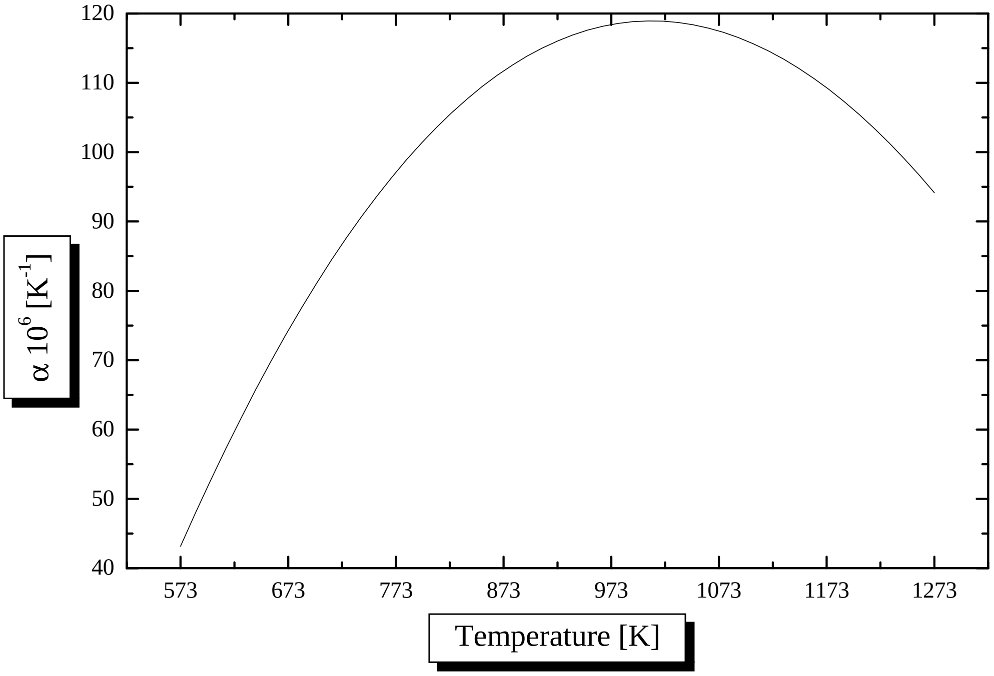

Figure 7.19: The volume thermal expansion coefficient of cubic $SrFeO_x$ as a function of temperature in air.

The crystal structure of $SrFeO_3$ was studied by several groups and led to the conclusion that it forms a cubic perovskite structure [17, 125, 127, 139]. The high temperature cubic form with an oxygen deficiency was discovered later [127,159] and by analogy it was assumed to have the perovskite structure too. However, this model is only suitable for $SrFeO_3$ and does not provide a satisfactory description of oxygen deficient cubic phases such as $Sr_8Fe_8O_{23}$, $Sr_4Fe_4O_{11}$ and $Sr_2Fe_2O_5$. Using the face-centered cell introduced in this chapter it is possible to describe the cubic crystal structure for any oxygen stoichiometry. $SrFeO_3$ can be expressed in terms of this model as a cell with composition $Sr_8Fe_8O_{24}$ consisting of eight ideal perovskite blocks (each containing only Fe^{4+}). The sole reason why the perovskite cell is used for $SrFeO_3$ is the crystallographical requirement to reduce the unit cell to the smallest building block which retains the translation symmetry. The other end member of the composition range $Sr_2Fe_2O_5$ ($x = 2.5$) has a unit cell with composition $Sr_8Fe_8O_{20}$ and contains only Fe^{3+}. From the thermogravimetric experiments we know that the composition of the oxide changes continuously so the cubic material with composition $SrFeO_x$ can be seen as a solid solution of two end members. The formula for the ferrite with the oxygen content x

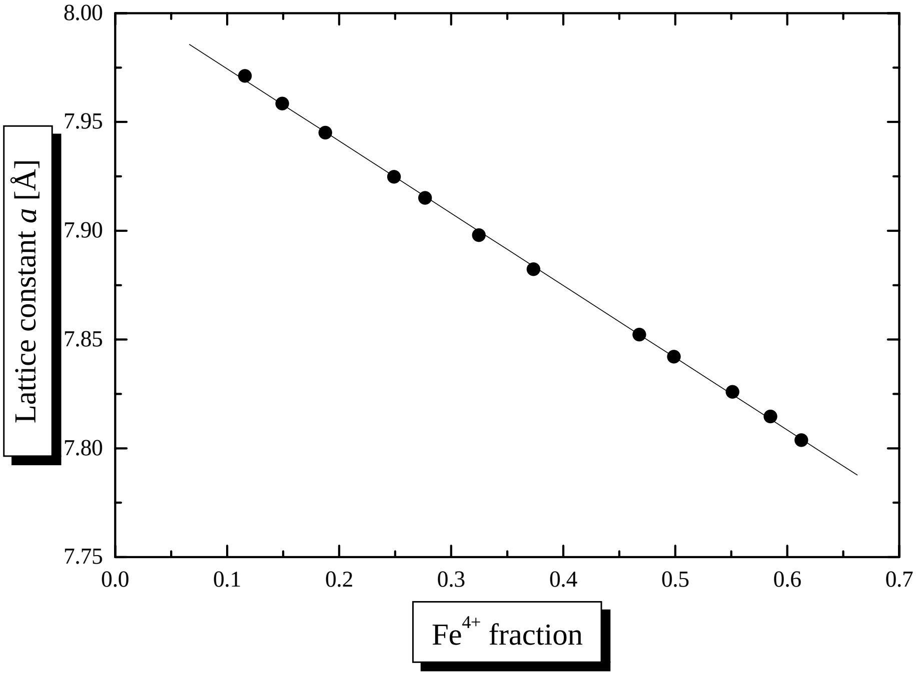

Figure 7.20: The lattice constant of the cubic ferrite in equilibrium with air as a function of the tetravalent iron fraction. The solid line shows the linear fit is described in the text.

can be written in the following manner:

$$Sr_8Fe^{4+}_{8-2y}Fe^{3+}_{2y}O_{24-y} \tag{7.7}$$

where $y = 24-8x$. This is a temperature induced analogue of a substitutional solid solution [130], but instead of replacing iron with other transition metal tetravalent iron is replaced by trivalent. The replacement causes formation of oxygen vacancies. This approach assures that for any stoichiometry x the crystal structure is expressed in terms of two compounds with whole numbers of oxygen per unit cell, even if the average stoichiometry is not an integer. However, there are three other phases with whole number of oxygen atoms per unit cell: $Sr_8Fe_8O_{21}$ ($x = 2.625$), $Sr_8Fe_8O_{22}$ ($x = 2.75$), $Sr_8Fe_8O_{23}$ ($x = 2.875$). They correspond to the tetravalent to trivalent iron ratios of 1:3, 1:1, 3:1 respectively. $Sr_8Fe_8O_{21}$ does not exist at room temperature as a single phase but the rest do. It is therefore possible to treat these compounds as separate entities and follow the phase behaviour found at room temperature. In this way a phase with oxygen stoichiometry x can be depicted as a solution of two nearest phases with integer number of oxygens per cell. The two interpretations are equivalent and yield the same result.

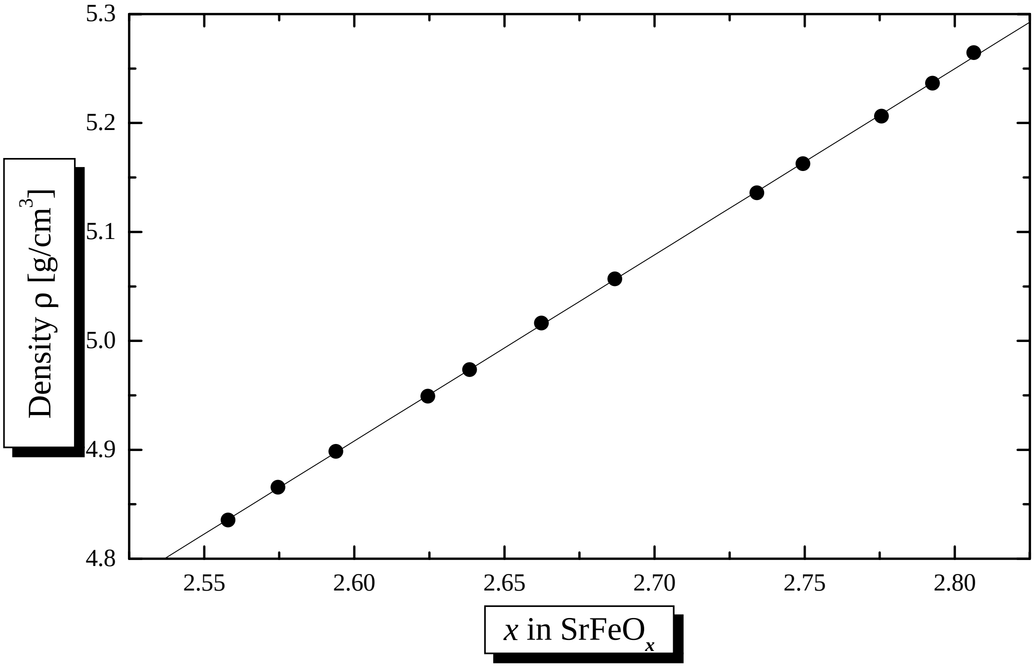

Figure 7.21: The calculated density of cubic $SrFeO_x$ in equilibrium with air as a function of its composition. The solid line shows the linear fit described in the text.

The solid solution representation is impossible in the perovskite model which has only one phase with a non-fractional number of oxygen atoms per cell.

7.4.2 Equilibrium Phase Diagram

Figure 7.22 shows a tentative equilibrium phase diagram. So far phase relations have been presented as a function of the oxide composition [127, 128], however this is inappropriate since the oxide can have the same composition over a range of temperatures. These diagrams are nothing else than collections of phase transitions found using calorimetric methods and results are similar to those presented in Figure 7.1. The first attempt to draw the equilibrium phase diagram was made by Mizusaki *et al.* [128] however, some of the methods used to derive it and interpretation of certain parts are highly questionable as discussed on page 59.

The diagram contains data obtained by neutron, x-ray diffraction and Mössbauer experiments performed by the present author (circles), Mizusaki *et al.* (triangles) and Wißmann and Becker [151] (star). The empty symbols denote a low symmetry structure and the filled markers denote a single

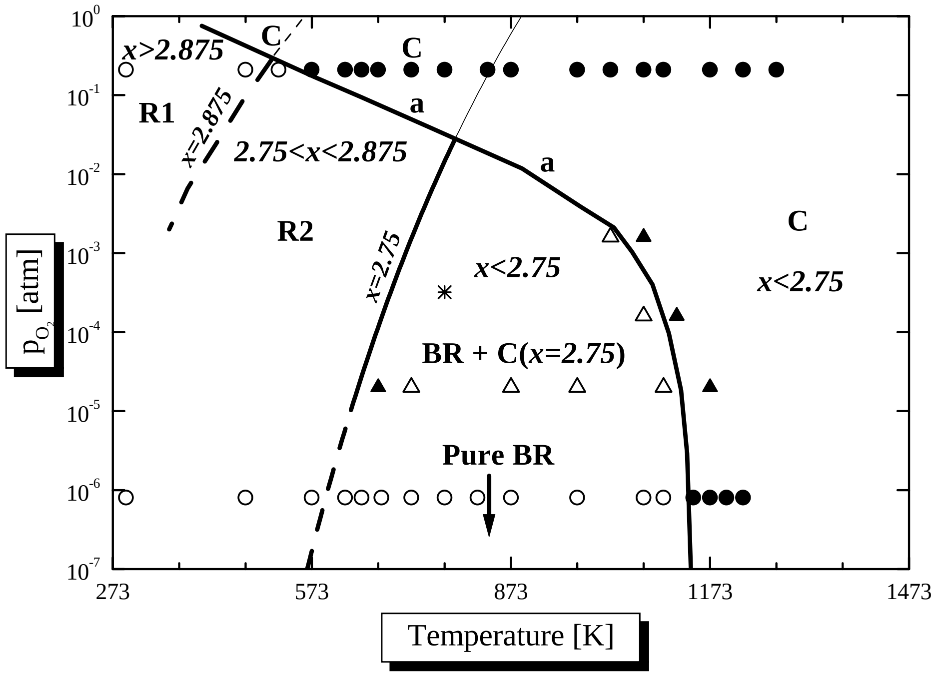

Figure 7.22: A phase diagram of the $SrFeO_x$ system. Solid and empty symbols represent the cubic and lower symmetries respectively. The circles and triangles represent the experimental points collected by the author and Mizusaki *et al.* [128] respectively. The star represents the result of a Mössbauer experiment of Wißmann and Becker [151]. C and BR refer to the cubic phase and the orthorhombic $Sr_2Fe_2O_5$ (brownmillerite, $x = 2.5$) respectively. R1 and R2 indicate different regions of the diagram discussed in the text. The x parameter is the oxygen content of the ferrite and the 'a' line separates the cubic phase area from the low symmetry parts.

phase cubic structure with bold lines representing phase boundaries. The line 'a' shows the border of the cubic phase (C) determined by neutron diffraction experiments in argon and air. The boundary was additionally guided by results of Mizusaki *et al.* for intermediate partial pressures of oxygen. The temperature of the transition to the cubic form decrease with increasing partial pressure of oxygen. Mizusaki *et al.* indicated the existence of a region containing the orthorhombic brownmillerite $Sr_2Fe_2O_5$ (BR) denoted by BR+C($x = 2.75$). Mizusaki *et al.* interpreted this region as a single phase area, however reference to Figure 4.6 shows that the equilibrium composition in this range exceeds $x = 2.5$ and to makeup the stoichiometry, the brownmillerite phase has to be accompanied by an oxygen rich phase. Although Mizusaki *et al.* [128] did not show full diffraction patterns, the published fragments indicate the presence of the second phase. Since for compositions

$2.5 < x < 2.75$ the ferrite at room temperature forms a mixture of $Sr_2Fe_2O_5$ and $Sr_4Fe_4O_{11}$ the second phase should be a cubic form of $Sr_4Fe_4O_{11}$ marked by C($x = 2.75$). The two phase character of the BR+C($x = 2.75$) area was confirmed by Mössbauer measurement, denoted as the star on the diagram, which showed the coexistence of $Sr_2Fe_2O_5$ and the second phase.

The brownmillerite (BR) disappears with decreasing temperature since the material gains oxygen. This was noted by Mizusaki *et al.* on the diffraction pattern taken at $T = 673\,\mathrm{K}$ and $p_{O_2} = 2 \times 10^{-5}\,\mathrm{atm}$. Since $Sr_2Fe_2O_5$ vanishes when the stoichiometry reaches 2.75, the line corresponding to the composition $x = 2.75$ should form the other border line of this area. The $x = 2.75$ line was calculated from the Ellingham plot for $Sr_4Fe_4O_{11}$ presented on page 62. It is marked at lower temperatures than the cubic point reported by Mizusaki *et al.* , but the discrepancy is most likely due to an error in the temperature measurement during the x-ray diffraction experiments. The strip heaters commonly used in high temperature x-ray cameras suffer from gradients of temperature and the surface of the oxide which contributes to the diffraction pattern can be tens of degrees cooler than the heater itself. The temperature gradients are especially troublesome at low temperatures. In the two phase area BR+C($x = 2.75$) the amount of the cubic phase decreases with partial pressure of oxygen. The present neutron diffraction experiments at $p_{O_2} < 10^{-6}\,\mathrm{atm}$ do not show any traces of the C($x = 2.75$) phase. The two phase mixtures of $Sr_2Fe_2O_5$ and $Sr_4Fe_4O_{11}$ observed in samples prepared by quenching or by fast cooling under low oxygen pressure ($10^{-4} - 10^{-2}\,\mathrm{atm}$) most likely originate from this region (see Table 4.1).

At temperatures lower than given by the $x = 2.75$ line the $x = 2.875$ line is expected corresponding to a single phase $Sr_8Fe_8O_{23}$. It is marked by a dashed line because this composition was only attained in a pure oxygen atmosphere and there are not enough data to draw its exact position.

Both the $x = 2.75$ and the $x = 2.875$ lines divide the diagram into two regions R1 and R2. The region R1 should contain a mixture of cubic $SrFeO_3$ and $Sr_8Fe_8O_{23}$, while the region R2 should contain a mixture of $Sr_8Fe_8O_{23}$ and $Sr_4Fe_4O_{11}$. Another phase transition line in the R2 region corresponding to the transition of $Sr_4Fe_4O_{11}$ to the cubic phase is expected before it crosses line 'a'. However, it is doubtful if the regions R1 and R2 will ever be completely explored due to very long equilibration times and the necessity to use high resolution diffraction techniques for phase identification. On the other hand it should be possible to draw the 'a' line more precisely in the vicinity of

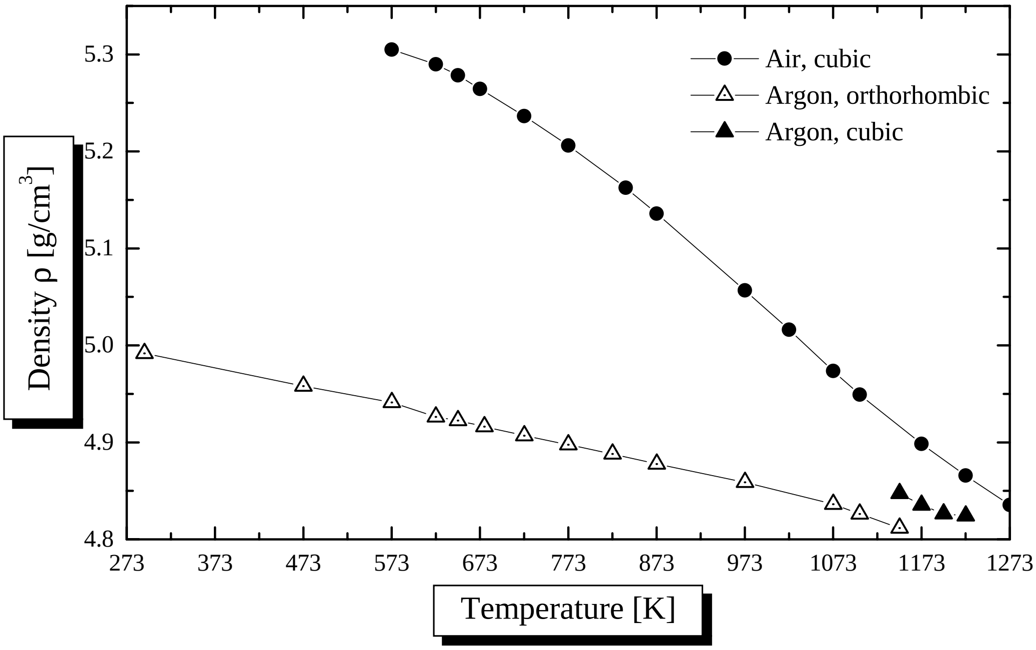

Figure 7.23: The calculated densities of cubic $SrFeO_x$ in air and $Sr_2Fe_2O_5$ in argon as a function of temperature.

the intersection with the $x = 2.75$ line. Also the expansion of the diagram into the oxygen pressures exceeding 1 atm should be interesting and possible using neutron powder diffraction.

7.4.3 Density and Thermal Expansion of the Ferrite

The wide range of composition and structure changes in the ferrite system cause substantial changes to its density. The calculated density as a function of temperature for air and argon atmospheres are presented in Figure 7.23. The discontinuity in the argon series is due to the phase transition and corresponds to the two phase sample however, the weighted average density is in the middle between the two points. The graph clearly shows the difference in the density changes caused by an ordinary thermal expansion and the process that involves oxygen vacancy formation (air). The difference in density is probably even larger in higher oxygen partial pressures. This information is very important if the oxide is to be considered as a material for electrochemical devices. The large difference in the density (unit cell volume) can give a raise to mechanical instability of a membrane subjected to oxygen partial pressure or temperature gradients. The difference in the cell volume creates stress which may cause spontaneous fracture.

Very different volume thermal expansion coefficients in different atmospheres (compare Figure 7.1 and Figure 7.19) can have similar effect during heating or cooling since different parts of the membrane will dilate at different rates. The effect of the stress is obviously smallest at very high temperatures where the densities and cell volumes are comparable since the equilibrium composition of the oxide approaches $x = 2.5$ irrespective of the oxygen partial pressure.

Chapter 8

Conclusions

8.1 Summary of the Most Important Findings

This thesis has examined a broad spectrum of the properties of the $SrFeO_x$ system.

Examination of the formation of the ferrite showed that the oxide is formed in a direct reaction without any other transient phases as inherent steps in the process. The reported occurrence of the transient phases is caused only by inhomogeneity of the reactant mixture. The formation reaction requires high temperatures ($> 873\,\mathrm{K}$) to proceed. Attempts to synthesize the material using mechanical energy at room temperature from a mixture of hematite and strontium carbonate were not successful. The ferrite was not formed from the mixture of hematite and strontium oxide at ambient temperature either despite of high reactivity of SrO towards other transition metal oxides.

The oxygen deficient phase $Sr_2Fe_2O_5$ ($x = 2.5$) can be formed thermally from Fe^{2+} bearing iron oxide (magnetite). $Sr_2Fe_2O_5$ reduces CO_2 to CO upon its formation from the magnetite-strontium carbonate mixture to oxidize the divalent iron. This is the first report a new route for ferrite preparation. The synthesis of $Sr_2Fe_2O_5$ from magnetite also proves that phases with the oxygen content $x < 2.5$ do not exist the $SrFeO_x$ system.

The formation from magnetite is chemically different from the hematite-strontium carbonate route and the former reaction requires higher temperature to initiate the reaction. The magnetite route does not exhibit any transient phases during formation even in poorly mixed reactants. This indicates that $Sr_2Fe_2O_5$ phase could have the lowest Gibbs free energy of formation in the entire Sr-Fe-O system.

The oxygen content x in $SrFeO_x$ depends on temperature T and the oxygen partial pressure p_{O_2}. The dependence has an equilibrium character and the material assumes the same composition if exposed to the same conditions (T, p_{O_2}). Study of the oxidation reaction at different temperatures and oxygen partial pressures proved that the $SrFeO_x$ system obeys the Gibbs-Helmholtz equation and the oxygen content was described as a function of temperature and oxygen pressure $x = f(T,\ p_{O_2})$. The plot of this function yields the equilibrium composition diagram an indispensable tool in studies of all properties of the material at elevated temperature. The plot also provides information that aids preparation of samples with controlled oxygen content.

The heat of oxidation of $Sr_2Fe_2O_5$ was measured as a function of temperature and oxygen partial pressure. The heat was found to decrease with temperature and decreasing concentration of oxygen in the atmosphere. However, the heat exhibits a jump around 1140 K which is associated with a phase transition in $Sr_2Fe_2O_5$ around this temperature. The examination of the temperature dependence of the heat showed that the phase transition in $Sr_2Fe_2O_5$ has a continuous character and occurs over a 100 K temperature range.

Thermal oxidation ceases below 473 K under pressure of 1 atm. However, $SrFeO_x$ can be oxidized at room temperature using mechanical energy. The study of milled materials are difficult due to the small crystalline size and the lattice strain. The mechanical oxidation differs from the thermally induced one. In the case of the mechanical process there are few concurrent chemical reactions which yield a mixture of more than two phases while the thermal process produces a single phase or two phase products. The thermal oxidation under 1 atm of oxygen can increase the oxygen content up to $x = 2.915$, milling on the other hand covers the entire range of compositions ($2.5 \leq x \leq 3.0$). Milling produces a powder with relatively small specific surface area despite the small crystalline size.

The ferrite also reacts with other gaseous oxides such as carbon dioxide. The reaction of $SrFeO_x$ with CO_2 leads to its decomposition to strontium carbonate and a strontium deficient ferrite ($SrFe_{12}O_{19}$). The carbonation reaction is controlled by temperature and CO_2 partial pressure. For fixed p_{CO_2} there is a critical temperature below which the ferrite decomposes. Above this temperature the material converts back to $SrFeO_x$. The presence of the tetravalent iron in the ferrite does not inhibit the carbonation process. The product of carbonation ($SrFe_{12}O_{19}$) is very resistant to further carbonation. The reaction producing $SrFe_{12}O_{19}$ has two stages with different kinetics. The first stage takes a few hours and is a solid-gas reaction that occurs on the surface $SrFeO_x$ and along the grain boundaries. It is followed by much slower stage, in which Sr^{2+} diffuses through the layer of $SrFe_{12}O_{19}$ built on the surface of grains. The surface stage is responsible for formation of cracks in the bulk of the $SrFeO_x$ which appear as a result of change of molar volume.

Mechanical carbonation of $SrFeO_x$ is also possible and as in the case of the mechanical oxidation the analysis is hampered by the small crystalline size and the strain. The mechanical carbonation is different from the thermal reaction and leads to complete decomposition of the ferrite to $SrCO_3$ and hematite without $SrFe_{12}O_{19}$ as the transient phase. But the carbonation reaction forms an unknown metastable carbonate which contains Fe^{3+} and possibly some strontium. The unknown carbonate causes a higher than expected mass loss of milled samples examined by heating in TGA but it can not be positively identified using x-ray diffraction.

Various phases of $SrFeO_x$ were examined using Mössbauer spectroscopy. Collected room temperature spectra of the $SrFeO_x$ are the same as published in the literature which indicates good quality of the prepared ferrites and reproducibility of experiments. However the patterns of $Sr_4Fe_4O_{11}$ and $Sr_8Fe_8O_{23}$ were interpreted in much more straight forward manner. The new interpretation avoids the introduction of spectral features which are difficult to justify from the experimental results (low intensity lines not observed directly in the spectrum) and the introduction of fractional iron valency. The new interpretation is based on the information deduced from the chemical composition of the ferrite. In the case of $Sr_4Fe_4O_{11}$ the Mössbauer spectrum was described in terms of two iron sites using a singlet belonging to the tetravalent state and a doublet associated with the trivalent iron in the high-spin state. For $Sr_8Fe_8O_{23}$ the spectrum was described in terms of three iron sites. Two singlets were assigned to two different crystallographical positions of tetravalent iron and the remaining singlet was assigned to the trivalent iron. The new interpretation yields correct calculated oxygen content when applied not only to the present results but also to the data published in the literature.

Examination of spectra belonging to composition range $2.75 \leq x < 3.0$

indicates that the $SrFeO_x$ system forms a mixture of $Sr_4Fe_4O_{11}$ and $Sr_8Fe_8O_{23}$ in the $2.75 < x < 2.875$ range and a mixture of $Sr_8Fe_8O_{23}$ and $SrFeO_3$ in the range $2.875 < x < 3.0$.

The high temperature Mössbauer spectra published in the literature indicate that the high-temperature cubic form of the ferrite has only one iron site despite the existence of two different oxidation states. This indicates the disorder among oxygen sites.

The high-temperature crystal structure of the $SrFeO_x$ system was investigated both in argon and air atmospheres. The measurements on the oxygen deficient phase $Sr_2Fe_2O_5$ ($x = 2.5$) were carried out in argon to prevent oxidation. This phase undergoes two phase transitions between room temperature and 1223 K. The first is the magnetic transition from the antiferromagnetic to the paramagnetic state (Néel point) at 668 K and the other transition is a change of the lattice from orthorhombic to cubic at around 1140 K. Neutron diffraction gave a better estimate of the Néel temperature and in the case of the second transformation it revealed the coexistence of the orthorhombic and the cubic phases. It is an indication that the transition around 1140 K is not first order and the neutron measurements are consistent with the findings from measurements of the oxidation heat of $Sr_2Fe_2O_5$.

The cubic phase of $Sr_2Fe_2O_5$ was described using a new structural model with the unit cell having the *Fm3c* symmetry.

In air the oxygen content x in $SrFeO_x$ varied in the range $2.56 \leq x \leq 2.81$. The unit cell of the cubic $SrFeO_x$ was described using the same unit cell as in the case of $Sr_2Fe_2O_5$. The oxidized ferrite in the cubic form obeys Vegard's law and its density increase linearly with the oxygen content. The new unit cell with the *Fm3c* allowed interpretation the cubic $SrFeO_x$ as a solid solution of $Sr_8Fe_8O_{24}$ and $Sr_8Fe_8O_{20}$ cells across the entire composition range.

The structural measurements and the equilibrium composition diagram were used to construct the phase diagram for the $SrFeO_x$ system.

8.2 Application of the $SrFeO_x$ System

The prospects of use for pure $SrFeO_x$ in oxygen conducting devices are rather poor. The system is very interesting from the scientific point of view but the variety of phases and transitions make the material useless since it would be mechanically unstable. The information gathered in Chapter 7 shows that the oxide has a high expansion rate. The volume expansion coefficients and densities of the oxygen deficient ($Sr_2Fe_2O_5$) and oxidized materials are different. These differences would cause a mechanical strain in a ceramic membrane exposed to temperature or oxygen partial pressure gradients and during heating of the membrane to the operational temperature. Moreover, the reactivity of $SrFeO_x$ towards CO_2 excludes the material as electrodes in fuel cells utilizing hydrocarbons as fuel. However, further research into more complicated systems based on $SrFeO_x$ may lead to a commercially viable material.

8.3 Directions for Future Research

The list of experiments that can be done on the $SrFeO_x$ system is long but and it is impossible to exhaust all possibilities. However, the major obstacle in studies of the $SrFeO_x$ system is the lack of single crystal specimens. Single crystals are difficult to produce because of high melting point of the ferrite, reactivity of the molten oxide towards most ceramic materials (crucibles) and the fact that it is difficult to obtain the desired composition x. However, it is worth trying to grow single crystals using fluxes, such as B_2O_3–Na_2O, $NaCO_3$, PbO–PbF_2, below the melting point of the ferrite. These compounds allow to control the size of crystals and gave very encouraging results in the case of $BaFe_{12}O_{19}$ and other spinels [172, 173]. The composition of resulting crystals could be then adjusted using the procedure described on page 70.

The single crystals would resolve ambiguities in the crystal structures of $Sr_4Fe_4O_{11}$ and $Sr_8Fe_8O_{23}$ at room temperature.

All phases of the $SrFeO_x$ system exhibit magnetic ordering however, only $Sr_2Fe_2O_5$ has a high ordering temperature. The other phases become magnetically ordered at subambient temperatures and their magnetic properties have only been studied using Mössbauer spectroscopy and magnetic susceptibility[*] [29, 125, 154]. The single crystals would allow precise studies of their magnetic structures using single crystal neutron experiments and many other properties such as transport, optical, mechanical properties, phonon excitations *etc.*

The phase diagram of $SrFeO_x$ could be extended into the high oxygen pressure region using high pressure cells for neutron powder diffraction or diamond anvils in the case of x-ray diffraction. These measurements could be

---

[*] $Sr_2Fe_2O_5$ and $SrFeO_3$ are exceptions and were studied using neutron diffraction [158, 160].

combined with equilibrium composition studies using high-pressure thermogravimetric analysers which are capable of reaching pressures up to 60 MPa and temperatures of 2300 K [174].

The temperature dependence of the heat capacity as a function of temperature from nearly 0 K would facilitate calculation of the Gibbs free energy of formation of various $SrFeO_x$ phases and thus thermodynamical calculations of chemical stability of the $SrFeO_x$ system in the presence of other species (compounds) at elevated temperature.

Appendix A

Results of Rietveld Refinement

This appendix contains the results of Rietveld refinements carried out on the high-temperature neutron diffraction patterns of $SrFeO_x$. The explanation of symbols and detailed analysis are presented in Chapter 7. The numbers in parentheses are standard deviations as given by the refinement program.

Table A.1: Results of Rietveld refinement of $Sr_2Fe_2O_5$ spectra in the temperature range 293–678 K. The results are discussed in section 7.2.3.

		293 K	473 K	573 K	623 K	648 K	678 K
a [Å]		5.66850(35)	5.6739(4)	5.6780(4)	5.6803(4)	5.6807(4)	5.6822(4)
b [Å]		15.5823(8)	15.6470(8)	15.6830(9)	15.7019(9)	15.7096(9)	15.7203(9)
c [Å]		5.52653(32)	5.53580(33)	5.5422(4)	5.54587(35)	5.5469(4)	5.5488(4)
V [Å^3]		488.15(5)	491.46(5)	493.52(5)	494.64(5)	495.01(5)	495.65(5)
m_z [μ_B]		3.92(3)	3.28(3)	2.72(3)	2.25(3)	1.99(3)	1.38(4)
Sr	x	0.0163(7)	0.0152(7)	0.0150(8)	0.0148(8)	0.0141(8)	0.0152(8)
Sr	y	0.10890(19)	0.10930(21)	0.10936(23)	0.10989(22)	0.10986(22)	0.10993(22)
Sr	z	0.4989(27)	0.4995(24)	0.5005(23)	0.5011(23)	0.5008(24)	0.4985(23)
Sr	U	0.64(9)	0.95(9)	0.97(10)	1.18(10)	1.19(10)	1.18(10)
Fe(1)	U	0.88(9)	1.33(10)	1.65(11)	1.71(11)	1.78(11)	1.84(11)
Fe(2)	x	0.9355(8)	0.9359(8)	0.9367(8)	0.9367(8)	0.9369(8)	0.9382(8)
Fe(2)	z	0.9833(24)	0.9756(23)	0.9715(24)	0.9702(24)	0.9700(24)	0.9675(23)
Fe(2)	U	2.49(13)	2.55(15)	2.48(15)	2.46(15)	2.57(16)	2.24(15)
O(1)	x	0.2574(24)	0.2545(26)	0.2510(29)	0.2480(29)	0.2438(25)	0.2438(24)
O(1)	y	0.99123(29)	0.99158(31)	0.99176(33)	0.99185(32)	0.99215(34)	0.99181(33)
O(1)	z	0.2537(35)	0.2589(33)	0.2586(35)	0.2528(36)	0.2513(35)	0.2529(33)
O(1)	U	0.09(12)	0.45(13)	0.63(13)	0.79(11)	0.96(12)	0.75(12)
O(2)	x	0.0500(8)	0.0506(8)	0.0500(9)	0.0485(9)	0.0486(9)	0.0490(9)
O(2)	y	0.14109(26)	0.14127(28)	0.14115(29)	0.14126(29)	0.14109(30)	0.14119(30)
O(2)	z	0.0010(36)	-0.0041(36)	-0.0029(35)	-0.0006(33)	-0.0060(36)	-0.0054(34)
O(2)	U	1.03(11)	1.64(12)	1.84(13)	2.18(13)	2.23(13)	2.39(13)
O(3)	x	0.8568(15)	0.8600(17)	0.8586(17)	0.8566(17)	0.8579(17)	0.8556(17)
O(3)	z	0.6224(29)	0.6236(30)	0.6228(31)	0.6205(30)	0.6196(30)	0.6208(29)
O(3)	U	1.39(20)	2.22(23)	2.29(25)	2.41(24)	2.56(25)	2.69(26)
R_{wp} [%]		4.37	4.23	4.18	4.01	4.06	3.93
R_p [%]		3.39	3.36	3.26	3.12	3.20	3.15

$U = 100U_{iso}$ [Å^2]

Table A.2: Results of Rietveld refinement of $Sr_2Fe_2O_5$ spectra in the temperature range 723–1148 K. The results are discussed in section 7.2.3.

		723 K	773 K	823 K	873 K	973 K	1073 K	1103 K	1148 K†
a [Å]		5.6839(4)	5.6864(4)	5.6892(4)	5.6918(4)	5.6973(4)	5.7037(4)	5.7068(4)	5.7149(5)
b [Å]		15.7354(9)	15.7488(9)	15.7626(10)	15.7769(9)	15.8016(10)	15.8292(10)	15.8401(10)	15.8528(13)
c [Å]		5.5522(4)	5.5556(4)	5.5590(4)	5.5632(4)	5.5707(4)	5.5805(4)	5.5853(4)	5.5896(5)
V [Å^3]		496.58(5)	497.53(6)	498.51(6)	499.57(6)	501.51(6)	503.84(6)	504.89(6)	506.41(7)
Sr	x	0.0137(8)	0.0146(8)	0.0147(8)	0.0156(8)	0.0143(9)	0.0142(9)	0.0133(9)	0.0139(12)
Sr	y	0.11004(22)	0.10962(22)	0.10985(22)	0.11040(22)	0.11075(24)	0.11135(23)	0.11152(24)	0.11113(35)
Sr	z	0.4985(23)	0.5029(24)	0.5021(26)	0.5027(24)	0.5038(25)	0.5024(24)	0.5037(26)	0.5017(34)
Sr	U	1.29(10)	1.57(11)	1.62(11)	1.75(11)	1.97(12)	2.29(12)	2.40(13)	2.47(18)
Fe(1)	U	1.99(11)	2.23(11)	2.21(11)	2.53(12)	2.70(13)	3.14(13)	3.26(14)	3.14(20)
Fe(2)	x	0.9376(8)	0.9374(8)	0.9368(9)	0.9393(9)	0.9396(9)	0.9394(9)	0.9396(9)	0.9400(12)
Fe(2)	z	0.9689(24)	0.9748(25)	0.9762(26)	0.9707(25)	0.9708(26)	0.9684(24)	0.9712(27)	0.9690(33)
Fe(2)	U	2.50(15)	2.55(15)	2.71(15)	2.79(16)	2.72(17)	2.81(17)	2.79(17)	2.86(23)
O(1)	x	0.2484(30)	0.2569(26)	0.2573(27)	0.2417(23)	0.2412(24)	0.2380(21)	0.2418(25)	0.2439(39)
O(1)	y	0.99219(34)	0.99185(33)	0.99176(35)	0.99216(35)	0.99230(38)	0.99196(37)	0.99241(39)	0.9913(5)
O(1)	z	0.2532(37)	0.2545(36)	0.2542(39)	0.2486(34)	0.2501(37)	0.2486(35)	0.2465(38)	0.254(6)
O(1)	U	1.11(12)	0.96(13)	1.21(14)	1.40(12)	1.50(13)	2.07(14)	2.14(14)	2.29(21)
O(2)	x	0.0477(9)	0.0487(9)	0.0482(10)	0.0482(10)	0.0469(11)	0.0474(11)	0.0465(11)	0.0486(15)
O(2)	y	0.14121(30)	0.14178(29)	0.14146(31)	0.14165(30)	0.14161(33)	0.14140(33)	0.14103(34)	0.1428(5)
O(2)	z	-0.0031(35)	0.0029(32)	0.0003(36)	-0.0017(33)	-0.0034(37)	-0.0037(35)	0.0030(36)	-0.005(5)
O(2)	U	2.61(13)	2.45(14)	2.66(14)	2.69(14)	3.25(16)	3.71(16)	4.04(18)	4.23(24)
O(3)	x	0.8577(17)	0.8595(18)	0.8589(18)	0.8571(17)	0.8573(19)	0.8544(18)	0.8546(19)	0.8581(27)
O(3)	z	0.6210(31)	0.6242(31)	0.6254(33)	0.6222(30)	0.6241(32)	0.6271(31)	0.6333(34)	0.623(5)
O(3)	U	2.98(27)	3.20(27)	3.21(27)	3.30(28)	3.61(32)	4.10(33)	4.40(34)	5.22(50)
R_{wp} [%]		3.76	3.82	3.81	3.67	3.80	3.56	3.51	2.97
R_p [%]		2.95	2.99	3.00	2.88	2.95	2.81	2.84	2.40

†-two phase pattern; $U = 100U_{iso}$ [Å^2]

Table A.3: Octahedral bond lengths (in angstroms) and angles (in degrees) in $Sr_2Fe_2O_5$ as a function of temperature. The figures in the square brackets denote the number of bonds if they have equal length. The results are discussed in section 7.2.3.

T [K]	Fe(1)-O(1)	Fe(1)-O(1)	O(1)-Fe(1)-O(1)	O(1)-Fe(1)-O(1)
293	2.028(17)	1.94(17)	92.5(9)	88.301(27)
473	2.039(18)	1.933(18)	90.7(9)	88.316(33)
573	2.025(20)	1.951(20)	89.9(9)	88.344(33)
623	1.991(21)	1.986(20)	90.5(9)	88.395(22)
648	1.969(19)	2.009(19)	89.9(9)	88.436(25)
678	1.976(18)	2.004(18)	89.5(8)	88.419(27)
723	1.996(21)	1.984(21)	90.5(9)	88.44(23)
773	2.037(18)	1.946(18)	92.1(10)	88.446(29)
823	2.039(19)	1.947(19)	92.3(10)	88.453(31)
873	1.954(18)	2.033(18)	89.9(8)	88.506(26)
973	1.961(19)	2.031(19)	89.4(9)	88.541(29)
1073	1.945(18)	2.053(18)	89.0(8)	88.587(31)
1103	1.953(20)	2.047(20)	90.3(9)	88.59(29)
1148†	1.996(30)	2.011(30)	89.1(13)	88.47(4)
T [K]	Fe(1)-O(2),[2]	O(1)-Fe(1)-O(2)	O(1)-Fe(1)-O(2)	
293	2.217(4)	88.3(8)	90.9(6)	
473	2.229(4)	88.3(8)	92.7(6)	
573	2.232(5)	88.3(8)	93.4(6)	
623	2.235(5)	88.4(8)	92.7(5)	
648	2.234(5)	88.4(9)	93.3(5)	
678	2.237(5)	88.4(8)	93.7(5)	
723	2.239(5)	88.4(9)	92.7(5)	
773	2.25(5)	88.4(8)	91.0(6)	
823	2.247(5)	88.5(9)	90.8(7)	
873	2.252(5)	88.5(8)	93.1(5)	
973	2.254(5)	88.5(9)	93.5(5)	
1073	2.255(5)	88.6(8)	93.8(5)	
1103	2.25(6)	88.6(8)	92.5(5)	
1148†	2.28(8)	88.5(12)	93.9(8)	

†-two phase pattern

Table A.4: Tetrahedral bond lengths (in angstroms) and angles (in degrees) in $Sr_2Fe_2O_5$ as a function of temperature. The figure in the square brackets denote the number of bonds or angles if they have equal value. The results are discussed in section 7.2.3.

T [K]	Fe(2)-O(2),[2]	Fe(2)-O(3)	Fe(2)-O(3)	O(2)-Fe(2)-O(2)	O(2)-Fe(2)-O(3),[2]	O(3)-Fe(2)-O(3)
293	1.820(5)	2.044(13)	1.827(10)	137.7(4)	107.5(4)	102.3(4)
473	1.825(5)	1.995(13)	1.868(10)	137.6(4)	107.1(4)	103.6(4)
573	1.830(5)	1.983(13)	1.875(11)	137.8(5)	106.2(4)	103.6(4)
623	1.829(5)	1.992(13)	1.863(10)	138.0(5)	105.72(34)	103.4(4)
648	1.830(5)	1.995(13)	1.869(10)	138.5(5)	106.2(4)	103.3(4)
678	1.829(5)	1.980(13)	1.874(10)	138.5(5)	105.6(4)	103.3(4)
723	1.829(5)	1.985(13)	1.879(10)	138.7(5)	105.52(35)	103.5(4)
773	1.825(5)	1.998(14)	1.881(11)	138.1(5)	105.87(34)	103.4(4)
823	1.829(5)	2.000(14)	1.875(11)	138.5(5)	106.2(4)	103.4(4)
873	1.825(5)	1.995(13)	1.886(10)	139.0(5)	105.4(4)	103.0(4)
973	1.824(6)	1.988(14)	1.895(11)	139.7(6)	105.3(4)	103.1(4)
1073	1.833(6)	1.965(14)	1.895(11)	139.4(6)	104.9(4)	103.6(4)
1103	1.839(6)	1.948(15)	1.907(12)	139.6(6)	104.2(4)	103.9(4)
1148†	1.816(9)	1.988(21)	1.910(16)	138.9(8)	105.6(6)	103.2(6)

†-two phase pattern

Table A.5: Strontium polyhedron bond lengths (in angstroms) in $Sr_2Fe_2O_5$ as a function of temperature. The results are discussed in section 7.2.3.

T [K]	Sr-O(1)	Sr-O(1)	Sr-O(1)	Sr-O(1)	Sr-O(2)	Sr-O(2)	Sr-O(2)	Sr-O(3)
293	2.658(14)	2.584(15)	2.644(13)	2.563(14)	2.804(21)	2.826(21)	2.509(5)	2.473(7)
473	2.648(13)	2.571(14)	2.676(12)	2.596(13)	2.840(20)	2.800(21)	2.514(6)	2.469(7)
573	2.645(14)	2.568(15)	2.686(13)	2.609(14)	2.841(19)	2.804(20)	2.520(6)	2.472(7)
623	2.662(14)	2.584(15)	2.683(13)	2.607(14)	2.832(18)	2.813(19)	2.529(6)	2.467(7)
648	2.653(14)	2.575(14)	2.691(13)	2.618(13)	2.861(19)	2.786(19)	2.532(6)	2.463(7)
678	2.644(13)	2.565(14)	2.705(12)	2.632(12)	2.845(18)	2.803(19)	2.524(6)	2.476(7)
723	2.660(14)	2.581(15)	2.696(13)	2.619(14)	2.834(19)	2.817(20)	2.541(6)	2.470(7)
773	2.691(15)	2.616(16)	2.661(13)	2.580(14)	2.830(19)	2.830(19)	2.534(6)	2.474(8)
823	2.696(16)	2.619(17)	2.666(14)	2.583(15)	2.840(20)	2.820(21)	2.536(6)	2.477(8)
873	2.671(13)	2.600(13)	2.694(12)	2.630(13)	2.855(18)	2.807(18)	2.532(6)	2.471(7)
973	2.678(14)	2.601(14)	2.707(13)	2.637(13)	2.873(20)	2.794(20)	2.548(7)	2.468(8)
1073	2.685(13)	2.598(13)	2.731(12)	2.654(12)	2.870(19)	2.804(20)	2.546(7)	2.476(8)
1103	2.706(13)	2.625(14)	2.711(12)	2.636(13)	2.842(20)	2.834(21)	2.555(7)	2.481(9)
1148†	2.692(21)	2.592(23)	2.742(20)	2.648(21)	2.885(28)	2.807(29)	2.550(9)	2.470(12)

†-two phase pattern

Table A.6: Rietveld refinement results for the cubic $Sr_2Fe_2O_5$ phase at different temperatures. The results are discussed in section 7.2.3

		1148 K†	1173 K	1198 K	1223 K
a [Å]		7.9512(5)	7.95779(23)	7.96275(24)	7.96388(23)
V [Å^3]		502.68(6)	503.938(26)	504.882(26)	505.096(25)
Sr	$100u_{ii}$ [Å^2]	4.42(22)	4.30(6)	4.52(6)	4.48(6)
Fe	$100u_{ii}$ [Å^2]	4.46(18)	4.14(5)	4.35(5)	4.38(5)
O	$100u_{\parallel}$ [Å^2]	4.1(4)	4.98(13)	5.32(13)	5.16(13)
O	$100u_{\perp}$ [Å^2]	8.06(30)	8.05(10)	8.16(10)	8.26(10)
R_{wp} [%]		2.97	2.85	2.99	2.78
R_p [%]		2.40	2.29	2.36	2.24

†-two phase pattern

Table A.7: Results of Rietveld refinement of cubic SrFeO$_x$ at different temperatures in air. The results are discussed in section 7.3.2.

T [K]	δ	a [Å]	V [Å^3]	Sr: $100u_{ii}$ [Å^2]	Fe: $100u_{ii}$ [Å^2]	O: $100u_\parallel$ [Å^2]	O: $100u_\perp$ [Å^2]	R_{wp} [%]	R_p [%]
573†	0.93546	7.78716(13)	472.212(14)	1.539(32)	0.970(26)	1.59(6)	2.83(5)	4.31	3.23
623†	0.93546	7.79345(14)	473.357(15)	1.621(35)	1.050(28)	1.63(7)	2.90(5)	4.51	3.44
648†	0.93546	7.79802(14)	474.191(14)	1.678(34)	1.062(28)	1.76(7)	3.00(5)	4.39	3.29
673	0.93546	7.80367(14)	475.223(15)	1.733(35)	1.151(28)	1.88(7)	3.14(5)	4.41	3.31
723	0.93087	7.81453(14)	477.210(15)	1.885(35)	1.302(29)	2.00(7)	3.46(5)	4.31	3.24
773	0.92520	7.82593(14)	479.300(15)	2.091(34)	1.515(28)	2.27(7)	3.81(5)	4.01	3.10
838	22/24	7.84204(14)	482.266(15)	2.367(34)	1.782(28)	2.52(7)	4.26(6)	3.81	3.01
873	0.91137	7.85220(15)	484.144(16)	2.57(4)	1.963(30)	2.68(7)	4.59(6)	3.90	3.06
973	0.89560	7.88224(16)	489.720(18)	3.08(4)	2.467(34)	3.20(9)	5.42(7)	3.84	3.04
1023	0.88748	7.89798(18)	492.661(19)	3.35(4)	2.79(4)	3.64(10)	5.82(8)	3.92	3.10
1073	0.87948	7.91504(19)	495.861(21)	3.57(5)	3.14(4)	4.12(10)	6.35(8)	3.90	3.06
1103	21/24	7.92473(21)	497.684(22)	3.76(5)	3.33(4)	4.18(11)	6.69(9)	4.00	3.15
1173	0.86463	7.94503(22)	501.518(24)	4.15(6)	3.76(5)	4.61(12)	7.27(10)	3.96	3.08
1223	0.85819	7.95844(25)	504.063(27)	4.37(6)	4.03(5)	4.96(13)	7.65(11)	4.10	3.12
1273	0.85266	7.97115(23)	506.481(26)	4.71(6)	4.40(5)	5.29(13)	8.26(10)	3.72	2.91

†-sample not in equilibrium with the atmosphere

Appendix B

List of Publications

1. F. Stobiecki, J. Dubowik, B. Szymański, H. Rohrmann, K. Roell and M. Schmidt. High-quality Ni-Fe/Cu multilayer films with antiferromagnetic coupling *Acta Phys. Polon.*, **A 91**:277–280, 1997.

2. T. Luciński, F. Stobiecki, D. Elefant, D. Eckert, G. Reiss, B. Szymański, J. Dubowik, M. Schmidt, H. Rohrmann and K. Roell. The influence of sublayer thickness on GMR and magnetization reversal in permalloy/Cu multilayers. *J. Magn. Magn. Mater.*, **174**:192–202, 1997.

3. T. Luciński, F. Stobiecki, B. Szymański, J. Dubowik, M. Schmidt and M. Urbaniak. High-sensitive giant magnetoresistance in permalloy/Cu multilayers. *J. Phys. IV France (J. de Physique IV)*, **8**:Pr2-453–456, 1998.

4. F. Stobiecki, T. Luciński and M. Schmidt. GMR and magnetisation studies of (Py=$Ni_{83}Fe_{17}$)/Cu multilayers as a function of the Py thickness. *Mol. Phys. Rep.*, **21**:159–162, 1998.

5. F. Stobiecki, M. Schmidt, R. Gontarz, T. Luciński and M. Ślusarek. Thermal stability of GMR effect in Permalloy/Copper multilayers. *Mol. Phys. Rep.*, **21**:171–173, 1998.

6. F. Stobiecki, T. Luciński, J. Dubowik, B. Szymański, M. Urbaniak and M. Schmidt. Giant magnetoresistance in Permalloy/copper multilayers. *Electron Technology*, **31**:80–87, 1998.

7. M. Schmidt and W.A. Kaczmarek. Synthesis of $SrFeO_{2.5}$ from mechanically activated reactants. *J. Alloys and Compounds*, **283**:117–121, 1999.

8. W.A. Kaczmarek, S.J. Campbell and M. Schmidt. Structural investigation of milled α-Fe and barium ferrite nano-mixtures. *Mater. Sci. Forum*, **312–314**:197–202, 1999. (*J. Metastable Nanocrystalline Mater.*, **2–6**:197–202, 1999).

9. M. Schmidt. Mechanically induced oxidation of $SrFeO_{3-\delta}$. *Mater. Res. Bull.*, **35**:169–175, 2000.

10. M. Schmidt. Composition adjustment of non-stoichiometric strontium ferrite $SrFeO_{3-\delta}$. *J. Phys. Chem. Solids*, **61**:1363–1365, 2000.

11. M. Schmidt and S.J. Campbell. Crystal and magnetic structures of $Sr_2Fe_2O_5$ at elavated temperature. *J. Solid State Chem.*, **156**:292–304, 2001.

Bibliography

[1] P.G. Bruce, editor. *Solid State Electrochemistry.* Cambridge University Press, Cambridge, 1995.

[2] M. Faraday. Experimental Researches in Electricity.-Fourth Series. *Phil. Trans. Roy. Soc. London*, pages 507–522, 1833.

[3] M. Faraday. Experimental Researches in Electricity.-Twelfth Series. *Phil. Trans. Roy. Soc. London*, pages 83–121, 1838.

[4] E. Warburg. *Ann. Physik u Chem. N. F.*, **21**:662, 1884.

[5] W. Nernst. Über die elektrolitysche leitung fester körper bei sehr hohen temperaturen. *Z. Elektrochem.*, **6**:41–43, 1899.

[6] C. Tubandt and E. Lorentz. Molekularzustand und elektrisches Leitvermögen kristallisierter Saltze. *Z. Physik. Chem.*, **87**:513–542, 1914.

[7] E. Bauer and H. Preis. Überbrennstoff-ketten mit festleitern. *Z. Elektrochem.*, **43**:727–732, 1937.

[8] C. Wagner. Galvanische Zellen mit festen Electrolyten mit gemischter Stromleitunng. *Z. Elektrochem.*, **60**:4–7, 1956.

[9] R. Stevens. *Zirconia and zirconia ceramics.* Magnesium Electron Ltd., 1986.

[10] U. Balachandran, M.S. Kleefish, T.P. Kobylinski, S.L. Morrisette, and S. Pei. Oxygen Ion-Conducting Dense Ceramics. Technical Report U.S. Patent No.5,723,074, AMOCO Corp., 1998.

[11] B. C. H. Steele. Ceramic Electrochemical Reactors Incorporating Solid Oxide Electrolytes. In B.C.H. Steele and D. P. Thompson, editors, *British Ceramic Proceedings. Advanced Ceramics in Chemical Process Engineering.*, number 43, pages 163–171, Stoke-on-Trent, England, Dec 1988. Institute of Ceramics.

[12] A.J. Appleby. Fuel Cell Technology: Status and Future Prospects. *Energy*, **21**:521–653, 1996.

[13] L.J.M.J Blomen and M.N. Mugerwa, editors. *Fuel Cell Systems.* Plenum Press, New York, 1993.

[14] B. C. H. Steele. Ceramic ion conducting membranes. *Curr. Opin. Solid State Mater. Sci.*, **1**:684–691, 1996.

[15] G. H. Jonker and J. H. Van Santen. Ferromagnetic compounds of manganese with perovskite structure. *Physica*, **16**:337–349, 1950.

[16] G.H. Jonker and J.H. Van Santen. Magnetic Compounds with Perovskite Structure III. Ferromagnetic Compounds of Cobalt. *Physica*, **19**:120–130, 1953.

[17] H. L. Yakel. On the structure of some compounds of the perovskite type. *Acta Cryst.*, **8**:394–398, 1955.

[18] Z. Friedman and S. Shtrikman. Neutron Diffraction Study of Dicalcium Ferrite. *Phys. Lett.*, **25A**:9–10, 1967.

[19] T. Takeda, Y. Yamaguchi, S. Tomioshi, M. Fukase, M. Sugimoto, and H. Watanabe. Magnetic Structure of $Ca_2Fe_2O_5$. *J. Phys. Soc. Japan*, **24**:446–452, 1968.

[20] Y. Takeda, S. Naka, M. Takano, T. Shinjo, T. Takada, and M. Shimada. Preparation and Characterization of Stoichiometric $CaFeO_3$. *Mater. Res. Bull.*, **13**:61–66, 1978.

[21] E. Lucchini, S. Meriani, and D. Minichelli. An X-Ray Study of Two Phases of $BaFeO_{3-x}$. *Acta Cryst.*, **B29**:1217–1219, 1973.

[22] A.J. Jacobson. A Powder Neutron Diffraction Study of the Structure of and Oxygen Vacancy Distribution in 6H $BaFeO_{2.79}$. *Acta Cryst.*, **B32**:1087–1090, 1976.

[23] J.-C. Grenier, A. Wattiaux, M. Pouchard, P. Hagenmuller, M. Parras, M. Vallet, J. Calbet, and M.A. Alario-Franco. On the System $BaFeO_{3-y}$ $(0 < y \leq 0.50)$. *J. Solid State Chem.*, **80**:6–11, 1989.

[24] J.M. Gonzalez-Calbet, M. Parras, M. Vallet-Regi, and J.C. Grenier. Nonstoichiometry in $BaFeO_{3-y}$ $(0.35 < y < 0.50)$. *J. Solid State Chem.*, **86**:149–159, 1990.

[25] T. Takeda, Y. Yamaguchi, and H. Watanabe. Magnetic Structure of $SrCoO_{2.5}$. *J. Phys. Soc. Japan*, **33**:970–972, 1972.

[26] H. Taguchi, M. Shimada, and M. Koizumi. The Effect of Oxygen Vacancy on the Magnetic Properties in the System $SrCoO_{3-\delta}$ $(0 < \delta < 0.5)$. *J. Solid State Chem.*, **29**:221–225, 1979.

[27] J. H. Van Santen and G. H. Jonker. Electrical conductivity of ferromagnetic compounds of manganese with perovskite structure. *Physica*, **16**:599–600, 1950.

[28] G. H. Jonker. Semiconducting properties of mixed crystals with perovskite structure. *Physica*, **20**:1118–1122, 1954.

[29] H. Watanabe. Magnetic properties of perovskites containing strontium. I. Strontium rich ferrites and cobaltites. *J. Phys. Soc. Japan*, **12**:515–522, 1957.

[30] J. Hombo, Y. Matsumoto, and T. Kawano. Electrical conductivities of $SrFeO_{3-\delta}$ and $BaFeO_{3-\delta}$ perovskites. *J. Solid State Chem.*, **84**:138–143, 1990.

[31] J. H. Kuo, H. U. Anderson, and D. M. Spralin. Oxidation-reduction behavior of undoped and Sr-doped $LaMnO_3$: defect structure, electrical conductivity, and thermoelectric power. *J. Solid State Chem.*, **87**:55–63, 1990.

[32] Y. Moritomo, A. Asamitsu, H. Kuwahara, and Y. Tokura. Giant magnetoresistance of manganese oxides with a layered perovskite structure. *Nature*, **380**:141–144, 1996.

[33] M. R. Ibarra and J. M. De Teresa. Colossal magnetoresistance in manganese oxide perovskites. *J. Magn. Magn. Mater.*, **177–181**:846–849, 1998.

[34] M. Izumi, Y. Murakami, Y. Konishi, T. Manako, M. Kawasaki, and Y. Tokura. Structure characterisation and magnetic properties of oxide superlattices $La_{0.6}Sr_{0.4}MnO_3/La_{0.6}Sr_{0.4}FeO_3$. *Phys. Rev.*, **B60**:1211–1215, 1999.

[35] C. Brisi and P. Rolando. Ricerche sul sistema ossido di stronzio-ossido ferrico-ossigeno. *Ann. d. Chimica (Rome)*, **59**:385–399, 1969.

[36] P. Batti. Diagramma D'equilibrio Del Sistema SrO-Fe_2O_3. *Ann. d. Chimica*, **52**:941–961, 1962.

[37] P. K. Gallagher, J. B. MacChesney, and D. N. E. Buchanan. Mössbauer Effect in the System $Sr_3Fe_2O_{6-7}$. *J. Chem. Phys.*, **45**:2466–2471, 1966.

[38] E. Lucchini, D. Minichelli, and G. Sloccari. The crystal structure of α-$Sr_3Fe_2O_{7-x}$. *Acta Cryst. B*, **29**:2356–2357, 1973.

[39] E. Lucchini, D. Minichelli, and G. Sloccari. Polymorphism in $Sr_3Fe_2O_{7-x}$. *J. Mater. Sci.*, **9**:212–216, 1974.

[40] S. E. Dann, M. T. Weller, and D. B. Currie. Structure and oxygen stoichiometry in $Sr_3Fe_2O_{7-x}$, $0 \leq x \leq 1.0$. *J. Solid State Chem.*, **97**:179–185, 1992.

[41] R. Scholder, H. V. Bunsen, and W. Zeiss. Über Orthoferrate (IV). *Z. Anorg. Allgem. Chem.*, **283**:330–337, 1956.

[42] S. E. Dann, M. T. Weller, and D. B. Currie. The synthesis and structure of Sr_2FeO_4. *J. Solid State Chem.*, **92**:237–240, 1991.

[43] E. Lucchini, D. Minichelli, and G. Sloccari. X-ray characterization of $7SrO{\cdot}5Fe_2O_3$. *J. Am. Cer. Soc.*, **57**:42–43, 1974.

[44] F. Kanamaru, M. Shimada, and M. Koizumi. Crystallographic properties of and Mössbauer effect in $Sr_4Fe_6O_{13}$. *J. Phys. Chem. Solids*, **33**:1169–1171, 1972.

[45] A. Yoshiasa, K. Ueno, F. Kanamaru, and H. Horiuchi. Structure of $Sr_4Fe_6O_{13}$, a new perovskite-derivative in the Sr-Fe-O system. *Mater. Res. Bull.*, **21**:175–181, 1986.

[46] J. Beretka and T. Brown. Studies on the Reaction Between Strontium Carbonate and Iron (III) Oxide. *Aust. J. Chem.*, **24**:237–242, 1971.

[47] F. Habery and A. Kockel. The formation of strontium hexaferrite $SrFe_{12}O_{19}$ from pure iron oxide and strontium carbonate. *IEEE Trans. Magn.*, **12**:983–985, 1976.

[48] V. Adelsköld. Magnetoplumbit, $PbO{\cdot}Fe_2O_3$. *Z. Kristallogr. (Structurbericht VI 1938)*, **6**:74–75, 1941.

[49] A.R. West. *Basic Solid State Chemistry.* Wiley, New York, 1988.

[50] A.R. West. *Solid State Chemistry and its Applications.* Wiley, New York, 1984.

[51] F. Daniels and R.A. Alberty. *Physical Chemistry.* John Wiley & Sons, Inc., New York, 3rd edition, 1966.

[52] Shimadzu Corporation, Analytical Instruments Division, Kyoto, Japan. *TGA-50 Thermogravimetric Analyser Instruction Manual*, 1989.

[53] Shimadzu Corporation, Analytical Instruments Division, Kyoto, Japan. *DTA-50 Differential Thermal Analyzer, Instruction Manual*, 1989.

[54] Shimadzu Corporation, Analytical Instruments Division, Kyoto, Japan. *DSC-50 Differential Scanning Calorimeter, Instruction Manual*, 1989.

[55] M. J. Buerger. *Vector space and its application in crystal-structure investigation.* John Wiley & Sons, Inc., New York, 1959.

[56] M. J. Buerger. *Crystal-structure analysis.* John Wiley & Sons, Inc., New York, London, 1960.

[57] M. M. Woolfson. *An introduction to x-ray crystallography.* Cambridge University Press, 2nd edition, 1997.

[58] M.M. Woolfson. *Direct Methods in Crystallography.* Oxford at the Clarendon Press, 1961.

[59] H. Lipson and W. Cochran. *The Determination of Crystal Structures.* The Crystalline State. Vol. III. G. Bell and Sons Ltd., London, 1953.

[60] G.S. Pawley. Unit-Cell Refinement from Diffraction Scans. *J. Appl. Cryst.*, **14**:357–361, 1981.

[61] A. Le Bail, H. Duroy, and J.L. Fourquet. Ab-Initio Structure Determination of $LiSbWO_6$ by X-Ray Powder Diffraction. *Mater. Res. Bull.*, **23**:447–452, 1988.

[62] R.B. Von Dreele. Rietveld Analysis of High Pressure Powder Diffraction Data. *High Pressure Research*, **14**:321–326, 1996.

[63] H. P. Klug and L. E. Alexander. *X-ray diffraction procedures for polycrystalline and amorphous materials.* John Wiley & Sons, New York, 2nd edition, 1974.

[64] D.L. Bish and J.E. Post, editors. *Modern Powder Diffraction.* Reviews in Mineralogy, Volume 20. Mineralogical Society of America, 1989.

[65] H. M. Rietveld. A profile refinement method for nuclear and magnetic structures. *J. Appl. Cryst.*, **2**:65–71, 1969.

[66] A.C. Larson and R.B. Von Drele. GSAS General Structure Analysis System. Technical Report LAUR 86-748, Los Alamos National Laboratory, 1994.

[67] G. Caglioti, A. Paoletti, and F. P. Ricci. Choice of collimators for a crystal spectrometer for neutron diffraction. *Nucl. Instrum.*, **3**:223–228, 1958.

[68] M.J. Cooper and J.P. Sayer. The Asymmetry of Neutron Powder Diffraction Peaks. *J. Appl. Cryst.*, **8**:615–618, 1975.

[69] M.W. Thomas. Peak Shifts and Peak Broadening in Powder Neutron-Diffraction Patterns Due to Finite Aperture Counters. *J. Appl. Cryst.*, **10**:12–13, 1977.

[70] C.J. Howard. The Approximation of Asymmetric Neutron Powder Diffraction Peaks by Sums of Gaussians. *J. Appl. Cryst.*, **15**:615–620, 1982.

[71] R.A. Young and D.B. Wiles. Profile Shape Functions in Rietveld Refinements. *J. Appl. Cryst.*, **15**:430–438, 1982.

[72] B. Van Laar and W.B. Yelon. The Peak in Neutron Diffraction. *J. Appl. Cryst.*, **17**:47–54, 1984.

[73] P. Thompson, D.E. Cox, and J.B. Hastings. Rietveld Refinement of Debye-Scherrer Synchrotron X-Ray Data from Al_2O_3. *J. Appl. Cryst*, **20**:79–83, 1987.

[74] D.E. Finger, L.W.and Cox and A.P. Jephcoat. A Correction for Powder Diffraction Peak Asymmetry Due to Axial Divergence. *J. Appl. Cryst.*, **27**:892–900, 1994.

[75] P.W. Stephens. Phenomenological Model of Anisotropic Peak Broadening in Powder Diffraction. *J. Appl. Cryst.*, **32**:281–289, 1999.

[76] R. A. Young, editor. *The Rietveld method.* IUCr Monographs on crystallography. 5. International Union of Crystallography, Oxford University Press, 1993.

[77] W. Parrish, T.C. Huang, and G.L. Ayers. Profile Fitting: A Powerful Method of Computer X-Ray Instrumentation and Analysis. *Trans. Am. Cryst. Assoc.*, **12**:55–74, 1976.

[78] S. Enzo, S. Polizzi, and A. Benedetti. Applications of Fitting Techniques to the Warren-Averbach Method for X-Ray Line Brodening Analysis. *Z. Kristall.*, **170**:275–287, 1985.

[79] J.I. Langford. A Rapid Method for Analysing the Breadths of Diffraction and Spectral Lines Using the Voigt Function. *J. Appl. Cryst.*, **11**:10–14, 1978.

[80] A.R. Stokes. A Numerical Fourier-Analysis Method for the Correction of Widths and Shapes of Lines on X-Ray Powder Phothographs. *Proc. Phys. Soc. (London)*, **61**:382–391, 1948.

[81] B.E. Warren and B.L. Averbach. The Effect of Cold-Work Distortion on X-Ray Patterns. *J. Appl. Phys.*, **21**:595–599, 1950.

[82] B.E. Warren. X-Ray Studies of Deformed Metals. *Progress in Metal Physics*, **8**:147–202, 1959.

[83] W. H. Hall. X-ray line broadening in metals. *Proc. Phys. Soc. London*, **A62**:741–743, 1949.

[84] G. E. Bacon. *Neutron diffraction.* Oxford at the Clarendon press, 2nd, 1962.

[85] G.E. Bacon. *Applications of Neutron Diffraction in Chemistry.* Pergamon Press, Oxford, 1963.

[86] H. Dachs. Principles of Neutron Diffraction. In H. Dachs, editor, *Neutron Diffraction*, pages 1–40. Springer-Verlag, Berlin, 1978.

[87] W. Marshall and S. W. Lovesey. *Theory of thermal neutron scattering. The use of neutrons for the investigation of condensed matter.* Oxford at Clarendon press, 1971.

[88] T. Hahn, editor. *International Tables for Crystallography*, volume C: Mathematical, Physical and Chemical Tables. D. Reidel Pub. Co., Dordrecht, Holland ; Boston, U.S.A., 1983.

[89] R. Jenkins. Instrumentation. In D.L. Bish and J.E. Post, editors, *Modern Powder Diffraction, Reviews in Mineralogy Volume 20*, pages 19–45. Mineralogical Society of America, 1989.

[90] Philips. *PW 1050/25 Goniometer.*

[91] Philips. *PW 1050 X'Change Goniometer Packages, Installation Manual*, 1st edition, September 1993.

[92] R.F. Garrett, D.J. Cookson, G.J. Foran, T.M. Sabine, B.J. Kennedy, and S.W. Wilkins. Powder Diffraction Using Imaging Plates at the Australian National Beamline Facility at the Photon Factory. *Rev. Sci. Instrum.*, **66**:1351–1353, 1995.

[93] Y. Amemiya and J. Miyahara. Imaging Plate Illuminates Many Fields. *Nature*, **336**:89–90, 1988.

[94] S.J. Kennedy. Applications of Neutron Powder Diffraction in Materials Research. *Adv. X-ray Analysis*, **38**:35–46, 1995.

[95] R. Knott. Neutron Scattering in Australia. *Neutron News*, **9**:23–32, 1998.

[96] J. Jing, S.J. Campbell, and J. Pellegrino. A Stand-Alone Mössbauer Spectrometer Based on the MC68008 Microprocessor. *Meas. Sci. Technol.*, **3**:80–84, 1992.

[97] U. Gonser. From a Strange Effect to Mössbauer Spectroscopy. In U. Gonser, editor, *Mössbauer Spectroscopy*, pages 1–51. Springer-Verlag, Berlin Heidelberg New York, 1975.

[98] P. Gütlich. Mössbauer Spectroscopy in Chemistry. In U. Gonser, editor, *Mössbauer Spectroscopy*, pages 53–96. Springer-Verlag, Berlin Heidelberg New York, 1975.

[99] A.Z. Juhász and L. Opoczky. *Mechanical Activation of Minerals by Grinding: Pulverizing and Morphology of Particles.* Ellis Horwood Ltd. Publishers, Chichester, 1990.

[100] D.R. Maurice and T.H. Courtney. The Physics of Mechanical Alloying: A First Report. *Metall. Trans.*, **21A**:289–303, 1990.

[101] V.V. Boldyrev. Mechanochemistry and Mechanical Activation of Solids. *Solid State Ionics*, **63–65**:537–543, 1993.

[102] V. Boldyrev and E. Boldyreva. Mechanochemistry of Interfaces. *Mater. Sci. Forum*, **88–90**:711–714, 1992.

[103] B.S. Murty and S. Ranganathan. Novel Materials Synthesis by Mechanical Alloying/Milling. *Inter. Mater. Rev.*, **43**:101–141, 1998.

[104] E. Gaffet, F. Bernard, J.-C. Niepce, F. Charlot, C. Gras, G. Le Caër, J.-L. Guichard, P. Delcroix, A. Mocellin, and O. Tillement. Some Recent Developments in Mechanical Activation and Mechanosynthesis. *J. Mater. Chem.*, **9**:305–314, 1999.

[105] A. Calka and A. P. Radlinski. Universal high performance ball-milling device and its applications for mechanical alloying. *Mater. Sci. Eng.*, **A134**:1350–1353, 1991.

[106] P. Millet, A. Calka, J.S. Williams, and G.J.H. Wantenaar. Formation of Gallium Nitride by a Novel Hot Mechanical Alloying Process. *Appl. Phys. Lett.*, **63**:2505–2507, 1993.

[107] W.A. Kaczmarek and B.W. Ninham. Preparation of Fe_3O_4 and γ-Fe_2O_3 Powders by Magnetomechanical Activation of Hematite. *IEEE Trans. Mag.*, **30**:732–734, 1994.

[108] S. Linderoth, J.Z. Jiang, and S. Mørup. Reversible α-Fe_2O_3 to Fe_3O_4 Transformation During Ball Milling. *Mater. Sci. Forum*, **235–238**:205–210, 1997.

[109] Z.L. Li, J.S. Williams, and A. Calka. The Role of Hydrogen and Iron in Silicon Nitridation by Ball Milling. *J. Appl. Phys.*, **81**:8029–8034, 1997.

[110] N.J. Welham. Novel Route to Submicrometer Tungsten Carbide. *J. Am. Inst. Chem. Eng.*, **46**:68–71, 2000.

[111] S. Brunauer, P.H. Emmett, and E. Teller. Adsorption of Gases in Multimolecular Layers. *J. Am. Chem. Soc.*, **60**:309–319, 1938.

[112] Micromeritics Instrument Corporation. *Gemini II 2370 Surface Area Analyzer, Operator's Manual v3.02*, 1994.

[113] S. Foner. Versatile and Sensitive Vibrating-Sample Magnetometer. *Rev. Sci. Instrum.*, **30**:548–557, 1959.

[114] S. Foner. The Vibrating Sample Magnetometer: Experiences of a Volunteer. *J. Appl. Phys.*, **79**:4740–4745, 1996.

[115] I. Barin, O. Knacke, and O. Kubaschewski. *Thermodynamical properties of inorganic substances*, volume Supplement 1977. Springer-Verlag, Berlin and New York, 1973.

[116] I. Barin. *Thermodynamical data of pure substances.* VCH Verlags Gesellschaft, Weinheim, 1989.

[117] O. Knacke, O. Kubaschewski, and K. Hesselmann. *Thermodynamical properties of inorganic substances.* Springer-Verlag, Berlin, Heidelberg, 1991.

[118] I. Barin. *Thermodynamical data of pure substances.* VCH Verlags Gesellschaft, Weinheim, 1993.

[119] K. Watanabe. Kinetics of Solid-State Reaction of BaO_2 and α -Fe_2O_3. *J. Am. Cer. Soc.*, **81**:733–737, 1998.

[120] S.E. Jacobo and M.A. Blesa. The Thermal Evolution of a Barium Ferrite Precursor Obtained by a New Chemical Coprecipitation Method. *Journal de Physique IV*, **7**:319–320, 1997.

[121] H.P. Steier, J. Requena, and J.S. Moya. Transmission Electron Microscopy Study of Barium Hexaferrite Formation from Barium Carbonate and Hematite. *J. Mater. Res.*, **14**:3647–3652, 1999.

[122] R.A. Swalin. *Thermodynamics of Solids.* John Wiley & Sons, New York, 2nd edition, 1972.

[123] H. Yokokawa, N. Sakai, T. Kawada, and M. Dokiya. Thermodynamic Stabilities of Perovskite Oxides for Electrodes and Other Electrochemical Materials. *Solid State Ionics*, **52**:43–56, 1992.

[124] N.J. Welham. Ambient-Temperature Formation of Metal Titanates from Ilmenite ($FeTiO_3$). *J. Mater. Sci.*, **33**:1795–1799, 1998.

[125] J.B. MacChesney, R.C. Sherwood, and J.F. Potter. Electric and Magnetic Properties of Strontium Ferrates. *J. Chem. Phys.*, **43**:1907–1913, 1965.

[126] B. C. Tofield, C. Greaves, and B. E. F. Fender. The $SrFeO_{2.5}$-$SrFeO_{3.0}$ system evidence of a new phase $Sr_4Fe_4O_{11}$ ($SrFeO_{2.75}$). *Mater. Res. Bull.*, **10**:737–746, 1975.

[127] Y. Takeda, K. Kanno, T. Takada, O. Yamamoto, M. Takano, N. Nakayama, and Y. Bando. Phase relation in the oxygen nonstoichiometric system, $SrFeO_x$ ($2.5 \leq x \leq 3.0$). *J. Solid State Chem.*, **63**:237–249, 1986.

[128] J. Mizusaki, M. Okayasu, S. Yamaguchi, and K. Fueki. Nonstoichiometry and Phase Relationship of the $SrFeO_{2.5}$-$SrFeO_3$ System at High Temperature. *J. Solid State Chem.*, **99**:166–172, 1992.

[129] S. Shin, Y. Hatakeyama, K. Ogawa, and K. Shinomura. Catalytic Decomposition of NO over Brownmillerite-Like Compounds, $Ca_2Fe_2O_5$ and $Sr_2Fe_2O_5$. *Mater. Res. Bull.*, **14**:133–136, 1979.

[130] F.D. Bloss. *Crystallography and Crystal Chemistry.* Mineralogical Society of America, Washington, D.C., 1994.

[131] P. K. Gallagher, J. B. MacChesney, and D. N. E. Buchanan. Mössbauer Effect in the System $SrFeO_{2.5-3.0}$. *J. Chem. Phys.*, **41**:2429–2434, 1964.

[132] A.I. Vogel. *A Text-book of Macro and Semimicro Qualitative Inorganic Analysis.* Longmans, 4th edition, 1954.

[133] A.I. Vogel. *A Text-Book of Quntitative Inorganic Analysis. Including Elementary Instrumental Analysis.* Longmans, 3rd edition, 1961.

[134] W.F. Hillebrand, G.E.F. Lundell, M.S. Bright, and J.I. Hoffman. *Applied Inorganic Analysis with Special Reference to the Analysis of Metals, Minerals and Rocks.* John Wiley & Sons, Inc., New York, 1959.

[135] H.K. Cammenga. Evaporation Mechanisms of Liquids. In E. Kaldis, editor, *Current Topics in Materials Science*, volume 5, pages 335–446. North-Holland Publishing Company, Amsterdam, 1980.

[136] T.B. Reed. The Role of Oxygen Pressure in the Control and Measurement of Composition in 3d Metal Oxides. In L. Eyring and M. O'Keeffe, editors, *The Chemistry of Extended Defects in Non-Metallic Solids*, pages 21–35, Amsterdam, 1970. North Holland Publishing Company.

[137] H. Taguchi. Electrical Properties of $SrFeO_{3-\delta}$ under Various Partial Pressures of Oxygen. *J. Mater. Sci. Lett.*, **2**:665–666, 1983.

[138] J.-C. Grenier, N. Ea, M. Pouchard, and P. Hagenmuller. Structural Transitions at High Temperature in $Sr_2Fe_2O_5$. *J. Solid State Chem.*, **58**:243–252, 1985.

[139] J.P. Hodges, S. Short, J.D. Jorgensen, X. Xiong, B. Dabrowski, S.M. Mini, and C.W. Kimball. Evolution of Oxygen-Vacancy Ordered Crystal Structures in the Perovskite Series $Sr_nFe_nO_{3n-1}$ ($n = 2, 4, 8, \text{and } \infty$), and the Relationship to Electronic and Magnetic Properties. *J. Solid State Chem.*, **151**:190–209, 2000.

[140] A. Wattiaux, L. Fournès, A. Demourgues, N. Bernaben, J.C. Grenier, and M. Pouchard. A Novel Preparation Method of the $SrFeO_3$ Cubic Perovskite by Electrochemical Means. *Solid State Comm.*, **77**:489–493, 1991.

[141] T.M. Lowry and A.C. Cavell. *Intermediate Chemistry.* Macmillan & Co. Ltd., New York, 6th edition, 1954.

[142] R.J. Reeder, editor. *Carbonates: Mineralogy and Chemistry.* Reviews in Mineralogy, Volume 11. Mineralogical Society of America, 1990.

[143] W. Stumm. *Chemistry of the Solid-Water Interface. Processes at the Mineral-Water and Particle-Water Systems.* A Wiley-Interscience Publication, New York, 1992.

[144] R.J. McKay and R. Worthington. *Corrosion Resistance of Metals and Alloys.* Reinhold Publishing Corporation, New York, 1936.

[145] E. Erdös and H. Altorfer. Ein Dem Malachit Ähnliches Basisches Eisenkarbonat Als Korrosionproduct Von Stahl. *Werkstoffe und Korrosion*, **27**:304–312, 1976.

[146] B.C. Tofield. Studies on Non-Stoichiometric Strontium Ferrate, $SrFeO_{3-x}$. In J Wood, O. Lindqvist, C. Helgesson, and N.-G. Vannerberg, editors, *Reactivity of Solids*, pages 253–259, New York, 1977. Plenum Press.

[147] M. Takano, T. Okita, N. Nakayama, Y. Bando, Y. Takeda, O. Yamamoto, and J.B. Goodenough. Dependence of the Structure and Electronic State of $SrFeO_x$ ($2.5 \leq x \leq 3.0$) on Composition and Temperature. *J. Solid State Chem.*, **73**:140–150, 1988.

[148] L. Fournes, Y. Potin, J.C. Grenier, and P. Hagenmuller. Ensemble Pour Spectrométrie Mössbauer Haute Température in Situ. Evolution Thermique Des Paramètres Mössbauer de $SrFeO_{2,50}$. *Reveue Phys. Appl.*, **24**:463–468, 1989.

[149] T.C. Gibb. Magnetic Exchange Interactions in Perovskite Solid Solutions. Part 5. The Unusual Defect Structure of $SrFeO_{3-y}$. *J. Chem. Soc. Dalton Trans.*, pages 1455–1470, 1985.

[150] L. Fournès, Y. Potin, J.C. Grenier, G. Demazeau, and M. Pouchard. High Temperature Mössbauer Spectroscopy of some $SrFeO_{3-y}$ Phases. *Solid State Commun.*, **62**:239–244, 1987.

[151] S. Wißmann and K.D. Becker. Localization of Electrons in Nonstoichiometric $SrFeO_{3-\Delta}$. *Solid State Ionics*, **85**:279–283, 1996.

[152] S. Nasu, T. Abe, K. Yamamoto, S. Endo, M. Takano, and Y. Takeda. ^{57}Fe Mössbauer Study of $SrFeO_3$ Under Ultra-High Pressure. *Hyperfine Interact.*, **67**:529–532, 1991.

[153] N.N. Greenwood and T.C. Gibb. *Mössbauer Spectroscopy.* Chapman and Hall Ltd., London, 1971.

[154] T. Takeda, Y. Yamaguchi, and H. Watanabe. Magnetic Structure of $SrFeO_3$. *J. Phys. Soc. Japan*, **33**:967–969, 1972.

[155] G.J. Long and F. Grandjean. *Advances in Solid-State Chemistry*, volume 2, chapter Mössbauer Effect, Magnetic and Structural Studies of Wüstite, Fe_xO, pages 187–221. JAI Press Ltd., 1991.

[156] A.A. Bahgat and M.K. Fayek. On the Hyperfine Structures in the M-Type Hexaferrite. *Hyperfine Interactions*, **8**:249–254, 1980.

[157] X. Obradors, X. Solans, A. Collomb, D. Samaras, J. Rodriguez, M. Pernet, and M. Font-Altaba. Crystal Structure of Strontium Hexaferrite $SrFe_{12}O_{19}$. *J. Solid State Chem.*, **72**:218–224, 1988.

[158] H. Oda, Y. Yamaguchi, H. Takei, and H Watanabe. Single Crystal Neutron Diffraction Study of $SrFeO_{3-x}$ ($x = 0.1$). *J. Phys. Soc. Japan*, **42**:101–106, 1977.

[159] S. Shin, M. Yonemura, and H. Ikawa. Order-Disorder Transition of $Sr_2Fe_2O_5$ from Brownmillerite to Perovskite Structure at an Elevated Temperature. *Mater. Res. Bull.*, **13**:1017–1021, 1978.

[160] C. Greaves, A.J. Jacobson, B.C. Tofield, and B.E.F. Fender. A Powder Neutron Diffraction Investigation of the Nuclear and Magnetic Structure of $Sr_2Fe_2O_5$. *Acta Cryst.*, **B31**:641–646, 1975.

[161] M. Harder and Hk. Müller-Buschbaum. Darstellung und Untersuchung Von $Sr_2F_2O_5$-Einkristallen ein Beitrag Zur Kristallchemie Von $M_2F_2O_5$-Verbindungen. *Z. anorg. allg. Chem.*, **464**:169–175, 1980.

[162] A.V. Shubnikov, N.V. Belov, et al. *Colored Symmetry.* Pergamon Press, Oxford, 1964.

[163] W. Prandl. The Determination of Magnetic Structures. In H. Dachs, editor, *Neutron Diffraction*, pages 113–149. Springer-Verlag, Berlin, 1978.

[164] T. Takeda, Y. Yamaguchi, H. Watanabe, S. Tomiyoshi, and H. Yamamoto. Crystal and Magnetic Structures of $Sr_2Fe_2O_5$. *J. Phys. Soc. Japan*, **26**:1320, 1969.

[165] *JCPDS-ICDD PDF-2*, **File No. 33-677**.

[166] M.A. Alario-Franco, J.C. Joubert, and J.P. Lévy. Anion Deficiency in Iron Perovskites: The $Sr_xNd_{1-x}O_{3-y}$ Solid Solution I: $0.6 < x < 0.8$. *Mater. Res. Bull.*, **17**:733–740, 1982.

[167] M.A. Alario-Franco, J.M. Gonzalez-Calbet, and M. Vallet-Regi. Brownmillerite-Type Microdomains in the Calcium Lanthanum Ferrites: $Ca_xLa_{1-x}FeO_{3-y}$ I. $\frac{2}{3} < x < 1$. *J. Solid State Chem.*, **49**:219–231, 1983.

[168] M. Vallet-Regi, J.M. Gonzalez-Calbet, J. Verde, and M.A. Alario-Franco. Microdomain Formation in the $CaFe_xMn_{1-x}O_{3-y}$ Ferrites I. $0.2 \leq x \leq 0.4$. *J. Solid State Chem.*, **57**:197–206, 1985.

[169] J.M. González-Calbet, M. Vallet-Regí, and M.A. Alario-Franco. Microdomains in the Reduction of $Ca_2LaFe_3O_{8+z}$. *J. Solid State Chem.*, **60**:320–331, 1985.

[170] N. Nakayama, M. Takano, S. Inamura, N. Nakaishi, and K. Kosuge. Electron Microscopy Study of the "Cubic" Perovskite Phase $SrFe_{1-x}V_xO_{2.5+x}$ $(0.05 \leq x \leq 0.1)$. *J. Solid State Chem.*, **71**:403–417, 1987.

[171] *JCPDS-ICDD PDF-2*, **File No. 40-905**.

[172] R.J. Gambino and F. Leonhard. Growth of Barium Ferrite Single Crystals. *J. Am. Cer. Soc.*, **44**:221–224, 1961.

[173] K. Watanabe. Growth of Minute Barium Ferrite Single Crystals from a Na_2O-B_2O_3 Flux System. *J. Cryst. Growth*, **169**:509–518, 1996.

[174] Rubotherm Präzisionsmeßtechnik. *http://www.rubotherm.de*. Bochum, Germany.